

**Centrifuge Modeling and Large Deformation Analyses of Axially Loaded Helical Piles in
Cohesive Soils**

by

Weidong Li

A thesis submitted in partial fulfillment of the requirements for the degree of

Doctor of Philosophy

in

GEOTECHNICAL ENGINEERING

Department of Civil and Environmental Engineering

University of Alberta

©Weidong Li, 2022

Abstract

In the past decades, helical piles have gained increasing popularity in civil engineering practice as an option of deep foundations. The design of axial load capacity of these piles relies on an appropriate selection of failure mode. Currently, the axial failure modes of multi-helix piles are categorized into the individual bearing mode (IBM) and cylindrical shearing mode (CSM). The ratio (S_r) of inter-helix spacing to helix diameter is used as the primary indicator of failure mode. The industry adopts S_r of 3.0 as the only criteria, but a number of field tests indicate that the soil strength and pile embedment depth may also affect the failure mode. However, a comprehensive study aimed at all these factors is unavailable yet.

To improve our understanding of the axial behavior of helical piles in cohesive soils, a centrifuge modeling test program for helical piles was conducted. A test frame was developed to install and axially load helical piles in flight. The real-time installation torque and axial shaft load distributions were measured. One single-helix pile and three double-helix piles with S_r varied from 1.5 to 3.5 were tested in two types of kaolinite clay with undrained shear strength (s_u) of approximately 50 kPa (denoted as “medium stiff clay” in this thesis) and 120 kPa (“stiff clay”), respectively. Each model pile was installed and axially loaded under 20 g centrifugal condition. Specifically, the research was aimed at pile installation torque, installation-induced excess pore pressure in the soil, and pile failure mechanisms under monotonic axial loads. An analytical solution to the installation torque of helical piles in cohesive soils was proposed and verified by measured torques. The analysis indicates that the residual s_u of the soil governs the soil-pile interactions during rotation. The pore pressure response to pile installation was monitored near two piles at two depths, in the stiff clay. An analytical solution to pile installation-induced spatial consolidation was adopted to assess the measured progression of excess pore pressure dissipation.

To observe the failure modes, the model piles were pulled out of the soil immediately after loading. Three failure modes were observed, i.e., IBM, CSM and a transitional failure mode (TFM) with a cone-shaped inter-helix soil mass. The axial load transfer mechanisms of the tested piles were assessed using the axial load distribution measurements. The results show that IBM and CSM models may over-predict the axial capacity of a helical pile governed by TFM. In addition, the failure modes depend on s_u and S_r .

To further explore the axial failure mechanisms of the double-helix piles in a wider range of controlling factors, finite element modeling of helical piles in cohesive soils was conducted. Because of the large displacement required for pile failure observation, large deformation finite element (LDFE) analyses based on the remeshing and interpolation technique with small strain were performed. The LDFE model was validated by the centrifuge model test results. The effects of S_r , s_u , and pile embedment depth on the generation of failure mode were assessed. The simulation results show that the failure mode changes gradually from CSM to IBM with an increasing inter-helix spacing. CSM occurs when S_r is adequately small, and s_u of the clay is sufficiently high. In general, CSM provide greater optimal uplift capacity as S_r increases. However, when S_r approaches 2.5, using CSM for axial capacity design may become inaccurate. The helix break-out factors of lower helices, which may be affected by the above inter-helix soil collapse mechanisms, change with the failure modes. The bearing factors of the lower helices, which may not be affected by the inter-helix soil behavior, remain essentially unchanged with the variation of failure modes.

Preface

The major contents of Chapters 4 have been submitted to *Soils and Foundations* for possible publication. Chapter 5 will be prepared as a technical paper soon. Although these manuscripts are coauthored by Lijun Deng and Rick Chalaturnyk, the majority of the writing, the laboratorial work, data processing, and numerical simulations were performed by the candidate.

Acknowledgements

I wish to extend the greatest thanks to my supervisor, Dr. Lijun Deng, for his leading and support in the past five years. Throughout this program, Dr. Deng's passion for geotechnical engineering research motivated and inspired me. I am grateful for the precious time and hard work that he has devoted to my learning and research. This research would not have been possible without the financial support of the Natural Sciences and Engineering Research Council of Canada (NSERC), under the Engage Collaborative R&D program (CRDPJ 485776-15), with the financial contribution from Almita Piling Ltd. I would also like to thank Amita for their technical support. Also, thanks to Yazhao Wang, Gonzalo Zambrano, Gilbert Wong, Lukas Duerkson, and staff of GeoCERF centrifuge lab facilities at the University of Alberta. Development of the centrifuge lab facilities was supported primarily by the Canada Foundation for Innovation.

Table of Contents

Abstract	ii
Preface.....	iv
Acknowledgements	v
Table of Contents	vi
List of Tables.....	xi
List of Figures	xii
1 Introduction.....	1
1.1 Background.....	1
1.2 Problem Statement.....	6
1.3 Research Objectives	7
1.4 Scope and Contribution of Present Research	7
1.5 Thesis Organization	9
2 Literature Review	11
2.1 Introduction	11
2.2 Axial Pile Capacities	11
2.2.1 Bearing Capacity of Pile Toe	12
2.2.2 Uplift Capacity of Soil Anchor	14
2.2.3 Current Design Frameworks of Helical Piles.....	18

2.2.4	Efficiency of Current Design Methods	22
2.3	Installation Torque.....	24
2.4	Installation-Induced Pore Pressure	27
2.4.1	Set-up Effect.....	27
2.4.2	Analytical Solutions to Installation-Induced Excess Pore Pressure.....	29
2.5	Axial Failure Mechanisms of Helical Piles	30
2.6	Centrifuge Modeling Methods.....	32
2.7	Finite Element Methods of Soil-Foundation Interaction.....	35
2.8	Summary.....	42
3	Development of Centrifuge Test System and Testing Program	44
3.1	Introduction	44
3.2	Loading Frame.....	45
3.2.1	Soil Container.....	45
3.2.2	Installation Gear Motor	46
3.2.3	Dual-Axis Actuator	49
3.3	Model Piles	50
3.3.1	Pile Fabrication	50
3.3.2	Pile Instrumentation	52
3.3.3	Principle of Strain Gauge Measurement and Calibration of Gauges	55
3.4	Pore Pressure Transducers.....	58

3.5	Soil Model Construction.....	62
3.5.1	Consolidation	63
3.5.2	Soil Properties Interpreted from Consolidation Results.....	64
3.6	Data Acquisition Control.....	69
3.7	Test Layout and Test Matrix	70
3.8	Summary, original contribution and limitations.....	74
3.8.1	Summary	74
3.8.2	Original contribution.....	74
3.8.3	Limitations of experimental setup.....	75
4	Centrifuge Modeling of Axially Loaded Helical Piles in Cohesive Soils.....	77
4.1	Introduction	77
4.2	Testing Program	79
4.2.1	Soil Properties	80
4.2.2	Model Pile and Instrumentation	84
4.2.3	Test Pile Layout	87
4.2.4	Install-and-Load Frame	88
4.2.5	Pore Pressure Transducers	88
4.2.6	Axial Loading Method	90
4.3	Results: Torque and Induced Pore Pressure	90
4.3.1	A Torque Model Based on Residual Strength.....	91

4.3.2	Installation Torque: Measured vs. Predicted.....	92
4.3.3	Excess Pore Pressure Induced by Pile Installation.....	95
4.4	Results: Axial Behavior of Piles.....	99
4.4.1	Pull-Out Results of Failure Modes.....	99
4.4.2	Axial Load vs. Displacement	100
4.4.3	Axial Load Transfer Mechanism.....	103
4.5	Conclusions	109
5	Large Deformation Finite Element Analyses of Axially Loaded Helical Piles in Cohesive Soils	1
5.1	Introduction	112
5.2	Procedure of RITSS-Based LDFE.....	117
5.3	Development and Validation of LDFE Model	119
5.3.1	Numerical Model and Assumptions.....	120
5.3.2	Selected Centrifuge Model Test Results for Validating LDFE.....	123
5.3.3	Mesh Size Evaluation.....	128
5.3.4	Examination of Boundary Effects.....	131
5.4	LDFE Results and Discussions.....	134
5.4.1	Failure Modes.....	134
5.4.2	Helix Bearing Resistance	137
5.4.3	Shaft Resistance Affected by Helix	139

5.5	Parametric Studies	140
5.5.1	Effect of Embedment Depth on Failure Mode	143
5.5.2	Effect of Soil Strength and Space Ratio.....	145
5.5.3	Summary of Effects of S_r , E_H , and s_u on Failure Mode	146
5.5.4	Summary of Effect of Failure Mode on Helix Bearing Resistance.....	147
5.6	Conclusions	151
5.7	Limitations.....	152
6	Conclusions, Limitations and Recommendations.....	153
6.1	Summary and Conclusions	153
6.1.1	Experimental Study.....	154
6.1.2	LDFE Analyses	155
6.2	Limitations.....	156
6.3	Recommendations for Future Study.....	157
	References	159
	Appendix A: Drawings of Test Equipment.....	169
	Appendix B: Command Scripts of Electric Actuator.....	181
	Appendix C: More Results of Tests and Simulation.....	185
	Appendix D: Python Code Example for LDFE Analyses.....	198

List of Tables

Table 1-1. Scale factors used to convert the model data to prototype units.....	5
Table 3-1. Dimensions of the model piles	51
Table 3-2. Calibration data of axial strain gauges.....	57
Table 3-3. Calibration data of torque strain gauges	57
Table 3-4. Summary of strain gauge calibration	58
Table 3-5. Results of PPT calibration tests	61
Table 3-6. Summary of consolidation tests of speswhite kaolinite, WL01	66
Table 3-7. Summary of consolidation tests of speswhite kaolinite, WL02	67
Table 3-8. Summary of soil properties from consolidation tests in WL01	68
Table 3-9. Summary of soil properties from consolidation tests in WL02	69
Table 3-10. Test sequence of WL01	71
Table 3-11. Test sequence of WL02	71
Table 4-1. Scale factors (prototype/model).....	80
Table 4-2. Kaolinite clay properties and 1-g consolidation parameters.....	83
Table 4-3. Pile geometry	86
Table 4-4. Test matrix	87
Table 4-5. Parameters adopted in the pore pressure analysis.....	97
Table 4-6. Summary of axial capacities, final installation torque and torque factors.....	101
Table 5-1. Summary of three numerical techniques used in LDFE (after Wang et al. 2015)	118
Table 5-2. Dimensions of multi-helix Piles in prototype scale	124
Table 5-3. Input soil parameters for the numerical modeling	127
Table 5-4. Simulation matrix for the parametric studies.....	142

List of Figures

Figure 1-1. A photo of helical piles (Almita Piling)	2
Figure 1-2. Sketch of typical helical piles: (a) single-helix piles, and (b) multi-helix piles	2
Figure 1-3. Installation method of helical piles	3
Figure 1-4. (a) Functioning components of the geotechnical centrifuge at UAlberta (adapted from Zambrano-Narvaez and Chalaturnyk 2014), and (b) principles of centrifuge model tests	5
Figure 2-1. (a) Mode of shaft deformation; (b) Stressed on soil element (after Randolph and Wroth, 1978).....	12
Figure 2-2. Segments of axially loaded pile for load-transfer analysis (after Coyle and Reese, 1966)	13
Figure 2-3. (a) Slip surface of shallow anchor; (b) Slip surfaces of circular anchor at various depths (after Vesic 1971)	15
Figure 2-4. Failure of soil displaced by an uplifted strip footing (after Meyerhof and Adams 1968)	17
Figure 2-5. Failure mechanisms of multi-helix piles at different S/D ratios and embedment depth: (a) and (b) CSM shallow failure; (c) CSM deep failure; (d) IBM deep failure; after Merifield (2011).....	19
Figure 2-6. Ineffective length of the shaft during uplift loading of helical piles in clay (after Narasimha et al. 1993)	21
Figure 2-7. Ratio of predicted to measured ultimate axial capacities of helical piles, after Tappenden and Segoo (2007)	24
Figure 2-8. Calculation of installation torque using the power screw theory, after Tsuha and Aoki (2010).....	26

Figure 2-9. (a) Components of torsional resistance for vane shear test; (b) Components of torsional resistance for helix rotation, after Sakr (2013)	27
Figure 2-10. Diagram of instantaneous response of excess pore water pressure induced by helical pile installation (modified after Randolph and Wroth 1979)	28
Figure 2-11. Radial distribution of excess pore pressure around a driven helical pile, after Weech and Howie (2012)	29
Figure 2-12. Progression of the dissipation of installation –induced excess pore pressure given by the approach of Randolph and Wroth (1979)	30
Figure 2-13. Currently recognized axial failure modes of helical piles: (a) IBM, and (b) CSM after Lanyi-Bennett and Deng (2019)	31
Figure 2-14. A servo-controlled loading test setup for helical piles on centrifuge (Schiavon et al. 2016)	33
Figure 2-15. Mesh domains used for analyzing: (a) rectangular or square anchors, and (b) circular anchors (adopted from Merifield et al. 2003)	36
Figure 2-16. A typical FE mesh of a double-blade anchor (Merifield, 2011)	37
Figure 2-17. Displacement contours for anchors in clay: (a) double-bladed; (b) triple-bladed; H/D = the embedment depth ratio of the top blade (Merifield 2011)	37
Figure 2-18. RITSS procedure in ABAQUS, after Hu and Radolph (1998)	39
Figure 2-19. CEL model of the penetration of pipeline into clay (Dutta et al. 2015)	40
Figure 2-20. Mesh around a 3-plate tensile pile (Wang et al. 2013)	41
Figure 3-1. Effect of g level of pile installation on axial pile resistance measured in flight (after Ko et al. 1984)	44
Figure 3-2. Soil container: all four walls were fabricated with aluminum plates	46

Figure 3-3. Positioning of gasket for sealing purpose.....	46
Figure 3-4. Gear motor and adaptors designed for installing model piles at a constant rotational speed	48
Figure 3-5. Results of calibrating the gear motor at 1 g condition: output rotational speed vs. applied torque.....	48
Figure 3-6. Dual-axis electric actuator: horizontal movement of frame box and vertical movement of a carriage in frame box are enabled	49
Figure 3-7. Photo of model piles: P1 to P4 from left to right	51
Figure 3-8. (a) Approximate locations of strain gauge stations and the protection technique; (b) Photo of strain gauges installed inside the gauge grooves; and (c) Position of axial and torque strain gauges; units are in the model scale.....	53
Figure 3-9. (a) Half bridge circuit for axial strain on model piles; (b) Full bridge circuit for the torque gauge on pile head; and (c) schematic of principle of torque measurement, where torque gauges were arranged to form a 45° and 135° rosette. Note: R = resistors (or dummy gauges) placed in the data logger; SG = active strain gauges installed on pile shaft; ε = anticipated strain to be recorded by the SG; E_0 = output voltage; E_{in} = constant excitation.....	54
Figure 3-10. A complete instrumented pile.....	55
Figure 3-11. Setup for the calibration of (a) torque strain gauges, and (b) axial strain gauges	56
Figure 3-12. Soil surface settlement initiated by centrifuge spin-up, during the over-night consolidation before Stage 1 of WL01, in model scale	59
Figure 3-13. Dimensions of PPT's, by manufacturer	60
Figure 3-14. Installation of pore pressure transducers at 1 g condition	61
Figure 3-15. Data logger reading vs. applied pore pressure	62

Figure 3-16. Kaolinite slurry: in a vacuum mixer (left) and in the soil container (right)	63
Figure 3-17. Loading frame for kaolinite consolidation	64
Figure 3-18. Consolidation curve under vertical stress of 500 kPa, WL01	65
Figure 3-19. End-of-primary void ratio vs. consolidation stress in two test series: (a) WL01, and (b) WL02.....	65
Figure 3-20. Test layout of WL01 and WL02.....	72
Figure 3-21. Layout of vane shear test (e.g., BH1A1) and model piles.....	72
Figure 3-22. Pore pressure change, during the spin-down and spin-up procedure before load test P1T, WL02.....	73
Figure 4-1. (a) Test layout of WL01 and WL02; and (b) vertical profile at A-A section of WL02. Dimensions are in model scale. Note: model piles were installed and loaded during different centrifuge flights.	81
Figure 4-2. Flow chart of each testing stage. The 20-g consolidation was aimed to stabilize pore pressure.	82
Figure 4-3. Strength parameters of model soil: (a) average peak and residual s_u in WL01, (b) average peak and residual s_u in WL02, (c) OCR of the soil model at 20 g centrifugal acceleration, and (d) average sensitivity of the soil	84
Figure 4-4. Schematics of helical piles and locations of strain gauges: (a) P1; (b) P2; (c) P3; (d) P4; (e) pile shaft cross-section and (f) a model pile with strain gauges glued inside the slots but not filled by epoxy.	85
Figure 4-5. Install-and-load system.....	88
Figure 4-6. Progress of pore pressure before test P1T of WL02	90

Figure 4-7. (a) Components of torsional resistance; (b) a vertical cross-sectional view through the pile axis. The “true” helix configuration is shown as a right angle.	93
Figure 4-8. Curves of installation torques vs. lower helix penetration depth in the prototype scale: (a) WL01A, (b) WL01B, (c) WL02A, and (d) WL02B.	94
Figure 4-9. Estimated T_{end} and torque components vs. the measured T_{end} of 14 installed piles	95
Figure 4-10. Histories of u induced by P1T and P4C2 installation in WL02.	98
Figure 4-11. Pull-out tests: a) WL01 in medium-stiff clay and b) WL02 in stiff clay	99
Figure 4-12. Axial load-displacement curves of selected tests. L1 to L6 are labels for axial gauge stations.	101
Figure 4-13. Mobilization of ending bearing or break-out pressure q_h of lower helix during (a) compression and (b) tension tests. The pressure q_h is normalized by the undrained shear strength at the helix location.	102
Figure 4-14. Axial load distributions at the limit state of selected piles. The factor δ is the ratio of the measured values to the estimates based on assumed failure mode sketched to the right of each plot.	106
Figure 4-15. Ratio of measured to estimated axial load distributions along pile segments. Results are taken from eight piles different from piles shown in Figure 4-13.	107
Figure 4-16. Mobilization of shaft resistance along selected pile segments in (a) medium stiff clay in WL01 (b) stiff clay in WL02; (c) illustration of pile shaft segments. Q_{su} is the estimate of ultimate shaft resistance.	109
Figure 5-1. Current understanding of multi-helix pile failure modes	117

Figure 5-2. Illustration of the axis-symmetric model on the platform of ABAQUS showing the mesh and boundary conditions.....	121
Figure 5-3. Illustration of soil-pile interaction: (a) soil-pile contact types, (b) “rough” tangential contact, (c) hard contact before separation, (d) hard contact after separation.	122
Figure 5-4. Pull-out tests: a) WL01 in medium-stiff clay shows CSM for P2, TFM for P3 and IBM for P4; and b) WL02 in stiff clay shows CSM for P2, IBM for P3 and P4.....	124
Figure 5-6. Measured and calculated axial load vs. displacement curves of selected piles in tension from test series: (a) WL01; and (b) WL02. Results are presented in the prototype scale.	127
Figure 5-7. Evaluation of the mesh size effect: (a) Mesh A where finest mesh length $\approx 20\% r_h$, (b) Mesh B where finest mesh length $\approx 10\% r_h$, and (c) Mesh C where finest mesh length $\approx 5\% r_h$, and (d) computed axial load-displacement curves with varied mesh sizes. Note: $r_h =$ radius of helix.....	129
Figure 5-8. Comparison of exaggerated mesh distortion from the finite element analyses using two techniques: (a) the standard Lagrangian method and (b) RITSS	130
Figure 5-9 Examination of bottom boundary effect: (a) illustration of bottom boundaries at B0 to B3, where $d_{base}/D = 2.8$ for B0 and $d_{base}/D = 5.8$ for B3; and (b) effects of bottom boundary on the axial load vs. displacement curves of P2C in WL01. Note: $d_{base} =$ spacing between the bottom helix and the container base; B0 is the actual boundary in the centrifuge tests and the adopted boundary for following LDFE analyses.....	132
Figure 5-10. Examination of soil width effect: (a) illustration of the varied soil side boundary, and (b) computed load-displacement curves of P2C in WL01. Note: the spacing in the centrifuge	

test layout was $4.2 D$; this soil width was adopted in the analyses presented in following sections.

..... 133

Figure 5-11. PEEQ contours of P2 at downward pile displacements $w/D =$ (a) 2.6%, (b) 7.9%, (c) 13.1%, and (d) 26.2%. Note: $S_r = 1.5$, $s_u = 46$ kPa..... 135

Figure 5-12. PEEQ contours of P3 at downward pile displacements $w/D =$ (a) 2.6%, (b) 13.1%, (c) 31.5%, and (d) 39.4%. Note: $S_r = 2.5$, $s_u = 46$ kPa..... 136

Figure 5-13. PEEQ contours of P4 at downward pile displacements $w/D =$ (a) 2.6%, (b) 13.1%, (c) 26.2%, and (d) 52.5%. Note: $S_r = 3.5$, $s_u = 46$ kPa..... 137

Figure 5-14. Normalized helix resistances vs. normalized axial displacement of selected piles from LDFE analyses: (a) compression tests, and (b) tension tests. Note: LH = lower helix, UH = upper helix. 139

Figure 5-15. Soil-shaft separation caused by the neighboring cylindrical shear stress zone (P2C, WL01)..... 140

Figure 5-16. Effect of embedment depth on the axial failure mode of a compressive pile in the parametric study. In this series of simulations, $S_r = 2.5$, $s_u = 40$ kPa. Ratio of the embedment depth ratio of upper helix to helix diameter is: (a) 1.4, (b) 2.4, (c) 4.4, (d) 6.4..... 144

Figure 5-17. PEEQ contour maps of selected simulations with various soil strength, space ratio, and loading direction. Note: normalized pile displacement $w/D = 25\%$ 145

Figure 5-18. Summary of the parametric studies – failure modes of double-helix piles against s_u and S_r : (a) at $E_{HL} = 3.9$ adopted in the centrifuge model tests, (b) at $E_{HL} = 5.9$ adopted in the parametric study, and (c) at $E_{HU} = 7.4$ adopted in the parametric study..... 147

Figure 5-19. Summary of uplift break-out factors and compressive bearing factors of selected helices: (a) and (b) for break-out factors of lower helices, (c) and (d) for compressive bearing factors of lower helices, and (e) for compressive bearing factors of upper helices..... 150

1 Introduction

This research project contains four major sectors: a literature review of the axial behavior of helical piles in soils, the development of the centrifuge model test system, inflight pile installation and axial load tests, and numerical simulations. The present chapter provides an overview of the background of helical piles, the research objectives, and the thesis organization.

1.1 Background

Helical piles, also known as screw piles or screw anchors, are deep foundation systems used to support axial compression, axial tension, and/or lateral loads. A typical helical pile is illustrated in Figure 1-1. In general, a helical pile consists of a steel central shaft and one or multiple helical plates welded to the shaft as presented in Figure 1-2. The shaft cross-section is usually circular and sometimes square. The diameter of helical plates can be consistent or gradient over depth, i.e., smaller helix at greater depth to reduce torsional resistance thus avoids “over-torque” damage of the shaft during installation. This type of pile is broadly used in various industries such as power transmissions, commercial buildings, and infrastructure constructions. Advantages of helical piles over conventional straight piles such as toe bearing piles and frictional piles are fast installation, low noise and ground vibration during installation, enhanced uplift capacity, ease of remediation, reusability, and instant load action upon installation. The installation of helical piles is usually accomplished by a torque rig carried by a regular excavator as shown in Figure 1-3. With the guidance of a swamper monitoring the positioning and verticality, a regular-sized (less than 10 meters long) helical pile can be screwed into the ground within 30 minutes according to experienced engineers.



Figure 1-1. A photo of helical piles (Almita Piling)

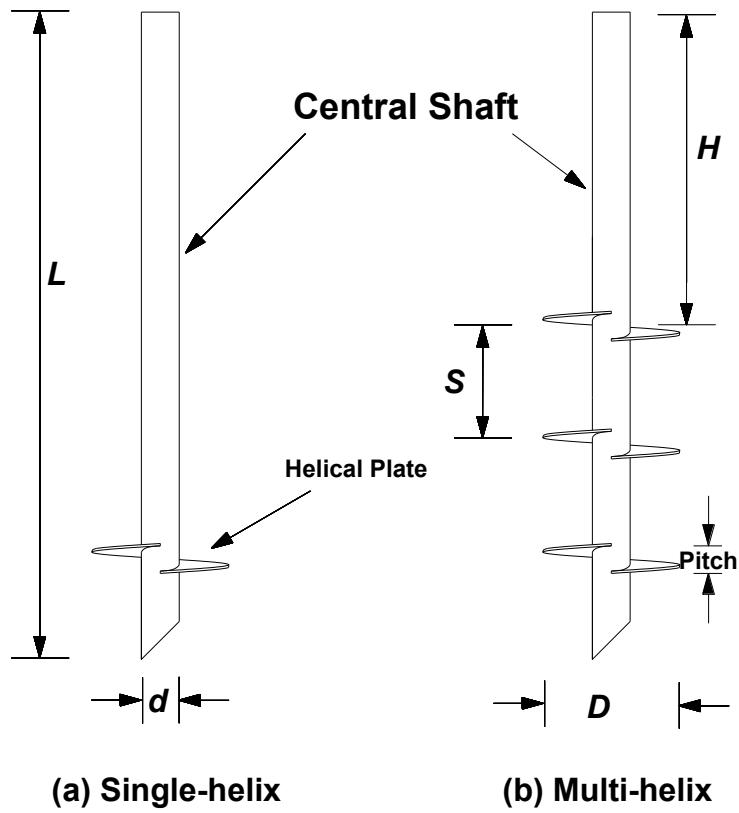


Figure 1-2. Sketch of typical helical piles: (a) single-helix piles, and (b) multi-helix piles

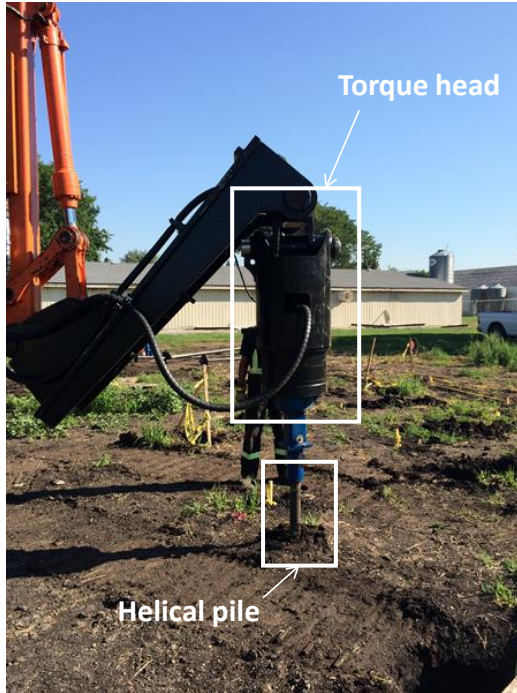


Figure 1-3. Installation method of helical piles

Two kinds of design methods can be chosen by engineers to predict the axial capacity of helical piles, including the torque factor method and semi-empirical method based on soil-pile interaction models. The torque factor method is simply an empirical correlation between the final installation torque value and the ultimate capacity proposed by Hoyt and Clemence (1989) and fulfilled by numerous field load tests thereafter. However, this method is more of a verification tool after the pile is already installed to the ground. The semi-empirical method adopts the well-known Terzaghi's (1943) or Vesic's (1973) bearing capacity equations to estimate the plate capacity. In most cases, the shaft friction is neglected since too many uncertainties remain unclarified, mainly because of overlapped stress zones mobilized by the helix and the shaft in its vicinity.

The load transfer mechanism is the basis of semi-empirical design method for the axial capacity of helical piles. Assuming each helical plate fails the soil in a localized manner is very often misleading when the stress zones of two helices overlap with each other thus change the mode of

failure. Mooney et al. (1985) found that the inter-helix soils may act as a cylindrical body as the pile moves and create a global vertical failure surface. This failure mode is now known as “cylindrical shear mode” (CSM). Comparatively, when the helical plates act individually, the failure mode is called “individual bearing mode” (IBM). A number of physical tests and numerical studies have been conducted to assess the failure-mode-based analytical design method. It is currently recognized that the failure mode is affected by the inter-helix spacing ratio and likely the strength of soil. Overall, inappropriate prediction of failure mode can lead to significant overestimation of the ultimate capacity of helical piles (Perko 2009), but our current understanding of the axial failure mechanisms is somewhat unsatisfactory.

In many cases, field load tests of helical piles are expensive or impractical and centrifuge modeling becomes an alternative. Centrifuge model tests are more cost effective and time efficient than field load tests, and able to offer comprehensive studies by manipulating the soil strength profile. The uncertainties of scaled-down soil stress level in 1 g model tests can be eliminated by applying an artificial gravitational acceleration on a geotechnical centrifuge. Figure 1-4 shows a sketch of the geotechnical centrifuge at the University of Alberta and the principles of centrifuge model tests. The radius of the beam centrifuge is 2 m, and the payload is limited to 150 g-ton. Some commonly used scale factors are presented in Table 1-1.

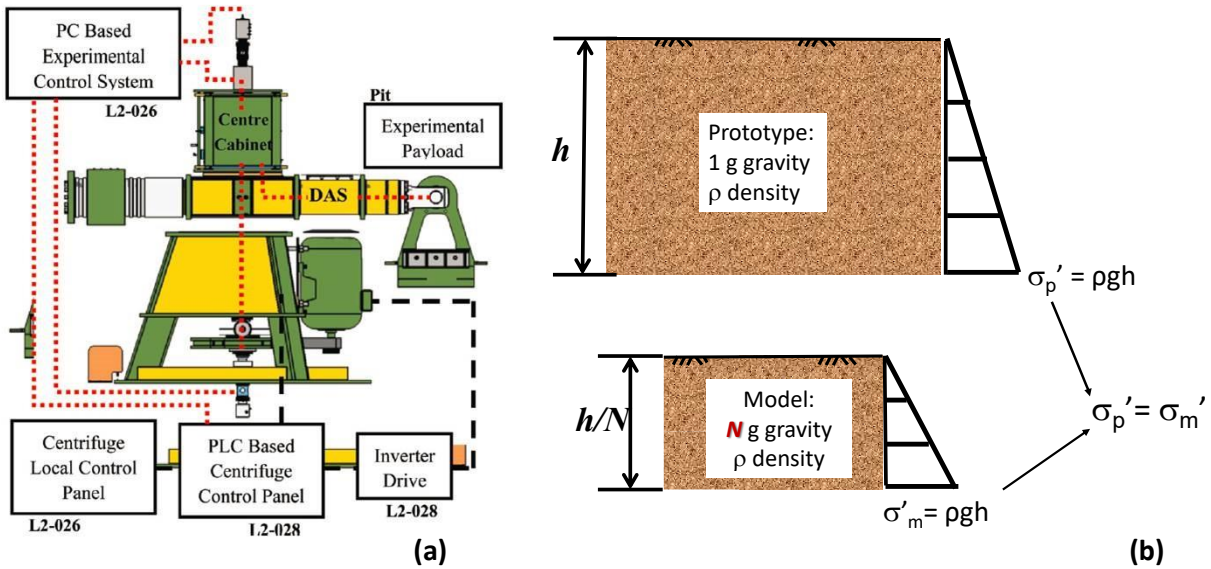


Figure 1-4. (a) Functioning components of the geotechnical centrifuge at UAlberta (adapted from Zambrano-Narvaez and Chalaturnyk 2014), and (b) principles of centrifuge model tests

Table 1-1. Scale factors used to convert the model data to prototype units

Quantity	Factor
Force (static)	400/1
Displacement, Length	20/1
Acceleration, Gravity	1/20
Pressure, Stress	1/1
Torque	8000/1

Numerical simulation is another broadly adopted technique to investigate the soil-pile interactions. The soil parameters and pile dimensions can be varied to explore the pile behavior in a much wider range of scenarios. Lower bound theorem and large deformation finite element (LDFE) analyses are frequently applied to such problems. The lower bound method assumes rigid

plastic soil coupled with flow mechanisms to solve the pile failure problem at equilibrium. This method avoids the convergence problems that may emerge at large strain and produces conservative solutions to the ultimate capacity of piles. LDFE enables more possibilities for the simulation of failure mechanisms at large strain. It is a more powerful tool than the lower bound method for studying the axial failure modes of helical piles which can be only seen after a large displacement.

1.2 Problem Statement

Numerous field load tests of helical piles in various types of soils have been reported in the past decades. But most of the results serve as a database of axial capacity design for the helical piling operator in the local area. Studies aimed at the axial failure mechanisms with quality axial load distribution measurements are very limited. The current research gaps of the axial behavior of helical piles in cohesive soils can be summarized as follows:

- The installation torque of helical piles and installation induced excess pore pressure in cohesive soils are yet to be investigated
- Various critical space ratio values that distinguish different failure modes have been reported, but there is no solid framework to systematically describe the factors that affect the failure modes.
- Axial load distributions of helical piles are available in limited studies, but there is no further analysis other than back calculations of total pile capacity
- A comprehensive numerical parametric study aiming at a wide range of soil strength, inter-helix space ratio and pile embedment depth to assess their effects on the failure mode of helical piles is unavailable.

1.3 Research Objectives

The following research objectives are identified:

- Develop the centrifuge modeling test equipment and techniques for research in axial soil-helical pile interaction
- Develop and verify an analytical solution to the progressive installation torque of helical piles in cohesive soils
- Evaluate the generation and dissipation of installation-induced pore pressure in cohesive soils
- Evaluate the axial load transfer mechanisms of helical piles in clay using the measured axial load distributions and LDFE analyses
- Assess the effect of inter-helix space ratio, pile embedment depth and undrained shear strength (s_u) of clay on the axial failure mechanisms of double-helix piles with a comprehensive parametric study using the validated LDFE model.

1.4 Scope and Contribution of Present Research

Two series of centrifuge model tests of helical piles in clay, denoted to be WL01 and WL02, were conducted from April 2019 to November 2019 at the University of Alberta in Edmonton, Canada. Each test series consisted of eight in-flight pile installation followed by corresponding axial loading tests, and they were replicated in two saturated kaolinite clay models with undrained shear strength (s_u) of approximately 50 kPa for WL01 and 120 kPa for WL02. All test piles share the same length (L) of 271.8 mm, shaft diameter (d) of 12.7 mm, and helix diameter (D) of 38.1 mm. The type of test piles was defined by the number of helix and inter-helix space ratio $S_r = S / D$, where S is the distance between the centers of two adjacent helices. Specifically, P1 represents the

test pile with one helix; P2, P3 and P4 denote the double-helix piles with $S_r = 1.5, 2.5$ and 3.5 , respectively.

All test piles were instrumented with multiple stations of half-bridge strain gauges for axial shaft strains, and one station of full-bridge strain gauges at the pile head for torsional strains. The measured strains were thereafter converted into axial loads and installation torques to characterize the behavior of these piles in the clays. Two pore pressure transducers (PPT) were buried in the soil of WL02 at the depths of 100 mm and 150 mm to measure the excess pore pressure induced by pile installation.

A LDFE model based on the remeshing and interpolation technique with small strain (RITSS) was developed to simulate the axial behavior of double-helix piles in clay. The LDFE model was validated with the centrifuge model test results. A comprehensive parametric study was carried out with the validated LDFE model to investigate the effect of undrained shear strength, inter-helix space ratio, and pile embedment depth on the axial failure modes of double-helix piles. The undrained shear strength was varied from 20 kPa (very soft) to 130 kPa (hard), the inter-helix space ratio was varied from 1.25 to 3.5 (a typical value is 2~3), and the helix embedment depth ratio was varied by adopting $E_{HL} = 3.9, 5.9$ or $E_{HU} = 7.4$. Herein, E_{HL} is the ratio of the helix embedment depth to the helix diameter for the lower helix, and E_{HU} is the embedment depth ratio for the upper helix.

The contributions of the present study to geotechnical academic and practical communities are stated as follows. The research program developed the first centrifuge modeling framework for helical pile installation and axial load testing at the University of Alberta. The techniques and hardware developed in the experimental program facilitate the future research in the soil-foundation-structure interaction. The present research provide experience in the instrumentation,

pile installation, axial loading, and data acquisition. The proposed approach for calculating the pile installation torque in cohesive soils can offer an alternative to the preliminary design of helical pile axial capacity. The proposed analytical solution to the transfer of installation induced excess pore pressure around a helical pile can improve our understanding of the setup effect in cohesive soils. Several charts that describe the variation of axial failure modes and helix capacity factors against the space ratio, pile embedment depth and soil strength have been developed based on the analyses of the axial load transfer mechanisms and failure modes using centrifuge model test results and LDFE simulations. The LDFE modeling method will enable further research in soil-foundation-structure interaction. The charts provide a quick method of assessing the axial capacity of multi-helix piles rather than simply adopting the conventional theories developed for the straight pile toe bearing capacity or single anchor uplift capacity.

1.5 Thesis Organization

This thesis consists of six chapters. Chapter 1 contains an introduction, which includes the background information and research objectives and scope. A literature review pertaining to the axial failure mechanisms of helical piles, pore pressure transformation around a driven pile, installation torque profile, and LDFE techniques are contained in Chapter 2. Chapter 3 describes the development of the centrifuge model test system, instrumentation of test piles, and testing program. Chapter 4 is a manuscript that investigates the behavior and performance of helical piles, installation-induced pore pressure, and an analytical torque model based on the experimental results. Chapter 5 is a manuscript focused on the numerical simulations of the axially loaded helical piles in clay. This chapter describes the effect of soil strength, pile embedment depth and pile dimensions on the failure mode and pile resistance. In Chapter 6, conclusions, limitation, and recommended future research are presented.

Several appendices are available to present additional information of the present study. Detailed drawings of the equipment used in the centrifuge model tests are documented in Appendix A. The scripting files that controlled the movements of the electric actuator for pile installation and axial loading are shown in Appendix B. More experimental and LDFE results excluded from the main chapters are attached in Appendix C. The Python codes that empowered the RITSS-based LDFE analyses are included in Appendix D.

2 Literature Review

2.1 Introduction

This chapter contains a summary of literature relating to the axial capacities, installation torque, axial failure mechanisms, centrifuge model tests, and numerical simulations of helical piles in cohesive soils. First, the currently available analytical design methods will be summarized, followed by the pile installation torque solutions, and then the axial failure mechanisms and failure mode at ultimate state will be presented. In the end, the techniques and studies of centrifuge model tests and LDFE analyses are summarized.

Helical piles are usually used to support compressive loads as an alternative of conventional toe bearing piles or to provide tensile resistance as soil anchors. To deal with lateral loads, for instance, in offshore scenarios with noteworthy winds and tides, the shaft segment of a designated length near ground surface may be enlarged, and this type of helical pile is called “bucket pile”. Relative studies about the lateral capacity of helical piles can be found in Li (2016). When a large vertical load coupled with bending moment is imposed by the superstructure such as a power transmission tower, a design of helical pile group is essentially the optimal option. The group effect and pile installation effect of helical pile group were described in Lanyi-Bennett and Deng (2019a). The present study focuses on the axial capacities and axial load transfer mechanisms of helical piles in clay. Therefore, only axial behavior of helical piles is presented in the following review work.

2.2 Axial Pile Capacities

Although the failure mechanisms of helical piles are more complex than straight piles and soil anchors, the current axial capacity design method for helical piles is developed from the existing theories for conventional deep foundations. Therefore, the existing theories for the behavior of conventional piles and soil anchors are necessary and reviewed in the first place.

2.2.1 Bearing Capacity of Pile Toe

2.2.1.1 Theoretical Derivation

The well-known Terzaghi's (1943) equation for shallow foundation bearing capacity was derived by assuming a general shear failure mechanism under plane-strain condition. Although the pile tip usually fails in a different manner, pile manufacturers tend to use this equation with adjusted factors according to pile dimensions and toe embedment depth.

There have been numerous theoretical studies that address the bearing behavior of piles in different ways from Terzaghi's. Randolph and Wroth (1978) simplified the soil-shaft interaction to independent slices as shown in Figure 2-1. The influence of pile toe behavior on the overlying soil-shaft relationship was also analytically evaluated.

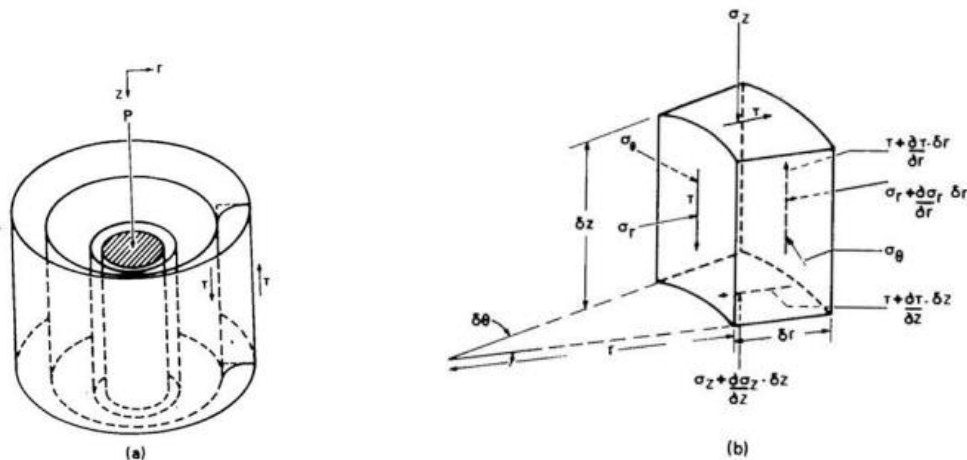


Figure 2-1. (a) Mode of shaft deformation; (b) Stressed on soil element (after Randolph and Wroth, 1978)

Coyle and Reese (1966) and Kraft et al. (1981) adopted boundary element method coupled with load-transfer functions to characterize the clay-pile interactions. Figure 2-2 illustrates the soil-pile interactions used in the analyses of Coyle and Reese (1966): shaft shearing, also known as “ t - z

behavior”; and end bearing, also known as “ q - z behavior”. The quantitative correlations between the pile settlement and applied load can be found in these studies.

The soil response may also be investigated using the elastic continuum theory (e.g., Butterfield and Banerjee 1971, Banerjee and Davies 1978, and Poulos and Davis 1980). However, the real soil fails as a non-linear material hence the computational effort is beyond human capability. Finite element offers a powerful alternative for non-linear soil behaviors and will be discussed in a later section.

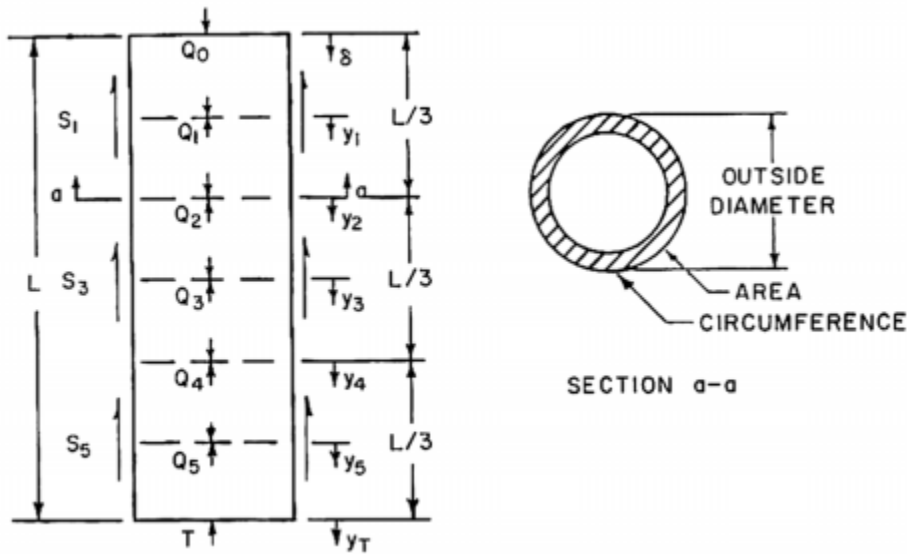


Figure 2-2. Segments of axially loaded pile for load-transfer analysis (after Coyle and Reese, 1966)

2.2.1.2 Semi-Empirical Theories

Considering the components of soil resistance against the pile settlement, Equation 2-1 includes both pile side friction and toe bearing resistance in the calculation of ultimate bearing capacity of a straight pile in cohesionless soils:

$$Q_u = N_t A \sigma_{vE} + \sum_{z=0}^{z=E} \pi d K \sigma_v \tan \delta \Delta z \quad (2-1)$$

where N_t is the toe bearing factor, A is the pile toe bearing area, σ_{vE} is the vertical effective soil stress at the pile toe, σ_v is the vertical effective soil stress over the depth z , E is the pile toe depth, K is a dimensionless horizontal earth pressure factor, and δ is the soil-pile interface friction angle.

For cohesive soils, Equation 2-2 is used as follows:

$$Q_u = N_t A s_{uE} + \sum_{z=0}^{z=E} \pi d \alpha s_u \Delta z \quad (2-2)$$

where s_{uE} is the undrained shear strength of the soil at pile toe, s_u is the vertical effective soil stress over the depth z , and α is a dimensionless cohesion factor for the soil-pile interface.

The N_t and α values in these two equations are most commonly semi-empirical or completely empirical. Meyerhof (1976) summarized a large number of semi-empirical bearing factors and side friction factors for the calculation of bearing capacity of piles in both cohesionless and cohesive soils.

2.2.2 Uplift Capacity of Soil Anchor

The uplift capacity of a helical pile is contributed by helix resistance and shaft friction. By ignoring the effect of pitch opening of helix, the helical plate is normally simplified as an equivalent flat anchor. The critical factors that affect the uplift capacity of soil anchors (e.g., anchor shape, embedment depth, and soil strength) are reviewed in this section.

2.2.2.1 Theoretical Derivation

A number of theoretical studies of uplift capacity of soil anchors are available: Meyerhof (1973), Vesic (1971), Yu (2000), etc. All these analytical approaches were based on the failure mechanisms of pulled-up anchors as shown in Figure 2-3. The embedment depth determines the volume of the displaced overburden soil and the geometries of failure surface.

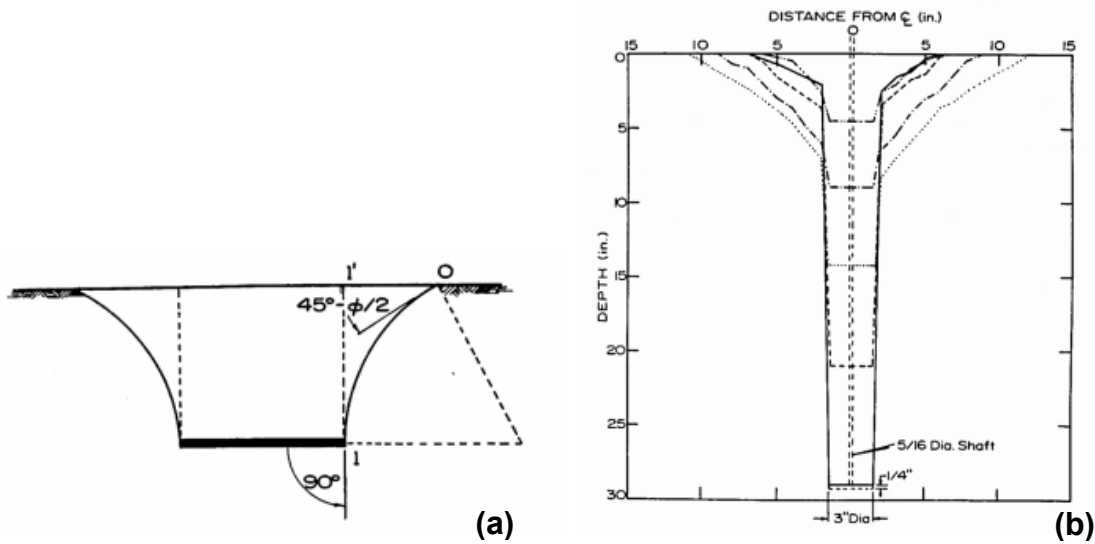


Figure 2-3. (a) Slip surface of shallow anchor; (b) Slip surfaces of circular anchor at various depths (after Vesic 1971)

Vesic (1971) gave an analytical solution to the uplift capacity of a horizontally buried anchor, circular or strip. The pull-out load was assumed to overcome the ultimate pressure of a cylindrical or spherical expanding cavity plus the soil weight transferred directly to the anchor. Meyerhof (1973) proposed a generalized theoretical framework for the uplift capacity of horizontal anchor based on a derived equation of N_t . However, this method was considered as over-conservative by Merifield et al. (2001) because several critical assumptions were made regarding the failure mechanisms and earth pressure distribution at the slip surface. Yu (2000) derived an expression for the break-out factor of anchors also based on cavity expansion theory. Compared to the work of Vesic (1971), Yu's solution took the internal friction of soil and dilation into account to improve the accuracy of this approach. In the derivation, it was assumed that the failure of anchor occurs once the plastic zone arrives at the ground surface. It also means the plastic zone exceeds the containment of outer elastic zone to reach failure. All of these theoretical studies assume a

condition of plane strain for the case of a strip anchor or axi-symmetry for the case of a circular anchor.

2.2.2.2 Semi-Empirical Theories

The uplift capacity of a horizontal soil anchor can be calculated using equations in a similar format with Equations 2-1 and 2-2. The end bearing factor N_t for bearing capacity calculation should be replaced with a break-out factor N_b . This simple adjustment remains true unless the anchor is defined as “shallow”. Meyerhof and Adams (1968) developed an approximate general theory of uplift capacity for anchors based on experimental data. Different failure mechanisms between shallow and deep anchors were considered in this approach. Figure 2-4 illustrates the contrast between these two failure mechanisms. The collapsed soil above the deep anchor does not reach the ground surface and eventually results in a localized failure. Notable difference will appear in a theoretical equation between shallow and deep anchor; however, simplifications have been made by Meyerhof and Adams based on test data to keep the equation consistent against anchor embedment depth. The empirical N_b values for strip, rectangular, and circular anchors in sand and clay and be found in Meyerhof and Adams (1968); this paper is widely referenced in related research works.

Numerous model tests on single anchors have been performed in an attempt to develop semi-empirical theories for calculating the uplift capacity of anchors in soil. Beside Meyerhof and Adams (1968), several widely recognized approaches and results for anchors in cohesive soils can be found in Vesic (1971), Meyerhof (1973), and Das (1978; 1980). Das (1980) summarized a number of previous studies to generate a database of evaluated N_b values over a wide range of s_u and anchor embedment depth.

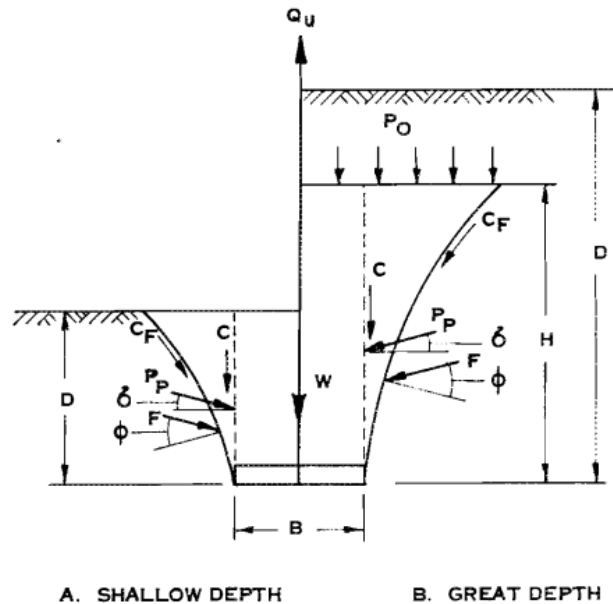


Figure 2-4. Failure of soil displaced by an uplifted strip footing (after Meyerhof and Adams 1968)

These well-developed semi-empirical theories and data base have proven satisfactory during the engineering application of past decades. However, one critical deficit shared by these approaches is that only single plate condition is considered. Therefore, it is difficult to apply these theories to multi-helix pile problems that present significant helix-to-helix interactions owing to overlapped stress zones as highlighted by Merifield and Smith (2010). In view of this knowledge gap, Merifield (2011) developed a framework to calculate the uplift capacity of multi-blade anchors based on a rigorous finite element analysis. The failure mode of multi-blade anchors was omitted in this approach. Wang et al (2013) extended this work to cover a wider range of helix numbers and embedment depth using an LDFE method. The details will be presented in Section 2.7.

Besides the numerical methods, Kulhawy (1985) proposed what seems to be the only method of analysis for the uplift capacity of shallow multi-blade anchors. In this method, the uppermost

blade creates a vertical shear plane extending from the perimeter of the blade to the ground surface; the inter-blade soil moves with the anchor as a rigid body and leaves another cylindrical failure surface behind. The shearing resistances acting on these two failure surfaces control the uplift behavior of such shallow multi-blade soil anchor. The shearing resistances can be derived with soil strength parameters and anchor geometries. However, the critical inter-blade spacing that decides if this model is valid remains unclarified. In addition, the effect of soil disturbance above the penetrated blades also relies on the experience of researchers and engineers to evaluate. Tsuha et al. (2012) estimated the effect of soil disturbance caused by anchor blades in sand using a series of centrifuge model tests, but this problem needs further investigations. Hence the overall design procedure given by Kulhawy (1985) is still semi-empirical in nature.

2.2.3 Current Design Frameworks of Helical Piles

Several simplifications have been made to apply the aforementioned theories for conventional straight piles and soil anchors to the problems of helical piles. Most of the simplifications have been following Mitsch and Clemence (1985) and Mooney et al. (1985), e.g., the helical-shaped plates are treated as flat blades and the projected area is used for the calculation of axial capacity. For axially loaded multi-helix piles governed by “individual bearing mode” (IBM), the ultimate capacity is the summation of shaft friction and bearing resistance of all helical plates; as for the “cylindrical shear mode” (CSM), all but one plate bearing resistances are replaced with relative cylindrical shear forces on the ‘rigid’ inter-helix soil bodies. Figure 2-5 shows the failure mechanisms of uplifted double-helix anchors subject to these two failure modes. The failure for compressively loaded piles is similar hence not depicted herein. Then it is straightforward to write the equation for the axial capacity of multi-helix piles.

For CSM:

$$Q_u = \pi D(n-1)S(s_u + K\sigma_v \tan \phi) + 0.25\pi D^2(1.3s_u N_c + \sigma_v N_q) \quad (2-3)$$

where D = helix diameter; S = inter-helix spacing; n = number of helical plates; σ_v = vertical soil pressure at the helices, s_u = cohesion of the soil; K = coefficient of lateral earth pressure; ϕ = angle of internal friction of the soil; and N_c and N_q are Terzaghi's bearing capacity factors for general shear.

For helical piles in clay, Equation (2-3) can be rewritten to be:

$$Q_u = \pi D(n-1)Ss_u + 0.25\pi D^2(1.3s_u N_c) \quad (2-4)$$

Or using the more popular semi-empirical plate capacity factors N_t for bearing and N_b for uplift:

$$Q_u = \pi D(n-1)Ss_u + 0.25\pi D^2 s_u N_t \quad (2-5)$$

$$Q_u = \pi D(n-1)Ss_u + 0.25\pi D^2 s_u N_b \quad (2-6)$$

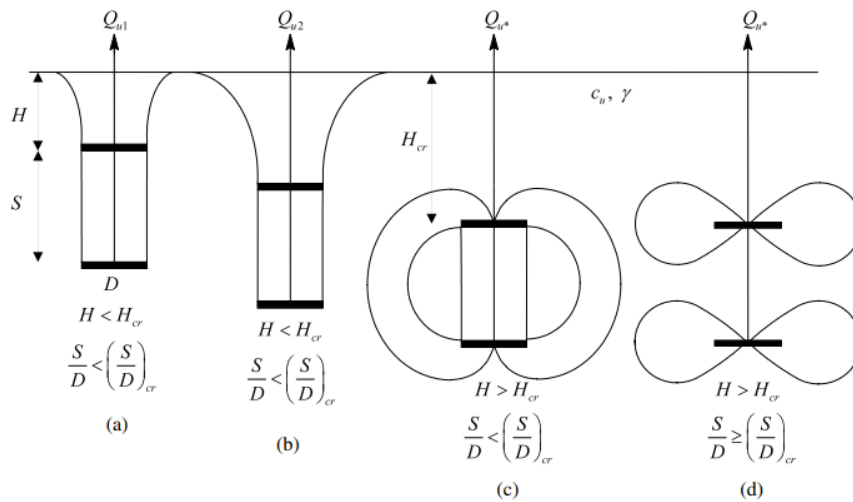


Figure 2-5. Failure mechanisms of multi-helix piles at different S/D ratios and embedment depth:

(a) and (b) CSM shallow failure; (c) CSM deep failure; (d) IBM deep failure; after Merifield (2011)

For IBM:

$$Q_u = \sum_n^1 A_n (1.3s_u N_c + \sigma_{vn} N_q + \frac{1}{2} \gamma B N_\gamma) \quad (2-7)$$

where A_n = projected area of the n^{th} plate; σ_{vn} = vertical soil pressure at the n^{th} helix.

For helical piles in clay, Equation (2-7) can be rewritten to be:

$$Q_u = \sum_n^1 1.3A_n s_u N_c \quad (2-8)$$

Or using N_t for bearing and N_b for uplift:

$$Q_u = \sum_n^1 A_n s_u N_t \quad (2-9)$$

$$Q_u = \sum_n^1 A_n s_u N_b \quad (2-10)$$

All the previously mentioned approaches neglected the shaft resistance in the calculation because of too many uncertainties for the soil-shaft shearing resistance. For CSM model, the inter-helix pile shaft is unlikely to contribute to the overall capacity because of the rigid nature of the soil cylinder; for IBM model, although the stress zone mobilized by the helix does not occupy the entire inter-helix space, the inter-helix shaft resistance is negligible implied by a number of axial load data from field tests on instrumented helical piles (Gavin et al. 2014, Li et al 2018, and Lanyi-Bennett and Deng 2019b).

As for the shaft segment above the uppermost helix, Rao et al. (1993) attempted to develop a semi-empirical approach to account for the contribution of it to the total uplift capacity of helical piles in clay. A series of small-scale laboratory helical piles were pulled out of soft to medium stiff clay. The ultimate uplift loads of these piles were back calculated with a certain length of shaft removed from the total length. There results indicate there is an “ineffective length” that will not

mobilize any shearing force as shown in Figure 2-6. This ineffective length was estimated to be D . Li and Deng (2019) extended this work with a number of axial field load tests in stiff clay and dense sand. The back calculations assisted with numerical simulations produced a greater estimation of ineffective length up to $5 D$. The discrepancy was attributed to the in-situ soil heterogeneity and high historical stress of the soils. Apparently, further studies regarding the shaft resistance of helical piles are necessary.

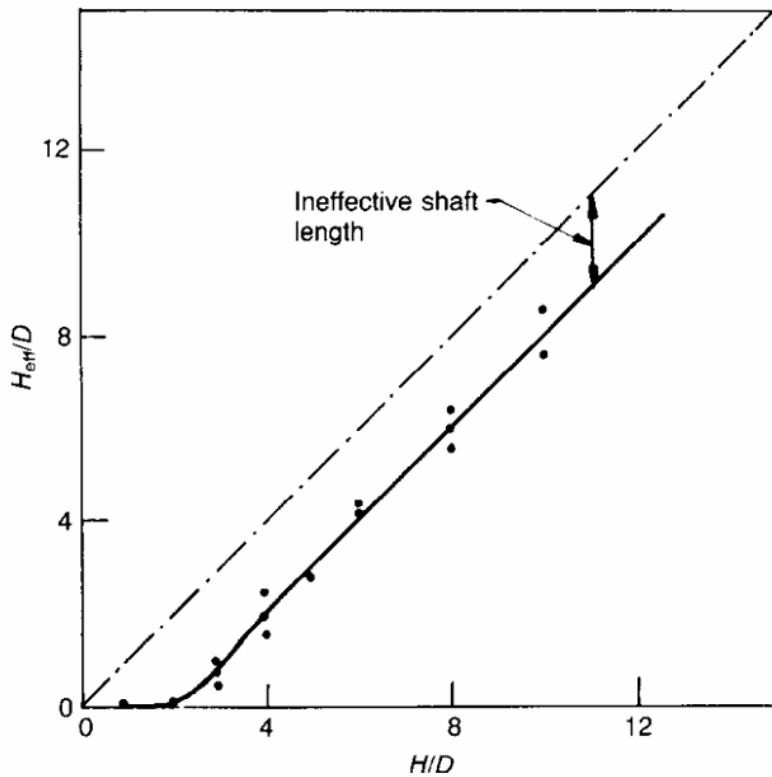


Figure 2-6. Ineffective length of the shaft during uplift loading of helical piles in clay (after Narasimha et al. 1993)

Besides these two semi-empirical methods, there is one more empirical method based on installation torque. Hoyt and Clemence (1989) proposed an empirical factor to relate the final

installation torque to the axial capacity of helical piles. The final installation torque multiplied by an empirical correlation factor produces the predicted ultimate pile capacity:

$$Q_u = K_T T_{\text{end}} \quad (2-11)$$

where K_T = torque factor and T_{end} = final installation torque.

This method is apparently easy to use but several limitations exist:

- a. The helix bearing resistance is sensitive to the strength of the underlying soil but the installation torque is not affected at all.
- b. The accurate value of the correlation factor is only available to those manufacturers who have access to a large data base which is usually confidential.
- c. This method can be applied only after the pile is installed.
- d. Theoretically, this torque factor depends on the helix diameter since the installation torque and axial capacity are somehow related to the third and second power of D , respectively; however, there is only one modification method for the torque factor based on pile shaft diameter (CGS 2006, Li and Deng 2019).

Therefore, the torque method is usually used as a verification method only.

2.2.4 Efficiency of Current Design Methods

It is obvious the accuracy of axial capacity design for helical piles depends on an appropriate selection of failure mode, i.e., IBM or CSM. Lutenegeger (2009) suggests that engineers apply both methods and adopt the smaller estimation. This strategy is effective for safe design, but not for economic design. As such, the efficiency of the design methods needs to be assessed.

Hoyt and Clemence (1989) analyzed 91 short-term load tests at 24 different sites with a variety of soils including clay, silt, and sand. All the three design methods based on IBM, CSM, and installation torque were applied to each test pile to generate predictions and compare with the

measured ultimate capacity. The results show that all three methods may produce over-prediction and under-prediction; the IBM method tends to overestimate the ultimate capacities more often than the other two theories; the CSM method appears to be more conservative for giving the most cases of under-predictions; for the IBM and CSM predictions combined, the ultimate capacities were over-predicted by about 50%.

Tapenden and Segoo (2007) evaluated the ultimate capacity predictions of 26 axial load tests of helical piles. The outcomes of semi-empirical methods, torque factor method, and LCPC method (a CPT-based direct method for toe bearing piles) were summarized. An ineffective length of $1 D$ above the uppermost helix of each pile was applied to all the predictions given by IBM and CSM methods. The criterion used for choosing CSM or IBM for the “theoretical” prediction is a critical inter-helix spacing ratio of 3.0, i.e., CSM was used if the ratio is less than 3.0 otherwise IBM was adopted. This criterion is also recommended by Canadian Foundation Engineering Manual (CGS, 2006). Figure 2-7 shows the ratios of the predictions to measured ultimate capacities in this evaluation.

It appears that the theoretical predictions are slightly conservative but by less than 20% of the measured field loads on average. Some outstanding under-predictions by 40% are observed but not severe over-predictions seem to have been made. These predictions are way better than those assessed by Hoyt and Clemence (1989) likely because of the use of space-ratio-based failure mode prediction and ineffective length. The torque factor method also produced satisfactory predictions but over-predictions up to 100% and under-predictions down to -50% occurred. Soil heterogeneity near the lowermost helices was most likely responsible for these cases. Other uncertainties might exist, but it was difficult to identify them for such empirical theory. However, the LCPC method was completely inappropriate to be applied to helical pile problems. The very different soil failure

mechanisms between a toe bearing pile and a helical pile must be clarified before any cross applications.

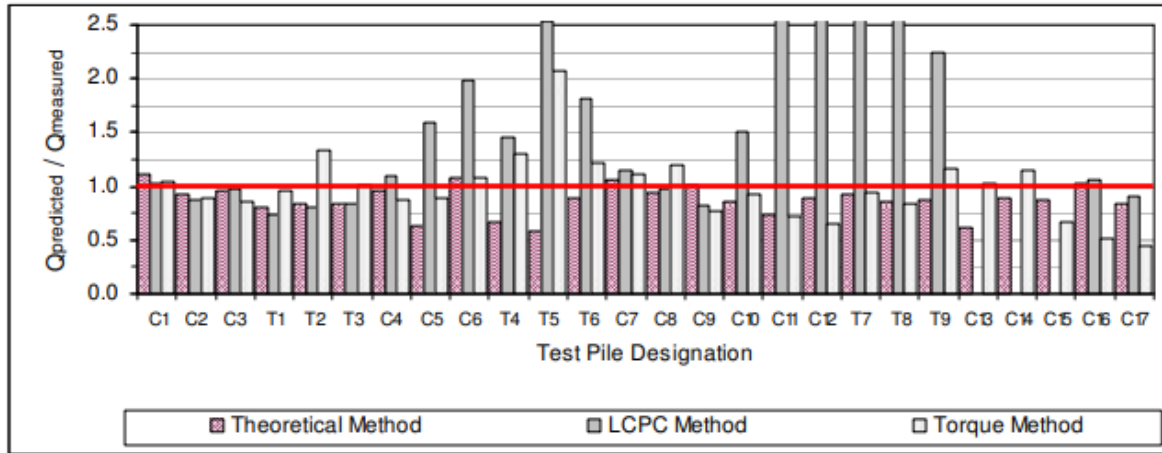


Figure 2-7. Ratio of predicted to measured ultimate axial capacities of helical piles, after Tappenden and Seg0 (2007)

In summary, it is deemed that the semi-empirical methods, i.e., the IBM and CSM theories are able to produce reliable predictions for axial capacities of helical piles with careful modifications in regard to the axial failure mechanisms. The current unsatisfactory parts of this semi-empirical theory can be summarized as follows:

- a. The prediction of failure mode for multi-helix piles in various soil conditions is unknown.
- b. Effect of the stress zone of helices on the nearby shaft resistance is not well known.

2.3 Installation Torque

When a helical pile is screwed into soil, the soil-pile interaction will result in a resisting torque. The torque value is believed to have a correlation to the axial capacity of helical piles. Although this correlation is completely empirical in the beginning, several experimental and theoretical studies attempted to establish a more reliable connection between the torque and uplift capacity.

Ghaly and Hanna (1991) derived a theoretical expression of the uplift capacity as a function of the installation torque by assuming the pull-out load is equal to the upward driving force generated by a rotating helix suspending at a fixed level. Tsuha and Aoki (2010) extended this solution to a multi-helix pile. Both studies were limited to cohesionless soils, but the theory can be easily applied to cohesive soils. In addition, a torque model for predicting the maximum installation torque with a given soil profile is also interesting to engineers for safety design of the pile installation procedure because of potential “over torque” damage if the helix is too big.

Tsuha and Aoki (2010) proposed a theoretical model of installation torque of helical piles in sand based on the power screw theory (Figure 2-8). The theoretical model assumes that the exerted torque during helical pile installation into cohesive soils is resisted by torsional shear along the pile shaft and torsional shear along the helices. The main assumptions that are considered for the development of the proposed torque model include the following:

- a. Crowd (downward pressure force) applied on the pile during installation is neglected.
- b. Torsional shear along the pile shaft is equal to axial unit shaft friction.
- c. The soil layer is assumed to be a homogenous layer that extends to infinite depth.
- d. Resisting torque during pile installation is independent of the speed of the robust hydraulic head.
- f. Helices are a true spiral shape, and their projected area is equal to the size of a disk with a diameter equal to the helix diameter.

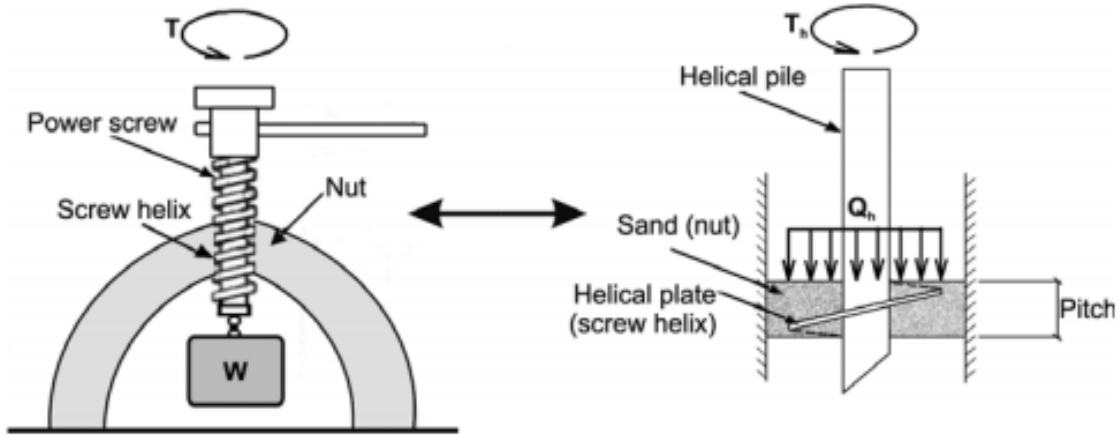


Figure 2-8. Calculation of installation torque using the power screw theory, after Tsuha and Aoki (2010)

Sakr (2013) developed an installation torque model to produce the torque values along with penetration depth. The soil-pile interactions are illustrated in Figure 2-9. Clearly seen in Figure 2-9(a), the soil surrounding the helix is assumed to move with it as a cylindrical rigid. A possible conflict between the rotation and penetration of helix may exist under this assumption; however, no experimental observation is available in the literature to clarify this concern. In this model, the peak undrained shear strength was assumed to govern the soil-pile interaction for the leading helix, and the residual shear strength for the following helix or helices and shaft. This justification is very reasonable considering the remolded soil left behind by the leading helix.

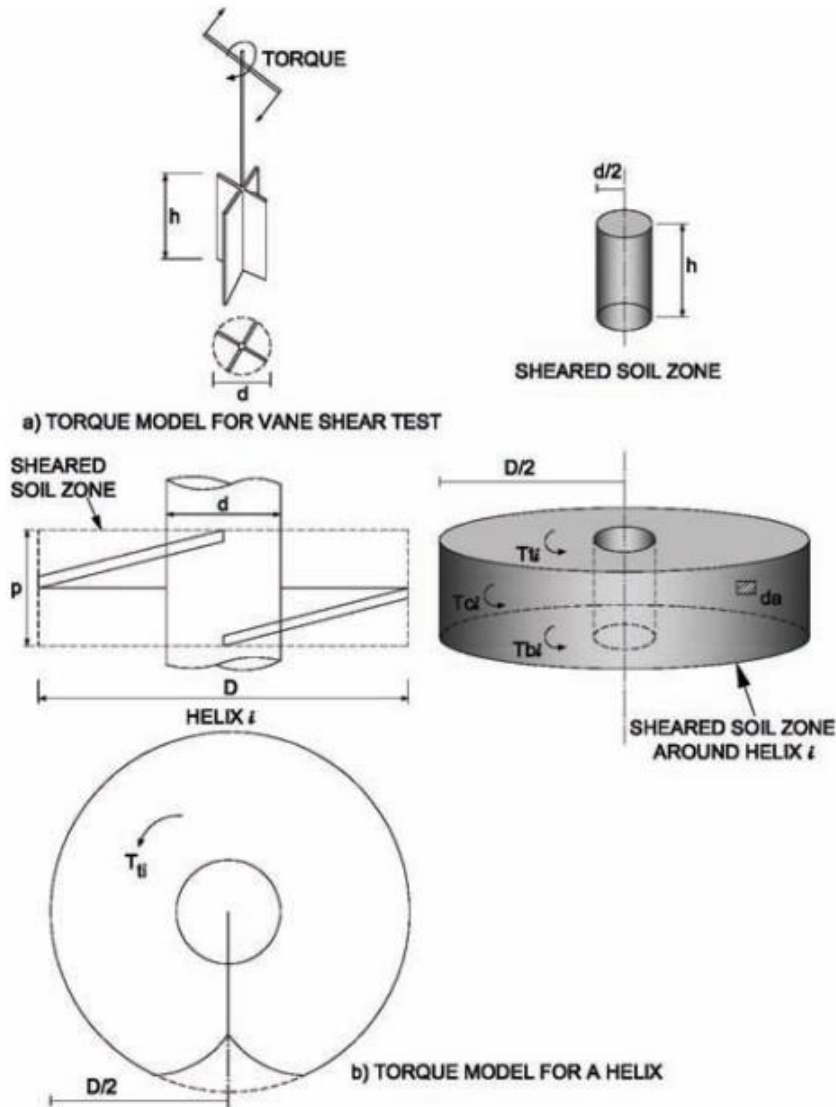


Figure 2-9. (a) Components of torsional resistance for vane shear test; (b) Components of torsional resistance for helix rotation, after Sakr (2013)

2.4 Installation-Induced Pore Pressure

2.4.1 Set-up Effect

Excess pore pressure, u_e , generated around the shaft during pile installation in cohesive soils has a significant impact on the short-term axial behavior of piles. Figure 2-10 describes the pore pressure

initiation and transformation around a driven pile. The bearing capacity of a straight pile driven into soft clay experienced a six-time increase over a period of 30 days according to Reese and Seed (1955). Lanyi-Bennett and Deng (2019a, 2019b) observed that the bearing capacity of helical piles loaded 5 hours after installation was 30 to 40% less than that of the piles loaded one week later, which implied a considerable soil strength recovery.

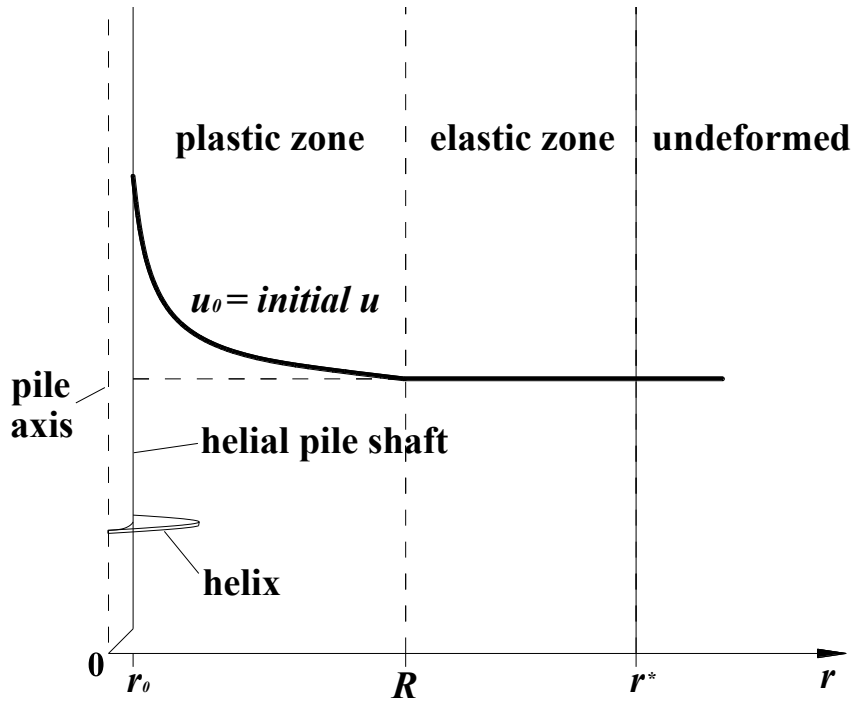


Figure 2-10. Diagram of instantaneous response of excess pore water pressure induced by helical pile installation (modified after Randolph and Wroth 1979)

Weech and Howie (2012) measured the pore pressure response to helical pile installation in soft clay at the shaft surface and at distance. Figure 2-11 shows their results of a radial propagation of u_e . They suggested that u_e was very slightly affected by the helices. Since u -induced installation is

crucial to the axial behavior of helical piles, the validation of such a theoretical model for evaluating the progression of u_e around helical piles may be important.

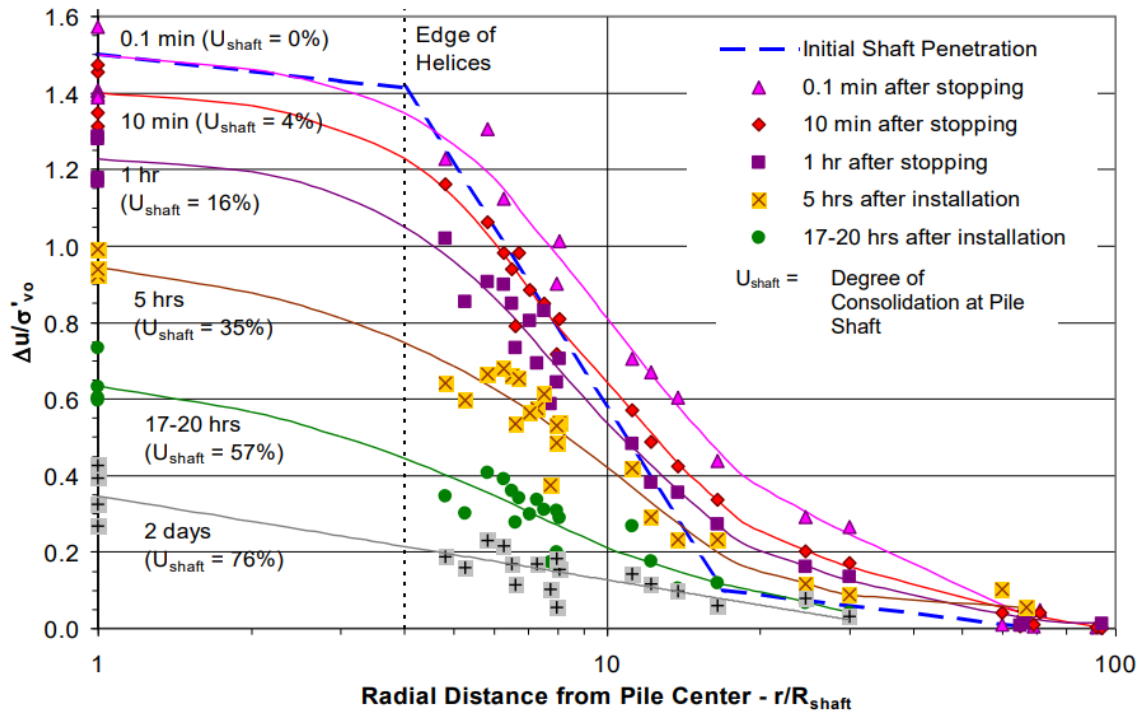


Figure 2-11. Radial distribution of excess pore pressure around a driven helical pile, after Weech and Howie (2012)

2.4.2 Analytical Solutions to Installation-Induced Excess Pore Pressure

The time-based dissipation of excess pore pressure around a driven pile is usually important for a continuous construction project with a group of piles. Three-dimensional numerical modeling is sometimes adopted for such analysis, but it is too expensive. An analytical solution for a single driven pile coupled with superposition theory may be more efficient and cost-effective. There are two widely referenced studies that provide analytical solutions to the consolidation of soil around a pile, i.e., Soderberg (1962) and Randolph and Wroth (1979). Both derivations assume plane strain with axial symmetry and the pore water flow follows Darcy's law. The solution of Soderberg

is more of an approximate strategy and the solution of Randolph and Wroth was rigorously derived using Bessel's functions with an extra assumption regarding the initial excess pore pressure distribution, as shown in Figure 2-10. The mathematical techniques for the derivation can be found in the theories developed for heat transfer problems by Carslaw and Jaeger (1959).

Using the derived solution, Randolph and Wroth gave a normalized progression of pile installation-induced excess pore pressure in the soil (see Figure 2-12). The solution may be effective to a helical pile considering the similar cavity initiated by the penetration pile shaft to a straight pile. The impact of helices on the lateral deformation of surrounding soil is trivial.

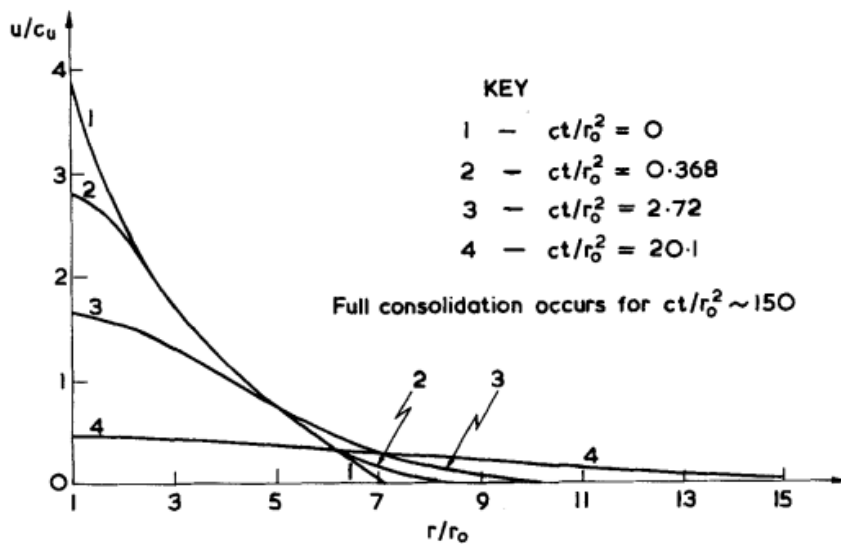


Figure 2-12. Progression of the dissipation of installation –induced excess pore pressure given by the approach of Randolph and Wroth (1979)

2.5 Axial Failure Mechanisms of Helical Piles

There are currently two recognized axial failure modes (see Figure 2-13) for multi-helix piles: IBM and CSM. IBM assumes that soil collapse takes place at individual helical plates; CSM proposed by Mooney et al. (1985) assumes that, during the axial movement of pile, the inter-helix

soil acts as a cylindrical body shearing against the surrounding soil. Given the radical difference in the composition of soil resistance, the axial capacity design of helical piles depends on an appropriate selection of failure mode. As encoded in commercial design guidelines such as CGS (2006), a ratio defined as $S_r = S/D$, where S is the inter-helix spacing and D is the helix diameter, is usually used as the indicator of potential failure mode.

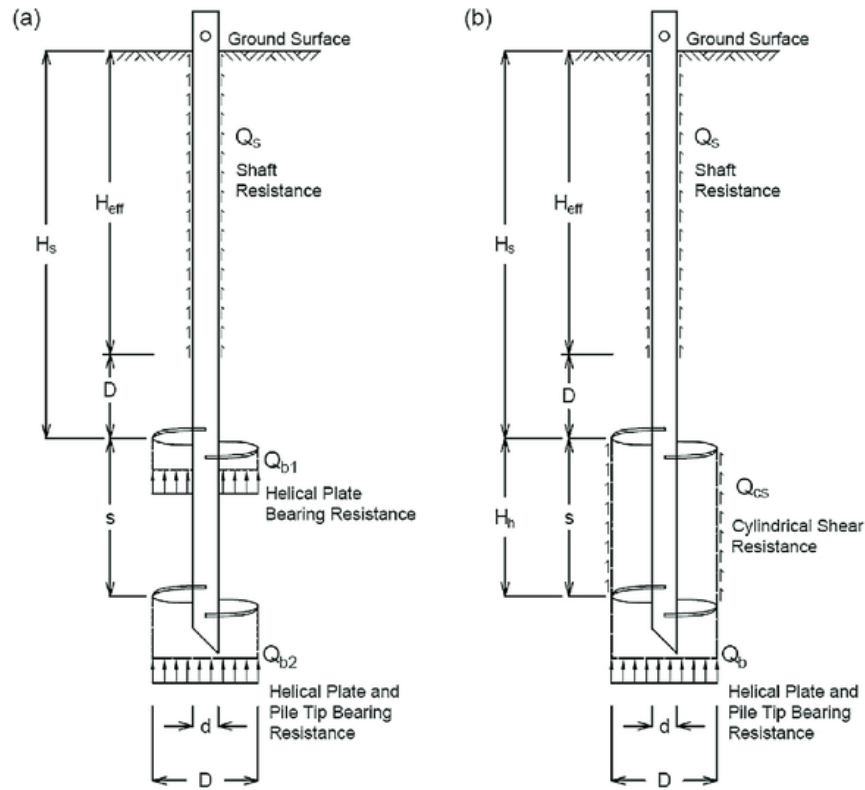


Figure 2-13. Currently recognized axial failure modes of helical piles: (a) IBM, and (b) CSM after Lanyi-Bennett and Deng (2019)

An empirical value of critical S_r (termed S_{rc} herein) of 3.0 is very often adopted in the industry. Lutenege (2009) conducted a parametric study of uplift capacity of helical piles in clay and sequentially derived a critical S_r , i.e., $S_{rc} = 2.25$. The primary assumption that the break-out factor

of an individual plate $N_c = 9.0$ and the pile would bide to the failure governed by IBM or CSM whichever produces the smaller uplift capacity. Several helical pile tests have reported various S_{rc} values corresponding to the subsurface conditions: $S_{rc} = 1.5$ for soft marine clay (Rao et al. 1991), $S_{rc} > 3.2$ for very soft clay (Wang et al. 2013), $S_{rc} > 3.0$ for soft to medium clay with very stiff crust (Lutenegger 2009), $S_{rc} < 1.5$ for stiff clay (Elkasabgy and El Naggar 2015), and $S_{rc} > 3.0$ for dense oil sand (Sakr 2009). Elkasabgy and El Naggar (2015) and Lutenegger (2009) attributed the observed failure modes inconsistent with prediction to the soil disturbance resulted from pile installation. These results based on the back-analysis and observation raise a concern whether there is a unique S_{rc} or IBM and CSM are the only failure mode of helical piles. Load tests of helical piles with various S_r and soil strength profiles may be warranted to address the concern.

2.6 Centrifuge Modeling Methods

In many cases, however, field tests are impractical because of the high testing cost or undesirable field conditions. Centrifuge modeling overcomes these limitations and enables a reliable simulation of geotechnical problems by reproducing the subsurface stress distribution of the prototype soil. Schiavon et al. (2016) developed an efficient setup for centrifuge model tests of helical piles as shown in Figure 2-14. A series of pull-out tests on different reduced models of helical anchor in sand were performed using this setup to address the scaling effects. Zhang and Kong (2006) built a test setup for in-flight pile installation and torque measurements. All these techniques have proven effective for the research of helical pile behavior.

Centrifuge modeling has been adopted in the studies of helical piles in sand, primarily aiming at the installation torque, axial capacity, and torque-capacity correlations (Zhang and Kong 2006, Tsuha and Aoki 2010, Tsuha et al. 2012, Schiavon et al. 2016, Al-Baghdadi et al. 2017). Wang et al. (2013) installed eight helical anchors in soft clay (about 20 kPa undrained shear strength, s_u) at

1-g condition, and loaded the piles in-flight to assess the tensile failure of the anchors intended for offshore use. Notably, there is a lack of experience in the instrumentation of model piles intended for in-flight installation since helical piles were not instrumented in previous studies (except in Zhang and Kong 2006). Based on a review of the state-of-art centrifuge modeling of helical piles in cohesive soils, the following deficiencies may be identified: 1) the technique of installing helical piles in flight, 2) the measurement of installation torque, and 3) a further examination of axial failure mechanisms.

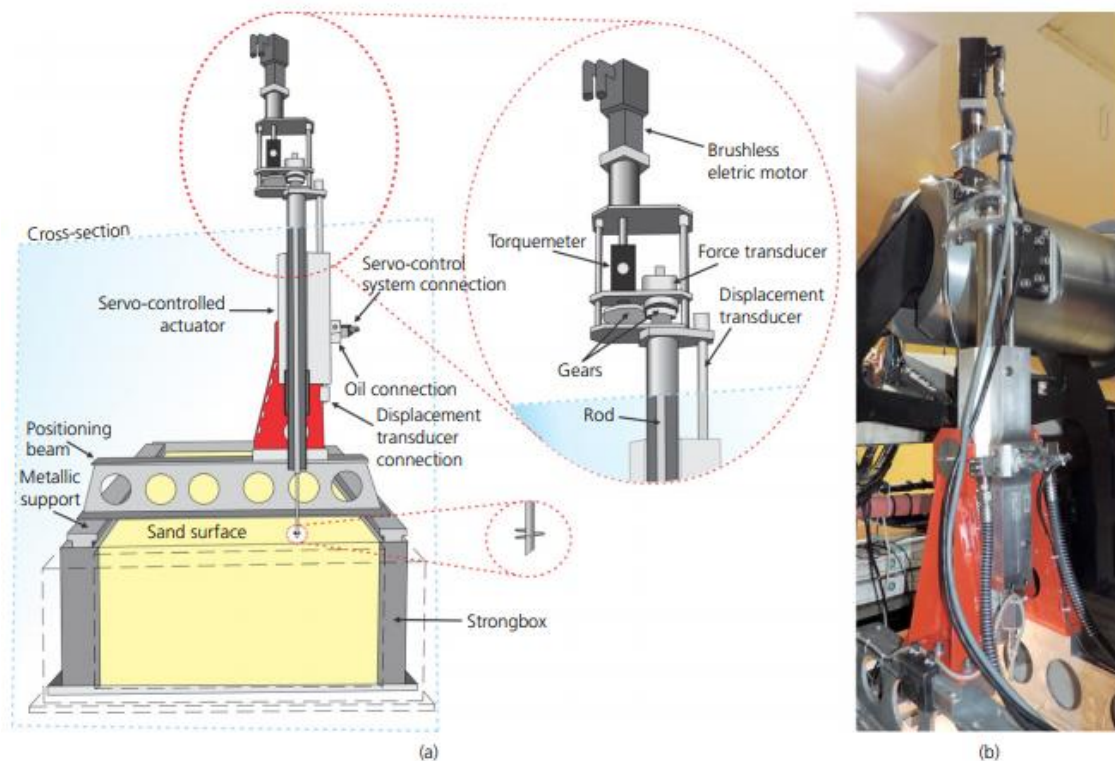


Figure 2-14. A servo-controlled loading test setup for helical piles on centrifuge (Schiavon et al. 2016)

In centrifuge test, the effect of loading rate may be exaggerated by the high g level considering the scale factor of pile penetration speed. Tsuha (2007) and Wang et al. (2013) conducted constant

axial load tests on helical piles in centrifuge at constant penetration rate, which is different from the protocols provided by ASTM D1143-81 (2013). The axial loading tests in the present research were also displacement controlled, which is more reliable and effective to operate in centrifuge. Potential discrepancy may be caused by a constant penetration rate test method in contrary to static load tests. Deeks and Randolph (1992) proposed Equation 2-12, based on the work of Smith (1962) and Gibson and Coyle (1968), to estimate the increased shaft resistance at an elevated penetration rate:

$$\tau_d = \tau \left(1 + \alpha \left(\frac{\Delta v}{v_0} \right)^\beta - \alpha \left(\frac{\Delta v_{min}}{v_0} \right)^\beta \right) \quad (2-12)$$

where τ_d is the ultimate shaft resistance at an elevated penetration rate; τ is the ultimate shaft resistance at the low penetration rate of a static load tests; Δv is the penetration rate of a displacement-controlled loading tests; Δv_{min} is the penetration rate of a static load tests; v_0 is a reference velocity equal to 1 m/s; and α and β are parameters related to penetration rate. By comparing the penetration rate of the current load tests to the reference strain rate of 1 m/s, Equation (2-12) suggests the difference of shaft resistance between the current displacement-controlled piles tests and a static load test is negligible.

Brown et al. (2006) conducted rapid load tests on instrumented bored piles at a penetration rate of 500 mm/s in clay and found the pile capacity was only 15% higher than the equivalent constant load tests. The diameter of the piles used in Brown et al. (2006) was 700 mm which is approximately equal to the prototype helix diameter of the present study, 762 mm. However, the higher penetration rate adopted in this study, in prototype scale, was 200mm/min (3.3 mm/s) which is 0.67% of 500 mm/s. Therefore, the axial pile resistance measured in the present study should be firmly considered as same as an equivalent constant load test.

2.7 Finite Element Methods of Soil-Foundation Interaction

Numerical simulation technique is frequently used to conduct a feasibility study before physical experiments, an alternative modeling when the physical modeling is impossible, or a parametric study to cover many input variables, etc. Finite element (FE) method is recognized as one of the most effective approaches to the modeling of soil-structure interaction. This section describes the available FE studies of helical piles and soil anchors.

Three-dimensional (3D) FE modeling provides one of the best approximations of reality. Merifield et al. (2003) conducted a 3D FE analysis of the uplift capacity of horizontal anchors in undrained clay. The simulation was based on the lower bound theorem of limit analysis, in which the soil model was assumed to be perfectly plastic. The FE model spaces are shown in Figure 2-15. Different quarter-domain geometries have been adopted to simplify the simulation for rectangular (Figure 2-15a) and circular (Figure 2-15b) anchors. The computed uplift capacities of the simulated anchors were comparable with selected small scale laboratory test results, which proved the effectiveness of the FE model and lower bound theorem. The agreement may be attributed to the simple mode of soil-anchor interaction of such single anchors. The uplift capacity was only contributed by the anchor normal resistance, and the soil-shaft interaction was negligible. However, for a multi-helix pile, the interference between helix and helix or shaft and helix may not be appropriately characterized by a perfectly plastic soil model, because the complex failure mechanisms of multi-helix piles is a combination of pile shaft, helical plates and inter-helix soil cylinder (if applicable). These local failures may be achieved at various soil strains. Therefore, a nonlinear soil model seems to be necessary for the problem of multi-helix piles.

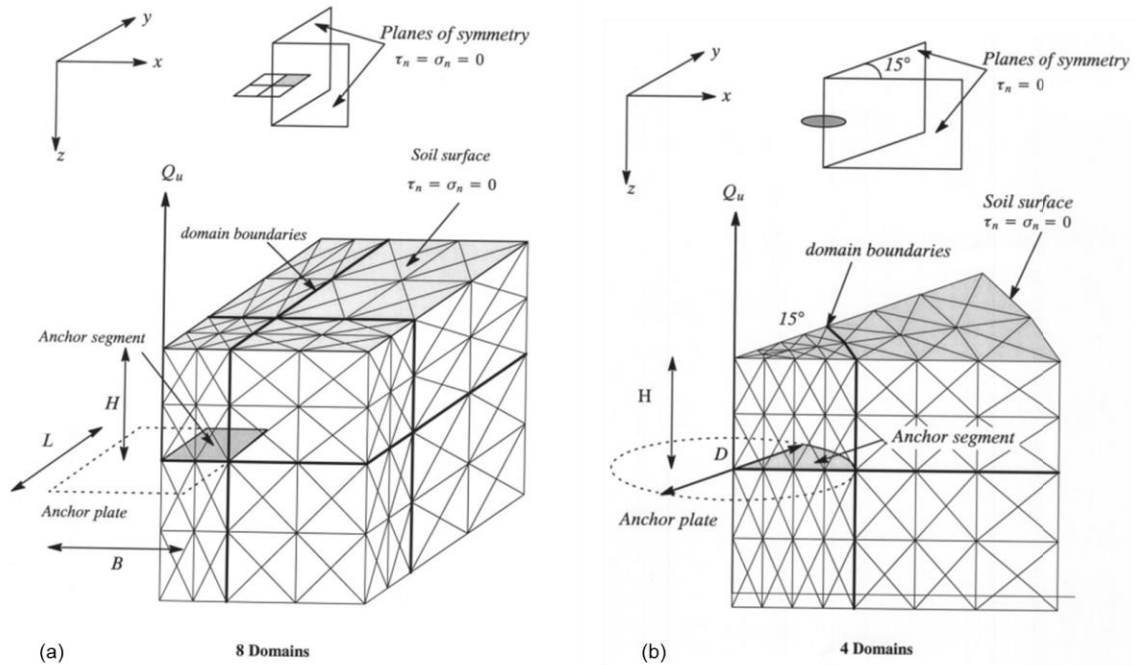


Figure 2-15. Mesh domains used for analyzing: (a) rectangular or square anchors, and (b) circular anchors (adopted from Merifield et al. 2003)

Although 3D modeling is effective, the analysis is usually time costly. In some cases where the problem shows significant symmetry in terms of geometry, load, material and boundary condition, the 3D approach can be replaced by a 2D approach. Considering the nearly perfect axis-symmetry of an axially loaded circular anchor in an isotropic clay, Merifield (2011) adopted a simplified 2D FE model. Figure 2-16 shows the geometry and mesh of the model. Small strain analyses were performed neglecting the large strain aspects of the problem. In addition, the soil-shaft interaction was neglected in this FE model for uncertainties as per Merifield (2011). Figure 2-17 shows the displacement contours of the simulated anchors. Different failure modes can be observed from these contours while the inter-blade spacing varies.

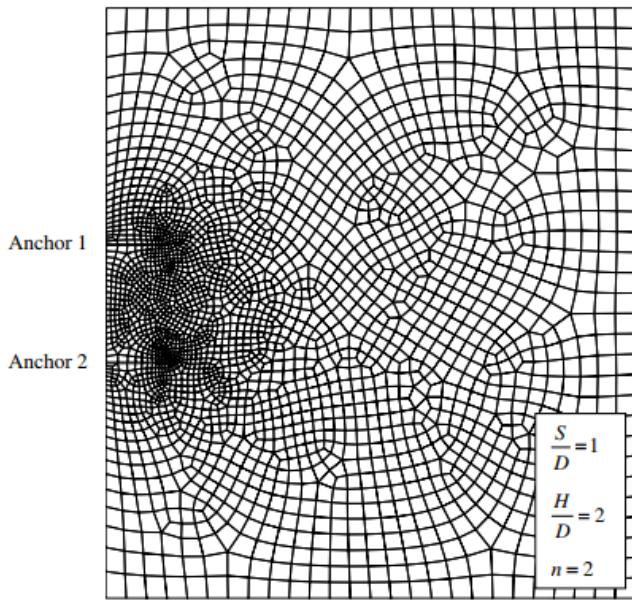


Figure 2-16. A typical FE mesh of a double-blade anchor (Merifield, 2011)

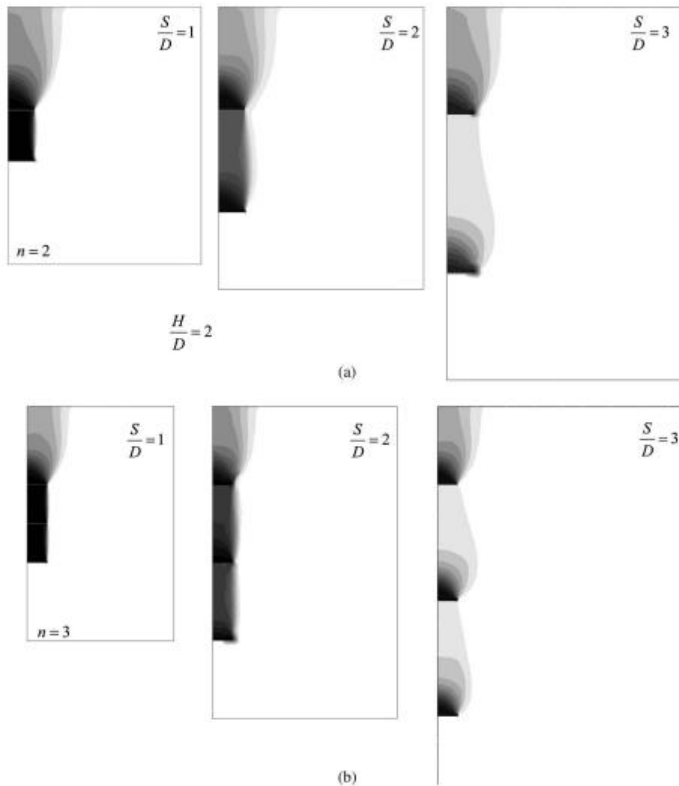


Figure 2-17. Displacement contours for anchors in clay: (a) double-bladed; (b) triple-bladed; H/D = the embedment depth ratio of the top blade (Merifield 2011)

Because of the large displacement of helical piles required by failure, a LDFE method is in need. The early development of LDFE analysis was focused on an updated Lagrangian approach, where the finite element mesh was tied to the solid and sophisticated stress and strain formulations were required to deal with the large cumulative strains and rotations in each element (Bathe et al., 1975; Hughes and Winget, 1980). The updated Lagrangian approach eventually becomes limited by the gross distortion of elements as the analysis progresses. This difficulty was overcome by the so-called arbitrary Lagrangian-Eulerian (ALE) modification, where Eulerian flow of the solid through the mesh was included (Liu et al., 1986; Ghosh and Kikuchi, 1991; Liu et al., 1988). Specific application of the ALE approach to geomechanics problems was considered by Nazem et al. (2006) who developed an efficient ALE (EALE) protocol. In ALE, the material and mesh displacements were separated to avoid the mesh distortion in a Lagrangian analysis. However, this separation usually introduces unknown mesh displacements to the governing equations, leading to significantly more expensive analyses. Nazem et al. (2006) proposed alternative algorithms for integrating rate-type constitutive equations in a large deformation analysis and concluded that it is slightly more efficient to apply rigid body corrections while integrating the constitutive equations.

Randolph and Hu (1998) proposed a remeshing and interpolation technique with small strain (RITSS) to achieve a LDFE analysis. In essence, the RITSS is a form of arbitrary Lagrangian Eulerian method, with small strain Lagrangian calculation in each incremental step and “convection” of the stresses and material properties from the old to the new mesh (Liu et al. 1986; Ghosh and Kikuchi 1991; Randolph et al. 2008). Figure 2-18 shows a complete loop of procedures of RITSS approach on the platform of ABAQUS. The remeshing and interpolation algorithms can be coupled with any standard FE package through user-written interface codes.

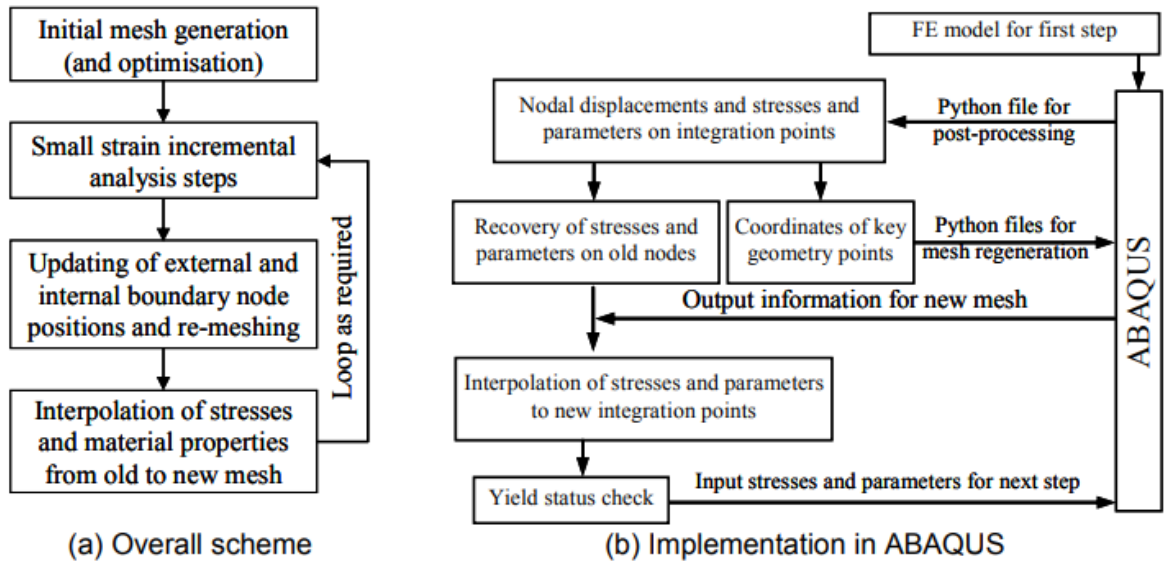


Figure 2-18. RITSS procedure in ABAQUS, after Hu and Radolph (1998)

Early application of 2D RITSS in geomechanics was built around the FE code, AFENA (Carter and Balaam 1995; Hu and Randolph 2002; Zhou and Randolph 2007; Song et al. 2008). Three-dimensional large deformation analyses usually need powerful algorithms in mesh generation and computational efficiency. By using 2D models, when a perfect symmetry is present in a problem, the analyses can be significantly more efficient.

Another LDFE approach is known as Coupled Eulerian-Lagrangian (CEL) method. In this method, the material domain with expected high/extreme deformations are processed using Eulerian approach, and the structure domain with expected small deformations are processed with Lagrangian approach. The Eulerian mesh part and Lagrangian mesh part are coupled with contact interactions. CEL has been frequently adopted in dynamic and quasi-static soil-pipeline interaction problems (Dutta et al. 2015, Wang et al. 2015, Keim et al. 2019). Dutta et al. (2015) conducted an analysis of the vertical and lateral penetration of offshore pipeline into marine clay. The soil had an undrained shear strength less than 10 kPa and was expected to significantly flow during the analysis. Figure 2-19 shows the model space and meshed parts of the pipeline problem described

in Dutta et al. (2015). Void mesh was setup to prevent the soil material from escaping the space of the mesh, otherwise the solver would lose track of the material nodes. The comparison between the simulation results and a series of centrifuge model test results proved the effectiveness of this CEL method.

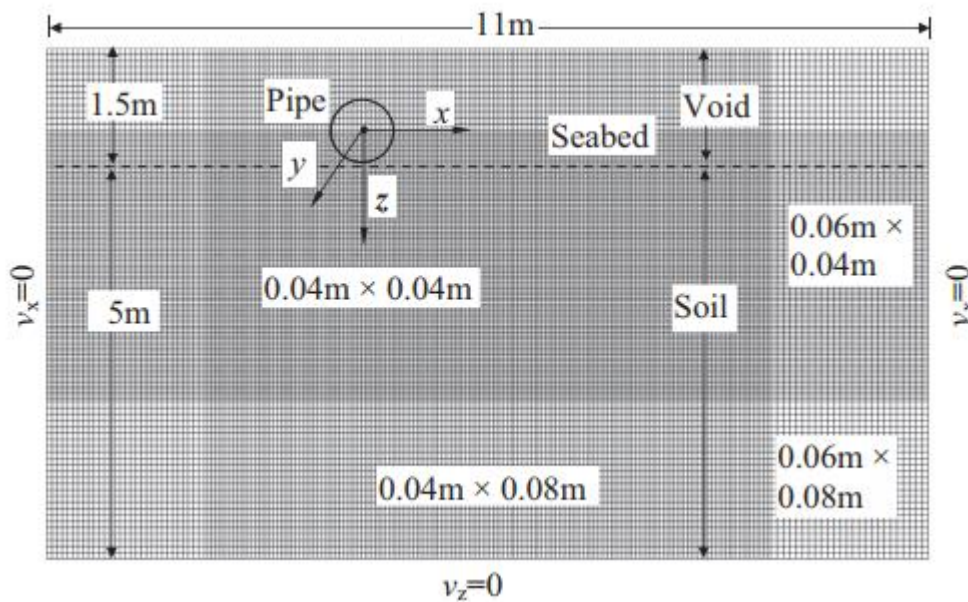


Figure 2-19. CEL model of the penetration of pipeline into clay (Dutta et al. 2015)

CEL analyses are dynamic with explicit integration scheme, it is very powerful for dynamic simulations. But the inertia effects must be carefully controlled if the problem is quasi-static. Notably, the Eulerian material may penetrate the contact interface into the Lagrangian side at corners, so that necessary measures should be taken to minimize it. In addition, Dassault Systèmes claimed that prescribed non-zero displacement boundary conditions cannot be applied to Eulerian nodes whose displacements are fixed. As a result, displacement-controlled loads are impossible through a node or node region in CEL approach.

A comprehensive comparison between EALE, CEL, and RITSS is available in Wang et al. 2015. In most cases, all three approaches are able to provide LDFE analyses with reasonable accuracy. The discrepancy concentrates on the loading methods, boundary conditions, application scenarios

and human effort. Generally speaking, RITSS and ALE are most suitable for a static problem, and CEL is more suitable for a dynamic analysis. In addition, ALE requires a heavy in-house coding, CEL can be accomplished purely on the graphical interface of ABAQUS, and RITSS requires significantly less scripting effort than ALE.

For a static loading analysis, RITSS seems to be the most suitable option among these three approaches. Moreover, the remeshing and interpolation algorithms can be coupled with any standard FE package through user-written interface codes. Wang et al. (2013) performed a LDFE parametric study of the uplift behavior of multi-helix piles in soft clay using RITSS method in ABAQUS. In this research, the problem was mimicked by a 2D axis-symmetric model as shown in Figure 2-20; the soil was assumed to be elasto-perfectly plastic in undrained condition. The soil-shaft interaction was neglected to simplify the soil-pile contacts. At a large displacement, two different failure modes of these uplifted multi-helix piles were observed. The behavior of helical piles or buried anchors was well discussed regarding the number of helices, embedment depth of helices, and inter-helix spacing.

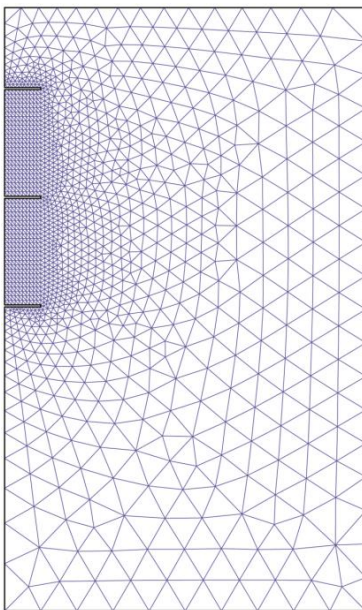


Figure 2-20. Mesh around a 3-plate tensile pile (Wang et al. 2013)

2.8 Summary

The centrifuge modeling technique for soil-helical pile interaction is under-developed. The centrifuge model tests in the literature are limited to the total axial load measurement only. Axial load distribution measurements required by the analyses of axial failure mechanisms are unavailable because the instrumentation in such tiny model helical piles is difficult. There are a few studies that present full-scale field load tests of helical piles with axial load distribution data, but the analyses of axial failure modes suffered from the heterogeneity of the in-situ soils. The interpretation of axial failure mode, which cannot be seen directly, has been essentially based on the back calculation of total capacity using the estimated in-situ soil strength parameters and assumed failure modes. As a result, significantly inconsistent indication factors of failure modes have been reported by various studies.

The current design method for the axial capacity of helical piles is somewhat unsatisfactory because uncertainties in the axial failure mechanisms of such piles in soil remain unclarified, especially for multi-helix piles. Conventional pile toe bearing factors and anchor break-out factors are simply applied to the problem of helical piles. The cylindrical shear force is adopted in the axial capacity design only when a CSM failure is guaranteed, which is usually unknown. Large discrepancy between predicted and measured ultimate capacity of helical piles are frequently reported by field loading studies. Until now, a study that systematically examines all possible factors that may affect the formation of the failure modes of multi-helix piles remains unavailable. The only indicating factor existing in the commercial design codes, i.e., $S_r = 3.0$, seems to be far from adequate. Therefore, in the helical piling industry, the axial capacity design tends to be over conservative by neglecting the shaft resistance and relies on in-situ pile installation torque verification.

To conduct a comprehensive investigation of the axial failure modes of multi-helix piles, a LDFE analysis is a viable option. Compared to in-situ filed load tests, a numerical method, once validated by test results, can implement various input parameters at a much lower cost. There are several LDFE analyses of the uplift capacity of helical piles regarding the effect of number of helices, pile embedment depth, and inter-helix spacing. These analyses were primarily set for the use of the offshore geotechnics, where the cohesive soil was typically much softer than onshore soils. However, all of the available studies excluded the analyses of soil-shaft interaction and the effect of soil shear strength from the LDFE models. In fact, the contribution of shaft resistance to the total axial capacity is not negligible. Moreover, the soil-shaft interaction may also affect the soil-helix interaction in its vicinity. In summary, a LDFE parametric study of helical piles regarding several control factors (e.g., inter-helix space ratio, pile embedment depth and soil strength) with a complete soil-pile interaction assembly is needed.

3 Development of Centrifuge Test System and Testing Program

3.1 Introduction

This chapter presents the development of centrifuge test system and the testing program. Since one objective of the present research is to examine the installation torque mechanism in flight, a primary requirement of the new test system is that the pile installation and axial loading must be performed in flight at the same g level. Ko et al. (1984) installed two piles at 1 g and 70 g conditions, respectively, and loaded both in flight at 70 g. A remarkable discrepancy in the axial behavior of these two piles illustrated in Figure 3-1 implies that a significant difference can occur if the pile installation is not conducted in the same stress regime as the axial loading test.

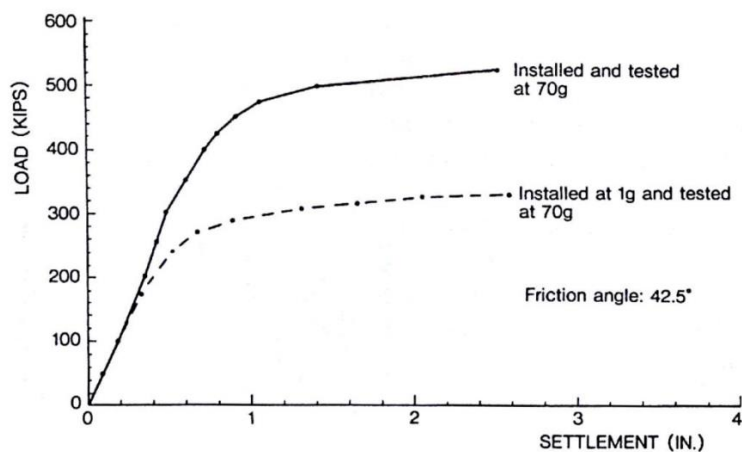


Figure 3-1. Effect of g level of pile installation on axial pile resistance measured in flight (after Ko et al. 1984)

The second requirement for the new test system is that a sufficient time period must be allowed for the vertical effective stress in the soil to establish before pile installation and load tests. Axial capacity of piles increases as the time elapses after pile are installed, because the excess pore pressure around the pile is progressively dissipated, according to Randolph and Wroth (1979) and Lanyi-Bennett and Deng (2019b). Although sometimes loads are applied to helical piles

instantaneously after installation, the performance after the set-up effect vanishes is more commonly considered; in the meantime, it is also the focus of the present study.

3.2 Loading Frame

The loading frame consists of a newly fabricated soil container, a dual-axis electric actuator, and an electric gear motor.

3.2.1 Soil Container

A new soil container was designed and fabricated for the present research. Figure 3-2 shows a three-dimensional overview of the soil container. This container was designed by Jakob Brandl and the author. This box was able to sustain 50 g centrifugal acceleration and a maximum consolidation pressure of 1500 kPa at 1 g condition. The inner dimension of the container, 709×300×400 mm, is sufficiently spacious to support the present test program and similar research projects in the future. The net weight of the container is about 84 kg. Rubber gasket was used to seal all corners as shown in Figure 3-3. The grooves in the bottom plate were aimed to collect pore water and drain the water through the hidden sink holes at both ends of the longitudinal groove. The material was aluminum because aluminum provides a light weight and a high strength. The container enables two-way vertical drainage of the model soil. The soil container was fabricated by Nexus CNC, Edmonton. Detailed drawings are available in Appendix A.

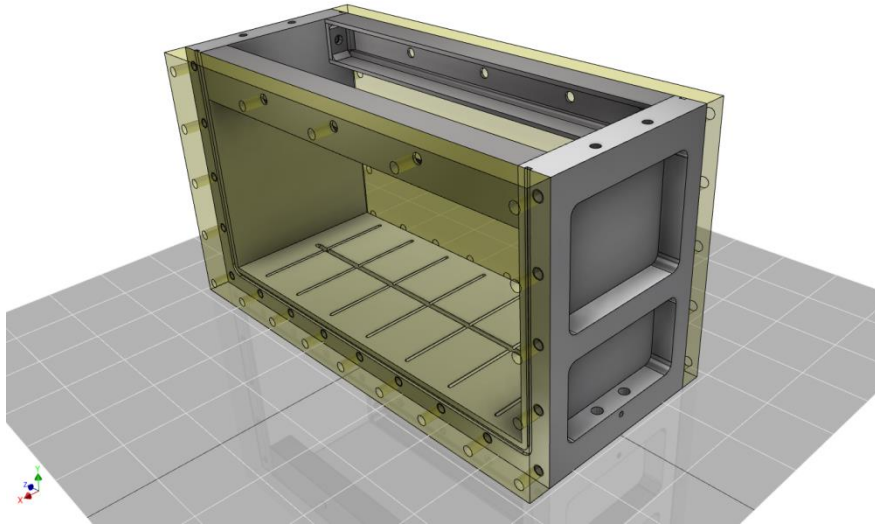


Figure 3-2. Soil container: all four walls were fabricated with aluminum plates

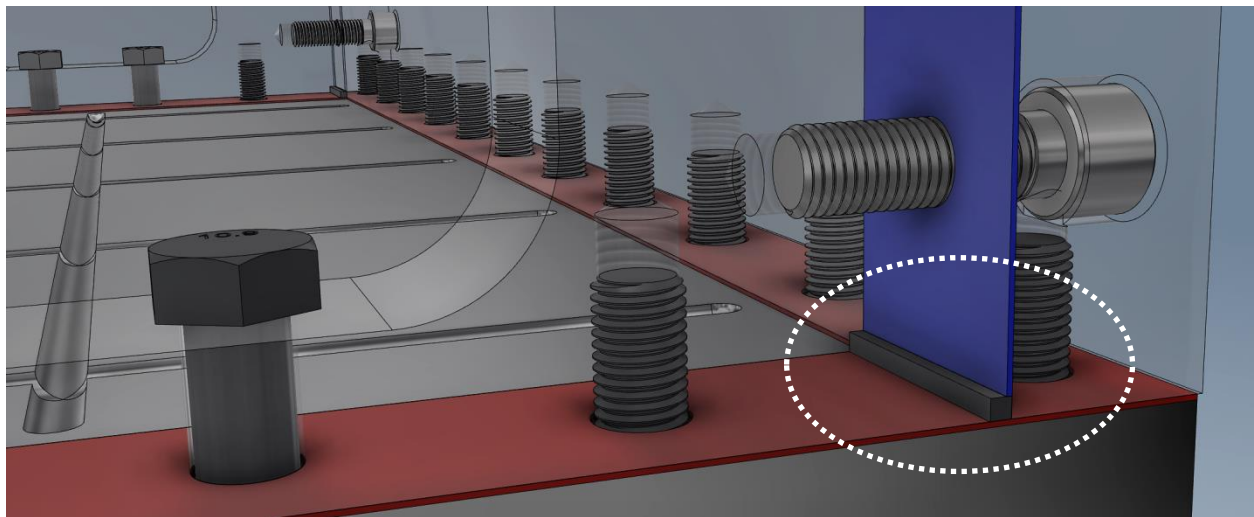


Figure 3-3. Positioning of gasket for sealing purpose

3.2.2 Installation Gear Motor

A gear motor, MMP S17-400A-12V manufactured by Midwest Motion Products, was selected to install piles by torque at the designated centrifugal acceleration. The gear motor can fit in the working space of the current test setup. This motor, powered by 12 V and 6.7 A DC, outputs a constant speed of 23 rotations per min (rpm) approximately. A set of adaptors were designed to

connect the test piles to the output shaft of the gear motor for pile installation and load tests. Figure 3-4 shows a photo of the gear motor and the adaptors. The adaptors were used to mount the model pile to the gear motor (Adaptor 1) and then to the actuator (Adaptor 2). They were designed by the author and fabricated by CME Shop at the University of Alberta. Detailed drawings of the adaptors are included in Appendix A.

A steady rotational speed of this gear motor is critical to the pile installation test. To confirm the capability of the motor for installing piles at a constant rpm regardless of torque resistance, the correlation between the shaft rotational speed and output torque (Nm) of the motor was calibrated prior to the use. An aluminum plate with grooved edge was fixed onto the shaft of the motor, and a nylon string was tied around the plate to hang a free dead weight. A total number of ten different weights were tested. The rotational speed of the motor corresponding to each dead weight was then measured by counting the elapsed time over five revolutions. The results are presented in Figure 3-5. It is shown that the speed of the motor is maintained at 22.5 rpm over the range of applied torque values. With this constant rotational speed, an equivalent vertical penetrating speed can be designated so that the pile installation will be conducted at one pitch advancement per revolution thus to minimize the soil disturbance. The pile penetration is to be executed by an electric actuator mounted on a carriage that can move vertically at a designated vertical speed. The typical rotational speed for the installation of production piles varies between 30 and 60 rpm according to personal communication with the industrial collaborator. Normally the principle of “one pitch advancement per revolution” when installing helical piles is not rigorously followed in engineering practice since there is no economic way to control the advancing rate of full-scaled piles in the field. Nonetheless, a competent operator can approximate the designated pile penetration speed by manually moving the torque head. In addition, the effects of rotational speed

on the installation torque or pile axial behavior have not been studied in the literature. The gear motor used in this study for pile installation holds on to a constant rotational speed about 22.5 rpm, which is smaller than the aforementioned range for practice. This may be a limit of the load test.

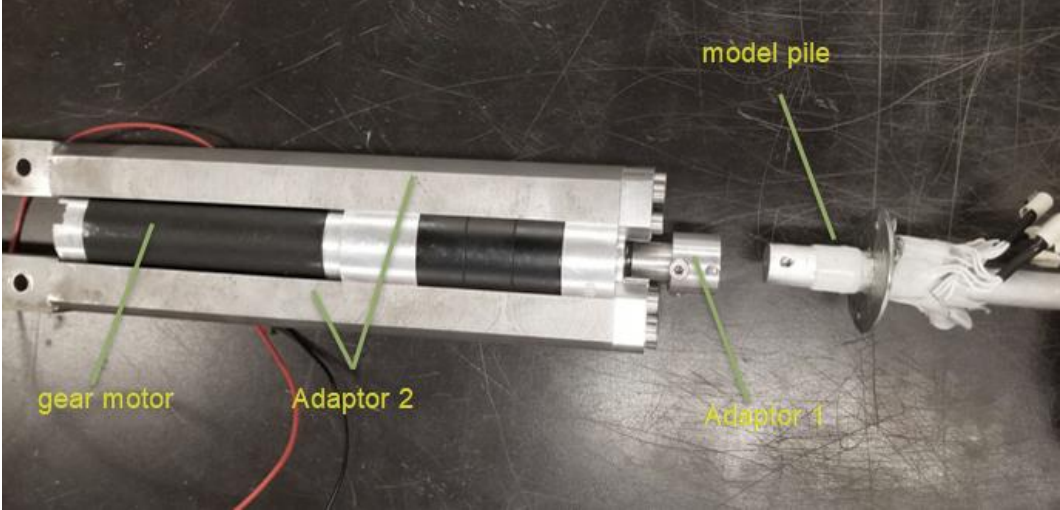


Figure 3-4. Gear motor and adaptors designed for installing model piles at a constant rotational speed

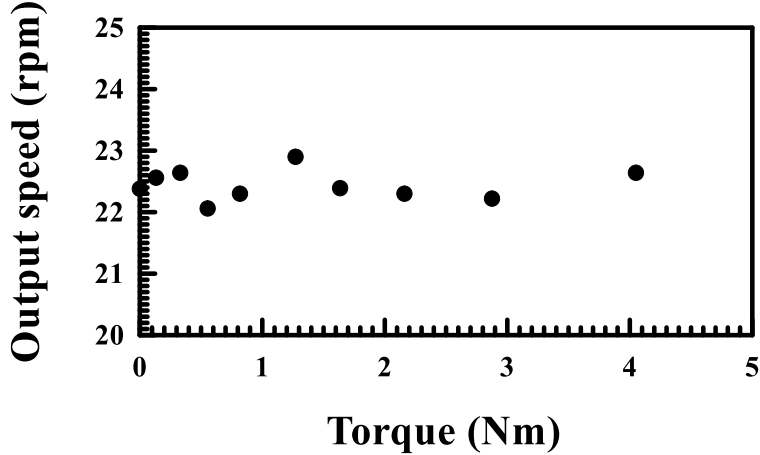


Figure 3-5. Results of calibrating the gear motor at 1 g condition: output rotational speed vs. applied torque

3.2.3 Dual-Axis Actuator

The electric dual-axis actuator consists of an aluminum base with two parallel rails, and a standing frame that can slide on the rails. A rectangular carriage that can move vertically is built inside the frame. The horizontal movement of the standing frame and the vertical movement of the carriage are controlled by two step gear motors. Figure 3-6 shows an overview of the actuator. By mounting the test pile to the carriage via adaptors and installation motor, the pile can move in vertical and horizontal directions at designated speed. Four M16 bolts were used to fix the actuator to the top of the container for centrifuge model tests. A customized program was used to give orders to the step gear motors for dual-axis travels. The programming code is presented in Appendix B.

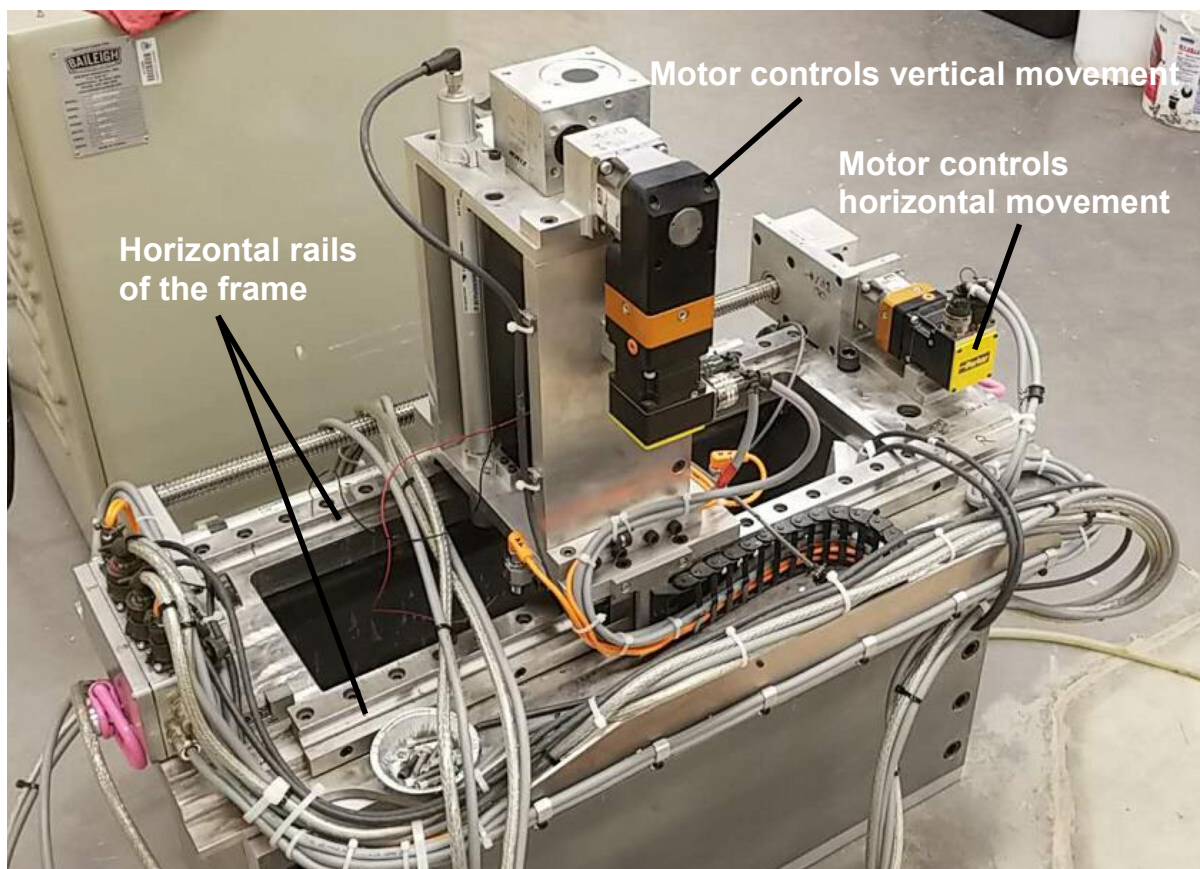


Figure 3-6. Dual-axis electric actuator: horizontal movement of frame box and vertical movement of a carriage in frame box are enabled

3.3 Model Piles

3.3.1 Pile Fabrication

The dimensions of the model piles were designed approximately from a common prototype pile size provided by the industrial collaborator. The inter-helix spacing of model piles was varied to consider the effects of spacing on the axial load transfer mechanism, which is one of the primary objectives of the present research. The shaft and helix diameters of the prototype pile are 254 mm and 762 mm, respectively, which are common in practice. The model piles, fabricated by the CME Shop, were scaled down by 20 times since the target centrifugal acceleration was set 20 g. Although the prototype pile shaft is made of steel pipes, aluminum was selected to be the material of the model piles for three reasons: 1) the Young's modulus of aluminum is about one third of steel such that smaller strain can be measured by the strain gauges; 2) an aluminum pile is able to act as a "rigid body" as well as a steel pile in the interaction with clay; 3) it is easier to machine aluminum than steel. The dimensions of all test piles are summarized in Table 3-1. Figure 3-7 shows a photo of all model piles and the ID of each pile P1 to P4. More detailed drawings of these model piles are presented in Appendix A.

The pitch of a helix is defined as the opening size of the helix. The model pitch of 12.7 mm was scaled from the pitch size of a prototype pile at 254 mm. The helices of the model piles may not be defined as "true helix" whose radial direction makes a right angle with the pile shaft throughout the pitch. Nonetheless, the pitch size of the helices was controlled in the machine shop.

Table 3-1. Dimensions of the model piles

Pile Code	No. helices	L (mm)	d (mm)	D (mm)	P (mm)	E (mm)	H (mm)	S (mm)	S/D
P1	1							N.A.	N.A.
P2	2	21.8	12.7	38.1	12.7	169.1	150	57.2	1.5
P3	2							95.2	2.5
P4	2							133.4	3.5

Note: d = shaft diameter; D = helix diameter; P = pitch of helix; E = length of pile from soil surface to tip; H = length of pile from soil surface to leading edge of lower helix; S = spacing of two adjacent helices.



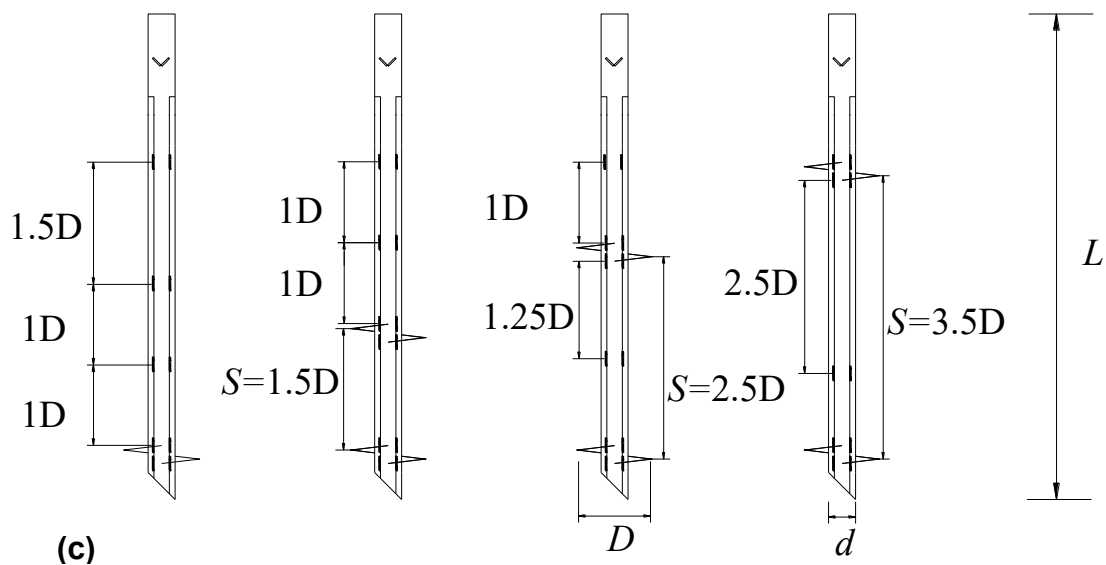
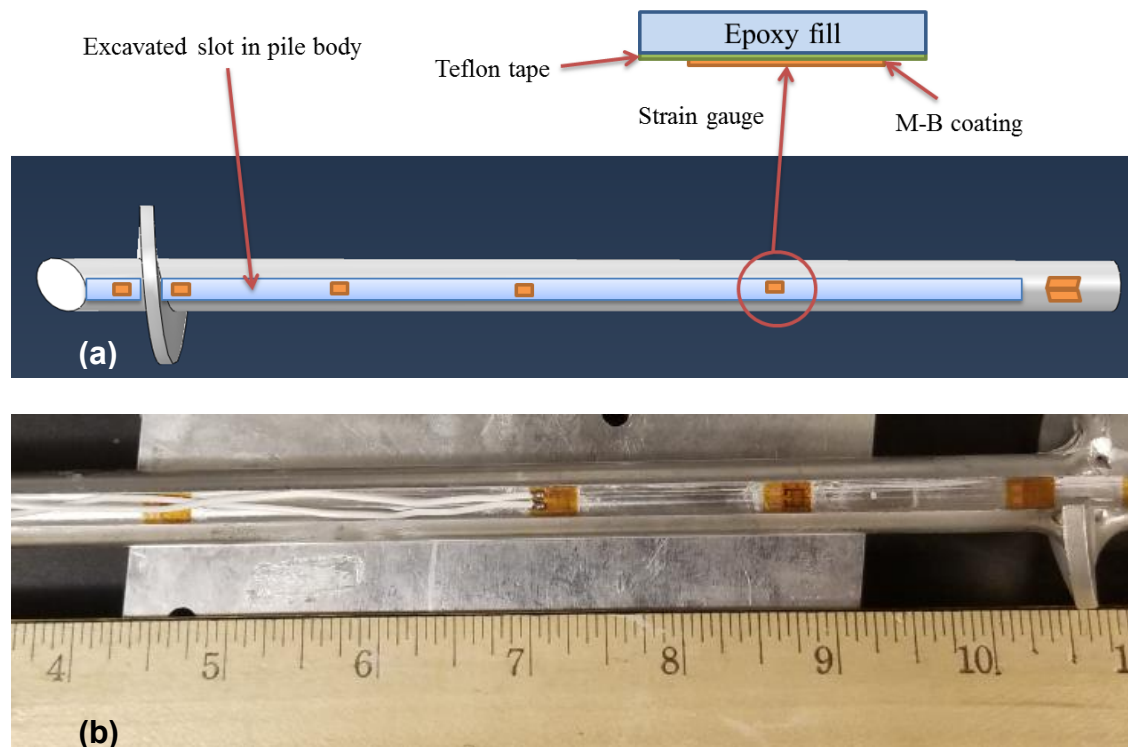
Figure 3-7. Photo of model piles: P1 to P4 from left to right

3.3.2 Pile Instrumentation

A literature review suggests that research that involves the installation of fully instrumented helical piles has been rare. In fact, experience with axial strain gauges on driven piles in centrifuge model tests is also deficient in the literature. In the present research, model piles are instrumented with axial strain gauges and torsional strain gauges that measure the internal axial forces during pile loading tests and the torque during pile installation, respectively. The present research developed a new technique for placing and protecting axial strain gauges on helical piles. As shown in Figure 3-8, two grooves were cut along the axial direction of model piles and gauges were placed inside the grooves. The arrangement of the pile instrumentation is presented in Figure 3-8.

Two types of strain gauge circuits were adopted. For torque measurement, a full Wheatstone bridge consisting of two pads of strain gauges was used; the gauge model is CEA-06-062UV-350 (manufactured by Micro Measurements VPG) that is a universal general-purpose type with a strain range of $\pm 3\%$. Two strain gauges, on a base pad, were placed at the 45 and 135° rosette, with respect to the pile cross-sectional plane. The full-bridge configuration will compensate the effects of temperature, pile axial strain, and bending moment on the pile.

For axial strain measurement, a half Wheatstone bridge circuit consisting of two active single gauges was adopted, considering the limited space along the strain gauge groove. The gauge model is CEA-13-062UW-350 (made by Micro Measurements VPG) that is a universal general-purpose type with a strain range of $\pm 3\%$. The gauges were placed on two oppositely positioned grooves cut into the pile shaft. The active gauges were wired to two dummy gauges secured in the data acquisition box. The locations of strain gauge stations are determined with the consideration of anticipated load distribution, so that the axial load transfer mechanism along the shaft and helical plates can be inferred. The axial and torque strain gauge circuits are shown in Figure 3-9.



$D=38.1$ $d=12.7$ $L=271.8$ Unit: mm

Figure 3-8. (a) Approximate locations of strain gauge stations and the protection technique; (b) Photo of strain gauges installed inside the gauge grooves; and (c) Position of axial and torque strain gauges; units are in the model scale

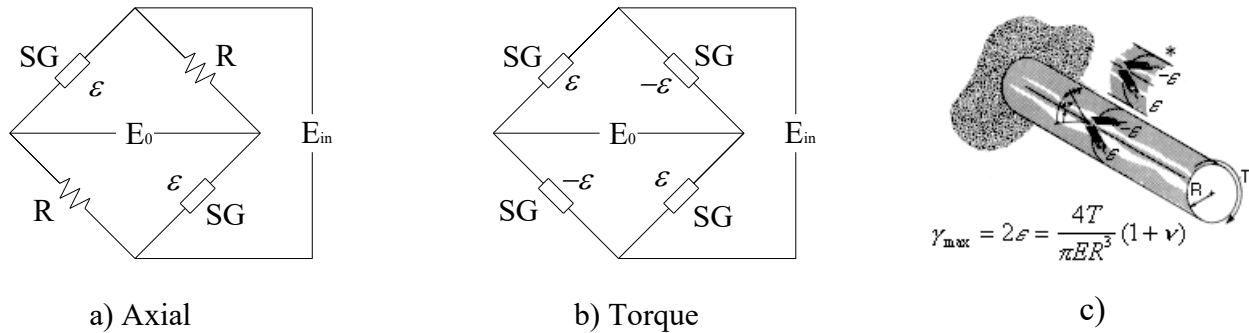


Figure 3-9. (a) Half bridge circuit for axial strain on model piles; (b) Full bridge circuit for the torque gauge on pile head; and (c) schematic of principle of torque measurement, where torque gauges were arranged to form a 45° and 135° rosette. Note: R = resistors (or dummy gauges) placed in the data logger; SG = active strain gauges installed on pile shaft; ϵ = anticipated strain to be recorded by the SG; E_0 = output voltage; E_{in} = constant excitation.

In order to protect the strain gauges from potential damages caused by moist invasion or physical abrasion, especially for these axial gauges embedded in soil, the following technique was adopted. Two grooves that are 5 mm wide and 4.75 mm deep are excavated along the shaft on the opposite sides. Axial strain gauges were then glued to the bottom of the grooves. To prevent moisture attack and electric leakage, the strain gauges were covered with insulating coating and Teflon tapes, and then the grooves were carefully filled with epoxy. The electric wires were also fixed inside the grooves by the epoxy filling. The surfaces of the cured epoxy were smoothed with #240 sandpapers and polished with soft cloth in the end. Figure 3-10 shows a finished model pile with wire connections and protection. This new technique has demonstrated the efficiency in preserving strain gauges from mechanical damage or moisture invasion.

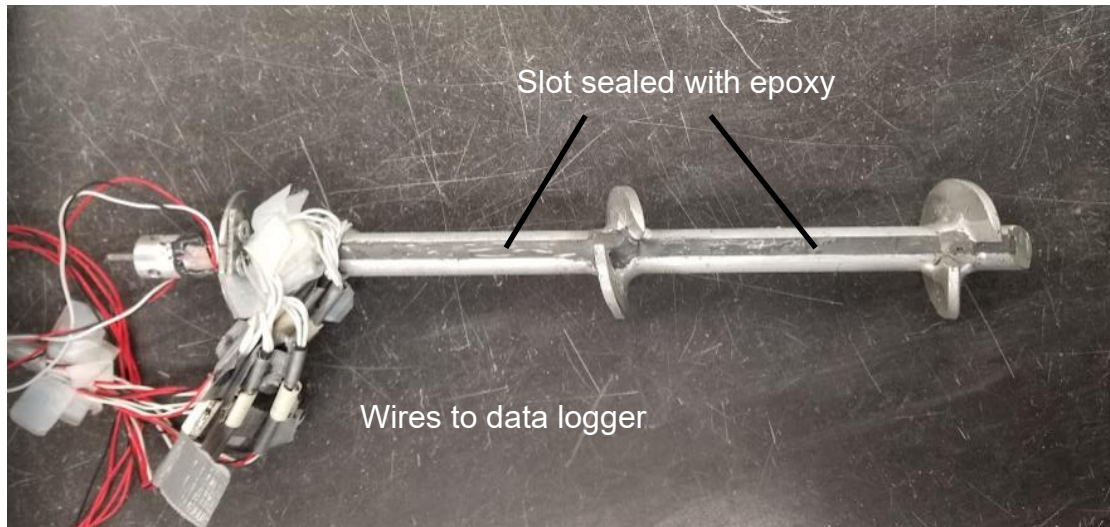


Figure 3-10. A complete instrumented pile

3.3.3 Principle of Strain Gauge Measurement and Calibration of Gauges

The measured strain can be interpreted using the following equations. For axial gauges, the axial strain is expressed as:

$$\varepsilon_{\text{axial}} = \frac{2aE_0}{E_{\text{in}} \cdot GF} \quad (3-1)$$

where a is the output signal amplification factor, E_0 is the output voltage, E_{in} is the constant excitation and GF is the gauge factor obtained from the manufacturer's specification for the strain gauge model. For the data logger used in this study, $a = 200$ and $E_{\text{in}} = 15 \text{ V}$.

For torque gauges, the maximum shear strain induced by the external torque is:

$$\gamma_{\text{max}} = 2\varepsilon_{45^\circ} = \frac{2aE_0}{E_{\text{in}} \cdot GF} \quad (3-2)$$

where ε_{45° is the normal strain measured by the individual gauge on the torque gauge pad at 45° with respect to the longitudinal axis of the shaft.

The target force or torque can then be calculated from the measured strain:

$$\text{Axial Force: } F = E_{\text{al}} A \varepsilon_{\text{axial}} = E_{\text{al}} A \frac{2aE_0}{E_{\text{in}} \cdot GF} \quad (3-3)$$

$$\text{Torque: } T = G_{\text{al}} \gamma_{\text{max}} J / r_{\text{pile}} = \pi E_{\text{al}} \gamma_{\text{max}} r_{\text{pile}}^3 / [4(1 + \nu)] \quad (3-4)$$

where E_{al} is the Young's modulus of the aluminum that is the material of model piles, A is the cross section area of the pile head, G_{al} is the shear modulus of aluminum, γ_{max} is the shear strain at the surface of pile shaft, $J (= \pi r_{\text{pile}}^4 / 2)$ is the polar moment of inertia of the pile head, r_{pile} is the radius of the pile head, and ν is the Poisson's ratio of aluminum and selected to be 0.3.

Calibration of the strain gauges was performed prior to the pile testing. The torque and axial strain gauges were calibrated using the setup shown in Figure 3-11. During this calibration, only the data logger readings and the applied axial load or plain torque were used. The detailed calibration results are presented in Table 3-3 and Table 3-4.

The results show that the HBM data logger produces 1 mV/V per 1.87 kN·m for the torque gauges, and 1178 kN for the axial strain gauges. The calibration factor stands for the average values of all gauges. Notably, the calibration factors of all axial strain gauges are very consistent.

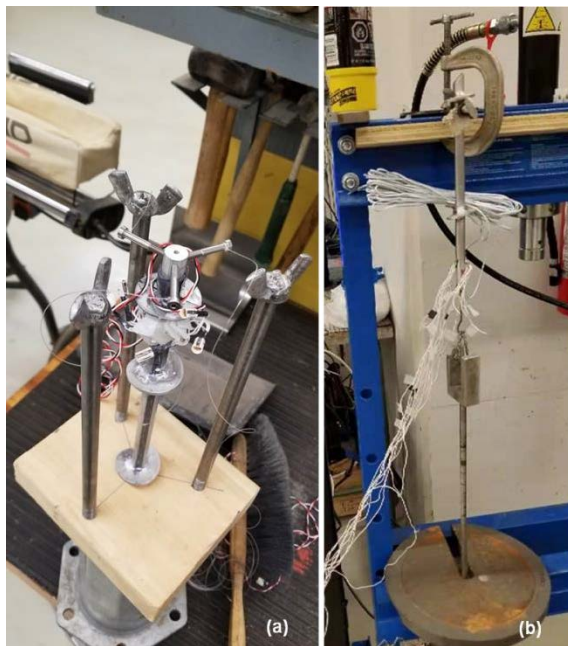


Figure 3-11. Setup for the calibration of (a) torque strain gauges, and (b) axial strain gauges

Table 3-2. Calibration data of axial strain gauges

	Pile	Applied load (N)			Average calibration factor, kN·m/(mV/V)
		47.25	84.61	132.47	
Data logger readings (10 ⁻³ mV/V)	P1	0.039	0.071	0.111	1195
	P2	0.040	0.070	0.111	1201
	P3	0.041	0.073	0.114	1159
	P4	0.041	0.073	0.115	1157

Table 3-3. Calibration data of torque strain gauges

	Pile	Applied torque (N·m)			Average calibration factor, kN·m/(mV/V)
		0.148	0.51	0.86	
Data logger readings (10 ⁻³ mV/V)	P1	0.079	0.273	0.461	1.867
	P2	0.083	0.27	0.469	1.847
	P3	0.084	0.28	0.456	1.851
	P4	0.074	0.285	0.46	1.853

Table 3-4. Summary of strain gauge calibration

SG type	Gauge Factor, GF	Bridge type	Rosette	Excitation (V)	Average calibration factor
Axial	2.15	Half	Axial	10	1178 kN/(mV/V)
Torque	2.17	Full	45°	15	1.85 kN·m/(mV/V)

The results of calibration tests were compared with the theoretical values. The theoretical axial force and torque per 1mV/V of the data logger output can be calculated according to Equations 3-5 and 3-6:

For axial gauge:

$$F = E_{al} A \frac{2aE_0}{E_{in} \cdot GF} = 70\text{GPa} \cdot 95.68\text{mm}^2 \cdot \frac{2 \cdot 200}{2.15} \cdot 1\text{mV} / \text{V} = 1246\text{kN} \quad (3-5)$$

For torque gauge:

$$T = \pi E_{al} \frac{2aE_0}{E_{in} \cdot GF} r_{pile}^3 / [4(1 + \nu)] = 3.14 \cdot 70\text{GPa} \cdot \frac{2 \cdot 200}{2.17 \cdot [4(1 + 0.3)]} (6.35\text{mm})^3 \cdot \frac{\text{mV}}{\text{V}} = 2.00\text{kN} \cdot \text{m} \quad (3-6)$$

Overall, the average calibration factors listed in Table 3-4 are in a reasonable agreement with the theoretical values with a small error, which in turn confirmed that the gauges were installed appropriately, and the data logger and Wheatstone bridges were correctly configured. The average calibration factors rather than the theoretically derived factors were used in the following data processing.

3.4 Pore Pressure Transducers

The soil consolidation during centrifugal spinning is a critical issue of this centrifuge model tests with clay. Before performing pile installation and axial loading tests, the pore pressure inside the soil should reach the hydrostatic level corresponding to the steady g level; otherwise, the effect of

excess pore pressure on the tests would be difficult to clarify. In the test series WL01, prior to installing piles, an over-night spinning at 20 g was conducted for the setup of pore pressure in the clay. The settlement of the soil was monitored by a laser distance sensor and the result is presented in Figure 3-12. It shows that the consolidation initiated by the spin-up was complete within two hours. However, as the test proceeded, it was noticed that the laser measurement method was not capable of monitoring the soil reaction or pore pressure changes owing to the limitations as follows.

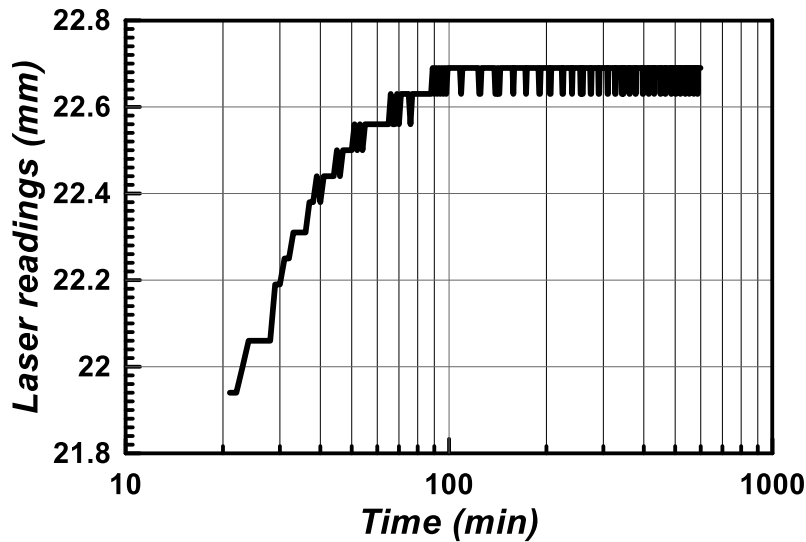


Figure 3-12. Soil surface settlement initiated by centrifuge spin-up, during the over-night consolidation before Stage 1 of WL01, in model scale

Firstly, the centrifuge spinning must be paused on the following occasions: moving the loading frame from one test station to the next, adding water to prevent the soil surface from drying up, and fixing unexpected problems such as broken zip ties and entangle wires. During the spin-down, the pore pressure inside the clay would decrease in response to the lowering g level. Among the occasions mentioned, moving the loading frame and adding water will severely disturb the laser sensor. Secondly, the residual excess pore pressure induced by pile installation may also introduce uncertainties to the soil resistance against axial movement of the test piles, but the laser sensor

cannot measure any pore pressure change in the soil. Therefore, pore pressure transducers (PPT's) were added into the WL02 tests to monitor the change of pore pressure.

KPE-1MPB (Figure 3-13) manufactured by Tokyo Measuring Instruments was selected. The brass casing of KPE-1MPB is a cylinder with 10 mm diameter and 13.5 mm height. The range of the PPT is limited to 1 MPa.

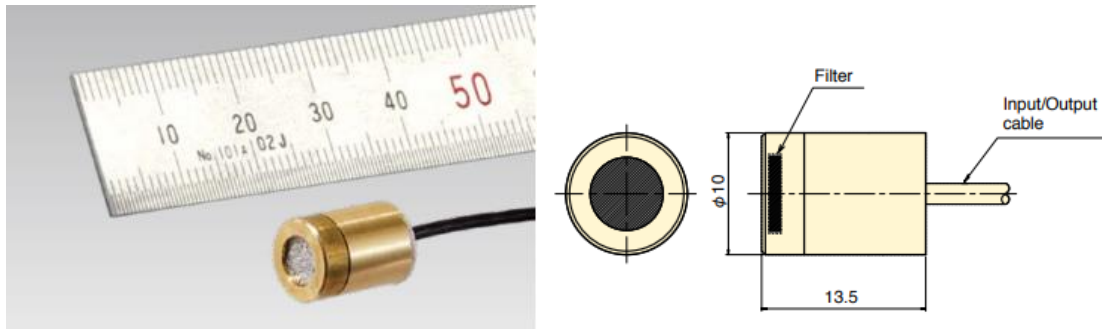


Figure 3-13. Dimensions of PPT's, by manufacturer

Two PPT's were installed in the clay model of WL02 tests at two different depths. To install the PPT, a thin-walled plastic tube with an external diameter of 12.7 mm was inserted to the designated depths. Then the tube was pulled out with a soil plug inside, leaving a borehole behind. The saturated PPT was then pushed into the borehole with the filter side down to reach the bottom. The soil plug in the tube was extruded to fill back into the borehole. The backfill gained some strength during the following in-flight consolidation. However, the backfill may have less strength and greater permeability than the nearby undisturbed soil. Each PPT has a bulk density of about 2.17 gm/cm^3 , which is slightly greater than that of the clay (about 1.84 gm/cm^3). The effect of the differential density on PPT sinking or the excess water pressure was estimated to be negligible, given the high soil strength.

PPT was calibrated using standpipes and rubber tubes. The filter side of the PPT's was inserted into the soft rubber tube connected to standpipes. The range of applied pressure is 0 to 2 m of water. The calibration results are presented in Table 3-5 and Figure 3-15. It shows that the PPT measures about 1 kPa per 10^{-3} mV/V of HBM output. The output offset of each transducer was removed when calculating the calibration factors.

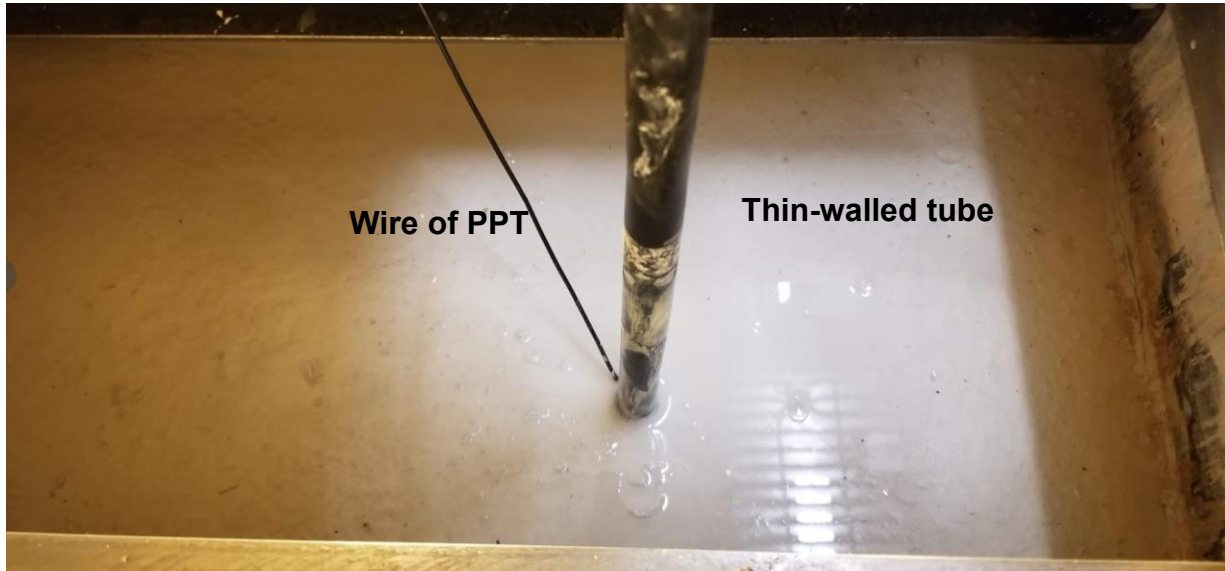


Figure 3-14. Installation of pore pressure transducers at 1 g condition

Table 3-5. Results of PPT calibration tests

Height of water (m)	Pore pressure (kPa)	HBM Output PPT1 (10^{-3} mV/V)	HBM Output PPT2 (10^{-3} mV/V)	Calib. factor PPT1 [kPa/(mV/V)]	Calib. factor PPT2 [kPa/(mV/V)]
0.25	2.4525	2.48	2.42	988.9	1013.4
0.5	4.905	4.93	4.94	994.9	992.9
0.75	7.3575	7.32	7.3	1005.1	1007.9
1	9.81	9.9	9.74	990.9	1007.2
1.25	12.2625	12.32	12.36	995.3	992.1
1.5	14.715	14.68	14.74	1002.4	998.3
1.75	17.1675	17.29	17.2	992.9	998.1
2	19.62	19.74	19.65	993.9	998.5

Note: the calibration factor was calculated by removing the initial offset signal.

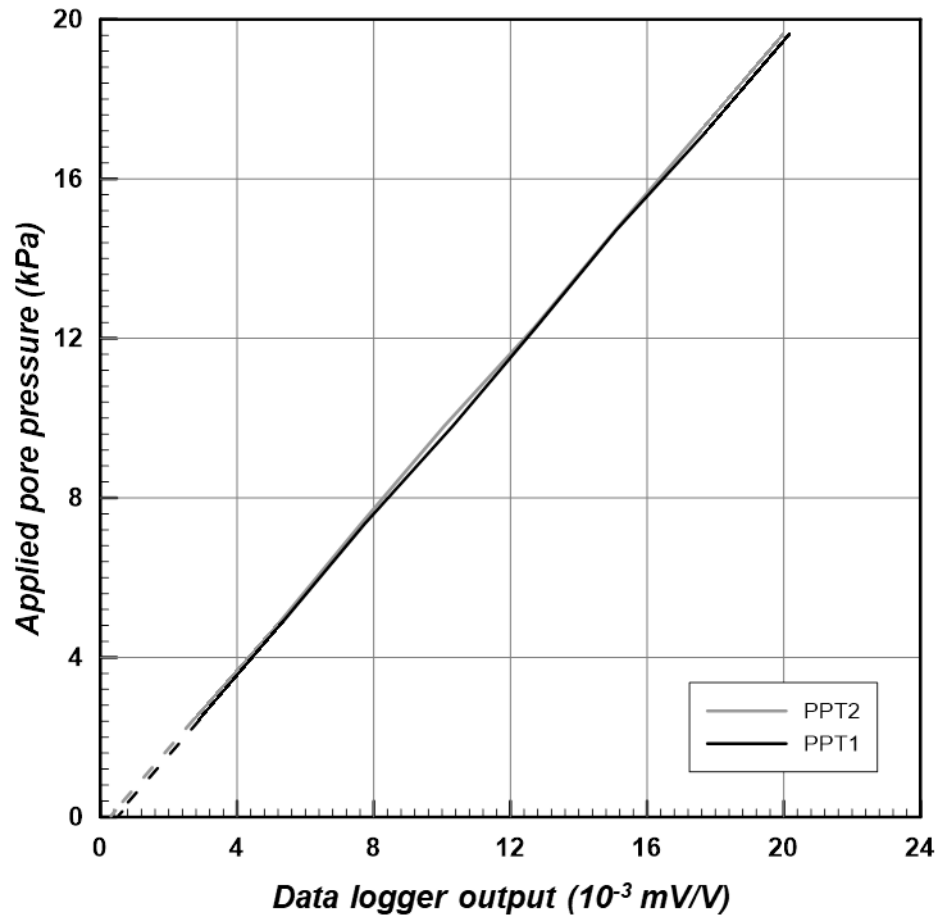


Figure 3-15. Data logger reading vs. applied pore pressure

3.5 Soil Model Construction

The soil model was constructed with tap water and the Speswhite Kaolinite produced by Imerys S.A. from its branch in British Columbia, Canada. Laboratory soil tests showed that the fundamental soil properties are as follows:

$$G_s = 2.65, PL = 33.8, LL = 54.6$$

where G_s is specific gravity of the soil, PL is the plastic limit, and LL is the liquid limit.

3.5.1 Consolidation

The clay models were prepared from kaolinite slurry using incremental consolidation pressure. Figure 3-16 shows the slurry made in a vacuum mixer and the soil transferred into the soil container. The initial water content of the slurry was selected to be 100% for WL01 and 80% for WL02, which was more than 50% of the LL. This selection was aimed to utilize the high liquidity to minimize the probability of air intrusion during the placement of the slurry and to maximize the soil uniformity.



Figure 3-16. Kaolinite slurry: in a vacuum mixer (left) and in the soil container (right)

The soil model was constructed in one lift. We filled the container with slurry almost to the top, and then moved the container onto a loading frame driven by a servo-controlled hydraulic pump. Figure 3-17 shows the setup of the loading frame. An incremental pressure sequence was performed in this consolidation progress. Including the weight of the loading cap, the vertical pressure on the top of the model clay was applied as follows: 5 kPa, 10 kPa, 20 kPa, 50 kPa, 100 kPa, 200 kPa, 500 kPa, 200 kPa, and 50 kPa for WL01; and 5 kPa, 10 kPa, 20 kPa, 50 kPa, 100

kPa, 200 kPa, 500 kPa, 1000 kPa, 1500 kPa, 500 kPa, 200 kPa, and 50 kPa for WL02. SHANSEP method (Ladd and Foote, 1974) was used to guide the prediction of final consolidation pressures and the details of the calculation are presented in Chapter 4. Notably, a quick vane shear test showed that the s_u value of the consolidated clay of WL01 at the depth of 140 mm was 20% smaller than the designated value of 50 kPa. To improve the strength, the clay was reloaded to 750 kPa. From one pressure increment to the next, the consolidation curve of settlement vs. log time was recorded to ensure the primary consolidation has been achieved. The load vs. displacement time history was recorded using an Agilent 34970A data logger. The soil was compressed under doubly drained condition.



Figure 3-17. Loading frame for kaolinite consolidation

3.5.2 Soil Properties Interpreted from Consolidation Results

A representative consolidation curve obtained at the load increment of 500 kPa of WL02 is shown in Figure 3-18. The end of primary consolidation (EOP) was associated with the inflection point

near 800 min. The coefficient of consolidation, C_v , interpreted from Figure 3-18 is $8.30 \times 10^{-3} \text{ cm}^2/\text{s}$ using Casagrande's method. Other consolidation curves and corresponding C_v values are presented in Appendix A. The compressibility curve of all load increments is shown in Figure 3-19. The estimated consolidation indices for the normal consolidation and unloading-reloading consolidation lines are as follows:

$C_c = 0.604$, $C_{cr} = 0.059$ and $C_c = 0.480$, $C_{cr} = 0.045$, for WL01 and WL02, respectively.

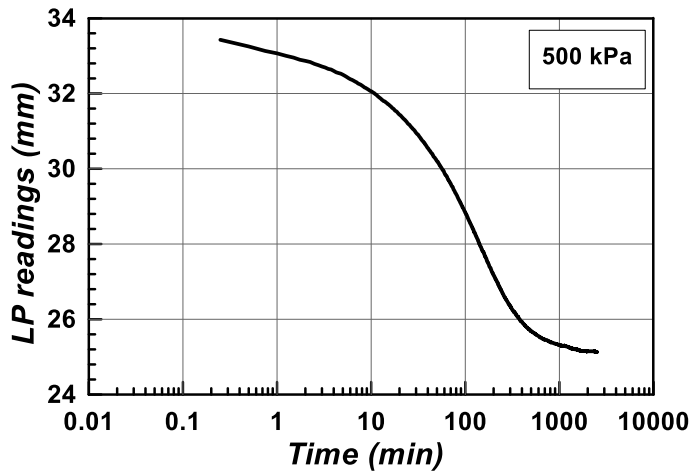


Figure 3-18. Consolidation curve under vertical stress of 500 kPa, WL01

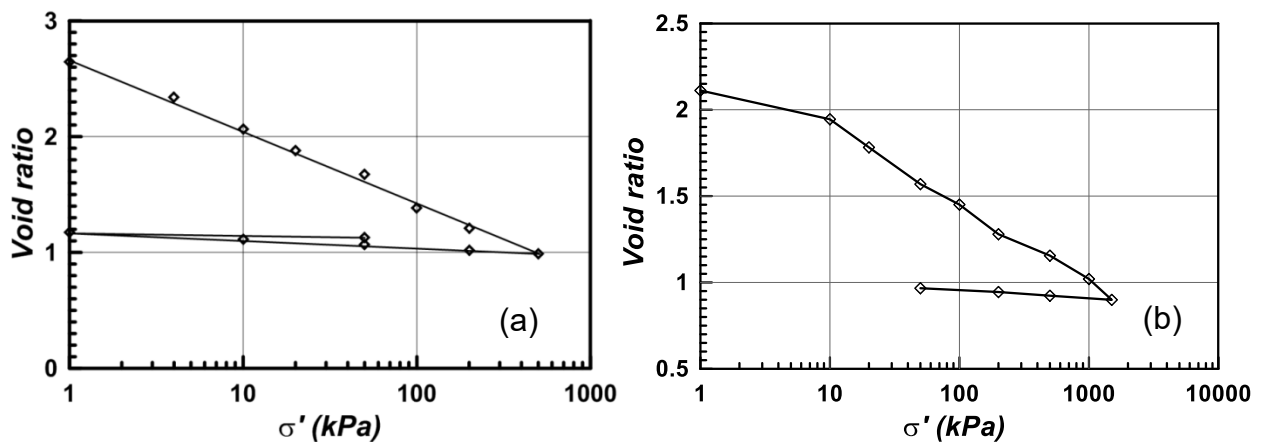


Figure 3-19. End-of-primary void ratio vs. consolidation stress in two test series: (a) WL01, and (b) WL02

Table 3-6 and Table 3-7 show the results of consolidation tests including loading and unloading stages. Table 3-8 and Table 3-9 show the interpreted soil properties. At the end of all consolidation stages, the consolidation stress was maintained at 50 kPa, which is close to the stress level at the designate centrifugal acceleration. The initial thickness of the slurry is 372 mm, and the ending thickness is 245 mm, which is close to the estimated thickness of 240 mm.

Table 3-6. Summary of consolidation tests of speswhite kaolinite, WL01

Increment		Stress	EOP Height, H_{100}	EOP strain	EOP Void ratio, e	H_0	H_{50}	t_{50}	t_{100}
		(kPa)	(cm)	(%)	(-)	(cm)	(cm)	(min)	(min)
0	Seating	4.8	36.15	-8.48	2.34	39.50	N/A	N/A	N/A
1	Load	10	33.15	-8.30	2.06	36.15	N/A	N/A	N/A
2	Load	20	31.16	-6.00	1.88	33.15	32.17	760	2500
3	Load	50	28.93	-7.13	1.67	31.16	N/A	N/A	N/A
4	Load	100	25.81	-10.81	1.39	28.93	27.37	570	2600
5	Load	200	23.92	-7.37	1.21	25.81	24.87	312	1600
6	Load	500	21.53	-10.00	0.99	23.92	22.73	131	820
7	Unload	200	21.84	1.44	1.02	21.53	23.04	142	960
8	Unload	50	22.42	2.66	1.07	21.84	22.13	166	1200
9	Unload	10	22.88	2.05	1.11	22.42	22.65	174	1300
10	Unload	4.8	23.53	3.11	1.18	22.82	23.18	212	1700
11	Reload	50	23.01	-2.21	1.13	23.53	23.27	60	1020
12	Reload	200	21.97	-4.52	1.03	23.01	22.49	49	840
13	Reload	750	20.72	-5.69	0.91	21.97	21.35	81	1120
14	Unload	0	23.28	12.35	1.16	20.72	N/A	N/A	N/A

Table 3-7. Summary of consolidation tests of speswhite kaolinite, WL02

Increment		Stress	EOP Height, H ₁₀₀	EOP strain	EOP Void ratio, <i>e</i>	H ₀	H ₅₀	t ₅₀	t ₁₀₀
		(kPa)	(cm)	(%)	(-)	(cm)	(cm)	(min)	(min)
1	Load	10	35.2	-5.37	1.94	37.2	36.3	1000	4600
2	Load	20	33.3	-5.52	1.78	35.2	34.2	420	2400
3	Load	50	30.7	-7.63	1.57	33.3	32.0	310	1550
4	Load	100	29.3	-4.63	1.45	30.7	30.1	190	1000
5	Load	200	27.2	-7.00	1.28	29.3	28.3	130	600
6	Load	500	25.8	-5.42	1.16	27.2	26.6	70	410
7	Load	1000	24.2	-6.29	1.02	25.8	25.1	41	300
8	Load	1500	22.7	-5.96	0.90	24.2	23.5	32	255
9	Unload	500	23.0	1.23	0.92	22.7	N.A.	N.A.	N.A.
10	Unload	200	23.3	1.13	0.94	23.0	N.A.	N.A.	N.A.
11	Unload	50	23.5	1.12	0.97	23.3	N.A.	N.A.	N.A.

Table 3-8. Summary of soil properties from consolidation tests in WL01

Increment	m_v (m ² /kN)	c_v (cm ² /s)	k_v (cm/s)	σ'_v (kPa)	Avg. σ'_v (kPa)
0	N/A	N/A	N/A	4.8	4.8
1	0.01612	N/A	N/A	10	10
2	5.88E-03	1.118E-03	6.45E-07	20	20
3	2.43E-03	N/A	N/A	50	50
4	2.09E-03	1.079E-03	2.22E-07	100	100
5	0.75E-03	1.627E-03	1.2E-07	200	200
6	0.33E-03	3.237E-03	1.05E-07	500	500
7	0.05E-03	3.069E-03	1.51E-08	200	200
8	0.17E-03	2.422E-03	3.92E-08	50	50
9	0.48E-03	2.42E-03	1.15E-07	10	10
10	6.38E-03	2.08E-03	1.3E-06	4.8	4.8
11	0.51E-03	7.408E-03	3.69E-07	50	50
12	0.31E-03	8.473E-03	2.6E-07	200	200
13	0.11E-03	4.619E-03	4.87E-08	750	750
14	0.18E-03	N/A	N/A	0	0

Table 3-9. Summary of soil properties from consolidation tests in WL02

Increment	m_v (m ² /kN)	c_v (cm ² /s)	k_v (cm/s)	σ'_v (kPa)	Avg. σ'_v (kPa)
1	5.37 E-03	1.082E-03	5.70E-07	10	10
2	5.52 E-03	2.29 E-03	1.24E-06	20	20
3	2.54 E-03	2.71 E-03	6.76E-07	50	50
4	0.93 E-03	3.91 E-03	3.56E-07	100	100
5	0.70 E-03	5.06 E-03	3.47E-07	200	200
6	0.18 E-03	8.30 E-03	1.47E-07	500	500
7	0.13 E-03	12.62 E-03	1.56E-07	1000	1000
8	0.12 E-03	14.17 E-03	1.66E-07	1500	1500

3.6 Data Acquisition Control

An HBM data acquisition system was used to take the readings at the frequency of 5 Hz and 20 Hz in installation and loading, respectively or as specifically noted. Due to the small axial loads in the model, the measured axial strain fell in the range of 200×10^{-6} . The drift of the signal received by the HBM data logger was sometimes as much as $\pm 50\%$ of the maximum measurement of the lowest strain gauge station that recorded the smallest axial load.

Axial strain induced by temperature change may be significant, compared to axial strain caused by the applied load. For aluminum, the thermal strain is around 22×10^{-6} per 1°C of temperature change. The maximum axial strain during our loading tests is around 190×10^{-6} . Even though the strain gauge circuits were temperature-compensated, and the room temperature was controlled and

monitored to be a constant, we had waited for a long period of time since the beginning of spinning for the real-time strain reading curves to flat out. The research team also suggests there is another cause for the drift: the differential settlement of the model clay and the model pile due to their significant difference in density during spinning-up.

The strain gauges were installed in the summer of 2018, but the tests were conducted in April and November of 2019. The effective period recommended by the supplier of the strain gauges and relative accessories is 3 months. The actual long waiting was unexpected and had likely caused some damages to some of the strain gauges that did not respond to the axial loading.

Model piles were installed in three 50-mm-penetration stages. The method was a compromise to the vertical travel limitation of the electric actuator. When the preset travel is set large, for example 50 mm, unexpected stop may be forced by the servo control system due to large cumulative error detected by the transducer. The installation method might have resulted in the discontinuity of the torque-depth curves. When the vertical penetration was stopped but the rotation was still ongoing, the helix would transverse the surrounding soils and increased the torque measured by torque gauges. The results of the torque vs. displacement will be carefully reviewed to eliminate the effects of pile installation.

3.7 Test Layout and Test Matrix

Given four model piles and eight intended loading tests in each soil model, the test sequence was divided into two stages as shown in Table 3-10. Test sequence of WL01 and Table 3-11: 1) Stage 1 consists of four compressive tests, one for each model pile; 2) Stage 2, by reusing the model piles pulled out after Stage 1, consists of three tension tests of P1, P2, and P3 and one compression test of P4. The test calendar, loading methods, and pile loading rate are shown per each test ID.

Table 3-10. Test sequence of WL01

Date	Start time	Stage	Test ID	Pile	Action	Loading rate (mm/min)
04/12/19	10:00 am	1	P2C	P2	Monotonic compression	0.333
04/12/19	1:41 pm	1	P4C1	P4	Monotonic compression	0.333
04/12/19	3:03 pm	1	P1C	P1	Monotonic compression	0.333
04/12/19	6:03 pm	1	P3C	P3	Monotonic compression	0.333
04/16/19	10:59 am	2	P3T	P3	Monotonic tension	10
04/16/19	3:33 pm	2	P2T	P2	Monotonic tension	10
04/17/19	9:19 am	2	P1T	P1	Monotonic tension	10
04/17/19	1:26 pm.	2	P4C2	P4	Monotonic compression	10

Table 3-11. Test sequence of WL02

Date	Start time	Stage	Test ID	Pile	Action	Loading rate (mm/min)
11/11/19	3:00 pm	1			Pile installation	
11/12/19	11:27 am	1	P1C	P2	Monotonic compression	0.333
11/12/19	2:57 pm	1	P4C1	P4	Monotonic compression	0.333
11/13/19	9:43 am	1	P2C	P1	Monotonic compression	0.333
11/13/19	11:35 am	1	P3C	P3	Monotonic compression	0.333
11/13/19	2:59 pm	2			Pile installation	
11/14/19	9:18 am	2	P3T	P3	Monotonic tension	10
11/14/19	1:33 pm	2	P2T	P2	Monotonic tension	10
11/15/19	9:14 am	2	P1T	P1	Monotonic tension	10
11/15/19	1:26 pm.	2	P4C2	P4	Monotonic compression	10

Figure 3-20 and Figure 3-21 show the layout of all test piles, vane shear test boreholes and PPT's. To monitor the progress of in-flight consolidation, two PPT's were installed in the soil. Figure 3-22 shows the pore pressure recovery during the spin-down and spin-up before loading test P1T. The pore pressure increased during the spin-down has dissipated in less than 30 min. These measurements confirmed that the pore pressure in the clay was hydrostatic.

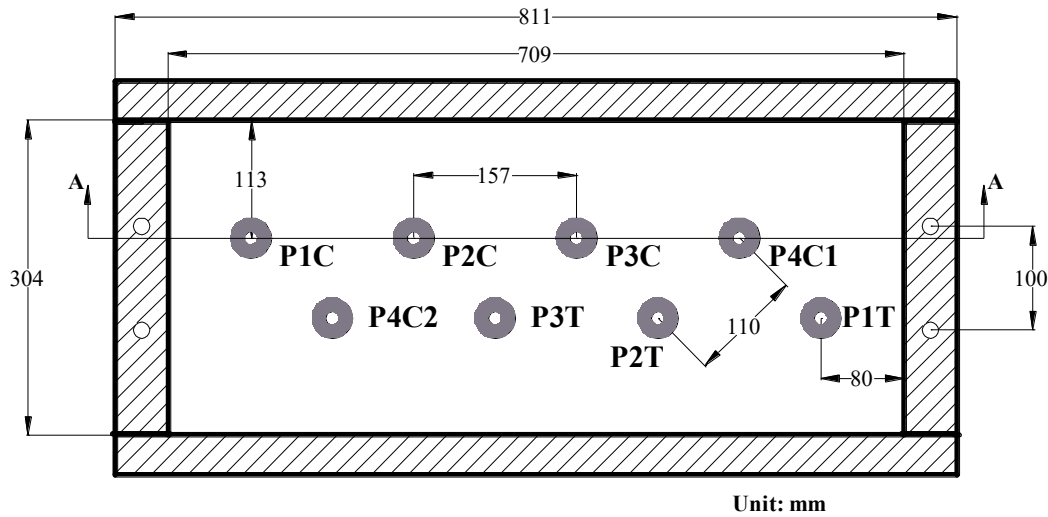


Figure 3-20. Test layout of WL01 and WL02

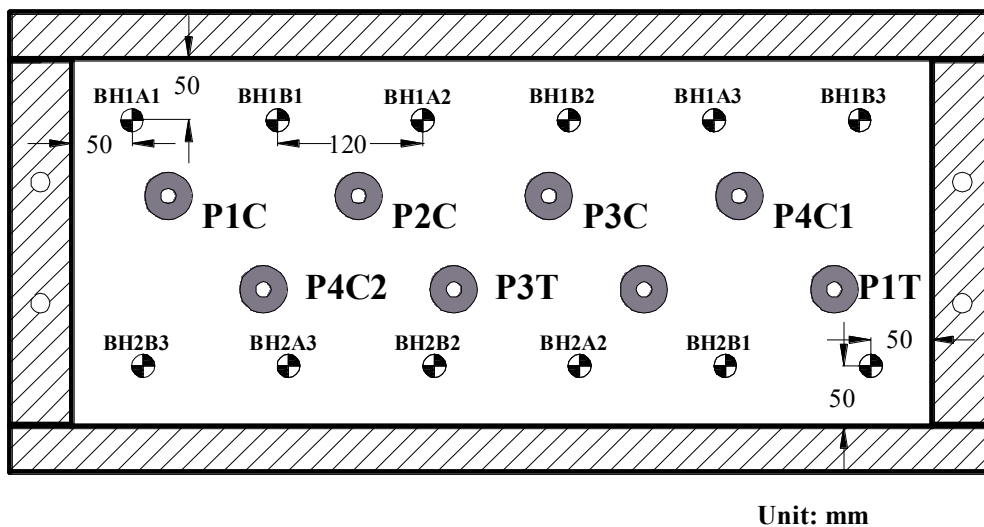


Figure 3-21. Layout of vane shear test (e.g., BH1A1) and model piles

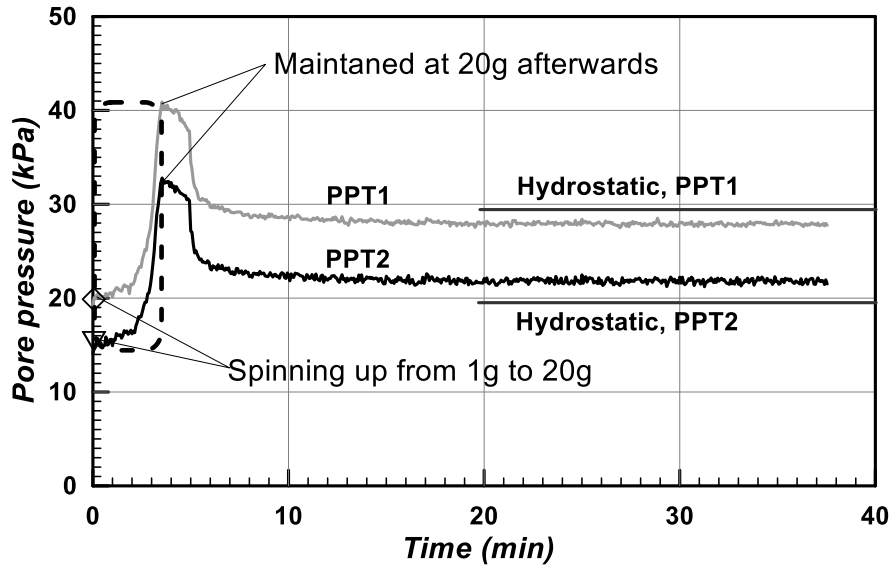


Figure 3-22. Pore pressure change, during the spin-down and spin-up procedure before load test P1T, WL02

Test piles for the first four loading tests of each series were installed in flight. After installation, the test setup was spun overnight for the clay to recover. The pile installation was accomplished in the second morning and then an overnight spin was performed for the soil to recover for the first four loading tests on the next day.

The electric dual-axis actuator can output vertical and horizontal movement at a wide range of constant speed, regardless of the reaction force. The axial displacement was measured by the displacement transducer and the axial loads were measured by the half-bridge strain gauge circuits installed along the pile shaft. Every model pile was axially loaded at a “quick” and constant advancing rate of more than 0.33 mm/min to ensure the failure of the pile was governed by undrained shear strength of the model clay. To be more specific, the loading tests of WL01_1 and WL02_1 were performed at 0.33 mm/min and WL01_2 and WL02_2 at 10 mm/min. After subtracting the influence of the s_u difference, the axial capacities of P4C1 and P4C2 (described in

the next section) were essentially the same for both WL01 and WL02, which means the advancing rate did not change the axial behavior as long as the clay was undrained during loading. Every load test was terminated when the limit state was noticed. According to the previously mentioned loading rate effect, the speed of the electric actuator must be assessed before being determined.

3.8 Summary, original contribution and limitations

3.8.1 Summary

A test setup was successfully constructed for pile installation and axial loading tests on centrifuge. A strong aluminum container was made to store the test soils and support the overlying loading frame. The loading frame consists of a dual-axis electric actuator and a constant-rpm gear motor that enable helical pile installation (rotation), axial loading tests, and switching between test locations. Four types of model piles were fabricated and instrumented with multiple strain gauges to measure the installation torques and axial loads in the pile shafts. Strict protection measures have been taken to secure the pile instrumentations and communicating wires to the data logger. Two soil models with different s_u values (about 50 kPa for WL01 and 120 kPa for WL02) were prepared through 1 g consolidation treatment starting from kaolinite slurries. The pore pressure change in the “stiff clay” can be monitored by the PPT’s installed at two different depths. Comprehensive calibration tests and theoretical derivations have been conducted to verify the reliability of the strain gauges, PPT’s and gear motor.

3.8.2 Original contribution

The innovative parts of this centrifuge test system can be summarized as two points:

- The in-flight real-time axial load distribution measurement is first time realized in centrifuge model tests of helical piles.

- The technique for protecting the strain gauges installed along the tiny model pile shaft is new and effective. The majority of the pile shaft surface is saved.

With these improvements of centrifuge model test technique for helical piles, the axial load transfer mechanisms can be obtained. Compared to the model pile protection method adopted by Zhang and Kong (2006), i.e., putting strain gauges on the pile shaft surface and then covering the entire shaft with a layer of epoxy about 3 mm thick, the soil-shaft interaction is more effectively modeled by the present technique.

3.8.3 Limitations of experimental setup

In the meantime, the limitations should also be noticed:

- The rotational speed of the installation motor may have an uncertain impact on the installation torque. However, the output speed of the used motor cannot be altered.
- The in-flight soil investigation technique is not available in the present experiment method. Instead, a quick vane shear test was performed immediately before and after the spin-up and spin-down of each test stage to obtain the s_u profile of the tested soils.
- Limited by the working space of the geotechnical centrifuge, the pile embedment depth was less than 5 times of helix diameter. According to Das (1980), all tested piles will be categorized as “shallow piles”. In the meantime, the distance between the lower helices and container bottom was less than 3 times of helix diameter thus might introduce boundary effect to the bearing pile resistance.
- The imperfection of pile machining and helix welding may also be a concern. All radius of a perfect helix or a “true helix” should be perpendicular to the shaft axis. However, the present helices were not perfect due to the difficulty of welding aluminum material. Therefore, an

analytical torque model based on the perfect helix geometry may lack accuracy for predicting the measure torque.

Although these limitations could not be avoided, the impact of pile embedment depth, bottom boundary effect, and lack of in-flight soil property measurements, can be evaluated using the axial load distribution measurements.

4 Centrifuge Modeling of Axially Loaded Helical Piles in Cohesive Soils

A centrifuge test of helical piles in cohesive soils was conducted to investigate the pile installation torque, installation-induced excess pore pressure in the soil, and pile behavior under axial loads. An analytical model for calculating the installation torque of helical piles screwed into cohesive soils was proposed and verified by test results. The pore pressure response to pile installation was monitored near two piles at two depths. It was found the excess pore pressure at pile surface completely dissipated within 6 days. The model piles were axially loaded under 20 g condition. The axial load distributions along pile shaft were measured with strain gauges. The results show that the axial failure modes of helical piles depend on the strength of soil and inter-helix spacing. In general, it may be easier for a stiffer clay to form an inter-helix soil cylinder during axial pile movement.

4.1 Introduction

Helical piles have become widely adopted as an alternative to certain conventional pile types since helical plates facilitate the pile installation process and increase the axial capacity. A study of the behaviour of helical piles in cohesive soils during installation and axial loading is particularly pertinent, since they are commonly used in central Canada where glaciolacustrine clay is prevalent.

Hoyt and Clemence (1989) proposed an empirical factor to relate the final installation torque to the axial capacity of helical piles. Tang and Phoon (2018) suggested that the torque factor method is more accurate than the theoretical method that is usually affected by the uncertainty in selecting a failure mode. Therefore, a reliable prediction of installation torque is important. Ghaly and Hanna (1991) derived an analytical expression to estimate the installation torque of a series of model helical piles in dry sand. The installation torque increased with the relative density of the sand and the installation depth. Tsuha and Aoki (2010) adopted a model frequently used in the design of

power screws and verified the correlation between installation torque and uplift capacity of helical piles in sand using centrifuge tests. In this model, residual friction angle was adopted to generate shear resistances for the entire soil-pile interface. Sakr (2013) proposed a theoretical model for helical piles in cohesive soils to calculate the installation torque by pile geometry and undrained shear strength (s_u). The peak s_u was adopted in this model for the torsional resistance against the leading helix and residual strength (s_{ur}) for pile shaft and the following helix/helices if applicable. Another notable assumption made by Sakr (2013) is that the soil surrounding a helix is sheared as a cylinder of $D \times P$, where P is the opening pitch of the helix. This model was verified by an in-situ test in very stiff clay, but the applicability to various s_u values may need to be assessed.

Excess pore pressure, u , generated around the shaft during pile installation in cohesive soils has a significant impact on the short-term axial behavior of piles. Lanyi-Bennett and Deng (2019a, 2019b) observed that the bearing capacity of helical piles loaded 5 hours after installation was 30 to 40% less than that of the piles loaded one week later, which implied a considerable setup effect. Weech and Howie (2012) measured the pore pressure response to helical pile installation in soft clay at the shaft surface and at distance; they showed a radial propagation of u and suggested that u was very slightly affected by the helices. Randolph and Wroth (1979) derived an analytical expression for the pore pressure response to a straight driven pile. Since u -induced installation is crucial to the axial behavior of helical piles, the validation of such a theoretical model for evaluating the progression of u around helical piles may be important.

Individual bearing mode (IBM) and cylindrical shear mode (CSM) for multi-helix piles are adopted to guide the design of helical piles. In the IBM model, end bearing forces are developed at each plate; in the CSM model (proposed by Mitsch and Clemence 1985), two adjacent helical plates interact with each other, and the inter-helix soil evolves into a cylinder. The spacing ratio

S_r , defined herein as S/D where S is the inter-helix spacing and D is the helix diameter, is normally used as an indicator of potential failure mode. An empirical value of critical S_r (termed S_{rc} herein) of 3.0 is sometimes adopted in the industry. A number of helical pile tests have reported various S_{rc} values corresponding to the subsurface conditions: $S_{rc} = 1.5$ for soft marine clay (Rao et al. 1991), $S_{rc} > 3.2$ for very soft clay (Wang et al. 2013), $S_{rc} > 3.0$ for soft to medium clay with very stiff crust (Lutenegger 2009), $S_{rc} < 1.5$ for stiff clay (Elkasabgy and El Naggar 2015), and $S_{rc} > 3.0$ for dense oil sand (Sakr 2009). Elkasabgy and El Naggar (2015) and Lutenegger (2009) attributed the observed failure modes inconsistent with prediction to the soil disturbance resulted from pile installation. These results based on back-analysis and observation raise a concern whether there is a unique S_{rc} or IBM and CSM are the only failure mode of helical piles. Load tests of helical piles with various S_r and soil strength profiles may be warranted to address the concern.

The present study is aimed at addressing the preceding issues related to the research and application of helical piles in cohesive soils. A series of centrifuge model tests of axially loaded helical piles were conducted at the University of Alberta. Four types of helical piles (one single-helix pile and three double-helix piles with various S_r values) were installed into two kaolinite soil models. The axial mechanical behaviour and the failure mode were elaborated, a modified model for installation torque in cohesive soils was proposed, and the excess pore pressure induced by pile installation was assessed.

4.2 Testing Program

The present program consists of two series of tests WL01 and WL02. Each test series included eight installation tests and axial load tests. Figure 4-1a shows the pile test layout and the locations of vane shear tests. Figure 4-1b shows the vertical profile of the installed piles in WL02, while the profile of WL01 is similar but without any pore pressure transducers (PPT). Each test series was

divided into two stages, named A and B. The preparation and test procedures of each stage are shown as a flow chart in Figure 4-2. The centrifugal acceleration was set at 20 g. Scale factors of selected parameters are listed in Table 4-1.

Table 4-1. Scale factors (prototype/model)

Term	Force	Length	Stress	Torque	Diffusional Time
Scale Factor	400	20	1	8000	400

4.2.1 Soil Properties

Kaolinite was used as the material of the soil model because of its high permeability that facilitates in-flight consolidation. The target soil model was a clay with s_u of about 50 kPa in WL01 test series and a clay with s_u of about 120 kPa in WL02. The target strengths were selected for two reasons. First, the target s_u is within the approximate s_u range of 50 to 150 kPa of glaciolacustrine clay or clay tills in Western Canada. Secondly, one objective of the centrifuge test program is to examine the effect of s_u on the failure mechanism of helical piles.

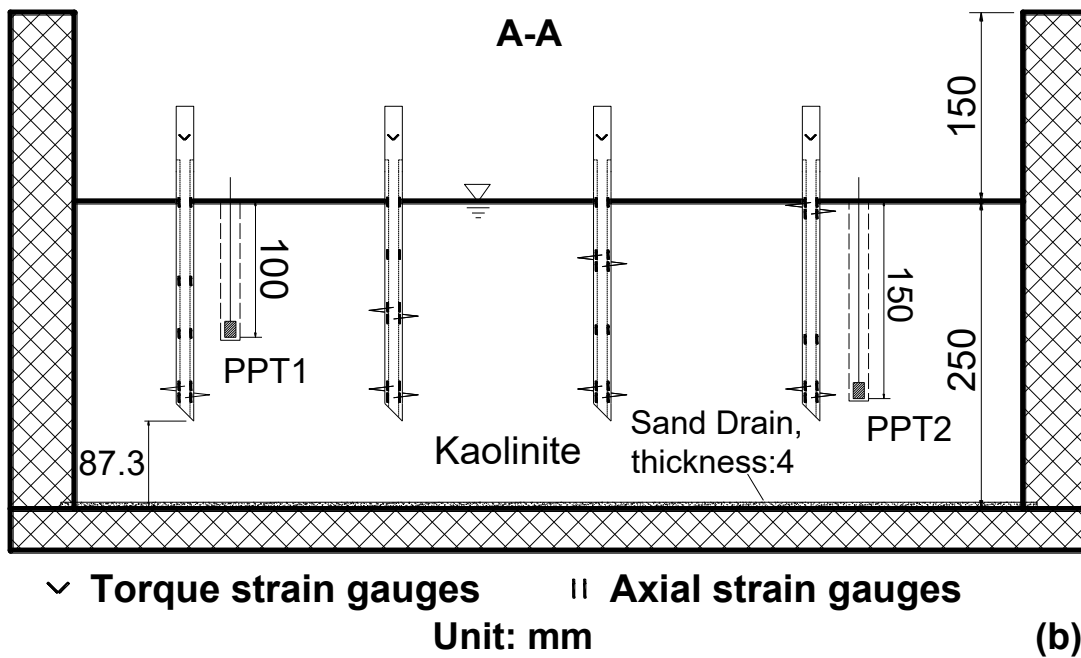
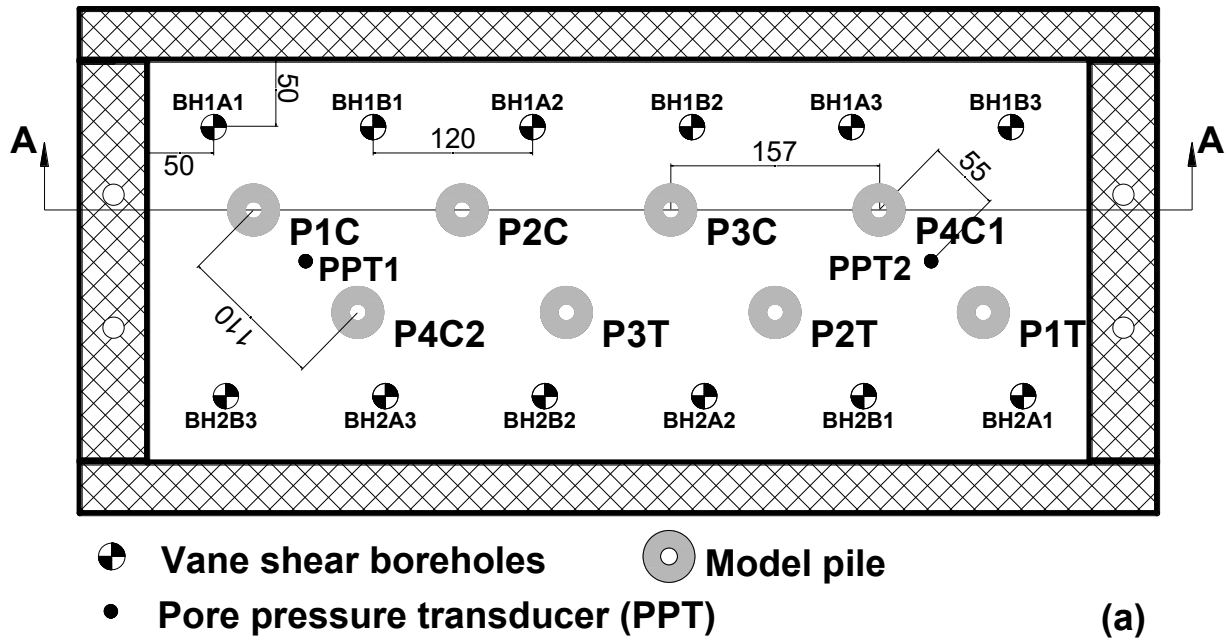


Figure 4-1. (a) Test layout of WL01 and WL02; and (b) vertical profile at A-A section of WL02. Dimensions are in model scale. Note: model piles were installed and loaded during different centrifuge flights.

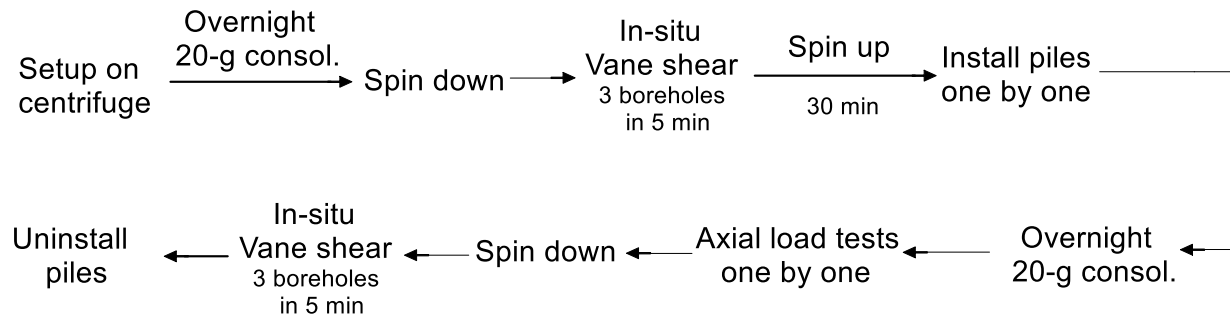


Figure 4-2. Flow chart of each testing stage. The 20-g consolidation was aimed to stabilize pore pressure.

In general, s_u changes with the stress history (Ladd 1991). As a result, a soil model with a uniform s_u distribution is difficult to achieve through a normal consolidation process in centrifuge. The target s_u was therefore attempted near the embedment depth of the helices, since the pile behavior is mainly determined by the helices. A control of 1-g consolidation pressure and centrifugal acceleration is able to provide the designated vertical effective stress (σ'_v) in the clay and thereby producing the target s_u .

The kaolinite slurry, with initial water content (w_0) greater than the liquid limit (LL), was prepared in a vacuum mixer and then transferred into a double-drained soil container for 1-g consolidation. A maximum consolidation pressure of 750 and 1500 kPa in WL01 and WL02 respectively was applied via several load increments. Once the consolidation at the maximum pressure was completed, the load was gradually decreased to 50 kPa, which was close to the vertical stress level near the lower helix at 20 g centrifugal acceleration. There was only one clay lift at 1-g consolidation and the total duration of consolidation construction was about 1 month. The properties of the clay before and after consolidation are presented in Table 4-2. Equation 4-1 (Ladd 1991) was taken as a guide to the soil preparation:

$$\left(\frac{s_u}{\sigma'_v}\right)_{OC} = 0.228 \left(\frac{s_u}{\sigma'_v}\right)_{NC} OCR^{0.8} \quad (4-1)$$

where OC and NC represent overconsolidated and normally consolidated clay respectively, and OCR is the over-consolidation ratio. The $(s_u/\sigma'_v)_{NC}$ ratio was estimated using the empirical equation $(s_u/\sigma'_v)_{NC} = 0.129 + 0.00435 \times PI = 0.22$ (Wroth and Houlsby 1985), where PI is the plasticity index.

Table 4-2. Kaolinite clay properties and 1-g consolidation parameters

Test series	G_s	PL	LL	e_0	ω_0	σ_{max} (kPa)	σ_e (kPa)	e_e	ω_e	γ_{sat} (kN/m ³)
WL01	2.65	33.8	54.6	2.65	100%	750	50	1.16	43.8%	17.3
WL02				2.12	80%	1500	50	0.97	36.7%	18.0

Note: G_s = specific gravity of kaolinite, PL = plastic limit, e_0 = initial void ratio of the kaolinite slurry, σ_{max} = maximum consolidation pressure, σ_e = end consolidation pressure after unloading, e_e = end void ratio of the soil model, ω_e = average water content of the soil model, and γ_{sat} = average saturated unit weight of soil model.

The undrained strength of the consolidated clay was measured by in-situ vane shearing at different locations (Figure 4-1a) and instants (Figure 4-2). The measured s_u profiles are shown in Figure 4-3a and Figure 4-3b, accordingly. The soil strength was shown homogeneous in the lateral domain. Owing to the limitation of equipment, vane shear tests were performed in-situ under 1-g condition within 5 min after spin-down as indicated in Figure 4-2. The consolidation time factor T_v at 5 min after spin-down was approximately 0.008 given the greatest coefficient of consolidation

c_v of $8 \times 10^{-3} \text{ cm}^2/\text{s}$. The degree of consolidation at 5 min in the soil model was less than 5% over the depth. Therefore, it is reasonable to assume that s_u measured on bench was equivalent to the s_u under 20 g condition. In-flight soil characterization method (such as cone penetration) would be ideal for determining the soil strength, but such equipment was unavailable at the centrifuge lab.

Figure 4-3c shows the profile of OCR calculated from the consolidation stresses at 1 g and 20 g. The distribution of s_{ur} , measured from the vane shear, is also shown in Figure 4-3a and b. The sensitivity ($= s_u/s_{ur}$, in Figure 4-3d) of the soil models ranged from 2.5 to 3.5.

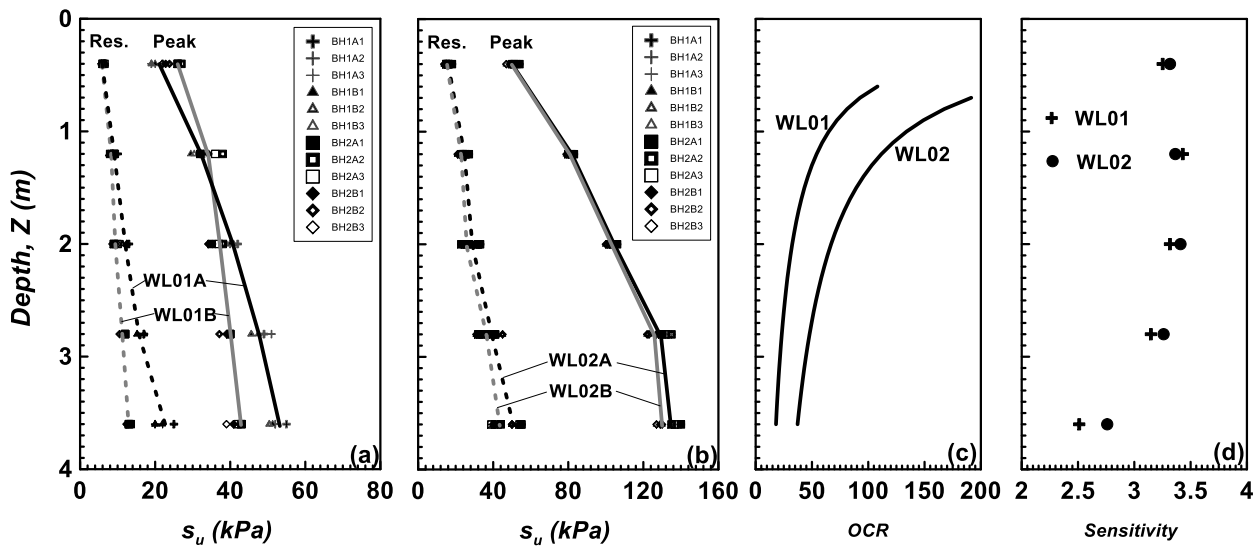


Figure 4-3. Strength parameters of model soil: (a) average peak and residual s_u in WL01, (b) average peak and residual s_u in WL02, (c) OCR of the soil model at 20 g centrifugal acceleration, and (d) average sensitivity of the soil

4.2.2 Model Pile and Instrumentation

Four types of model helical piles (Figure 4-4) were fabricated with solid aluminum rods. The model piles were named P1 to P4 in Figure 4-4a to Figure 4-4d. The pile dimensions are presented in Table 4-3. The prototype shaft diameter (d) is 0.254 m, and the helix diameter (D) is 0.762 m,

which are common in practice. The helix spacing was not scaled from any specific prototype piles. Instead, the S_r value was taken as 1.5, 2.5, and 3.5, in view of the range in the literature, to investigate the effect of S_r on the failure mechanism.

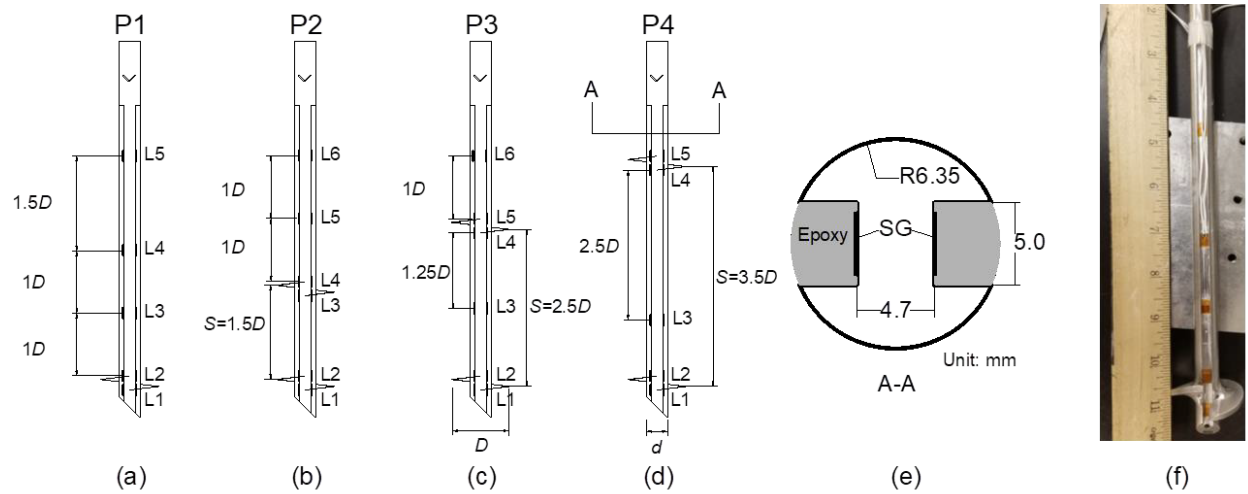


Figure 4-4. Schematics of helical piles and locations of strain gauges: (a) P1; (b) P2; (c) P3; (d) P4; (e) pile shaft cross-section and (f) a model pile with strain gauges glued inside the slots but not filled by epoxy.

Strain gauges (SG, in Figure 4) were installed along the pile shaft at multiple stations. To minimize the adverse effect of the SG protection measures on the soil-pile interaction during installation or axial loading, two oppositely positioned slots were cut along the shaft and then SGs were meticulously glued inside the slots. The SGs were sealed with protective coatings and Teflon tapes, and after that, the slots were carefully filled with epoxy. The surface of the cured epoxy was smoothed with sandpapers and then polished with soft cloth.

Table 4-3. Pile geometry

	Type	No. of helix	Shaft Dia. d (mm)	Helix Dia. D (mm)	Pile Length L (mm)	Helix Spacing S (mm)	Lower Helix Embedment E_H (mm)	S_r ($=S/D$)
Model Scale	P1	1	12.7	38.1	271.8	NA	150	NA
	P2	2	12.7	38.1	271.8	57.2	150	1.5
	P3	2	12.7	38.1	271.8	95.25	150	2.5
	P4	2	12.7	38.1	271.8	133.4	150	3.5
Prototype Scale	P1	1	254	762	5436	NA	3000	NA
	P2	2	254	762	5436	1144	3000	1.5
	P3	2	254	762	5436	1905	3000	2.5
	P4	2	254	762	5436	2668	3000	3.5

The axial SGs were wired into Wheatstone half bridges and the torque SGs were into full bridges. The centrifuge chamber room was maintained at constant temperature with a variation of $\pm 0.05^\circ\text{C}$ when the piles were tested, and hence a temperature compensation for the axial SG was considered non-essential. The torque SG circuit can compensate any axial strains caused by the crowd force or thermal strain during in-flight installation. Calibration factors of the axial and torque SG, obtained from calibration tests under 1-g condition, were consistent with the theoretical values.

4.2.3 Test Pile Layout

As shown in Figure 4-1a, WL01A includes four compressive tests, i.e., P1C, P2C, P3C, and P4C1, and WL01B includes three tensile tests, i.e., P1T, P2T, and P3T and one compressive test, P4C2. WL02 are similar to WL01 except that the soil in WL02 had great strength. The four piles in each test stage were installed in-flight in sequence within one day. Then the soil-pile-container would continue to spin over night to ensure the consolidation of soil. The pile-to-pile spacing in a row is over $4D$ so that the interaction between two tests can be neglected. The test matrix is presented in Table 4-4.

Table 4-4. Test matrix

Test stages	Test ID	Pile type	Load type	Model-scale advancing rate (mm/min)
WL01A	P1C	P1	Compression	0.333
	P2C	P2	Compression	0.333
	P3C	P3	Compression	0.333
	P4C1	P4	Compression	0.333
WL01B	P1T	P1	Tension	10
	P2T	P2	Tension	10
	P3T	P3	Tension	10
	P4C2	P4	Compression	10
WL02A	P1C	P1	Compression	0.333
	P2C	P2	Compression	0.333
	P3C	P3	Compression	0.333
	P4C1	P4	Compression	0.333
WL02B	P1T	P1	Tension	10
	P2T	P2	Tension	10
	P3T	P3	Tension	10
	P4C2	P4	Compression	10

4.2.4 Install-and-Load Frame

The install-and-load frame, as depicted in Figure 4-5, consisted of three major parts: the soil container, the dual-axis electrical actuator affixed on top of the soil container, and the gear motor (for pile installation) mounted to the actuator. The container, internally 709.2 mm (length) \times 300 mm (width) \times 400 mm (height), allowed a two-way vertical drainage of the clay. The gear motor exerted a driving torque to the model pile head at a constant rotational rate of 23 revolutions per min (rpm), and in the meantime, the electrical actuator pushed the pile at a constant speed of 4.87 mm/s. The rotational rate and vertical velocity were determined in this way so that the penetration rate was at one pitch per revolution to minimize the soil disturbance. To perform axial loading tests, the actuator pushed or pulled the piles at a designated constant rate.

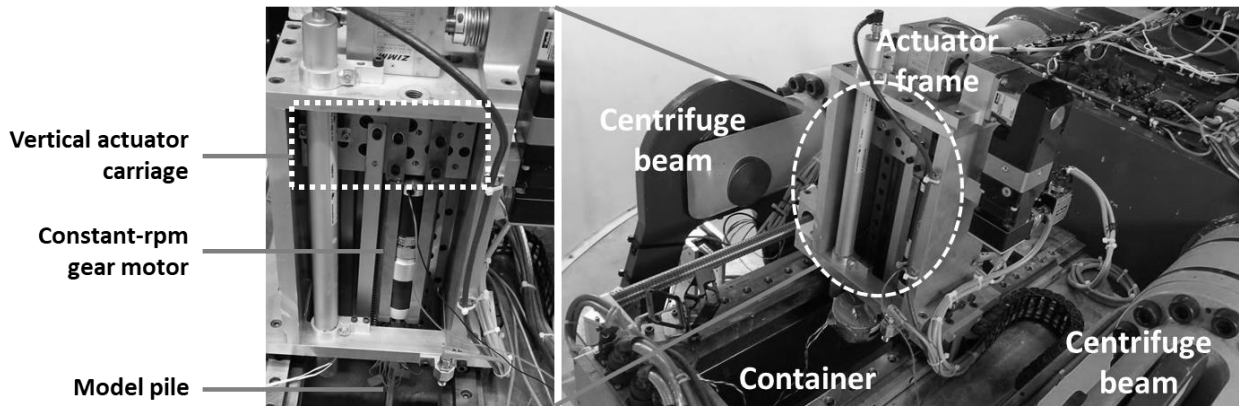


Figure 4-5. Install-and-load system

4.2.5 Pore Pressure Transducers

The pore pressure response to pile installation has a practical significance. In addition, the clay model experienced complex changes in pore water pressure during the in-flight consolidation, spin-up and spin-down in WL01 and raised some concerns. To monitor the pore water pressure,

two PPT's were buried in the soil of WL02 at 10 cm and 15 cm as shown in Figure 4-1b, before the centrifuge test was set up. PPT1 was placed near pile P4C2 and PPT2 was near P1T. To install the PPT, a thin-walled plastic tube with an external diameter of 12.7 mm was inserted to the designated depth. Then the tube was pulled out with the soil plug inside, leaving a borehole behind. The saturated PPT was then pushed into the borehole with the filter side down to reach the bottom. The soil plug in the tube was extruded to fill back into the borehole. The backfill gained some strength during the following consolidation spinning. However, the backfill may have less strength and greater permeability than the nearby intact soil. The cylindrical PPT has a 10 mm diameter and 13.5 mm height. Each PPT has a density of about 2.17 gm/cm^3 , which is slightly greater than that of the clay (about 1.84 gm/cm^3). The effect of the differential density on PPT sinking or the excess water pressure was estimated to be negligible, given the high soil strength.

After a consolidation at 20-g acceleration over one night (>12 h duration), a hydrostatic pore pressure distribution was realized inside the clay, as shown in Figure 4-6. A possible reason for the discrepancy between the measured and theoretical hydrostatic pore pressure is the uncertainty of PPT embedment depth. Figure 4-6 shows the progress of pore pressure during in-flight consolidation from a spin-down to spin-up. The pore pressure, initially low, started to increase when the centrifuge accelerated. The maximum excess pressure u in the spin-up stage was slightly less than the increments in total vertical stress from 1 g to 20 g, which were estimated as 34.4 kPa (PPT1) and 52.6 kPa (PPT2). That was because the spin-up process from 1 g to 20 g was not completed instantaneously; in fact, u might be partially dissipated during the spin-up stage. When the acceleration was stabilized at 20 g, the pore pressure decreased rapidly and almost reached the hydrostatic pressure. Figure 4-6 implies that the dissipation of u was completed within 20 min. Piles would be installed and loaded after the in-flight consolidation had been completed.

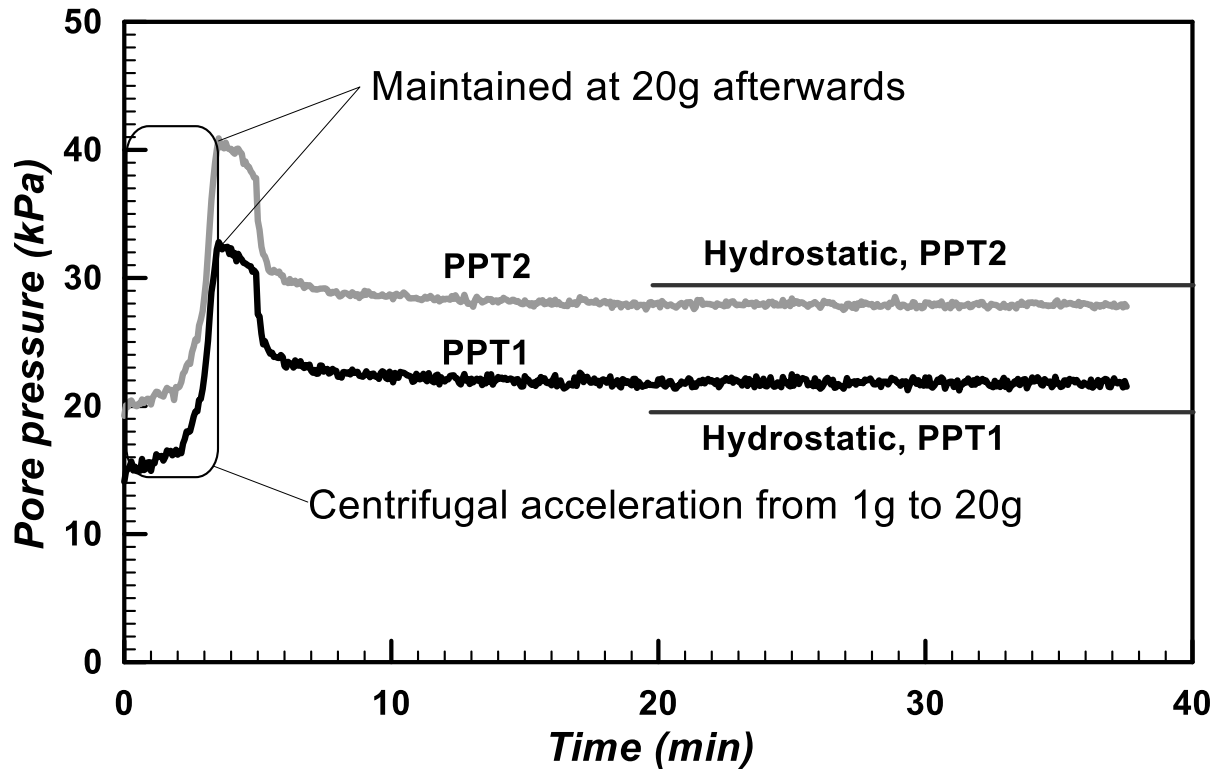


Figure 4-6. Progress of pore pressure before test P1T of WL02

4.2.6 Axial Loading Method

In the field, the load-controlled “static” testing method is common (ASTM D1143 2013), whereas the constant rate testing seems more common in the centrifuge modeling of soil-pile interaction (e.g., Tsuha et al. 2007 and Wang et al. 2013). Practically, the constant rate method is more reliable to operate than the static loading method in a centrifuge test. In the present study, model piles were axially loaded at a “quick” and constant rate to ensure that the failure of the pile was governed by the undrained behaviour of the clay. The loading rate for each test is presented in Table 4.

4.3 Results: Torque and Induced Pore Pressure

Sixteen piles were installed and axially loaded using the centrifuge modeling technique. The installation torques and induced pore water pressure were presented and analyzed in this section. Results are given in prototype scale unless otherwise noted.

4.3.1 A Torque Model Based on Residual Strength

The installation torque is a result of soil resistance against the traverse of helices and the spin of pile shaft. Because of the large relative displacement between the soil and pile shaft, s_{ur} is expected to mobilize at the soil-shaft interface. As for the helices, although the leading (or lower) helix penetrated the “fresh soil”, most of the helix trailed into the fully sheared gap left behind by its cutting edge. Hence, the present model assumes that the installation torque is governed by s_{ur} at the entire soil-pile interface.

Equation 4-2 summed up all components of the installation torque (T):

$$T = T_S + T_{H_s} + T_{H_c} \quad (4-2)$$

where T_S is the torque against the rotation of shaft, T_{H_c} is the torque against the rotation of the circumference of the helix/helices, and T_{H_s} is the torque acting on the upper and lower surfaces of the helix/helices (see Figure 4-7a). The soil resistance against the sharpened cutting edge of the helix is neglected. The torque components may be estimated by an integration of the interface adhesion and relevant areas, as in Equation 4-3, 4-4, and 4-5:

$$T_S = \int_0^{l_s} \pi \frac{d^2}{2} \alpha(z) s_{ur}(z) dz \quad (4-3)$$

$$T_{H_c} = \alpha s_{ur} \cdot \frac{P}{\sin\left(\theta\left(\frac{D}{2}\right)\right)} t_H \cdot \cos\left(\theta\left(\frac{D}{2}\right)\right) \cdot \frac{D}{2} \quad , \text{ for } \alpha \text{ and } s_{ur} \text{ at the helix depth} \quad (4-4)$$

$$= \frac{DPt_H}{2} \alpha s_{ur} \cot\left(\theta\left(\frac{D}{2}\right)\right)$$

$$T_{H_s} = 2 \int_{d/2}^{D/2} \alpha s_{ur} \cot(\theta(\rho)) P \rho d\rho, \text{ for } \alpha \text{ and } s_{ur} \text{ at the helix depth} \quad (4-5)$$

where l_s is the embedment depth of pile shaft, α is the clay-pile adhesion factor, P is the pitch opening of helix, t_H is the thickness of helix, ρ (a variable for integration purpose, over helix radius)

is the distance between a point on the helix and the shaft axis, and $\theta(\rho) = \text{atan}(P/(2\pi\rho))$ is the angle of the helix at ρ in the ‘hoop’ direction with respect to the horizontal plane. Refer to Figure 4-7 for these definitions. The adhesion factor was empirically taken from Tomlinson (1957) and CGS (2006) $\alpha = 0.21 + 0.26(p_a/s_u)$, where p_a equals 101 kPa. Both s_{ur} and α are a function of the depth z , as obtained from Figure 4-4a and b.

The helix angle, θ , varying with ρ was considered in Equation 4-5 to represent the helix angle of the popular “true helix” design, which sets the radial direction of the helix perpendicular to pile axis (Figure 4-7b). This is different from Sakr’s (2013) model that used the helix angle at the outer edge for the entire helix.

4.3.2 Installation Torque: Measured vs. Predicted

The torsional strain at pile head was recorded and converted into torque using the cross-sectional geometry and calibrated Young’s modulus of 71 GPa. The penetration depth, Z_h , was defined as the depth of the leading edge of the lower helix. The T vs. Z_h curves of all test piles in the prototype scale are shown in Figure 4-8. The wires of P4 were damaged in WL02. Nevertheless, P4 was expected to show the same T vs. Z_h curve as P1 before the upper helix of P4 touched the soil surface. Notably, P1 and P4 had essentially the same installation torques in WL01 (Figure 4-8a and b).

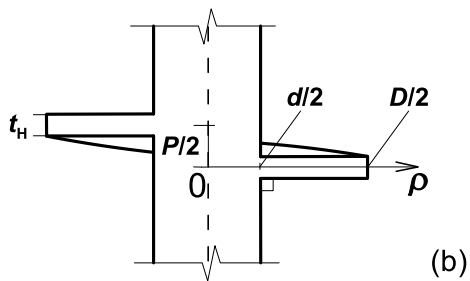
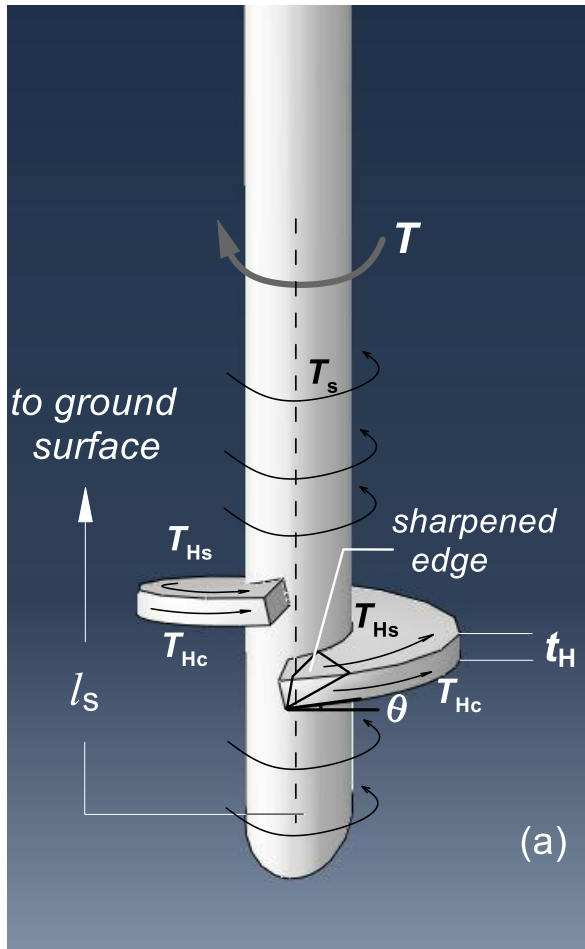


Figure 4-7. (a) Components of torsional resistance; (b) a vertical cross-sectional view through the pile axis. The “true” helix configuration is shown as a right angle.

As shown in Figure 4-8, the double-helix piles required a higher installation effort than the single-helix piles. P2 reached the greatest final torque among the double-helix piles because of the

greatest torsional resistance contributed by the upper helix. The curves of T vs. Z_h , using the present torque model in Equation 4-3 to 4-5, are also shown in Figure 4-8. The measured and estimated T vs. Z_h curves agreed with each other with a reasonable accuracy, although a discrepancy existed near the middle of depth. For comparison, a curve of T vs. Z_h for P2C in WL01 was estimated using the peak s_u to the lower soil-helix shearing was estimated and shown in Figure 4-8a. It showed that this s_u -based method significantly overestimated the measured T profile by about 50%. Since the kaolinite clay has a sensitivity of about 3 (shown in Figure 4-3d) and the soil might be considerably disturbed as the lower helix traverses, we suggest that s_{ur} be used in estimating T instead of s_u . All evidence implies that the present torque model based on s_{ur} is capable of explaining the soil-pile interaction during installation.

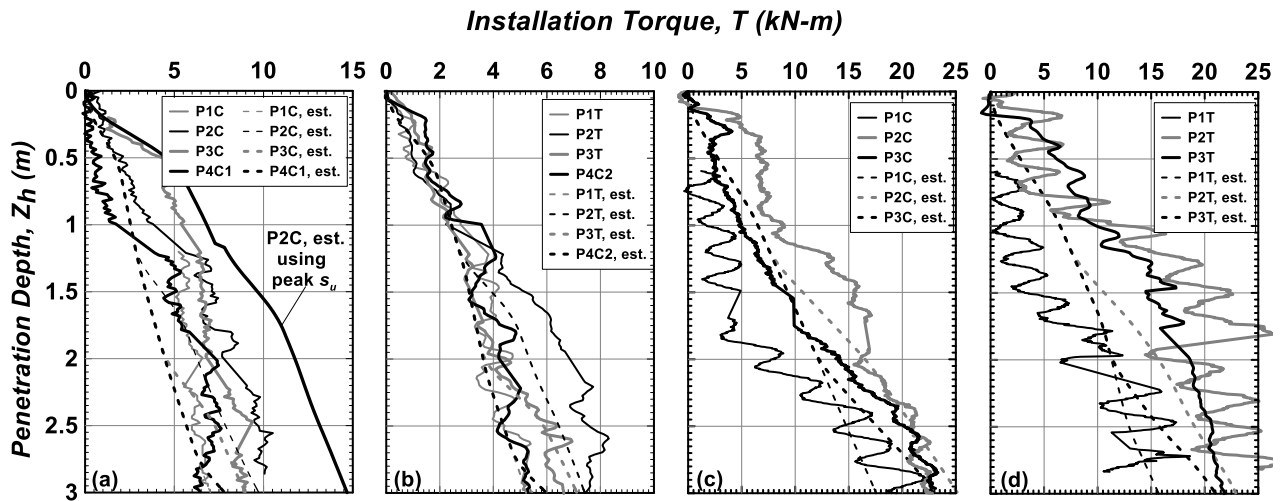


Figure 4-8. Curves of installation torques vs. lower helix penetration depth in the prototype scale: (a) WL01A, (b) WL01B, (c) WL02A, and (d) WL02B.

The final installation torque (T_{end}), often used for the empirical design of pile capacities, can be defined in practice as the average torque values in the final revolution(s) or the last 0.9 m

penetration depth. The present study estimates T_{end} as the average value over the last pile revolution. The estimated T_{end} is then compared with the measured T_{end} for all 14 monitored piles, as shown in Figure 4-9. The estimated T_{end} was decomposed into three components as per Equation 4-2. Figure 4-9 shows that the majority of T_{end} is contributed by the lower helix and pile shaft.

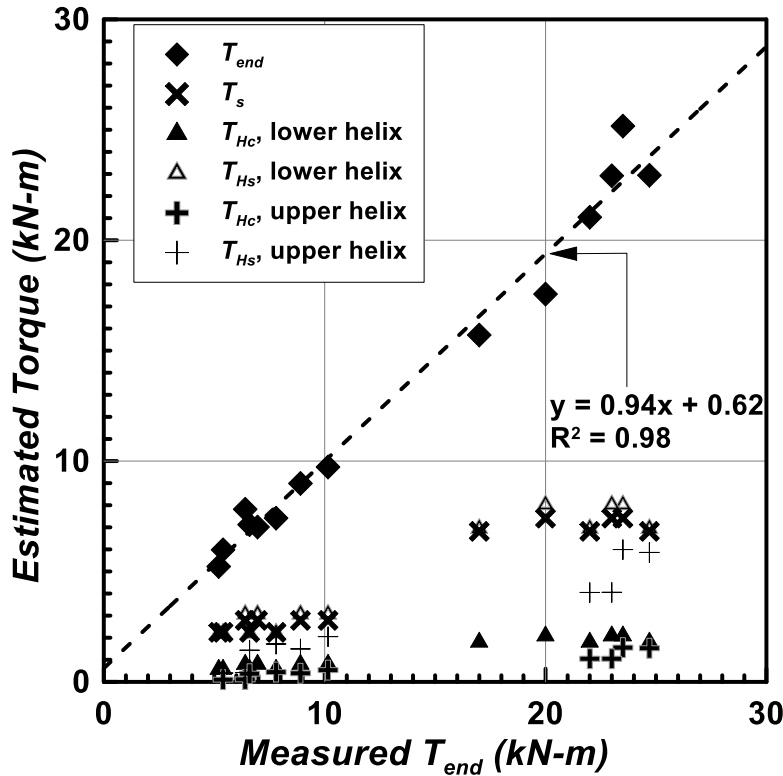


Figure 4-9. Estimated T_{end} and torque components vs. the measured T_{end} of 14 installed piles

4.3.3 Excess Pore Pressure Induced by Pile Installation

The cause of u is the cavity expansion generated during pile installation. A helical pile is similar to a driven pile because the shaft creates the cavity and induces u . The helices, which create spiral cavities, may induce u but may not have an impact as much as the pile shaft due to their small dimension. Hence, the theoretical solution in Randolph and Wroth (1979) for driven piles may be

approximately applied to helical piles. The following is a brief review of key equations in Randolph and Wroth's solution.

As the pile penetrates, the deformed soil can be divided into a plastic zone near the pile and an elastic zone on the outside. The subsequent u depends on pile radius (r_0) and the distance (r) to the pile axis. The initial u_0 is generated in the plastic zone and dissipated radially outward to the far field. The value of u_0 is calculated in Equation 4-6 (Randolph and Wroth 1979 and other preceding literature):

$$u_0 = u(r, 0) = 2s_u \ln(R / r) \quad (4-6a)$$

$$R = \sqrt{G / s_u} r_0 \quad (4-6b)$$

where R is the nominal limiting radius of the plastic zone of cavity expansion, G is the initial shear modulus of clay.

The progression of u was estimated using the analytical model (Randolph and Wroth 1979):

$$u(r, t) = \sum_{n=1}^{\infty} B_n e^{-c\lambda_n^2 t} [J_0(\lambda_n r) + m_n Y_0(\lambda_n r)] \quad (4-7a)$$

where:

$$B_n = \frac{4s_u}{\lambda_n^2} \frac{[J_0(\lambda_n r_0) + m_n Y_0(\lambda_n r_0) - J_0(\lambda_n R) - m_n Y_0(\lambda_n R)]}{\{r^{*2} [J_1(\lambda_n r^*) + m_n Y_1(\lambda_n r^*)]^2 - r_0^2 [J_0(\lambda_n r_0) + m_n Y_0(\lambda_n r_0)]^2\}} \quad (4-7b)$$

$$m_n = -\frac{J_0(\lambda_n r^*)}{Y_0(\lambda_n r^*)} \quad (4-7c)$$

$$c = \frac{k}{\gamma_w} \frac{2G(1-\nu)}{1-2\nu} \quad (4-7d)$$

The two boundary conditions described by Equation 4-8 and 4-9 enable the determination of λ_n by Equation 4-10:

$$u(r,t) = 0 \quad , \text{ for } r = r^* \quad (4-8)$$

$$\frac{\partial u}{\partial r} = 0 \quad , \text{ at } r = r_0 \text{ for } t > 0 \quad (4-9)$$

$$J_0(\lambda r^*)Y_1(\lambda r_0) - Y_0(\lambda r^*)J_1(\lambda r_0) = 0 \quad (4-10)$$

where r^* is the limiting radius of the deformed soil, J_i and Y_i are the Bessel's functions of the first and second kind respectively, the subscript i denotes the i^{th} order of Bessel's functions, k is the permeability of the clay, γ_w is the unit weight of water, and λ_n is the n^{th} root to be solved by Equation 4-10.

Table 4-5 shows the input parameters for this analytical solution. The value of k was interpreted from the consolidation curve under σ'_v of 50 kPa using Casagrande's method. The value of G was estimated using the chart in Duncan and Buchignani (1976) for OC clay based on PI , s_u , and OCR . The ratio of undrained elasticity modulus to s_u was estimated as 238 according to the chart for the present stiff clay. Given a Poisson's ratio of 0.49 for undrained condition, G of the clay at the depth of PPT1 and PPT2 was estimated as 8.3 MPa and 10.2 MPa, respectively.

Table 4-5. Parameters adopted in the pore pressure analysis

Model-scale Depth (mm)	γ_{sat} (kN/m ³)	G (MPa)	k (m/s)	ν	r^*
100, PPT1	18.1	8.3	1.2×10^{-9}	0.49	$7 r_0$
150, PPT2	18.4	10.2	1.2×10^{-9}	0.49	$7 r_0$

Figure 4-10 shows the curves of analytical results versus the measured pore pressure. The measured maximum u was 5.8 kPa and 6.4 kPa at the PPT1 and PPT2 respectively, which took

place nearly immediately after the pile tip passed the elevation of PPT's filter. The estimated maximum u was, however, 45 kPa at PPT1 and 47 kPa at PPT2. The overestimation of the maximum u was likely because the backfill soil of PPT boreholes had a lower strength and a greater permeability than intact soils. The long-term progress of radial consolidation from the analytical solution agreed with the measurements, and thus we might suggest that the analytical model was able to predict the pore pressure response caused by helical pile installation. The time history of pore pressure at the pile surface, established using the validated analytical solution, is added in Figure 4-10. A total pore pressure (= hydrostatic + excess) of 480 kPa was generated by the pile installation instantaneously and dropped to the hydrostatic levels in about 20 min (6 days in prototype scale). The dissipation curves at pile surface and at the locations of PPT's are similar, which implies that the measurements of the PPT's can be used as an indicator of the degree of consolidation near the shaft surface.

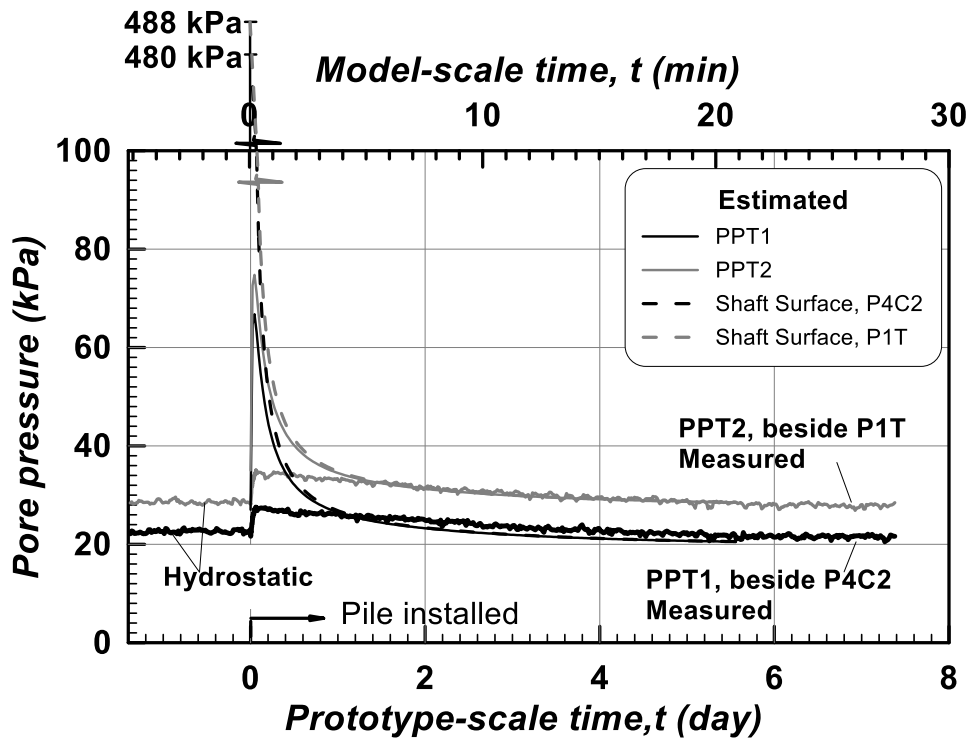


Figure 4-10. Histories of u induced by P1T and P4C2 installation in WL02.

4.4 Results: Axial Behavior of Piles

This section presents test results in term of the axial load versus displacement curves, failure modes, and prediction methods of axial resistance.

4.4.1 Pull-Out Results of Failure Modes

Photos of pulled-out piles after load tests can infer the failure mode during axial tests. Narasimha et al. (1991) pulled several small multi-helix piles out of soft clay (about 15 kPa of s_u) and observed that the transition from CSM to IBM occurred at S_r of 1.0 to 1.5. In the present study, the model piles were slowly pulled out of the soil under 1 g condition after load tests, as shown in Figure 4-11. Three different failure modes for the double-helix piles may be observed: 1) IBM, including P4 in WL01 and WL02, and P3 in WL02; 2) CSM, including P2 in WL01 and WL02; and 3) a mixed mode (termed the transitional failure mode TFM herein), for P3 in WL01. TFM implies that a unique S_{rc} that distinguishes IBM from CSM may not exist from the observed modes. When S_r decreased, the pile experienced IBM, then TFM and finally CSM at shown in tests of WL01.

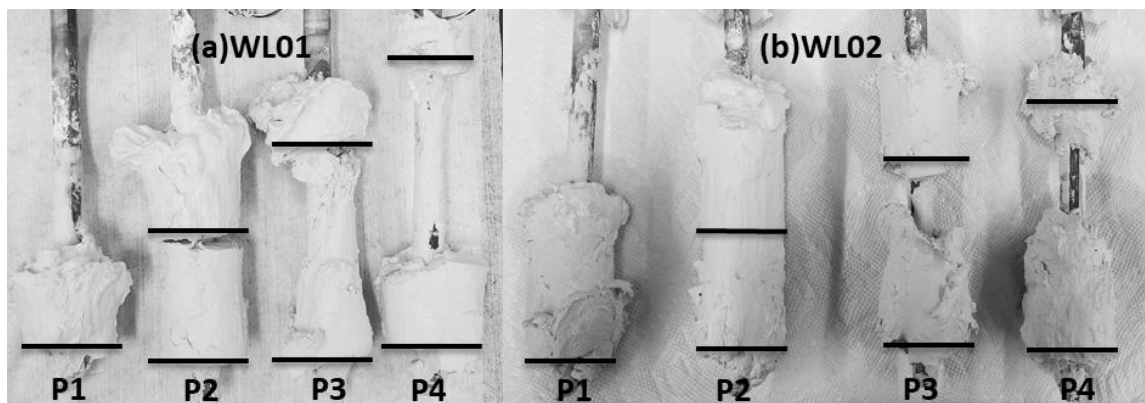


Figure 4-11. Pull-out tests: a) WL01 in medium-stiff clay and b) WL02 in stiff clay

The remaining soil above the lower helices of P1 and P4 in the stiff clay is about 50% longer than that in the medium clay. The inter-helix soil mass of P3 in the stiff clay has a larger diameter

than that in the medium clay. The gap between the inter-helix soil cylinder and the upper helix of P2 in Figure 4-11a implies considerable axial deformation of the soil cylinder due to the shear force against the surrounding soil. However, no gap was observed along P2 in Figure 4-11b. These observations suggested that a stiffer clay between two helices is more likely to become a cylinder.

4.4.2 Axial Load vs. Displacement

The load vs. displacement curves of selected piles are presented in Figure 4-12. They exhibit typical axial pile behavior in cohesive soils: an initial elastic stage followed by a yielding stage and then a plastic plunging failure. The ultimate axial capacities (Q_u), defined as the maximum soil resistance achieved, were interpreted from the curves of the uppermost SG's and compiled in Table 4-6. As shown in Table 4-6, the measured Q_u from the compressive tests are significantly greater than the tensile tests. This conforms to general observations from field tests of helical piles. When a helical plate (or anchor) is “deeply buried” in cohesive soils, the compressive bearing factor and tensile break-out factor are essentially equal; when a helix is shallowly buried, the break-out factor is expected to be less than the compressive bearing factor. Das (1980) suggested that the embedment depth of a “deep anchor” is 5 times greater than its diameter. In the present study, the lower helices were embedded at the depth of $3.9 D$ and the upper helices were even shallower. Therefore, a notable difference exists between the compressive capacity and uplift capacity of these helices.

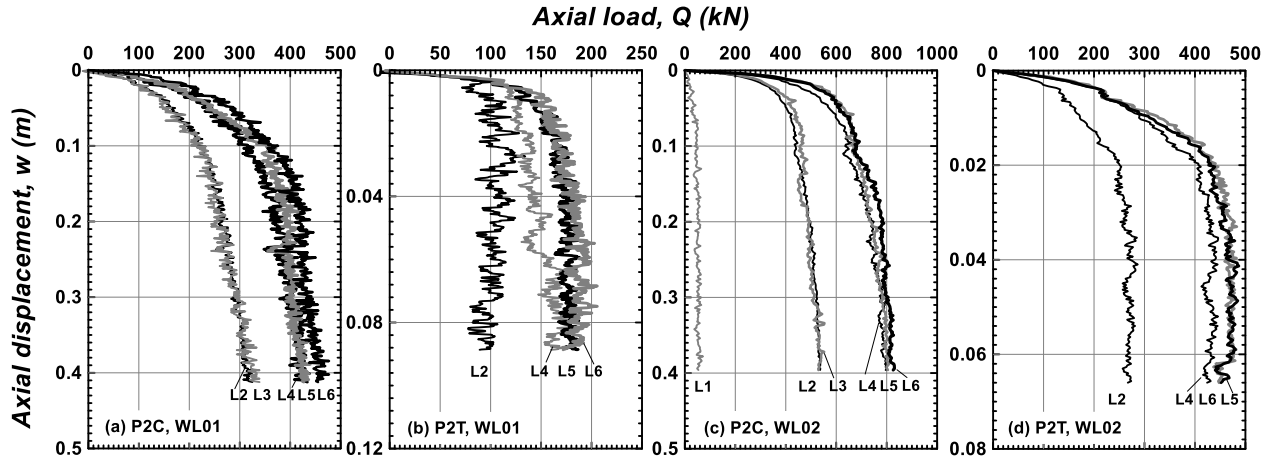


Figure 4-12. Axial load-displacement curves of selected tests. L1 to L6 are labels for axial gauge stations.

Table 4-6. Summary of axial capacities, final installation torque and torque factors

Series	Quantity	P1C	P2C	P3C	P4C1	P4C2	P1T	P2T	P3T
WL01	Q_u (kN)	248.2	420	384.6	323	246	159.1	186.2	151.8
	T_{end} (kN-m)	6.8	10	8.8	6.8	5.2	5.2	7.6	6.6
	K_T (m^{-1})	36.5	42	43.7	47.5	47.3	30.6	24.5	23
	Failure mode	IBM	CSM	TFM	IBM	IBM	IBM	CSM	TFM
WL02	Q_u (kN)	584.6	738	749.8	716	645.8	313.1	472.4	360.8
	T_{end} (kN-m)	18.5	22.5	23	18.5	15.5	15.5	23.5	22
	K_T (m^{-1})	31.6	32.8	32.6	38.7	41.7	20.2	20.1	16.4
	Failure mode	IBM	CSM	IBM	IBM	IBM	IBM	CSM	IBM

Figure 4-13 shows the normalized bearing or uplift pressure of the lower helical plate generated by taking the differential readings of SG stations L1 and L2. The pressure q_h is normalized by s_u at the helix location. The bearing factor $q_h/s_u = N_t$ of the lower helix in the stiff clay falls into the

range between 8.1 and 9.4 which is close to the value of 9.0 generally suggested for pile toe resistance. Several tests in the medium clay (Figure 4-13a) showed hardening behaviour and approached an N_t value of 12 to 13, likely because of the rigid boundary effect of the container base. The boundary effect was less obvious in the stiff clay than in the medium clay.

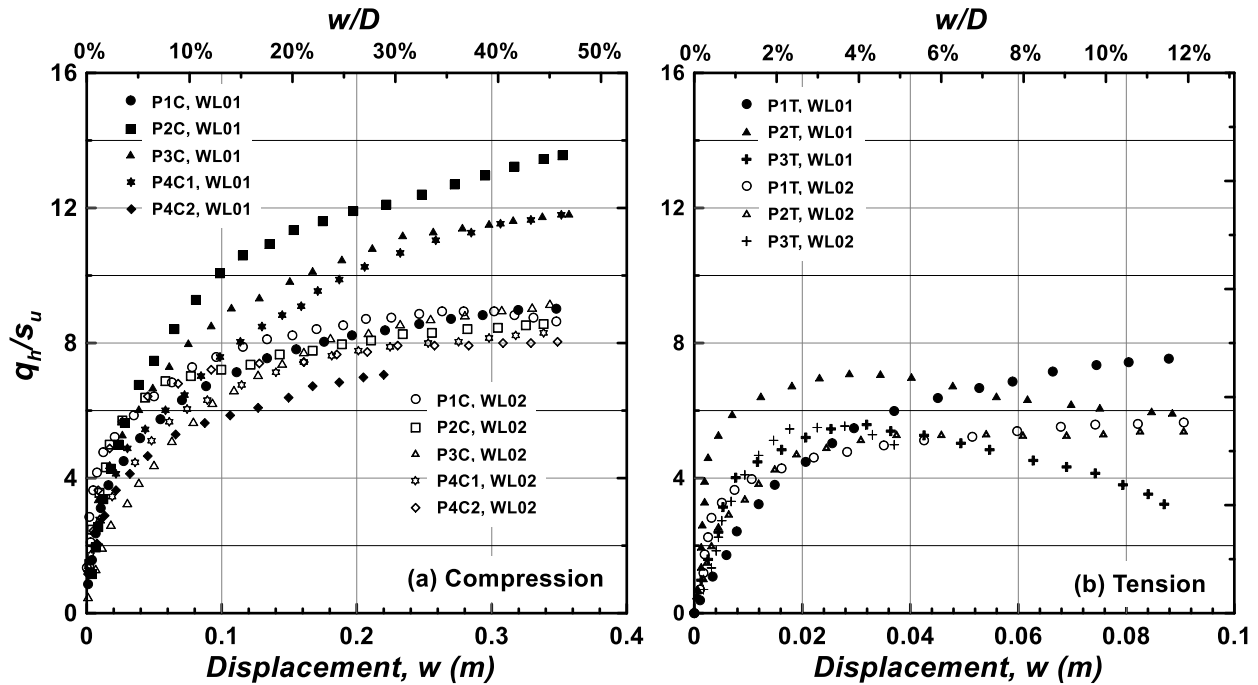


Figure 4-13. Mobilization of ending bearing or break-out pressure q_h of lower helix during (a) compression and (b) tension tests. The pressure q_h is normalized by the undrained shear strength at the helix location.

The tensile break-out factor N_b in Figure 4-13 ranged from 4.5 to 7.1. The single helix of P1T showed typical local shear failure behavior without softening, whereas P3T exhibited post-peak softening at 4% of w/D . The upper helices of P3's may account for this different behaviour because the heaving of the overlying clay resulted in a reduction of vertical soil stress on the lower helices. P2T mobilized a softening pattern in the medium clay but without softening in the stiff clay. The

remaining soil attached to the upper helix of P2 in Figure 11a exhibits an expanding failure surface of about 5° from the vertical direction in the medium clay, whereas Figure 11b shows a vertical failure surface in the stiff clay. The soil deformed by the upper helix reduces the shearing area at the cylindrical surface of inter-helix soil mass for the medium clay.

A torque factor (K_T), defined as Q_u / T_{end} , is often used to guide the design of pile resistance. A summary of K_T values from the present tests is listed in Table 4-6. The K_T factors of compressive piles (31.6 to 47.5 m^{-1}) were greater than the values of tensile piles (16.4 to 30.6 m^{-1}), because of the difference in bearing and uplift capacity. Notably, the measured K_T values of compressive piles are greater than those (about 10 m^{-1}) of helical piles with similar shaft diameters as reported in Li and Deng (2018) based on a series of field full-scale tests in cohesive soils. A primary reason for the discrepancy in K_T is the relatively large sensitivity of the soil models in present tests, which led to less T_{end} than cases in low-sensitivity soils. Present results suggest that T_{end} was dominated by the residual strength and Q_u was dominated by the peak strength; the fact also implies that the empirical torque factor method should be adopted with caution.

4.4.3 Axial Load Transfer Mechanism

Prediction of axial capacity of helical piles is conducted using conventional methods to verify the failure mode. The end bearing capacity (Q_b) of pile tip and lower helix is estimated with Equation 4-11:

$$Q_b = N_t s_u A_t \quad (4-11)$$

where N_t is the end bearing factor assumed to be 9.0 and A_t is the projected soil-helix contact area or the projected area of pile tip. The uplift capacity (Q_t) of the lower helix is estimated with Equation 4-12:

$$Q_t = N_b s_u + \gamma_{\text{sat}} H \quad (4-12)$$

where N_b is the break-out factor of circular anchors buried in clay. N_b was expected to increase with H/D and decrease with s_u , according to Adams and Hayes (1967), Ali (1969), Bhatnagar (1969), Kupferman (1971), and Das (1978, 1980). A wide range of clay categories from soft (s_u of 15 kPa) to stiff (s_u of 120 kPa) were covered in these studies. The suction force term was neglected since the helix was not enclosed at the pitch opening.

The upper helices are treated as “shallow anchors”. Values of Q_t of the upper helix may be calculated using Equation 4-13, and Q_b follows Equation 4-11 (CGS 2006 and Vesic 1975):

$$Q_b = A_t (s_u N_c S_c + q_s N_q S_q + \frac{1}{2} \gamma_{\text{sat}} D N_\gamma S_\gamma) \quad (4-13)$$

where N_c , N_q , and N_γ are dimensionless bearing capacity factors, S_c , S_q , and S_γ are dimensionless modification factors, and q_s is the vertical stress acting on the bottom of the helices.

The shear force Q_{s_cyl} acting on the inter-helix soil *cylinder* is estimated using Equation 4-14:

$$Q_{s_cyl} = \pi D S s_u \quad (4-14)$$

The ultimate resistance Q_{su} of clay-shaft interface was estimated using Equation 4-15,

$$Q_{su} = \pi d l \alpha s_u \quad (4-15)$$

where α is the adhesion factor and l is the length of shaft segment. Figure 4-11 shows that a thin clay layer remained on the shaft surface of pulled-out piles. It implies that the shear resistance developed on the pile shaft during the axial loading was more of an inter-clay shearing rather than a clay-shaft shearing in this study. Therefore, α was assumed to be 1.0.

The differential load of every two adjacent SG stations at the limit state is obtained from the load versus displacement curves to produce axial load distributions. Figure 4-14 exhibits the measured and estimated load distributions of eight selected tests. The estimation is based on the failure mode sketched to the right axis of each plot. Notably, the estimated load distributions of

P3C (Figure 4-14b) and P3T (Figure 4-14d) in WL01 are generated with IBM model since there is no prediction method for the observed TFM (Figure 4-11a). The accuracy of the estimates was quantified herein by a factor δ (Figure 4-14), defined as the ratio of the measured shaft resistance or plate bearing resistance to the estimated counterparts. The δ values show that all the distributed loads were appropriately estimated except for the lower helices affected by container base boundary effect and some shaft segments next to a helix. To further confirm the accuracy of prediction methods, Figure 4-15 summarizes the values of δ of various pile segments obtained from other eight test piles. It conforms to the observation from Figure 4-14 that most of the load distributions are well predicted, except for the noted components.

As shown in Figure 4-14a, 14c, 14e and 14g, inter-helix cylindrical shear forces of P2's (L3-L4 for compressive tests and L1-L2 for tensile tests) were reasonably predicted by CSM model within $\pm 8\%$ difference. This agreement also confirms that the values of s_u measured by the in-situ vane shear tests under 1 g condition can represent the soil strength under 20 g condition. The loads on the inter-helix shafts were nearly zero (e.g., between L3 and L2 in Figure 4-14a). It indicates that the shear force acting on the soil cylinder was transferred via the soil mass to the lower helix (tension) or upper helix (compression).

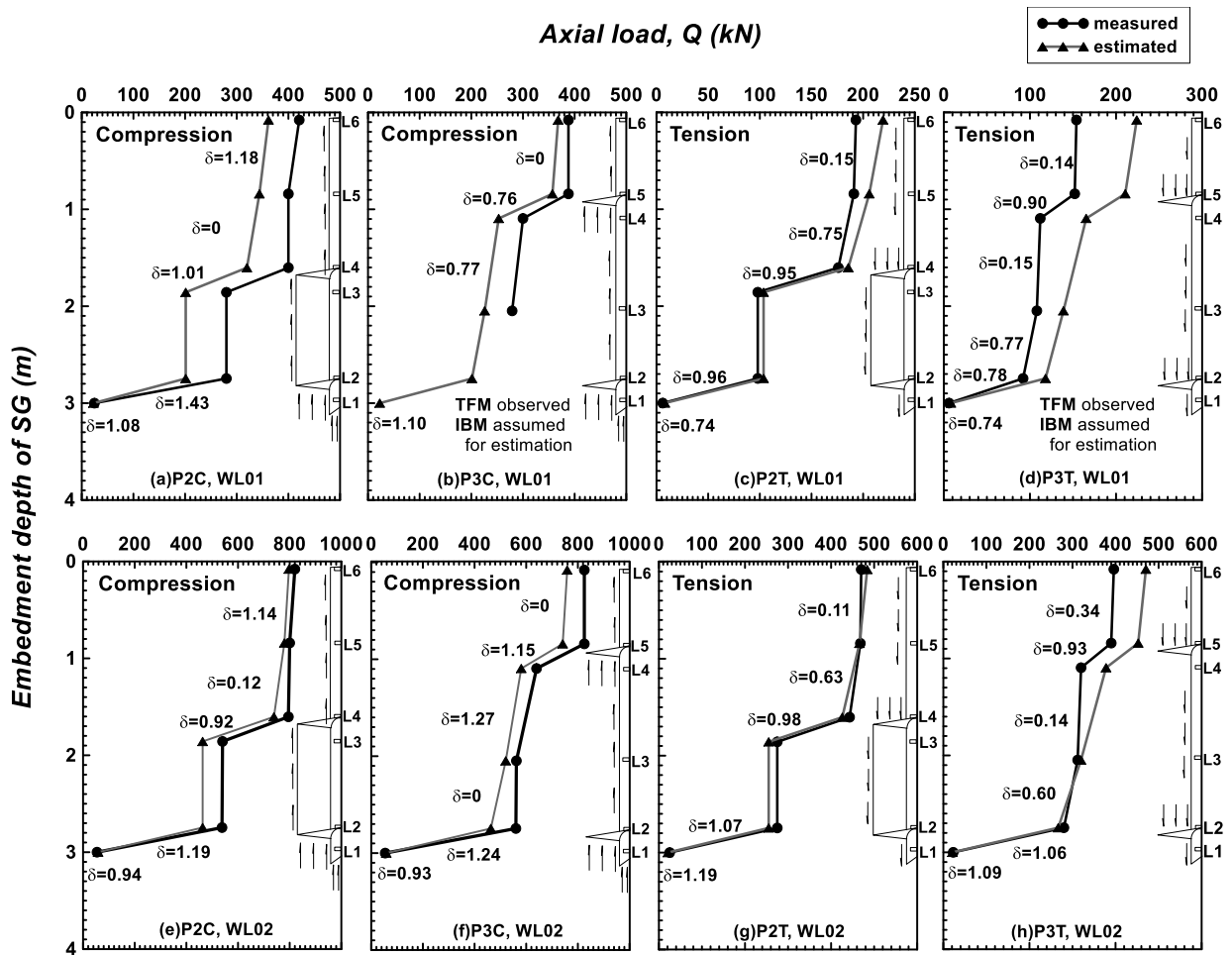


Figure 4-14. Axial load distributions at the limit state of selected piles. The factor δ is the ratio of the measured values to the estimates based on assumed failure mode sketched to the right of each plot.

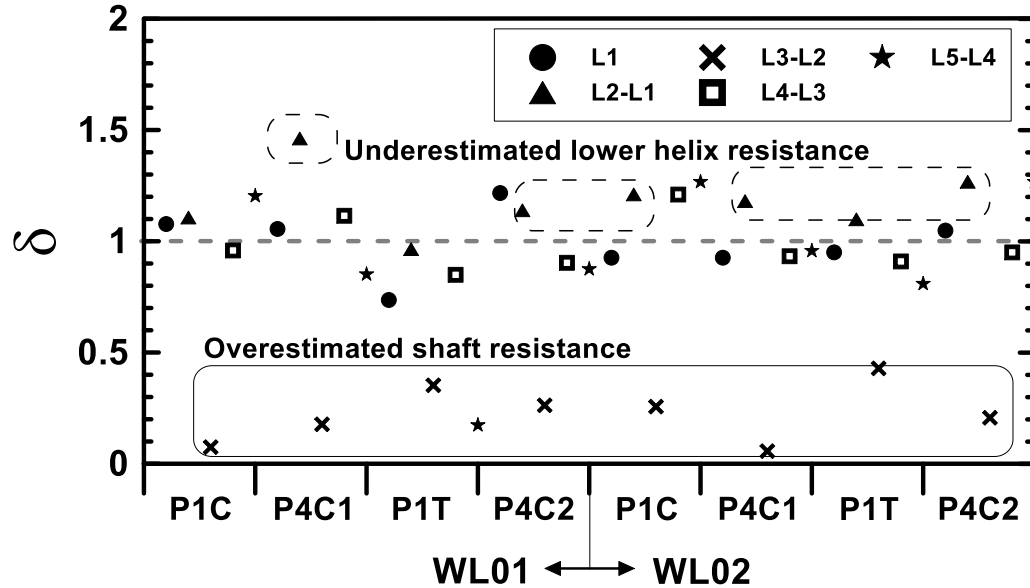


Figure 4-15. Ratio of measured to estimated axial load distributions along pile segments. Results are taken from eight piles different from piles shown in Figure 4-13.

The soil in the inter-helix space of P3 did not form a cylinder in the medium clay according to Figure 4-11a; instead, a cone-shaped failure surface formed. Figure 4-14d indicates that the resistance acting on the circumference of the soil cone of P3T in WL01 was transferred to the lower helix and the inter-helix shaft at the same time. A similar mechanism happened to P3C in WL01 (Figure 4-14b). Unlike P3 in the medium clay, the stiff clay mass in the inter-helix space of the P3's of WL02 (Figure 4-14f) was dominated by IBM. The axial loads carried by the inter-helix area of P3C and P3T (observed TFM) in WL01 are 105 kN and 106 kN, respectively; the corresponding estimates of P3C and P3T by IBM are 132 kN and 136 kN; the estimates by CSM are 197 kN and 159 kN, respectively. It seems IBM and CSM over-predict the axial resistance of a helical pile failed by TFM.

The shaft resistance, above the bottom helices of P1C and P4C1 and above the upper helices of P2C and P3C (Figure 4-14), was almost zero in both soil models. This reduction was related to a

certain span of approximately $1D$ starting from the helix. This area was called “ineffective zone” by Rao et al. (1993) and Li et al. (2018). Figure 4-16 shows the progress of mobilized shaft resistance (Q_s) along five selected pile segments, where Q_s is normalized by the estimated Q_{su} and the pile displacement w is normalized by d . For Segment A immediately above the helix in compression, Q_s reached 40% of Q_{su} , due to the presence of ineffective zone above the helix. In comparison, for Segment D that is above the helix in tension, Q_s was fully mobilized to Q_{su} and then exhibited post-peak softening. As for Segment E (Figure 4-16b), Q_{su} was achieved at w/d of 1%, likely because it was strongly affected by the soil cylinder formed in compression. The shear force outside of the ineffective zones (Segments B and C) reached Q_{su} and remained at peak values. The comparisons imply that both failure modes and loading directions affect the shaft resistance near a helix. In general, the maximum Q_s was reached at w/d ratios ranging from 1% to 4%; this range is greater than the order of $w/d = 0.25 - 1\%$ (as per Salgado 2008). One possible reason is that the kaolinite soil herein, with a high plasticity and ductility, required a large displacement to trigger a slip failure along the pile shaft.

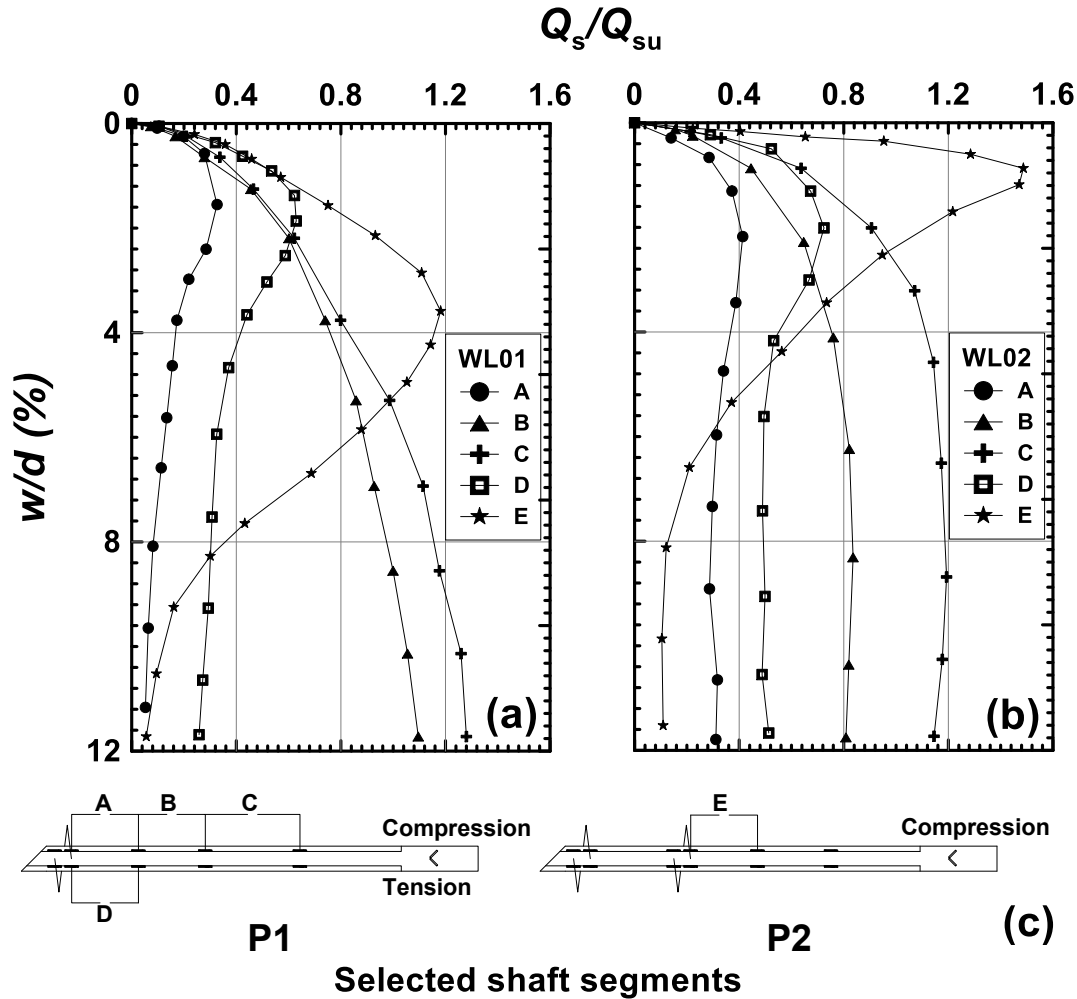


Figure 4-16. Mobilization of shaft resistance along selected pile segments in (a) medium stiff clay in WL01 (b) stiff clay in WL02; (c) illustration of pile shaft segments. Q_{su} is the estimate of ultimate shaft resistance.

4.5 Conclusions

Sixteen helical piles were installed and axially loaded in two cohesive soil models. The present study is aimed at the behavior of helical piles and soils in the installation and axial loading processes.

The following conclusions may be drawn:

1. A torque model that considers the residual strength distribution, shaft area, and helix area was developed. The model assumes that all of the clay-helix interface shearing performance is related to s_{ur} of clay. The model effectively predicted the installation torque profiles of 14 test piles.
2. The analytical solution developed by Randolph and Wroth (1979) was adopted to interpret the measured pore pressure response to pile installation in the stiff clay. The solution overestimated the maximum u but effectively predicted the major progress of dissipation. The installation-induced u was completely dissipated within 6 days in prototype scale. The results suggested that u was dominated by shaft-induced cavity expansion and the effects of helices may be neglected.
3. The u response at the pile surface was established using the validated analytical solution. This pore pressure decreased rapidly after pile installation. The long-term consolidation progress at the shaft surface was similar to the locations where the PPT's were installed. As such, the reading of a PPT installed within an appropriate distance can be used as an indicator of soil consolidation near the shaft surface.
4. The effect of soil strength on the failure modes of double-helix piles was observed and assessed. The observations suggested that a stiffer clay driven by helix is more likely to become a cylinder. A transitional failure mode, for which the soil failure zone was cone-shaped occurred at 2.5 of S_r in the medium clay of present test, implies that a unique S_{rc} that distinguishes IBM from CSM may not exist.
5. The end bearing or uplift capacities of the helical plates were reasonably well predicted by toe capacity or anchor capacity equations except for those affected by container base

boundary effect and TFM. Specifically, IBM and CSM models may over-predict the axial capacity of a helical pile governed by TFM.

6. The shaft resistances agreed with the prediction assuming an adhesion factor of 1.0, but the shaft segments next to a helix exhibit very low resistance. Ineffective zones accounted for the observed low shaft resistances. The shear force outside of the ineffective zones was fully mobilized. The shaft adhesion within the ineffective zone was affected by loading directions and failure modes of helix zone.

5 Large Deformation Finite Element Analyses of Axially Loaded Helical Piles in Cohesive Soils

In the past decades, helical piles have gained vast popularity in civil engineering practice as an option of deep foundations. The design of axial load capacity of these piles relies on an appropriate selection of failure mode. Currently, two failure modes, i.e., individual bearing and cylindrical shearing are generally recognized in research and engineering practice. The ratio of inter-helix spacing to helix diameter, S_r , is used as the primary indicator of failure mode. However, recent field test research of helical piles suggested that the failure mode might depend on not only the pile dimensions but also the soil's characteristics, which is confirmed by the centrifuge model test results presented in Chapter 4. The present chapter is aimed to use numerical modeling techniques to investigate the axial failure mechanisms of multi-helix piles in clay. The effect of pile embedment depth, S_r and undrained shear strength (s_u) on the mobilization of the inter-helix soil slip surface was assessed. In view of the large-strain nature of axial pile load tests, a large deformation finite element analysis (LDFE) technique was adopted in this research. It turns out to be accurate in capturing the results of the centrifuge model tests. Thereafter, the validated LDFE model was used to carry out several series of parametric studies to assess the effect of certain factors (e.g., S_r , s_u , and pile embedment depth) on the axial failure modes of helical piles in clay.

5.1 Introduction

A helical pile is composed of a pipe shaft and one or multiple helical plates welded to the shaft. The axial load is transferred via the pile shaft to the helix/helices. In the past decades, helical piles have been broadly used in various industrial sectors including electrical power transmission, commercial buildings, and infrastructure construction.

A number of semi-empirical theories have been developed to estimate the uplift capacity of single-blade anchors by Meyerhof and Adams (1968), Vesic (1971), Meyerhof (1973), and Das (1978, 1980). These theories are commonly applied to the prediction of uplift capacity for single-helix piles. Terzaghi's (1943) equation and Meyerhof's (1976) end bearing factors are broadly used for the estimation of bearing capacity of single-helix piles. However, the problem of multi-helix piles cannot be easily solved by the aforementioned methods because of potential overlapped stress zones of adjacent helical plates that may affect the overall failure mode of the pile (Merifield and Smith 2010). As illustrated in Figure 5-1, there are two recognized axial failure modes for multi-helix piles: individual bearing mode (IBM) and cylindrical shearing mode (CSM). IBM assumes that soil collapse takes place at individual helical plates. CSM, proposed by Mooney et al. (1985), assumes that during the axial movement of pile the inter-helix soil acts as a cylindrical body shearing against the surrounding soil. Given the radical difference in the composition of soil resistance, the axial capacity design of helical piles depends on an appropriate selection of failure mode. A ratio defined as $S_r = S/D$, where S is the inter-helix spacing and D is the helix diameter, is usually used as the indicator of potential failure mode.

Lutenegger (2009) conducted an analytical study of uplift capacity of helical piles in clay and derived a critical S_r of 2.25. The primary assumption was that the break-out factor of an individual plate $N_b = 9.0$ and the pile would be to the failure governed by IBM or CSM whichever produces the smaller uplift capacity. Rao et al. (1991) observed the soil mass remained on several multi-helix piles pulled out of a soft clay ($s_u \approx 20$ kPa) after a number of small-scale laboratorial loading tests. It was noted that S_{rc} for the tested soft clay was between 1.0 and 1.5. These discrepancies from the past observations suggest that a systematic assessment may be necessary for the previously described critical space ratio. The discussions about the pull-out tests in Chapter 4

suggest a transitional failure mode (TFM) that differs from IBM and CSM for a double-helix pile ($S_r = 2.5$) occurred in the kaolinite clay with s_u of about 50 kPa. The centrifuge model test results and data interpretation in Chapter 4 confirmed the effect of soil strength on the failure mode of double-helix piles. A further investigation to cover a wider range of s_u and S_r and the embedment depth will be helpful for interpreting the axial behaviour of multi-helix piles and guiding the industrial application. Numerical modeling method is more efficient and affordable than physical modeling tests when a large number of variables are involved.

Merifield et al. (2003) conducted several 3D finite element analyses to investigate the effect of anchor shape (square, rectangular, and circular) on its break-out factor in clay. Merifield (2011) performed 2D axisymmetric simulations for a wide range of multi-plate anchor geometries to assess the uplift capacity. For these two finite element studies, the lower bound theorem that based on a rigid plastic soil material was adopted to avoid large element distortion. However, the true ultimate capacity might not be reached within the allowed displacements in the finite element method; so arbitrary “cut-off” criteria were adopted with ultimate capacities determined according to displacement limits or the shape of load-displacement curves (Rowe and Davis, 1982). Such approximation may over-estimate the ultimate capacities of buried anchors since the soil was set to be rigid plastic with an infinitely large elastic modulus (Wang et al. 2010), especially for complex soil-structure problems with asynchronous mobilization of local resistances. For example, the ultimate capacity of an axially loaded helical pile is controlled by shaft friction, individual plate resistance and cylindrical shearing when applicable; these resistances are mobilized at different levels of axial displacements according to Salgado (2008) and Li et al. (2018). Moreover, the investigation of axial load transfer mechanism along with pile displacement requires a complete nonlinear or a simplified bilinear response of soil. Therefore, a large deformation finite element

(LDFE) analysis is more suitable for the modeling of helical piles than standard Lagrangian finite element analyses, since a large strain is required to trigger the failure of soil-pile interactive components.

Song et al. (2008) and Wang et al. (2010, 2013) conducted several LDFE analyses of the uplift behavior of helical anchors in ABAQUS using the remeshing and interpolation technique with small strain (RITSS) method proposed by Hu and Randolph (1998). In essence, the RITSS is a form of arbitrary Lagrangian Eulerian (ALE) method, by which small strain Lagrangian calculation is carried out in each incremental step and the stresses and material properties are transferred from the old mesh to the new mesh updated from the previous step (Liu et al. 1986; Ghosh and Kikuchi 1991; Randolph et al. 2008). The advantages of RITSS are that the periodical Lagrangian calculation is not affected by the mesh deformation from previous displacements, and the remeshing and interpolation algorithms can be coupled with any standard finite element (FE) package through customary interface codes. The early applications of 2D RITSS in geomechanics were mainly developed using the FE code AFENA (Carter and Balaam 1995; Hu and Randolph 2002; Zhou and Randolph 2007; Song et al. 2008). As of now, ABAQUS offers a powerful in-built mesh-to-mesh technique that facilitates RITSS in this framework. Therefore, ABQUS was selected in the present research.

Three-dimensional LDFE analysis usually requires a considerable amount of computational effort. Since the soil-pile interaction in the axial direction is an axis-symmetrical problem, a 2D model can produce as accurate simulation as 3D models at an economic computational cost. More recently, 2D RITSS analyses have been applied to a limited number of studies regarding the displacement of uplift piles (Wang et al. 2013), anchors (Ma et al. 2014), and pipelines (Wang et al. 2015). The behavior of helical anchors or flat anchors was discussed in Song et al. (2008) and

Wang et al. (2010, 2013) with regard to the break-away condition under plate, number of plates, embedment depth of plates, or inter-plate spacing. These studies were focused on the ultimate uplift capacities of buried anchors in offshore soft clay rather than axial load transfer mechanisms. In addition, the soil-shaft interaction was neglected in these numerical models for its contribution to the total uplift resistance was assumed minor. Song et al. (2008) used s_u in the analyses to normalize the plate embedment depth, but the effect of s_u on the axial failure mode of a multi-helix pile was absent.

In summary, a LDFE study of multi-helix piles with complete soil-pile interaction, i.e., soil-shaft interaction and soil-helix interaction is unavailable in the literature. Hence, the investigation of the load transfer mechanisms within the overlapped stress zones (shaft-to-helix and helix-to-helix) is still limited. A quantitative evaluation of the effects of S_r and s_u on the failure modes of multi-helix piles is also unavailable in the literature.

This chapter is aimed to examine the axial failure mechanisms of helical piles in clay using the LDFE technique. A numerical model with fully implemented soil-pile contacts, including soil-shaft and soil-helix interaction, was developed on the platform of ABAQUS (SIMULIA 2014, Ver. 6.14) using the RITSS approach. The model was validated by a series of axial loading tests of helical piles in clay performed on the geotechnical centrifuge at the University of Alberta. Onwards, parametric studies were conducted to assess the effect of s_u of clay, embedment depth, and inter-helix spacing of helical piles on the axial failure mechanisms. The values of end bearing and break-out factors of the helices were then assessed based on a series of parametric studies and summarized for practical use.

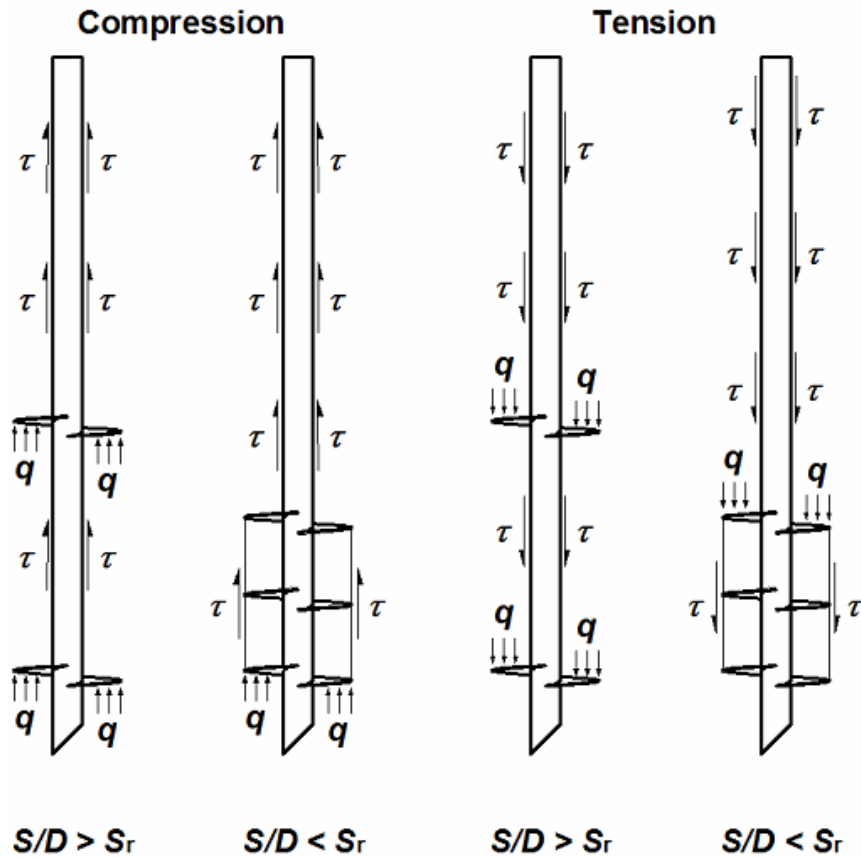


Figure 5-1. Current understanding of multi-helix pile failure modes

5.2 Procedure of RITSS-Based LDFE

In analytical studies of the axial capacity of buried horizontal anchors, according to Merifield et al. (2003, 2006), the problem is usually simplified to be plane-strain for strip anchors or axis-symmetric for circular anchors considering the geometrical symmetry of the problem. Merifield et al. (2003, 2006) and Wang et al. (2010) adopted three-dimensional numerical analyses to ascertain the effect of anchor shape on the uplift capacity of a buried single anchor. For circular-helix piles, Merifield (2010, 2011) and Wang et al. (2013) adopted 2D axisymmetric models and the methods were validated by laboratory load tests.

The selection of RITSS method in the present research was briefly justified in the Introduction section. Besides RITSS, the coupled Eulerian-Lagrangian (CEL) method is also popular in LDFE analyses, as well as the efficient ALE (EALE) technique developed at the University of Newcastle. Wang et al. (2015) summarized the advantages and disadvantages of these three approaches after comparing the algorithms, integration schemes, and operations (see Table 5-1). Accordingly, RITSS is the most suitable option among these techniques for a static modeling of axially loaded helical piles in soil.

Table 5-1. Summary of three numerical techniques used in LDFE (after Wang et al. 2015)

	RITSS Hu and Randolph (1998)	EALE Nazem et al. (2009)	CEL Dassault Systèmes (2012)
Integration scheme	Implicit	Implicit	Explicit
Elements	Quadratic	Quadratic, Quartic, Quintic	Linear
Implementation	2D, 3D	2D	3D
Meshing	Periodic mesh regeneration in global or local region	Mesh refinement by adjusting the location of nodal points	Mesh fixed in space
Mapping of field variables	Interpolation	ALE convection equation	First or second order advection
Cos of Lagrangian phase	Heavy	Heavy	Moderate
Cos of Eulerian phase	Minimal	Minimal	Heavy
Applications	Static, Dynamic, Consolidation	Static, Dynamic, Consolidation, Dynamic Consolidation	Quasi-static, dynamic
User-friendliness	Commercial pre- and post-processors, but requires script programs to control processors	In-house pre- and post-processors	Commercially available, graphical interface available

The RITSS approach divides the attempted large pile displacement into a sequence of small incremental steps. In each of the small displacement increment, the analysis is performed with the standard Lagrangian calculation. Between every two incremental steps, the solution mapping powered by ABAQUS enables the convection of the element nodal displacement field, element strain field, element stress field, and soil properties from the previous deformed mesh to the following new mesh. The procedures below are followed:

1. Set up the initial model with appropriately assigned geometries, material properties, meshing strategies, boundary conditions, and soil-pile interactions governed by tangential

- shear contact and normal “hard” contact, collaboratively. Notably, the adopted normal “hard” contact allows separation of the pile and soil surfaces under local tension stresses.
2. Perform a displacement-controlled analysis step with a small increment. In most cases, setting each incremental displacement to be 1% to 2% of D (or helix diameter) may ensure a sufficient accuracy (Tian et al. 2013). This small-strain strategy is aimed to avoid excessive mesh distortion so that the Lagrangian calculation can proceed with accuracy and convergence.
 3. An output database (ODB) file is created by each small-strain analysis. Extract the deformed orphan meshes from the previous ODB file and convert them to new solid geometries.
 4. Remesh the new geometries and map the solution variables from the old mesh to the new mesh. Then set up the simulation as in Step 1 and start the analysis for the next displacement increment.
 5. Repeat Steps 2 to 4 until the target total displacement is achieved.

In the present study, Python (the script language of ABAQUS) files were coded to generate the un-deformed mesh, control the remeshing process, and extract requested data from the ODB files. The entire LDFE analysis was performed automatically in ABAQUS without any intervention from the user. More detailed procedures regarding all steps can be found in Tian et al. (2014) and Ullah et al. (2018). The original Python codes are presented with necessary notes in Appendix D.

5.3 Development and Validation of LDFE Model

The cohesive soil in the present LDFE model was characterized by the Mohr-Coulomb constitutive model. Uncertainties in the input soil parameters, including s_u and undrained Young’s modulus (E_u), may affect the accuracy of numerical modeling. The numerical model built through the

procedures described in Section 5.2 was validated against the centrifuge model test results presented in Chapter 4.

5.3.1 Numerical Model and Assumptions

Although the problem of helical pile failure in cohesive soil is 3D in nature, the axisymmetric geometries of piles and surrounding soil make it reasonable to simplify the numerical model to be 2D, thereby improving the computational efficiency. In addition, the applied settlement and sequential stress field in the soil are also axisymmetric. Wang et al. (2013) adopted a 2D axisymmetric model to generate a series of load-displacement curves of uplift helical anchor in soft offshore clay; the agreement between the numerical analysis and centrifuge model tests in Wang et al. (2013) proved the effectiveness of 2D axisymmetric modeling. To enhance the efficiency of computation for the present FE analyses especially for the parametric studies, a 2D axisymmetric model was adopted.

In the present LDFE analyses, the response of homogeneous clay under undrained condition was characterized as an elasto-perfectly plastic material with a Mohr-Coulomb yield criterion. The input parameters of Mohr-Coulomb criterion include cohesion ($= s_u$ under undrained condition), internal friction angle and post-peak softening coefficients. In this analysis, the frictional angle was set to be 0, and the post-yielding strength remained a constant equal to the cohesion. Poisson's ratio ν of the clay was 0.495 to approximate the constant volume of undrained condition for the clay. The bulk unit weight of the clay was taken as $\gamma=18 \text{ kN/m}^3$ for the medium clay and 20 kN/m^3 for the stiff clay. The mesh size of the soil domain was controlled by seeding each edge at designated intervals. The grids are finer near soil-pile interfaces and coarser in the far field. A large value of E and yield strength was assigned to the pile shaft and helices. This is reasonable since the pile material has much greater rigidity relative to the surrounding soil. Figure 5-2 depicts the

profile of the numerical model. The element type for the clay was quadratic CAX4RH. The boundary conditions are also shown in Figure 5-2. The axial loading of the pile was displacement-controlled rather than load-controlled following the RITSS procedure.

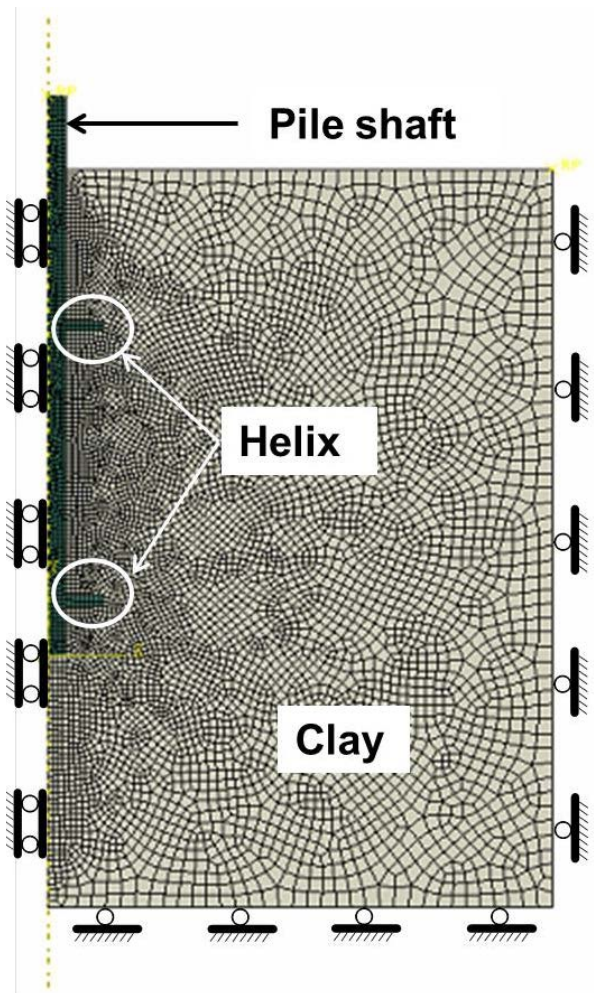


Figure 5-2. Illustration of the axis-symmetric model on the platform of ABAQUS showing the mesh and boundary conditions

The soil-shaft adhesion was excluded in Merifield and Smith (2010), Merifield (2011), and Wang et al. (2010, 2013) because these studies presumed negligible shaft contribution to the total pile capacity. However, according to the analyses of shaft resistance in Chapter 4, the progression

of soil-shaft shearing stress contains critical information about the mobilization of soil-helix resistances. Therefore, the shaft adhesion was included in the present numerical model.

In the present model, the soil-pile interaction is defined by two components: a tangential behavior aligned to the contact interface and a normal behavior in the diagonal direction as shown in Figure 5-3 (a). A “rough” friction formulation that does not allow soil-pile sliding is assigned to the tangential interaction according to the observation of the soil layer remained on the shaft surface after the pull-out tests shown in Figure 5-3 (b), (c) and (f). As a result, the maximum soil-pile shear stress τ_{max} is approximately equal to s_u . Considering the undrained condition and total stress approach, τ_{max} is independent from the normal contact pressure.

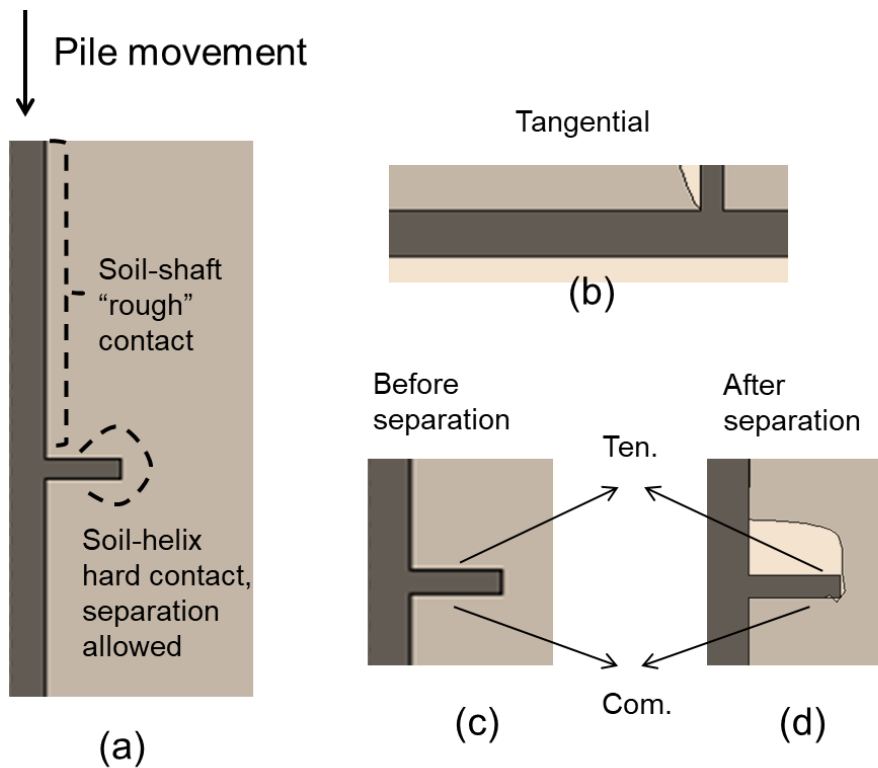


Figure 5-3. Illustration of soil-pile interaction: (a) soil-pile contact types, (b) “rough” tangential contact, (c) hard contact before separation, (d) hard contact after separation.

The hard contact prevents the pile elements from penetrating into the soil surfaces under local compression, thus transfers the normal stresses to the soil elements (Figure 5-3d). While under local tension, the separation between the contact surfaces is allowed (Figure 5-3e).

Helical pile's installation may cause a reduction in soil strength owing to strains and blending effects induced by shaft and helix penetrations. Apparently, the soil strength reduction due to pile installation is more severe for soils close to the edge of helices rather than soils beyond the horizontal reach of helices. In IBM failure, a greater volume of soil contributes to the plate resistance and much of this soil locates outside the edge of helices. Consequently, the value of the mobilized undrained shear strength in case of piles governed by IBM would be greater than piles experienced CSM. Hence, the value of S_{rc} for multi-helix piles would be greater than that for a pile installed in remolded clays. This statement is confirmed by Lutenegeger (2009) in field load tests that piles with spacing ratio equal to $3 \times D$ experienced CSM, which was greater than the derived analytical S_{rc} . In the present FE model, however, the installation induced disturbance is not accounted because there is no reliable approach for assessing the effect of pile installation on the pile behavior. However, an in-flight consolidation was performed in the centrifuge model tests of this study to minimize the installation effect. Therefore, using the centrifuge model test results with pile installation involved for the validation of this FE model without any pile installation process is considered as reliable.

5.3.2 Selected Centrifuge Model Test Results for Validating LDFE

The results of the centrifuge model test program are presented in Chapter 4 and briefly summarized herein. The axial load tests of two double-helix piles with S_r of 1.5, 2.5, and 3.5 in two clay models with s_u of about 50 kPa (test series WL01) and 120 kPa (WL02) are used for validation. After the loading tests were terminated, the piles were gently pulled out of the soil at 1 g condition. The soil

masses remained on the surface of the piles clearly showed the slip surfaces as illustrated in Figure 5-4, in which the three types of piles were called P2, P3, and P4, accordingly. Pile geometries are summarized in Table 5-2.

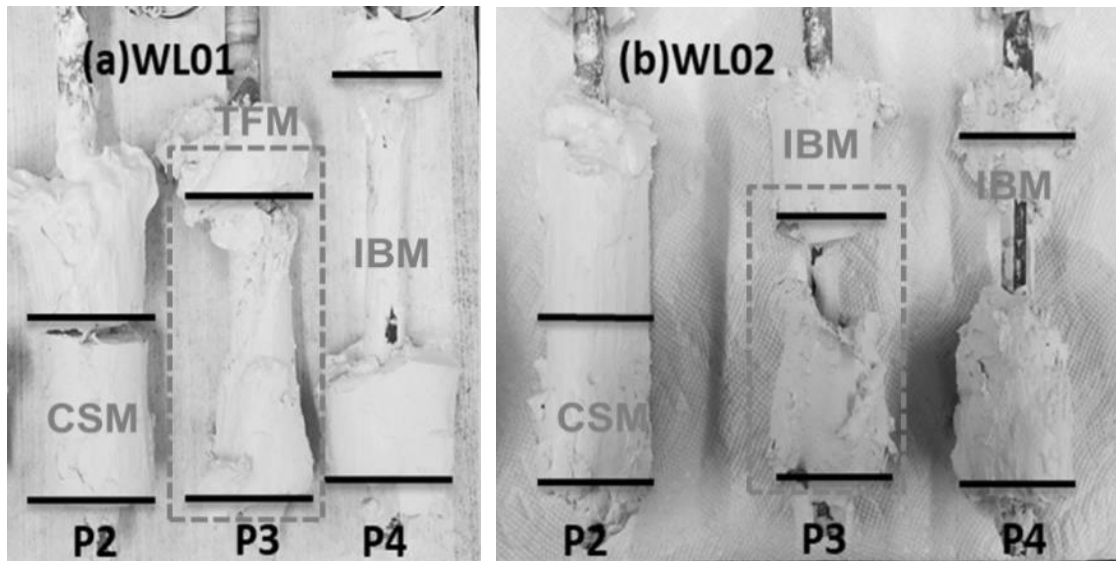


Figure 5-4. Pull-out tests: a) WL01 in medium-stiff clay shows CSM for P2, TFM for P3 and IBM for P4; and b) WL02 in stiff clay shows CSM for P2, IBM for P3 and P4

Table 5-2. Dimensions of multi-helix Piles in prototype scale

Pile ID	No. of helix	Shaft Dia. d (mm)	Helix Dia. D (mm)	Pile Length L (mm)	Helix Spacing S (mm)	Lower Helix Embedment Depth E_H (mm)	Space Ratio S_r
P2	2	254	762	5436	1144	3000	1.5
P3	2	254	762	5436	1905	3000	2.5
P4	2	254	762	5436	2668	3000	3.5

Note: Tests of pile P1 was not simulated in the LDFE because P1 had only one single helix.

The load vs. displacement curves of selected test piles obtained from the centrifuge model tests were used to validate the numerical model and calibrate the soil parameters of the LDFE model. The input s_u values were approximated from the vane shear test results presented in Figure 4-3 to constant values across the soil domain in the LDFE model. The corresponding E_u values were estimated using the chart proposed by Duncan and Buchignani (1976) for OC clay based on PI, s_u , and OCR . The exact values of input s_u and E_u are summarized in Table 5-3.

Because the present LDFE model was axis-symmetric, the axial load on the pile shaft and helix must be extrapolated to a load in an equivalent 3D model. For example, the axial load taken by the pile head is interpreted for an equivalent 3D model using Equation 5-1:

$$Q = \pi \sum_{i=1}^{n_e} \sigma_i (r_{i+1}^2 - r_i^2) \quad (5-1)$$

where n_e is the number of elements across the pile radius, σ_i is the element stress in the vertical direction of the i^{th} pile element starting from the axis to the shaft surface, r_i is the distance from the Gauss Point (integration point) of the i^{th} pile element to the pile shaft axis. Results of the chapter are presented for an equivalent 3D model unless otherwise noted.

Figure 5-5 compares the measured and calculated load vs. displacement curves of two selected piles in compression, and Figure 5-6 compares the measured and calculated load vs. displacement curves for tension. The input soil parameters were approximated from the vane shear test results presented in Section 4.2.1. Considering the value of s_u varies with depth, the loading direction will affect the approximation. In the present study, the input s_u was averaged from the two depths $1 D$ below the two helices for compression or $1 D$ above for tension. These input soil parameters are summarized in Table 5-3. Figure 5-5 and Figure 5-6 show an overall overestimation of the limit capacities within 20%. The soil disturbance induced by the pile installation may contribute to this

overestimation. Nonetheless, the general agreement between the simulation results and measurements validates the present LDFE method based on RITSS for the axially loaded helical piles in cohesive soils. The calibrated soil parameters are accordingly used in the following analyses.

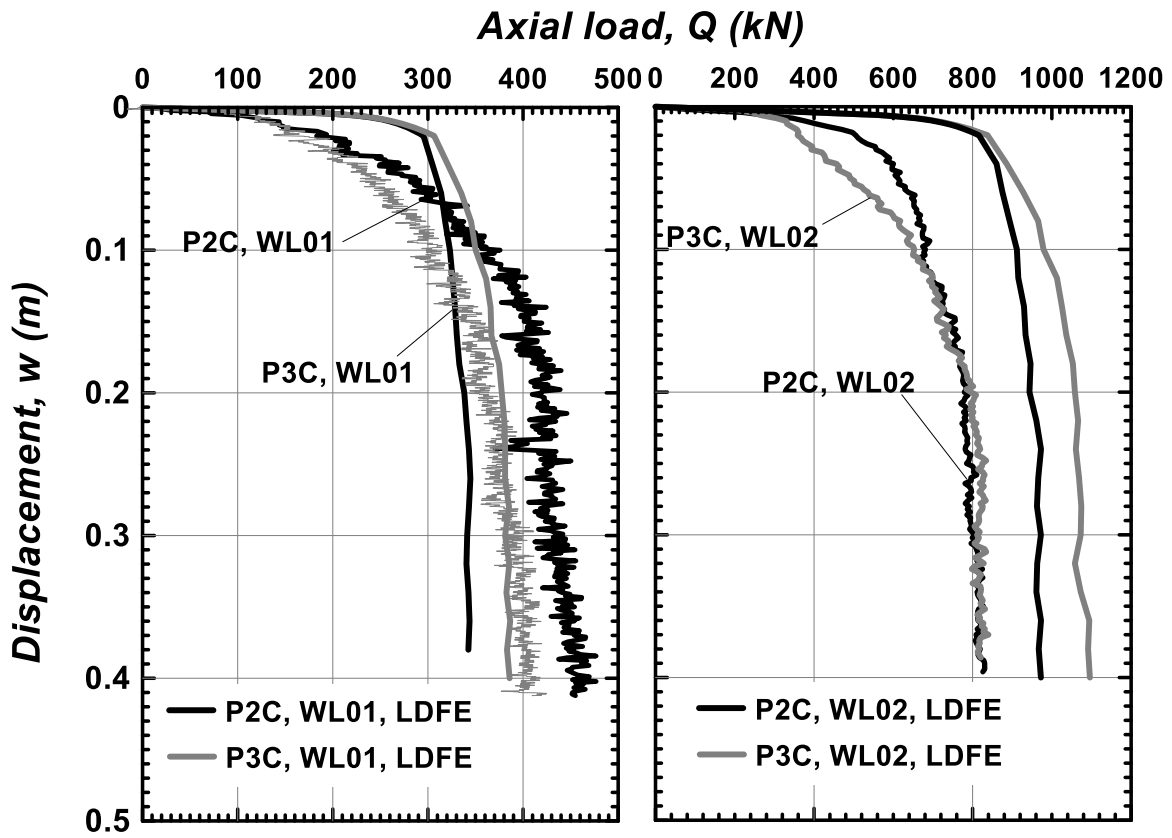


Figure 5-5. Measured and computed axial load vs. displacement curves of selected piles in compression from test series: (a) WL01; and (b) WL02. Results are presented in the prototype scale.

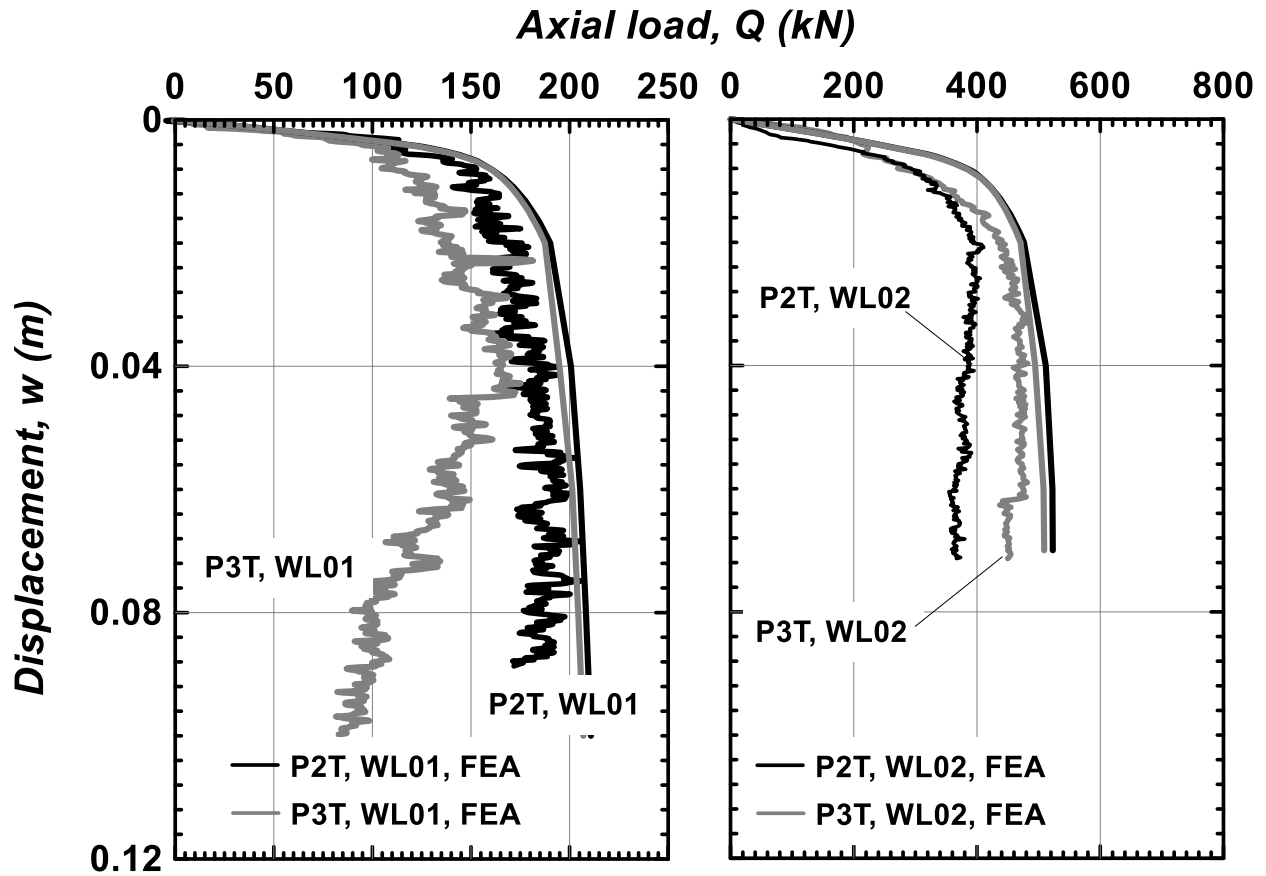


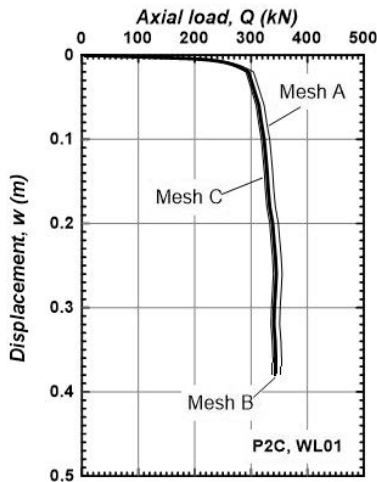
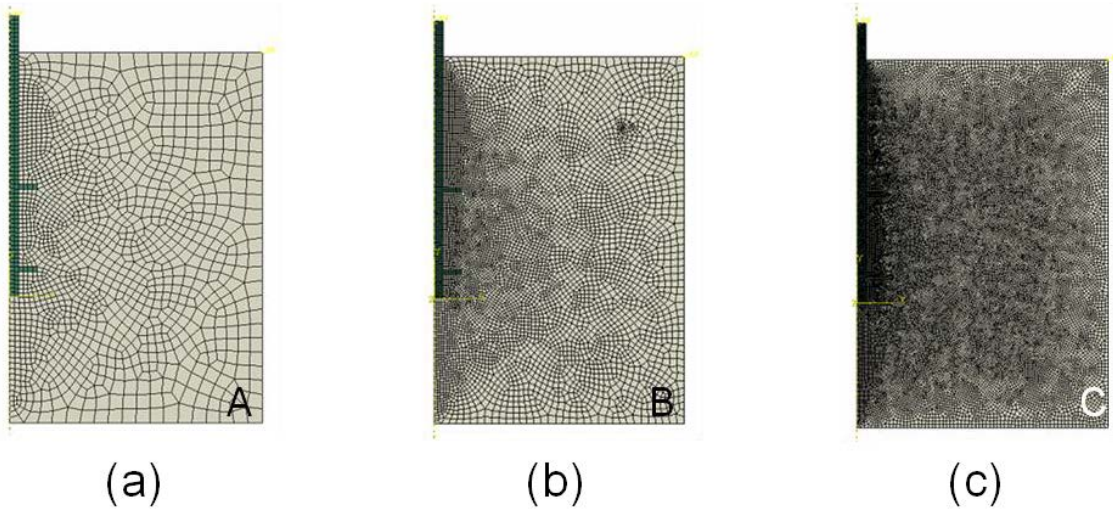
Figure 5-6. Measured and calculated axial load vs. displacement curves of selected piles in tension from test series: (a) WL01; and (b) WL02. Results are presented in the prototype scale.

Table 5-3. Input soil parameters for the numerical modeling

Test series	Loading Type	s_u (kPa)	E_u (MPa)	E_u/s_u	ν	γ (kN/m ³)
WL01	Compression	40	12.6	315	0.4	18.0
	Tension	36	11.5	319		
WL02	Compression	120	29.3	244	0.49	18.4
	Tension	90	24.4	270		

5.3.3 Mesh Size Evaluation

For finite element analyses, the mesh size can substantially affect the accuracy of the simulation and computational time. Moreover, remeshing is the most time-consuming procedure of RITSS approach. Therefore, an optimized mesh size can significantly improve the computational efficiency without compromising to simulation accuracy. The mesh dimensions were varied for P2C test of WL01 to examine the total analysis time and computed load displacement curves. The length of the finest soil element between the helices was set to be 20%, 10%, and 5% of the helix radius (r_h) when seeding the geometry edges. Notably, the actual mesh length of the seeded edges was automatically rounded according to the total length of each edge. The coarser elements in the far field were proportionally generated following the same meshing strategies. Three mesh sizes are presented in Figure 5-7.



Computational time

A: 1.2 h

B: 3.1 h (adopted mesh size)

C: 24.7 h

Figure 5-7. Evaluation of the mesh size effect: (a) Mesh A where finest mesh length $\approx 20\% r_h$, (b) Mesh B where finest mesh length $\approx 10\% r_h$, and (c) Mesh C where finest mesh length $\approx 5\% r_h$, and (d) computed axial load-displacement curves with varied mesh sizes. Note: r_h = radius of helix.

The computed load-displacement curves show a notable discrepancy between Mesh A and B but a negligible difference between Mesh B and C. However, the computational time demonstrates a fast increase as the mesh becomes denser. Because of the huge computational time input to Mesh C but trivial accuracy improvement compared with Mesh B, Mesh B is selected for the following

analyses. The computer used for this study has a 4-core i5-3470 CPU @ 3.20 GHz but only three cores were occupied with a memory of 8 GB.

To examine the effectiveness of RITSS in simulating axially loaded piles subjected to a large displacement, a standard Lagrangian (or small-strain) analysis was performed with the load-controlled method. The analysis was aborted due to convergence error at the vertical settlement equal to 3.8% of D due to large distortion of soil elements. A deformed mesh produced by the RITSS technique at the equivalent pile displacement is extracted for comparison as shown in Figure 5-8. The geometry deformation in Figure 5-8 is magnified by ten times for a better view. The distortion of the soil elements around the helix edges highlighted by rectangular boxes shows a vast contrast between the standard Lagrangian analysis and RITSS. It implies that the calculation of standard Lagrangian method highly depends on the previous deformation of geometries, whereas the RITSS approach eliminates the accumulative strain with periodical mesh updating and field mapping.

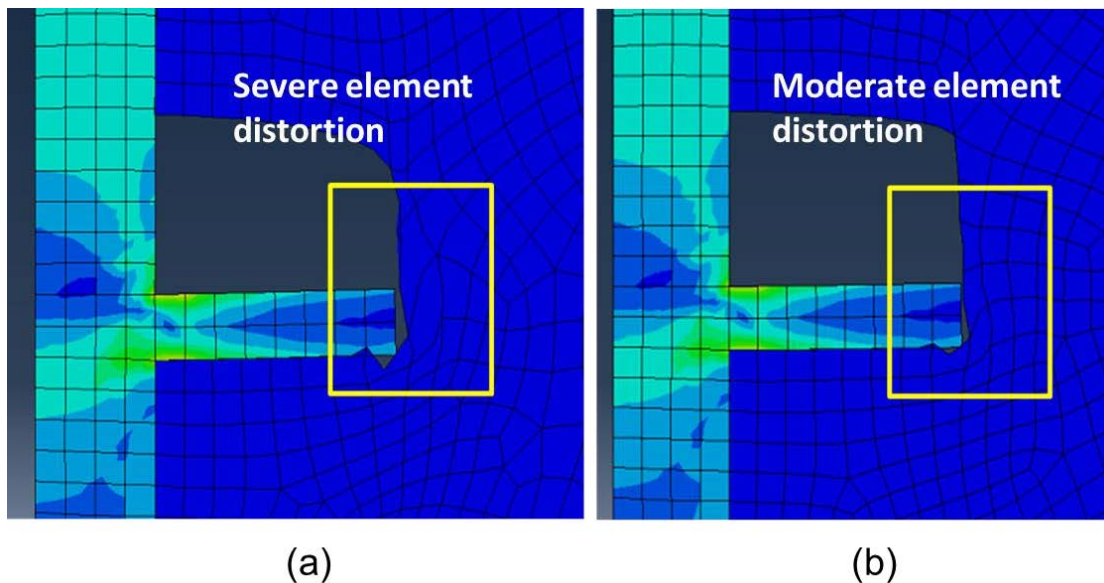


Figure 5-8. Comparison of exaggerated mesh distortion from the finite element analyses using two techniques: (a) the standard Lagrangian method and (b) RITSS

5.3.4 Examination of Boundary Effects

Bottom and side boundary effects may considerably affect the results of centrifuge model tests of piles. The spacing (d_{base}) between the bottom helices and the container base, which equals $2.8 D$, may not be sufficiently large to eliminate bottom boundary effect. The rigid container base enhances the rigidity of the soil below the lower helices thus increases the bearing resistances. The width of the soil domain (R_s) also needs to be examined to clarify the pile-to-pile interaction.

For the effect of container base, d_{base} was increased by three increments of $1 D$ in the numerical model to produce load-displacement curves accordingly for P2C and P3C in WL01. Figure 5-9 shows the computed curves corresponding to the increased d_{base} . The early phases of the load vs. displacement curves were not affected, but the ultimate bearing capacities decreased as d_{base} increased. In addition, the decrement of ultimate bearing capacity corresponding to the increment of spacing is smaller at larger total spacing. The boundary effect diminishes as the spacing approaches $5D$ and achieves an ultimate loss of ultimate capacity about 20%.

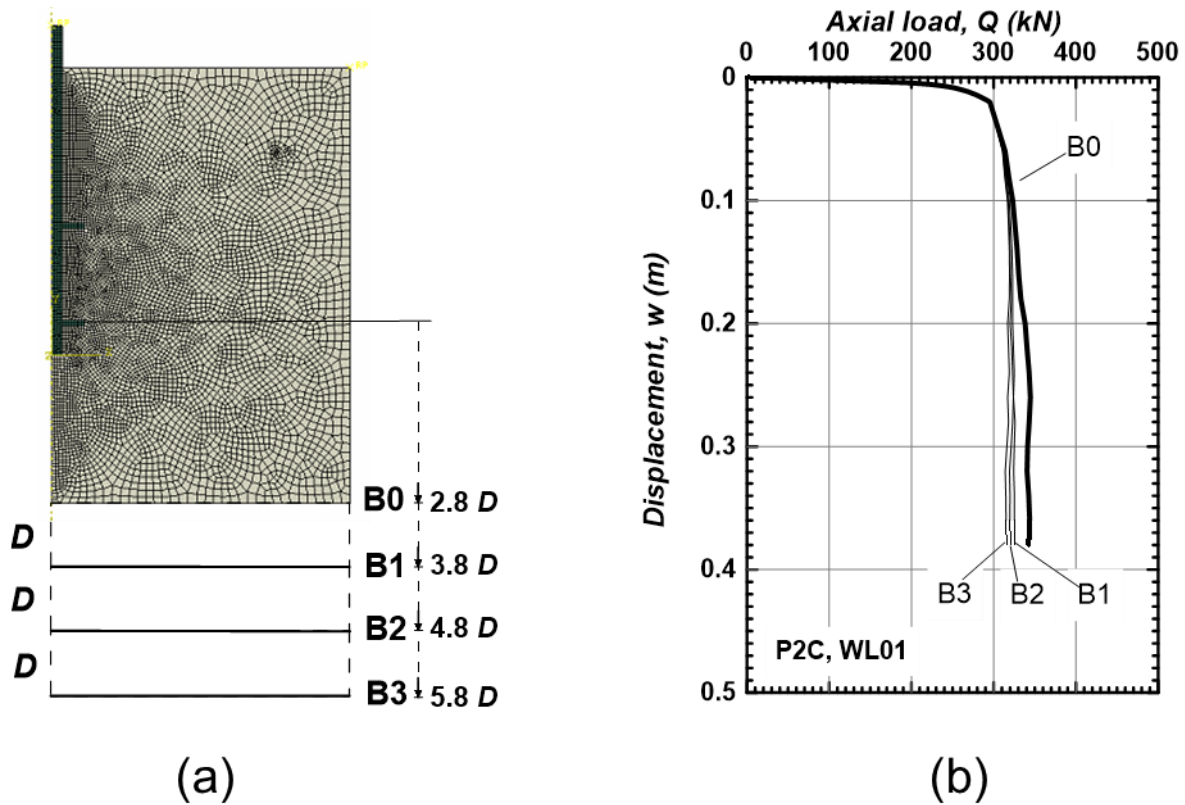


Figure 5-9 Examination of bottom boundary effect: (a) illustration of bottom boundaries at B0 to B3, where $d_{\text{base}}/D = 2.8$ for B0 and $d_{\text{base}}/D = 5.8$ for B3; and (b) effects of bottom boundary on the axial load vs. displacement curves of P2C in WL01. Note: d_{base} = spacing between the bottom helix and the container base; B0 is the actual boundary in the centrifuge tests and the adopted boundary for following LDFE analyses.

To examine the effect of soil width, R_s was varied from 2.5 to 4.2 to generate load-displacement curves accordingly for P2C in WL01. Since the model piles were tested sequentially one after another, the neighboring pile rather than the vertical center line is treated as the boundary condition. The effects of a neighboring pile on a test pile should be significantly less than that of a rigid vertical wall. The actual pile-to-pile spacing in the centrifuge load tests was $4.2 D$ and the examined soil widths are presented in Figure 5-10. As the restrained right edge of the soil moves towards the far field from $R_s = 2.0$, the axial resistance of P2 decreases significantly in the

beginning, which demonstrates a significant soil width effect. However, as this boundary approaches $R_s = 3.2$, the influence on the pile resistance diminished rapidly. A minor change of pile resistance was observed between the width of $3.2 D$ and $4.2 D$, which indicates a negligible pile-to-pile interaction in the centrifuge model tests, where $R_s = 4.2$. Hence, the following analyses were performed with $R_s = 4.2$.

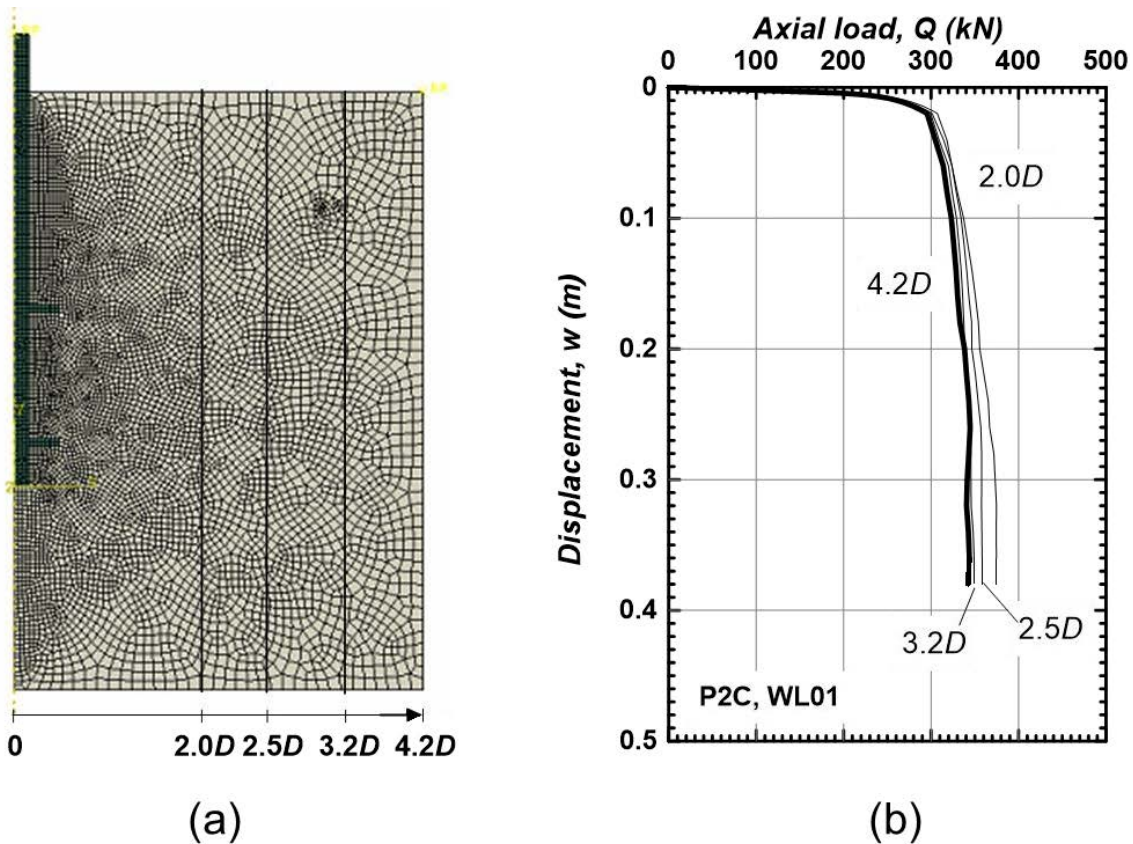


Figure 5-10. Examination of soil width effect: (a) illustration of the varied soil side boundary, and (b) computed load-displacement curves of P2C in WL01. Note: the spacing in the centrifuge test layout was $4.2 D$; this soil width was adopted in the analyses presented in following sections.

5.4 LDFE Results and Discussions

With the validated LDFE analysis method, a series of simulations were carried out to assess the behavior of double-helix piles in clay. In all the following analyses, d_{base} and R_s were selected to be $2.8 D$ and $4.2 D$, respectively, to ensure a fair comparison with the experiment results.

5.4.1 Failure Modes

In previous studies in the literature, it was observed that the inter-helix soil moves as a cylindrical body when S_r decreases to S_{rc} . Although direct observation of failure surface was limited in the literature (Rao et al., 1991), back calculations based on soil properties and axial load distributions have been conducted to approximate the potential failure mode (refer to examples in Gavin et al., 2014; Li et al., 2018; Lanyi-Bennett and Deng, 2019b). Discrepancies between the predicted and observed failure modes have been also noted and the cause was simply attributed to the soil disturbance or field soil heterogeneity (for example, as observed in Lutenegger, 2009; Elkasabgy and El Naggar, 2015). Perko (2009) reported significant overestimation of axial capacity of helical piles when adopting an inappropriate failure mode, which highlighted the significance of failure mode investigation.

The progressive mobilization of failure mode starting from the initial pile displacement is important for building a comprehensive understanding of the development of the inter-helix slip surface. Figure 5-11 shows the contours of equivalent plastic strain (PEEQ) of P2 WL01 under compression at selected critical pile displacements (w) where the failure mode forms. The pile displacements are normalized to the helix diameter D . PEEQ contour implies the location of slip surface in the soils thus demonstrates the failure mode of helical piles. At the initial pile displacement of $w/D = 2.6\%$ (Figure 5-11a), an inter-helix soil cylinder has not emerged yet. The potential slip surfaces tend to gain plastic strain at the boundaries of the rigid soil body created by

the helices. As w/D increases to 7.9% (Figure 5-11b), a vertical plastic strain band extends from the edge of the upper helix to the edge of the lower helix, i.e., an inter-helix soil cylinder shows up. Afterwards, as the pile continues to penetrate, the soil cylinder remains unchanged and CSM controls the behavior of this pile.

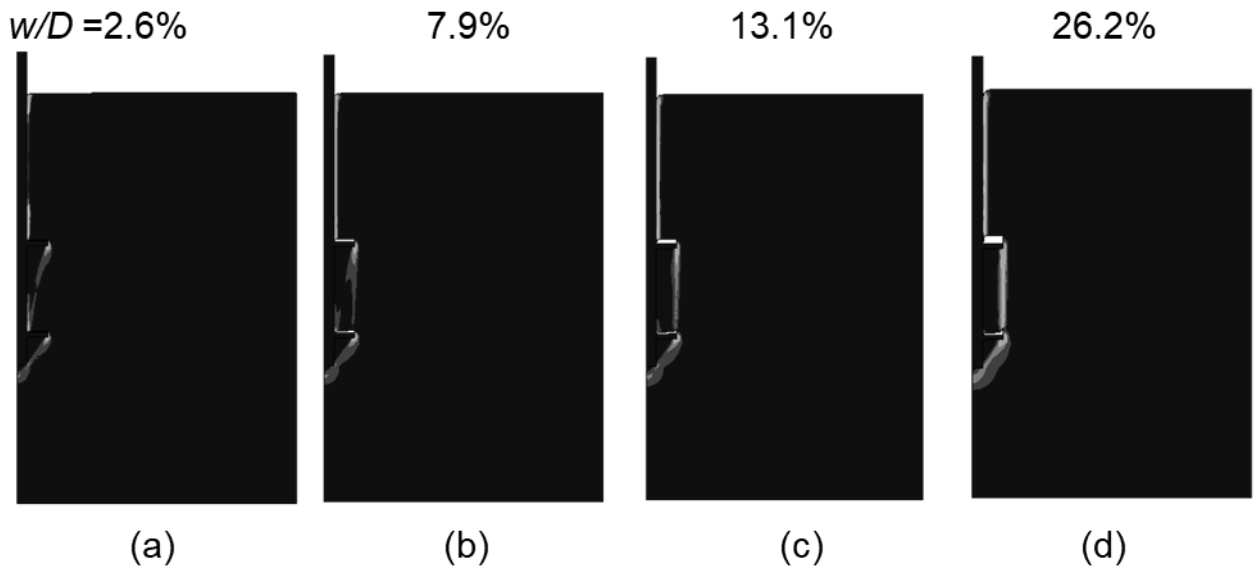


Figure 5-11. PEEQ contours of P2 at downward pile displacements $w/D =$ (a) 2.6%, (b) 7.9%, (c) 13.1%, and (d) 26.2%. Note: $S_r = 1.5$, $s_u = 46$ kPa.

When S_r increases to 2.5 for P3, the progressive failure mechanism shows a significant difference. Figure 5-12 shows the PEEQ contours of P3 at selected critical pile displacements. Figure 5-12 shows an increasing width of plastic deformation zone at the shaft surface along with the increase of pile displacement. Before reaching the displacement of 31.5%, the inter-helix soil slip surface forms a smooth cone-shaped plastic zone. After that, Figure 5-12c shows a tip extending downward to the elastic soil field from the cone-shaped plastic zone. This tip, as a second slip surface in the helix space, extends further as the displacement increases and creates a greater rigid soil body beneath the helix. Eventually, TFM may appear.

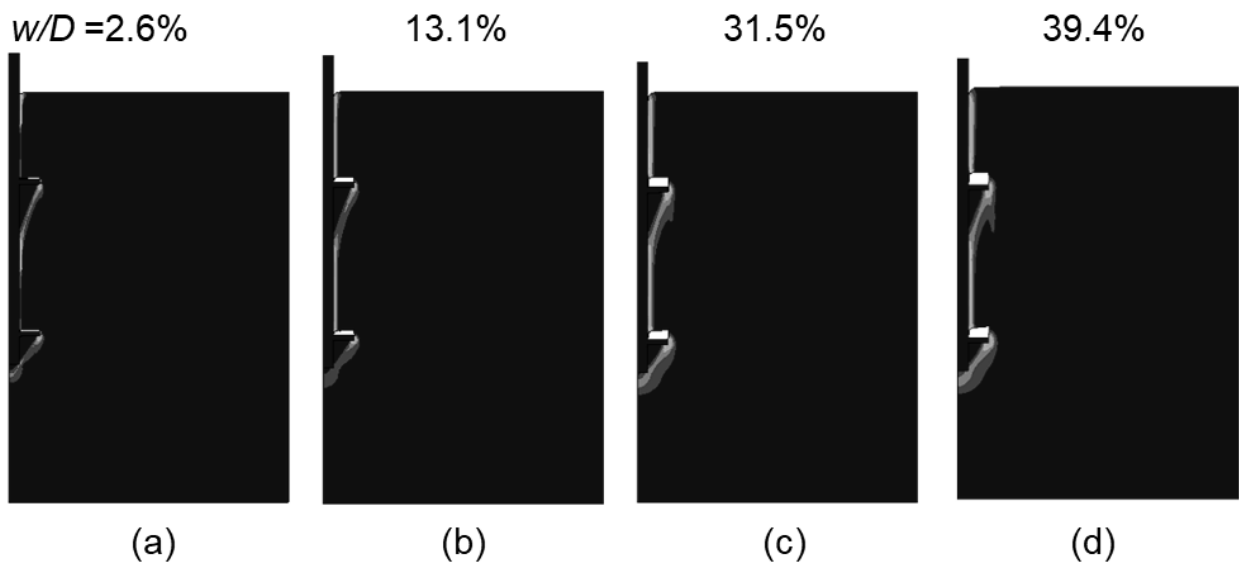


Figure 5-12. PEEQ contours of P3 at downward pile displacements $w/D =$ (a) 2.6%, (b) 13.1%, (c) 31.5%, and (d) 39.4%. Note: $S_r = 2.5$, $s_u = 46$ kPa.

For P4 with $S_r = 3.5$, as shown in Figure 5-13, no second slip surface (like the one for P2 or P3) is observed before a large displacement of $w/D = 52.5\%$. The plastic zones beneath the two helices extends in the direction perpendicular to the free surface of the rigid soil wedge contained by the helices. The behavior of the upper helix opposed no impact on the inter-helix soil out of its vicinity, which means IBM is present.

These simulation results are considered consistent with the observation of the failure modes in the centrifuge model tests. The mobilization of failure mechanisms of the double-helix piles with various inter-helix spacing are appropriately described by the PEEQ contours.

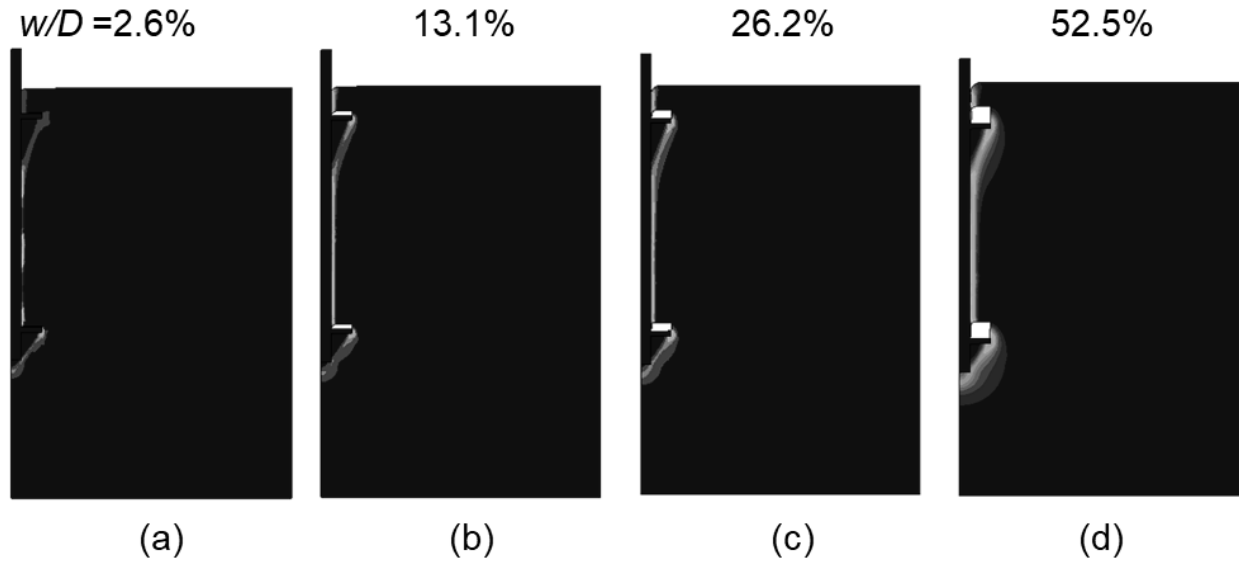


Figure 5-13. PEEQ contours of P4 at downward pile displacements $w/D =$ (a) 2.6%, (b) 13.1%, (c) 26.2%, and (d) 52.5%. Note: $S_r = 3.5$, $s_u = 46$ kPa.

5.4.2 Helix Bearing Resistance

In general, helical plates provide most of the total axial capacity of helical piles. The plate bearing factor N_t and uplift break-out factor N_b in clay depend on the ratio of plate embedment depth to the helix diameter according to Meyerhof (1976) and numerous studies. The previous analysis of the axial load distributions suggested that the bearing factor and uplift factor of the lower and upper helices, respectively, are not affected by the inter-helix stress zone. However, the inter-helix plate capacity factor is likely affected by the inter-helix stress zone.

In the present analysis, N_t and N_b are defined as follows:

$$N_t = 4Q_{cu_helix}/[\pi(D^2-d^2)] \quad (5-2)$$

$$N_b = 4Q_{tu_helix}/[\pi(D^2-d^2)] \quad (5-3)$$

where Q_{cu_helix} is the differential load at the limit state between two horizontal shaft cross-sections located at 0.1 m (about 13% of D) above and below a helix for compression analyses, and Q_{tu_helix} for tension analyses. Both Q_{cu_helix} and Q_{tu_helix} were obtained using Equation 5-2 based on pile

element stresses. The reason for the selection of these two shaft cross-sections 0.1 m away from the helix is to avoid the concentrated element stress near the corner of the helix and shaft.

Figure 5-14 shows the normalized bearing or uplift pressure of the selected helical plates. The pressure q_h was normalized by s_u at the helix level. The normalized pressure for helices of P2 is, in nature, the resultant shear force acting on the soil cylinder. The LDFE calculation is close to the calculation of conventional theories, i.e., Equation 5-5:

$$Q_{cyl} = \pi D S s_u \quad (5-4)$$

The bearing factor $N_t = q_h/s_u$ of the lower helix in the stiff clay is about 9.5, which is close to the value of 9.0 generally suggested for pile toe bearing capacity. Several tests in the medium clay (Figure 5-14a) showed the hardening behaviour and approached an N_t value of 10.5 owing to the rigid boundary effect of container base. For the upper helices of P3 in compression, the bearing factor is around 4. According to Terzaghi's bearing capacity equation for shallow footing, the bearing factor for a circular shallow foundation at the ground surface is 5.14 and this factor increases with depth. A number of studies, e.g., Meyerhof (1976) and Das (1980) agreed that a plate capacity factor increases with embedment depth until a certain critical point. For P3, by assuming no interaction exists between the two helices, a conservative estimation of the bearing factor for their upper helices is 6.0. In another word, the bearing capacity of the upper helix of P3 is reduced by the lower helix that penetrates downwards and leaves a weakened soil with undermined vertical support for the upper helix. Similarly, for the lower helices of the P3 pulled out of the clay, their break-out factors were also reduced by the upper helices, which caused a heave of the soil above. The N_b value around 4.3 is approximately equal to the recommended value (by Bhatnagar 1969 for medium clay and Adam and Hayes 1967 for stiff clay) for a circular anchor

embedded at $2.3 D$ below ground surface, which is close to the embedment depth of the lower helix ($3.9 D$) minus the depth of the soil above the upper helix ($1.4 D$).

In summary, the existing design methods that simply apply the capacity factors, developed for a pile toe or a single anchor, to the helical plate of a multi-helix pile may be inappropriate. Modification may be performed by taking the embedment depth and failure mode into consideration.

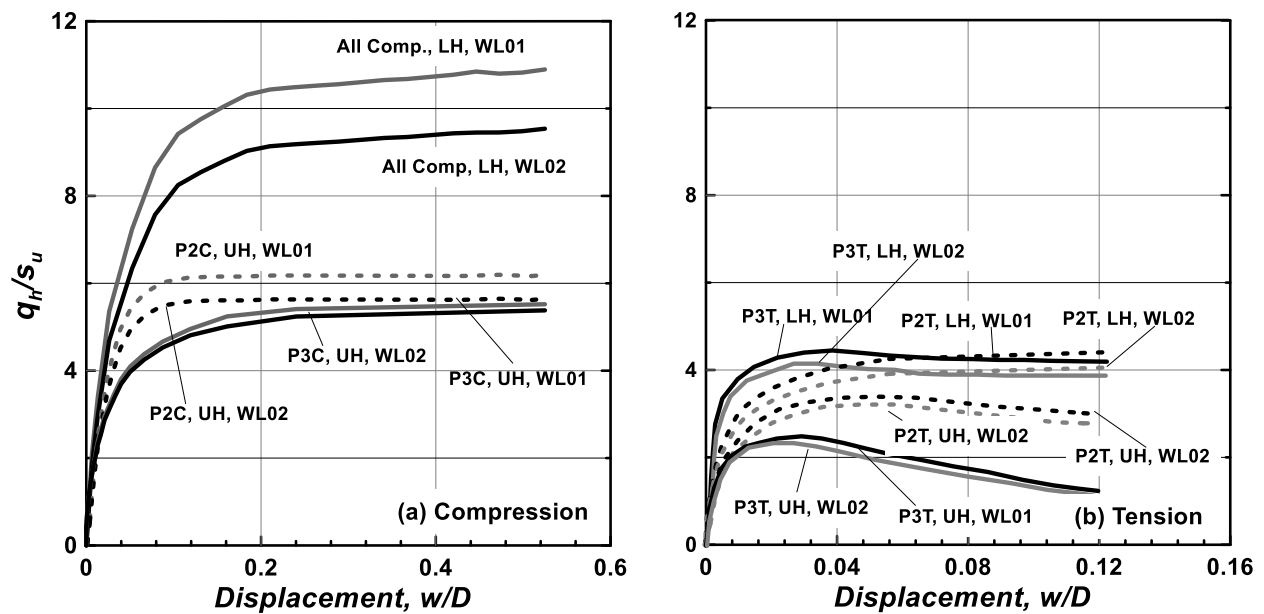


Figure 5-14. Normalized helix resistances vs. normalized axial displacement of selected piles from LDFE analyses: (a) compression tests, and (b) tension tests. Note: LH = lower helix, UH = upper helix.

5.4.3 Shaft Resistance Affected by Helix

Figure 4-16 shows the progress of shaft resistance mobilization. Segment A, B and E showed a softening behavior of the shaft resistance behind a shielding helix. Figure 5-15 shows the soil-shaft contact state after a large pile displacement. According to Figure 5-15, the soil-shaft slipping behind the helix reduced the contact area of Segment A and E, which resulted in a softening

behavior. As for Segment B, which is beyond the slipping area, the shaft resistance might be affected by the soil-shaft separation extending upward. This separation might be caused by the lateral soil displacement initiated in the vicinity of the shielding helix. For finite element analyses in ABAQUS with contacts involved, the contact interaction must be adjusted with a predefined clearance between the two contact surfaces. This clearance is a small absolute value of distance that the solver uses to determine if the separation occurs. In the present simulation, this clearance was set to be 0.5 mm. However, our understanding of such clearance is very limited. Therefore, the length of separation soil-shaft contact generated by the present LDFE models might not be of qualitative practical use. To perform a safe design in practice, the separation should be “over predicted”.

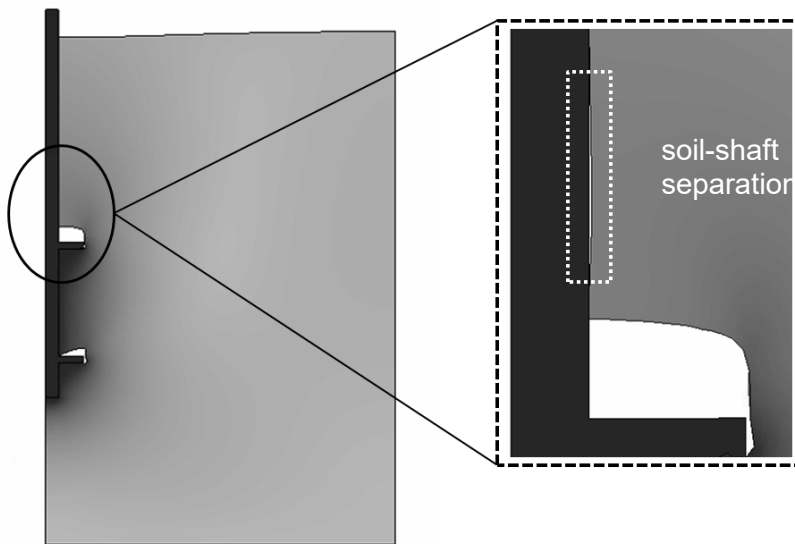


Figure 5-15. Soil-shaft separation caused by the neighboring cylindrical shear stress zone (P2C, WL01)

5.5 Parametric Studies


The advantage of LDFE for the prediction of Q_u of multi-helix piles is that there is no need to assume any failure mechanisms in advance; in contrary, the semi-theoretical methods such as the

cylindrical shear and individual bearing method must adopt the equations corresponding to the assumed FM to produce Q_u . The spacing between helices is of great interest to helical pile manufacturers as the ultimate uplift capacity of multi-plate anchors is sensitive to the plate spacing. From the available studies in the literature, it may be concluded that the axial failure mode of multi-helix piles varies with S_r , pile embedment depth, and soil types. Merifield (2011) noticed a phase of transitional failure when S_r was varied near 2.0 for a pile model in a clay soil with $s_u = 50$ kPa. However, this observation was based on the lower bound FE approach that did not allow a large displacement, and consequently the slip surface of the TFM inter-helix soil was not well developed.

In Section 5.3, the adopted LDFE approach has been validated against the centrifuge test results and by necessary discussions on various boundary conditions. In this section, a series of LDFE results is presented to show the failure mode of double-helix piles subject to a wider range of S_r and s_u values. The helix embedment depth ratio E_H , which is the ratio of helix embedment depth to helix diameter D , was also varied in the analyses to examine the effect of depth on the soil-pile failure mode. The embedment depth ratios are represented by the depth of the lower helix (E_{HL}) or upper helix (E_{HU}).

For the present analyses, S_r was varied from 1.25 to 3.5, s_u ranged from 20 to 120 kPa, E_{HL} ranged from 3.9 to 5.9, and $E_{HU} = 7.4$. Table 5-4 shows the matrix of the parametric study. These varied inputs were intended to cover typical inter-helix spacing and soil strength. Over 180 simulations in total were performed with S_r and s_u varying between the aforementioned values. The E_u/s_u values corresponding to the various input s_u were linearly interpolated between the verified boundary E_u/s_u values, i.e., 310 for WL01 and 235 for WL02.

Table 5-4. Simulation matrix for the parametric studies

	Helix embedment depth ratio	s_u (kPa)					
		20	46	60	80	100	130
S_r							
1.25	$E_{HL} = 3.9,$ for lower helix	FE0120A	FE0140A	FE0160A	FE0180A	FE01100A	FE01120A
1.5		FE0220A	FE0240A	FE0260A	FE0280A	FE02100A	FE02120A
1.75		FE0320A	FE0340A	FE0360A	FE0380A	FE03100A	FE03120A
2.0		FE0420A	FE0440A	FE0460A	FE0480A	FE04100A	FE04120A
2.25		FE0520A	FE0540A	FE0560A	FE0580A	FE05100A	FE05120A
2.5		FE0620A	FE0640A	FE0660A	FE0680A	FE06100A	FE06120A
2.75		FE0720A	FE0740A	FE0760A	FE0780A	FE07100A	FE07120A
3.0		FE0820A	FE0840A	FE0860A	FE0880A	FE08100A	FE08120A
3.25		FE0920A	FE0940A	FE0960A	FE0980A	FE09100A	FE09120A
3.5		FE1020A	FE1040A	FE1060A	FE1080A	FE10100A	FE10120A
1.25	$E_{HL} = 5.9,$ for lower helix	FE0120B	FE0140B	FE0160B	FE0180B	FE01100B	FE01120B
1.5		FE0220B	FE0240B	FE0260B	FE0280B	FE02100B	FE023120B
1.75		FE0320B	FE0340B	FE0360B	FE0380B	FE03100B	FE03120B
2.0		FE0420B	FE0440B	FE0460B	FE0480B	FE04100B	FE04120B
2.25		FE0520B	FE0540B	FE0560B	FE0580B	FE05100B	FE05120B
2.5		FE0620B	FE0640B	FE0660B	FE0680B	FE06100B	FE06120B
2.75		FE0720B	FE0740B	FE0760B	FE0780B	FE07100B	FE07120B
3.0		FE0820B	FE0840B	FE0860B	FE0880B	FE08100B	FE08120B
3.25		FE0920B	FE0940B	FE0960B	FE0980B	FE09100B	FE09120B
3.5		FE1020B	FE1040B	FE1060B	FE1080B	FE10100B	FE10120B
1.25		FE0120C	FE0140C	FE0160C	FE0180C	FE01100C	FE01120C
1.5		FE0220C	FE0240C	FE0260C	FE0280C	FE02100C	FE023120C
1.75		FE0320C	FE0340C	FE0360C	FE0380C	FE03100C	FE03120C

2.0	$E_{HU} = 7.4,$ for upper helix	FE0420C	FE0440C	FE0460C	FE0480C	FE04100C	FE04120C
2.25		FE0520C	FE0540C	FE0560C	FE0580C	FE05100C	FE05120C
2.5		FE0620C	FE0640C	FE0660C	FE0680C	FE06100C	FE06120C
2.75		FE0720C	FE0740C	FE0760C	FE0780C	FE07100C	FE07120C
3.0		FE0820C	FE0840C	FE0860C	FE0880C	FE08100C	FE08120C
3.25		FE0920C	FE0940C	FE0960C	FE0980C	FE09100C	FE09120C
3.5		FE1020C	FE1040C	FE1060C	FE1080C	FE10100C	FE10120C

Note: The coding of simulation ID consists of a header “FE”. Following the header, a space ratio tag varying from 01 to 10 represents S_r ranging from 1.25 to 3.5. Behind the space ratio tag, a nominal s_u value (in kPa) varies from 20 to 120.

5.5.1 Effect of Embedment Depth on Failure Mode

The failure modes of inter-helix soil can be determined by reviewing the PEEQ contour maps. Figure 5-11, Figure 5-12 and Figure 5-13 exhibit three types of failure modes: CSM, TFM, and IBM. In this section, the effect of E_H , S_r , and s_u on the failure modes are discussed respectively.

The embedment depth of the helical piles is one of the key factors that affect the bearing capacity of a pile toe and the uplift capacity of a single soil anchor. However, its impact on the inter-helix failure mode of multi-helix piles remains unknown. Figure 5-16 shows the variation of PEEQ maps for varied E_{HU} of P3C in the medium stiff clay with $s_u = 40$ kPa at the pile displacement of 25% D . It seems that the plastic strain zone gradually extends out of the cone-shaped area as the embedment depth increases. Accordingly, the failure mode evolves from TFM into CSM as E_{HU} grows from 1.4 to 6.4. Figure 5-16d demonstrates an approximately cylindrical inter-helix soil body bounded by the second slip surface. This second slip surface is slightly different from the vertical PEEQ band observed in Figure 5-11 for P2 with $S_r = 1.5$. Nonetheless, the author may claim that a greater embedment depth of double-helix piles facilitates the formation of a complete

inter-helix soil cylinder. A possible cause of such transition of failure mode may owe to the increasing confining stress with the increasing soil depth that enhance the capability of inter-helix soil to act as an integral body during the axial displacement.

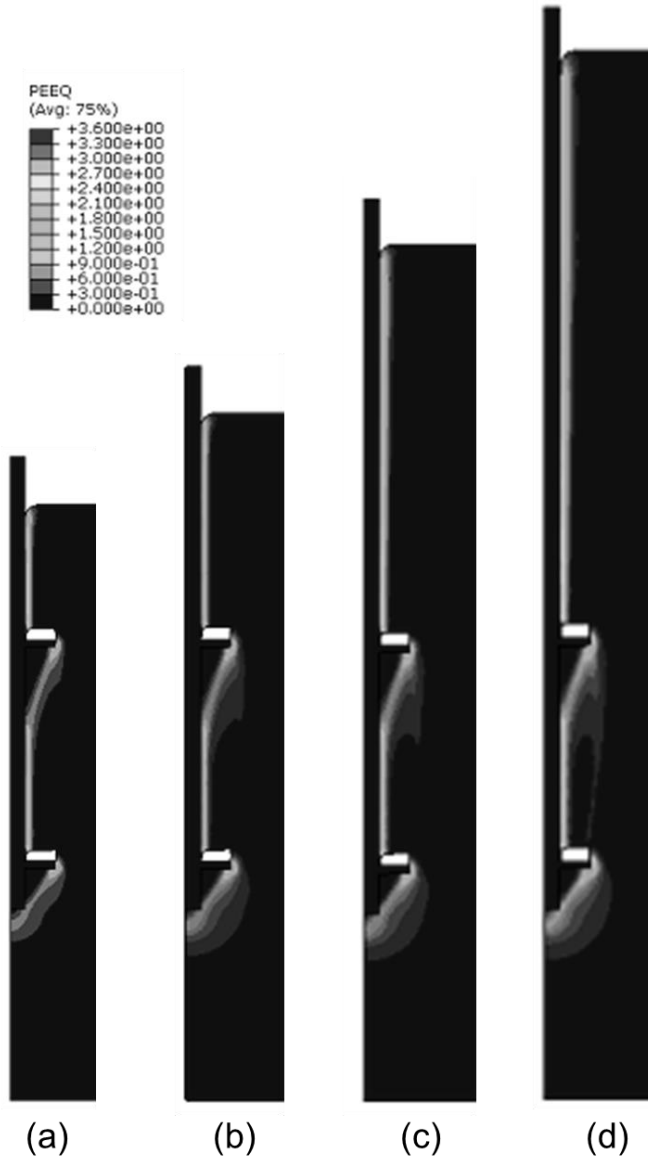


Figure 5-16. Effect of embedment depth on the axial failure mode of a compressive pile in the parametric study. In this series of simulations, $S_r = 2.5$, $s_u = 40$ kPa. Ratio of the embedment depth ratio of upper helix to helix diameter is: (a) 1.4, (b) 2.4, (c) 4.4, (d) 6.4.

5.5.2 Effect of Soil Strength and Space Ratio

The effect of S_r on the failure modes can be evaluated from Figure 5-11 to Figure 5-13. It implies that as S_r increases, the failure mode may evolve from CSM into TFM and eventually IBM when the inter-helix spacing is sufficiently big. Figure 5-17 shows more results of selected PEEQ contour maps with various S_r , s_u , and loading directions.

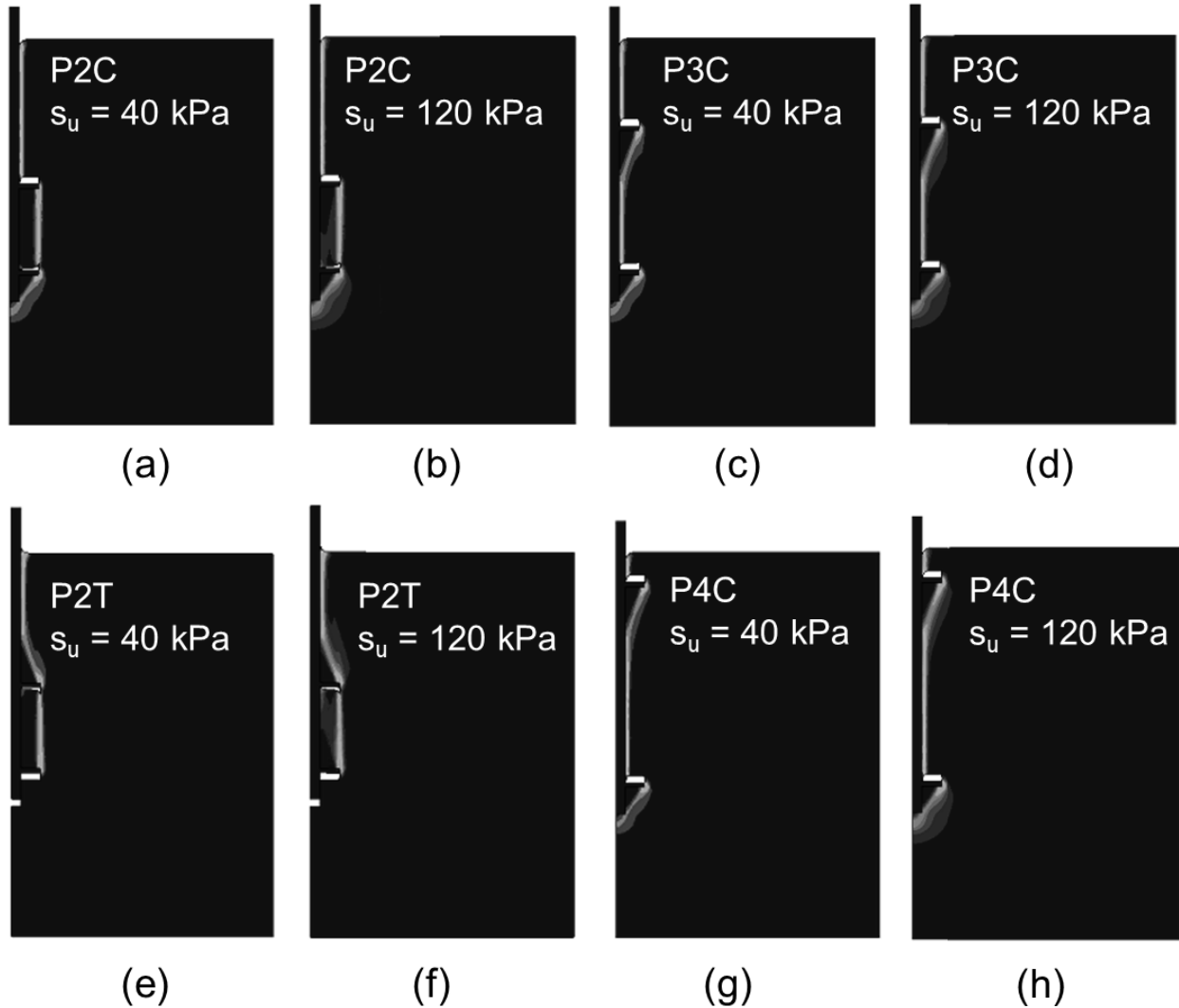


Figure 5-17. PEEQ contour maps of selected simulations with various soil strength, space ratio, and loading direction. Note: normalized pile displacement $w/D = 25\%$.

Figure 5-17 shows that the FM evolves from CSM to IBM as S_r increases regardless of soil strength or loading directions. Notably, the plastic zones in the soils with $s_u = 120$ kPa spread further than the plastic zones in the soils with $s_u = 40$ kPa. This soil behavior results in a further slip surface to be mobilized by the helix in the soil with greater s_u . The comparison between the two soil masses remained on the lower helices of P3 shown in Figure 5-4a and b conforms to this statement. Figure 5-17c and d also reflect the effect of s_u on the failure mode: TFM for $s_u = 40$ kPa and IBM for $s_u = 120$ kPa.

5.5.3 Summary of Effects of S_r , E_H , and s_u on Failure Mode

Figure 5-18 showed the failure modes observed from the simulation results with all combinations of S_r , E_H , and s_u . Based on the observation of PEEQ contours at $w/D = 25\%$, the mode of failure changes gradually from CSM to IBM with an increasing inter-helix spacing, decreasing E_H , or decreasing soil strength. CSM occurs when the space ratio is adequately small and the shear strength of the clay is sufficiently big. As the space ratio exceeds 3.0, only IBM is expected for such double-helix piles in clay. The zone occupied by TFM in Figure 5-18a for the smaller embedment depth is bigger than the equivalent zone in for the greater embedment depth shown in Figure 5-18b and Figure 5-18c, which indicates that the greater embedment depth restricts the formation of TFM.

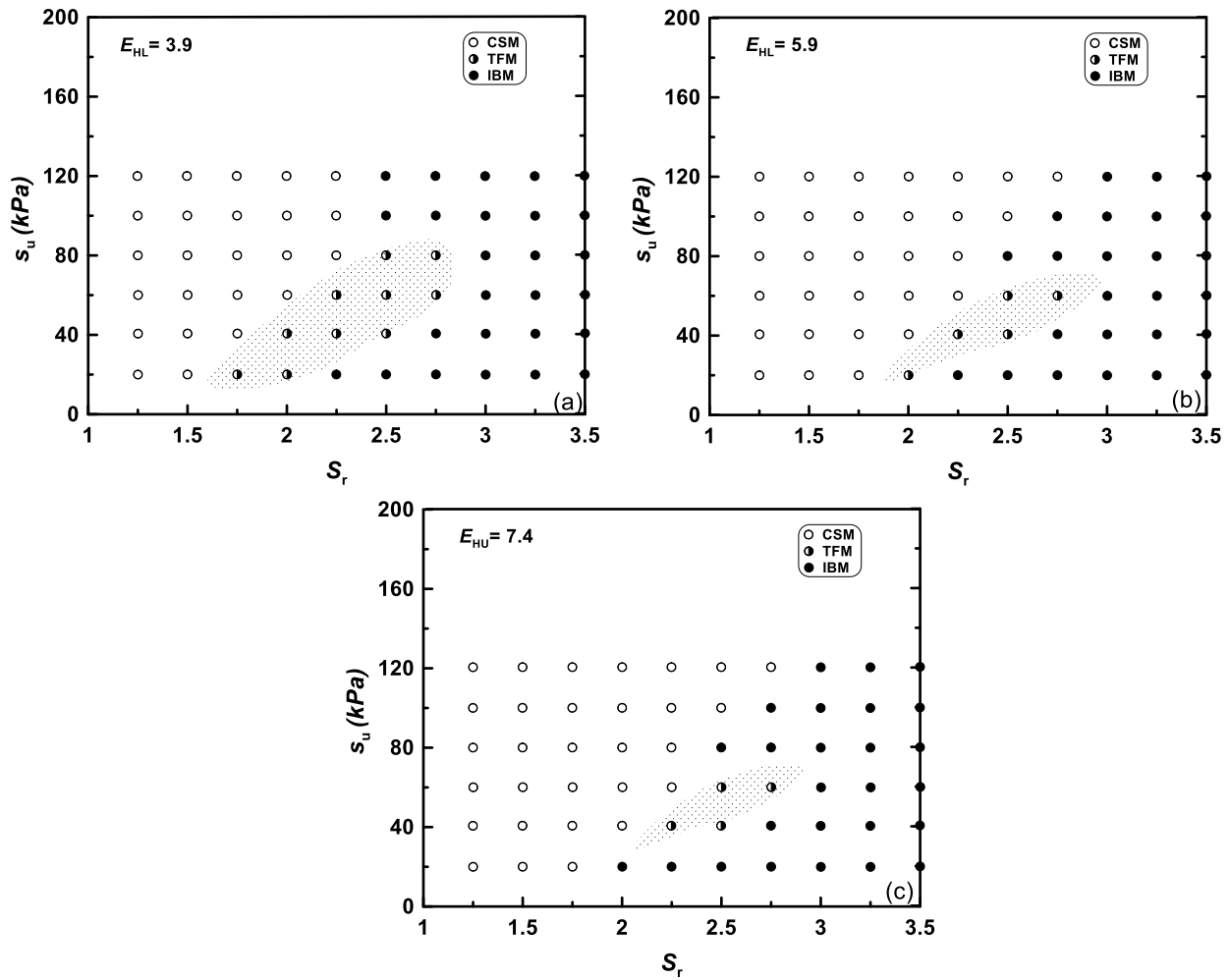


Figure 5-18. Summary of the parametric studies – failure modes of double-helix piles against s_u and S_r : (a) at $E_{HL} = 3.9$ adopted in the centrifuge model tests, (b) at $E_{HL} = 5.9$ adopted in the parametric study, and (c) at $E_{HU} = 7.4$ adopted in the parametric study.

5.5.4 Summary of Effect of Failure Mode on Helix Bearing Resistance

According to the IBM model, the plate spacing must be sufficiently large so that the soil displacements are contained mainly near each plate. The uplift capacity of each plate is independent of the existence of other plates. The capacity factor is varied with the embedment depth of each plate and the undrained shear strength of the clay (Das 1980). Chapter 4 reported a

considerable reduction of plate bearing capacity governed by TFM. In this section, the plate capacity factors are assessed for a wider range of s_u , S_r and E_H . For compressive loading, the bearing factors of the lower helices (LH) with $E_{HL} = 3.9$ and 5.9 and the upper helices (UH) with $E_{HU} = 7.4$ were selected to present; for tensile loading, the break-out factors of the lower helices with $E_{HL} = 3.9$ and 5.9 were selected.

The differential helical plate pressures were extracted from the FE results and normalized to the undrained shear strength to produce the helix capacity factors. To keep consistent between all possible failure modes in the analyses, the load carried by the whole inter-helix zone was used to produce the capacity factors when applicable. Specifically, for a tension loading, the entire inter-helix soil may contribute to the uplift capacity of the lower helix. Although it may not be true for IBM, the differential load between the lower sides of the two helices were adopted to cover the whole helix zone. For the upper helix under compression, similarly, the differential load between the upper sides of the two helices were adopted. Therefore, the capacity factors in this discussion are slightly different from conventional capacity factors for a single soil anchor or pile toe. Nonetheless, it can effectively reflect the axial resisting capability of such helical piles.

The selected results are presented in Figure 5-19. An increasing trend of N_b vs. S_r is observed in Figure 5-19a and Figure 5-19b for the piles sustained CSM; however, as CSM becomes invalid when S_r exceeds a critical value around 2.5, N_b decreases, regardless of embedment depth. In general, the greater embedment depth enhances the plate capacity factors no matter how s_u and S_r vary. A decreasing trend of N_b against s_u is also observed when the failure mode starts to gradually change from CSM to IBM. In engineering application, a large S_r that can sustain CSM may be cost-effective. But in the meantime, it may be unsafe when CSM turns out to be invalid. The N_b

factors presented in Figure 5-19a and Figure 5-19b may offer a viable optional consideration for the design of the uplift capacities of multi-helix piles.

The bearing factors of the lower helices remain essentially unchanged during the variation of s_u , S_r and E_H this parametric study. Therefore, the end bearing behavior of the lower helix is believed not to be affected by the inter-helix failure mechanisms. Figure 5-19e shows the end bearing factors of the upper helices that may be affected by the underlying failure modes. The N_t values increase almost linearly with S_r until CSM becomes invalid and IBM occurs. The degradation of N_t after this failure mode transition is much less than that of N_b shown in Figure 5-19a and Figure 5-19b may be attributed to the much deeper embedment depth. Because the N_b values were severely controlled by the thickness of the overlying soil and the heaving mechanisms caused by the upper helix.

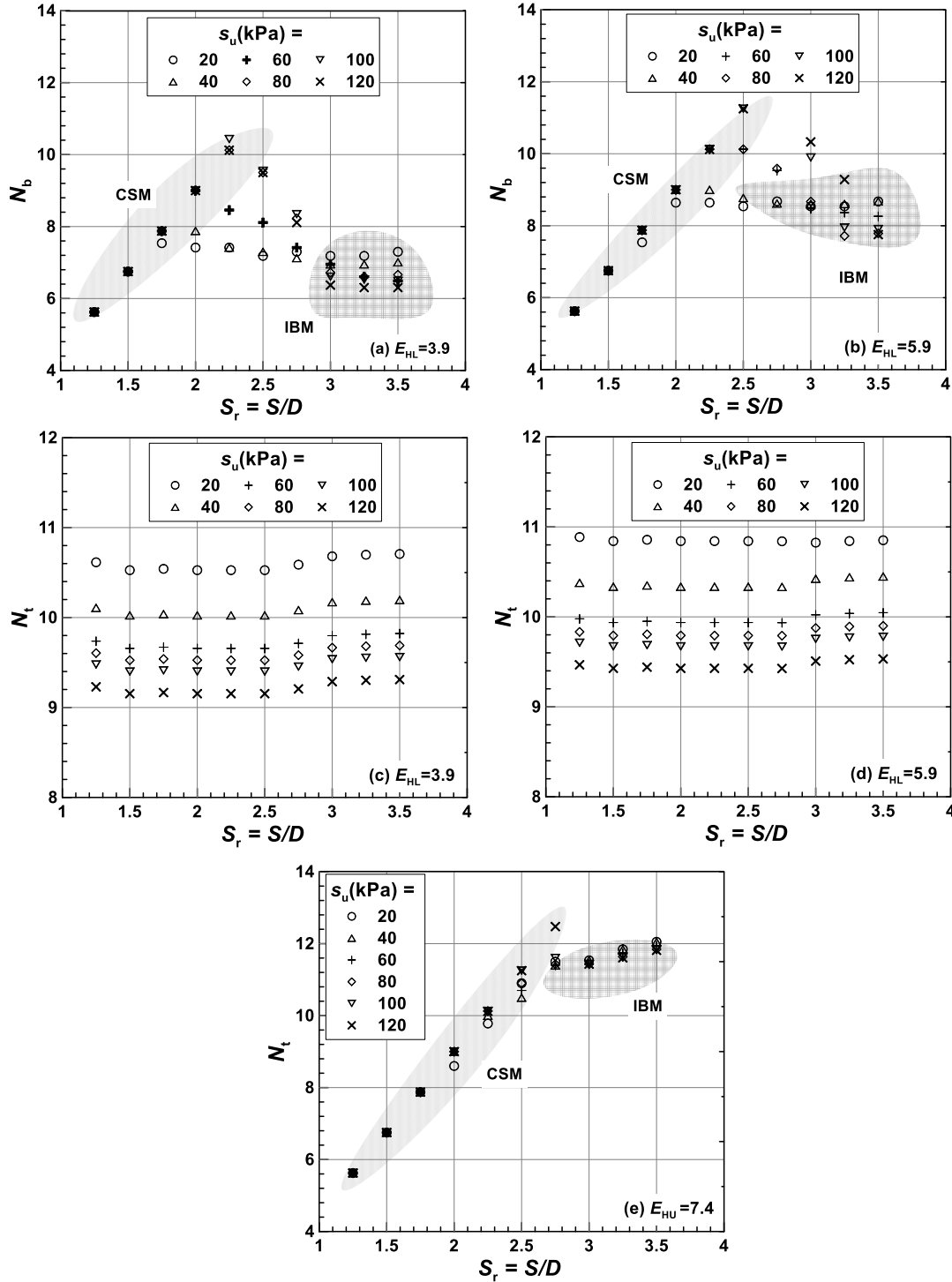


Figure 5-19. Summary of uplift break-out factors and compressive bearing factors of selected helices: (a) and (b) for break-out factors of lower helices, (c) and (d) for compressive bearing factors of lower helices, and (e) for compressive bearing factors of upper helices.

5.6 Conclusions

The failure mechanisms of three types of helical piles in two types of clay were simulated with a 2D axis-symmetric model abiding the RITSS approach. The effectiveness of the numerical model was verified by the comparison with available centrifuge model test results. A series of parametric study was thereafter conducted to investigate the effect of soil strength, pile embedment depth and inter-helix space ratio on the axial behavior of helical piles with varying S_r , s_u and E_H . A chart of failure mode is generated based on the parametric study and assessed with more than 120 simulations. The following conclusions can be drawn:

1. The LDFE model was able to predict the axial load vs. displacement curves of piles and the axial load distributions obtained from the centrifuge model tests. The LDFE approach exhibited an effective method, as opposed to Standard Lagrangian finite element method, for helical piles in cohesive soil when a large axial displacement was expected.
2. Contour maps of the equivalent plastic strain and total displacement suggested three potential failure modes for helical piles in cohesive soils. These failure modes are consistent with the observed modes from pullout tests after the centrifuge model tests. For CSM, the slip surface is located at the perimeter of the inter-helix cylindrical space; for TFM, the slip surface contains a cone-shaped continuous space; for IBM, the slip surfaces are located around independent helices.
3. The mode of failure changes gradually from CSM to IBM with an increasing inter-helix spacing and decreasing soil strength. CSM occurs when the space ratio is adequately small and the shear strength of the clay is sufficiently big. As the space ratio exceeds 3.0, only IBM is expected for such double-helix piles in clay.

4. The inter-helix soil tends to develop into a soil cylinder when the embedment depth increases. A possible cause of such transition of failure mode may owe o the increasing confining stress with the increasing soil depth that enhance the capability of inter-helix soil to act as an integral body during the axial displacement.
5. The helix break-out factors of lower helices change with the failure modes. In general, CSM provide greater optimal uplift capacity as the space ratio increases. However, a sufficiently large S_r may lead to an invalid CSM design. When S_r approaches 2.5, engineers should be careful to adopt CSM for axial capacity design. The bearing factors of the upper helices increase almost linearly with S_r until CSM becomes invalid and IBM occurs. The bearing factors of the lower helices remain essentially unchanged during the variation of s_u , S_r and E_H in this parametric study.

5.7 Limitations

The limitations of the present LDFE analyses are as follows.

1. A uniform clay domain is assumed in this numerical model that differs from the true gradient soil profile in the centrifuge model tests.
2. The bottom boundary effect was present in all FE analyses conducted. It may complicate the stress zone near the lower helices.
3. The soil was assumed weightless and hence the effect of confining stress on the generation of inter-helix failure surface remains unknown.
4. Installation induced reduction of soil strength was not considered in the analyses.

6 Conclusions, Limitations and Recommendations

6.1 Summary and Conclusions

A centrifuge test setup was successfully constructed for pile installation and axial loading tests on centrifuge. The installation torque and axial loads in the pile shafts can be measured by the pile instrumentations. The pore pressure change in the “stiff clay” can be monitored by the PPT’s installed at two different depths.

This innovative part of this centrifuge test setup is the intensive pile instrumentation coupled with effective data acquisition system. The in-flight real-time axial load distribution measurement is the first time realized in centrifuge model tests of helical piles. The in-flight soil investigation technique is not available in the present experiment method, but a quick vane shear test was used instead immediately before and after the spin-up and spin-down to obtain the s_u profile of the tested soils.

A centrifuge model test system has been developed with the capability to install and axially load helical piles in flight, and measure installation torque and axial load distributions. The axial behavior of three types of double-helix piles with S_r varying from 1.5 to 3.5 and one type of single-helix pile in two types of kaolinite clay. Sixteen pile installation and axial loading tests in two cohesive soil models have been accomplished. The installation torque, installation-induced excess pore pressure, and axial load transfer mechanisms were evaluated. LDFE analyses based on RITSS have been performed to explore the axial behavior of double-helix piles in clay for a wider range of inter-helix spacing ratio and soil strength. The effect of these two factors on the axial failure mode of double-helix piles in clay has been assessed in depth with FE analyses.

6.1.1 Experimental Study

A torque model that considers the residual strength distribution, shaft area, and helix area was developed. The model assumes that all of the clay-helix interface shearing performance is related to s_{ur} of clay. The model effectively predicted the installation torque profiles of 14 test piles.

The analytical solution developed by Randolph and Wroth (1979) was adopted to interpret the measured pore pressure response to pile installation in the stiff clay. The solution overestimated the maximum u but effectively predicted the major progress of dissipation. The installation-induced u was completely dissipated within 6 days in prototype scale. The results suggested that u was dominated by shaft-induced cavity expansion and the effects of helices may be neglected.

The u response at the pile surface was established using the validated analytical solution. This pore pressure decreased rapidly after pile installation. The long-term consolidation progress at the shaft surface was similar to the locations where the PPT's were installed. As such, the reading of a PPT installed within an appropriate distance can be used as an indicator of soil consolidation near the shaft surface.

The effect of soil strength on the failure modes of double-helix piles was observed and assessed. The observations suggested that a stiffer clay driven by helix is more likely to become a cylinder. A transitional failure mode, for which the soil failure zone was cone-shaped occurred at 2.5 of S_r in the medium clay of present test, implies that a unique S_{rc} that distinguishes IBM from CSM may not exist.

The end bearing or uplift capacities of the helical plates were reasonably well predicted by toe capacity or anchor capacity equations except for those affected by container base boundary effect and TFM. Specifically, IBM and CSM models may over-predict the axial capacity of a helical pile governed by TFM.

The shaft resistances agreed with the prediction assuming an adhesion factor of 1.0, but the shaft segments next to a helix exhibit very low resistance. Ineffective zones accounted for the observed low shaft resistances. The shear force outside of the ineffective zones was fully mobilized. The shaft adhesion within the ineffective zone was affected by loading directions and failure modes of helix zone.

6.1.2 LDFE Analyses

The failure mechanisms of three types of helical piles in two types of clay were simulated with a 2D axis-symmetric model abiding the RITSS approach. The effectiveness of the numerical model was verified by the comparison with available centrifuge model test results. A series of parametric study was thereafter conducted to investigate the effect of soil strength, pile embedment depth and inter-helix space ratio on the axial behavior of helical piles with varying parameters. A chart of failure mode is generated based on the parametric study and assessed with an extensive number of simulations.

The LDFE model was able to predict the axial load vs. displacement curves of piles and the axial load distributions obtained from the centrifuge model tests. The LDFE approach exhibited an effective method, as opposed to standard Lagrangian finite element method, for helical piles in cohesive soil when a large axial displacement was expected. These failure modes are consistent with the observed modes from pullout tests after the centrifuge model tests. For CSM, the slip surface is located at the perimeter of the inter-helix cylindrical space; for TFM, the slip surface contains a cone-shaped continuous space; for IBM, the slip surfaces are located around independent helices.

The mode of failure changes gradually from CSM to IBM with an increasing inter-helix spacing and decreasing soil strength. CSM occurs when the space ratio is adequately small and the shear

strength of the clay is sufficiently big. As the space ratio exceeds 3.0, only IBM is expected for such double-helix piles in clay. The inter-helix soil tends to develop into a soil cylinder when the embedment depth increases. A possible cause of such transition of failure mode may owe o the increasing confining stress with the increasing soil depth that enhance the capability of inter-helix soil to act as an integral body during the axial displacement.

The helix break-out factors of lower helices change with the failure modes. In general, CSM provide greater optimal uplift capacity as the space ratio increases. However, a sufficiently large S_r may lead to an invalid CSM design. When S_r approaches 2.5, engineers should be careful to adopt CSM for the axial capacity design. The bearing factors of the lower helices remain essentially unchanged when changing s_u , S_r and embedment depth in this parametric study.

6.2 Limitations

Based on the facts and assumptions made in the experimental preparation, centrifuge load tests and numerical simulations, the following limitations should be noticed:

- The rotational speed of the installation motor may have an uncertain impact on the installation torque. However, the output speed of the used motor cannot be altered.
- The in-flight soil investigation technique is not available in the present experiment method. Instead, a quick vane shear test was performed immediately before and after the spin-up and spin-down of each test stage to obtain the s_u profile of the tested soils.
- Limited by the working space of the geotechnical centrifuge, the pile embedment depth was less than 5 times of helix diameter. According to Das (1980), all tested piles will be categorized as “shallow piles”. In the meantime, the distance between the lower helices and container bottom was less than 3 times of helix diameter thus might introduce boundary effect to the bearing pile resistance.

- The imperfection of pile machining and helix welding may also be a concern. All radius of a perfect helix or a “true helix” should be perpendicular to the shaft axis. However, the present helices were not perfect due to the difficulty of welding aluminum material. Therefore, an analytical torque model based on the perfect helix geometry may lack accuracy for predicting the measure torque.
- A uniform clay domain is assumed in this numerical model that differs from the true gradient soil profile used for validation. There may be a self-adjustment of axial load distributions over the depth compared to the true gradient strength profile.
- The bottom boundary effect is always present in all FE analyses conducted. It may complicate the stress zone near the lower helices.
- The soil was assumed to be weightless and hence the effect of confining stress on the generation of inter-helix failure surface remains unknown.
- Installation-induced reduction of soil strength was not considered in the analyses.

Nonetheless, these uncertainties are believed to be contained at a trivial level throughout the research.

6.3 Recommendations for Future Study

An effective centrifuge model test system has been built to conduct comprehensive load tests of helical piles. However, there is still room for the improvement of such experimental technique. In flight soil investigation may be added to the system to minimize the uncertainties experienced in the 1 g vane shear tests here in this study. True triaxial tests of post-loading soils may be another great improvement of the current soil characterization technique; the in-situ confining stress and vertical stress in flight need to be reproduced in the test cell. The pile installation technique can also be improved by realizing continuous penetration advancement. The helix fabrication can be

more precisely controlled to create “true” helices. A modified PPT installation technique is needed, such as laterally inserted pipe from outside of the container. The bottom boundary condition can be eliminated by increasing the soil depth or using smaller model piles. A more intensive numerical simulation may be needed to explore the effect of pile embedment depth, confining stress, and over-consolidation ratio on the axial behavior of helical piles.

References

- Adams, J. I., and D. C. Hayes. 1967. "The uplift capacity of shallow foundations." *Ontario Hydro Research Quarterly*.
- Al-Baghdadi, T., Davidson, C., Brown, M., Knappett, J., Brennan, A., Augarde, C. E. and Blake, A. 2017. "CPT based design procedure for installation torque prediction for screw piles installed in sand." *In 8th Offshore Site Investigation and Geotechnics International Conference: 'Smarter Solutions for Future Offshore Developments'* (pp. 346-353). Society for Underwater Technology.
- Ali, M. S. 1969. "Pullout resistance of anchor plates and anchor piles in soft bentonite clay." Doctoral diss., Duke Univ., NC, USA.
- ASTM (American Standards for Testing and Materials). 2013. "Standard test methods for deep foundations under static axial compressive load." D1143, *West Conshohocken, PA, ASTM International*.
- Bathe, K. J., Ramm, E., and Wilson, E. L. 1975. "Finite element formulations for large deformation dynamic analysis." *International journal for numerical methods in engineering*, 9(2): 353-386.
- Banerjee, P. K., and Davies, T. G. 1978. "*The behaviour of axially and laterally loaded single piles embedded in nonhomogeneous soils.*" *Geotechnique*, 28(3): 309-326.
- Bhatnagar, R. S. 1969. "Pullout resistance of anchors in silty clay." Sch. of Eng., Duke Univ., NC, USA.
- Brown, M. J., Hyde, A. F. L., and Anderson, W. F. 2006. "Analysis of a rapid load test on an instrumented bored pile in clay." *Geotechnique*, 56(9): 627–638.

- Butterfield, R., and Banerjee, P. K. 1971. "The elastic analysis of compressible piles and pile groups." *Geotechnique*, 21(1): 43-60.
- Caslaw, H.S. and Jaeger, J.C. 1959. "Conduction of Heat in Solids," 2nd ed. Oxford Univ. Press. London, England.
- Carter, J. P., and Balaam, N. P. 1995. AFENA user's manual 5.0, Geotechnical Research Centre, The University of Sydney, Sydney, Australia.
- CGS. 2006. Canadian Foundation Engineering Manual. 4th Edition. Canadian Geotechnical Society, Technical Committee on Foundations, BiTech Publishers Ltd., Richmond, BC.
- Coyle, H. M., and Reese, L. C. 1966. "Load transfer for axially loaded piles in clay." *Journal of the Soil Mechanics and Foundations Division*, 92(2): 1-26.
- Das, B. M. 1978. "Model tests for uplift capacity of foundations in clay." *Soils and Foundations*, 18(2): 17 - 24.
- Das, B. M. 1980. "A procedure for estimation of ultimate uplift capacity of foundations in clay." *Soils and Foundations*, 20(1): 77 - 82.
- Deeks, A. J., and Randolph, M. F. 1992. "Accuracy in numerical analysis of pile-driving dynamics." *In International conference on the application of stress-wave theory to piles* (pp. 85-90).
- Duncan, J. M., and A. L. Buchignani. 1976. "An engineering manual for settlement studies." Dept. of Civil Eng., Univ. of California, Berkeley, CA.
- Dutta, S., Hawlader, B., and Phillips, R. 2015. "Finite element modeling of partially embedded pipelines in clay seabed using Coupled Eulerian–Lagrangian method." *Canadian Geotechnical Journal*, 52(1): 58-72.
- Elkasabgy, M., and M. H. El Naggar. 2015. "Axial compressive response of large-capacity helical and driven steel piles in cohesive soil." *Can. Geotech. J.* 52(2): 224 - 243.

- Gavin, K., Doherty, P., and Tolooiyan, A. 2014. "Field investigation of the axial resistance of helical piles in dense sand." *Canadian Geotechnical Journal*, 51(11): 1343-1354.
- Ghaly, A., and A. Hanna. 1991. "Experimental and theoretical studies on installation torque of screw anchors". *Can. Geotech. J.* 28 (3): 353–364.
- Ghosh, S., and Kikuchi, N. 1991. "An arbitrary Lagrangian-Eulerian finite element method for large deformation analysis of elastic viscoplastic solid." *Comput. Methods Appl. Mech. Eng.*, 862: 127–188.
- Gibson, G. C., and Coyle, H. M. 1968. "Soil damping constants related to common soil properties in sands and clays."
- Hoyt, R. M., and S. P. Clemence. 1989. "Uplift capacity of helical anchors in soil." In *Proc., 12th International Conf. on Soil Mechanics and Foundation Engineering*, 2: 13–18. Rio de Janeiro: CRC Press.
- Hoyt, R.M., and Clemence, S.P. 1989. "Uplift capacity of helical anchors in soil", Proceedings of the 12th International Conference on Soil Mechanics and Foundation Engineering, Rio de Janeiro, Brazil, 2: 1019-1022.
- Hu, Y., and Randolph, M. F. 1998. "A practical numerical approach for large deformation problems in soil." *Int. J. Numer. Analyt. Meth. Geomech.*, 22, 327–350.
- Hu, Y., and Randolph, M. F. 2002. "Bearing capacity of caisson foundations on normally consolidation clay." *Soil Found.*, 425, 71–77.
- Hughes, T. J., and Winget, J. 1980. "Finite rotation effects in numerical integration of rate constitutive equations arising in large-deformation analysis." *International journal for numerical methods in engineering*, 15(12): 1862-1867.

- Keim, V., Marx, P., Nonn, A., and Münstermann, S. 2019. “Fluid-structure-interaction modeling of dynamic fracture propagation in pipelines transporting natural gases and CO₂-mixtures.” *International Journal of Pressure Vessels and Piping*, 175: 103934.
- Ko, H. Y., Atkinson, R. H., Goble, G. G., and Ealy, C. D. 1984. “Centrifugal modeling of pile foundations. In Analysis and design of pile foundations” (pp. 21-40). ASCE.
- Kraft Jr, L. M., Ray, R. P., and Kagawa, T. 1981. “Theoretical t-z curves.” *Journal of the Geotechnical Engineering Division*, 107(11): 1543-1561.
- Kulhawy, F. H. 1985. “Uplift behavior of shallow soil anchors—An overview.” *In Uplift behavior of anchor foundations in soil* (pp. 1-25). ASCE.
- Kupferman, M. 1971. “The vertical holding capacity of marine anchors in clay subjected to static and cyclic loading.” Doctoral dissertation, Univ. of Massachusetts, MA, USA.
- Ladd, C. C. 1991. “Stability evaluation during staged construction.” *J. Geotech. Eng.* 117 (4): 540–615.
- Lanyi-Bennett, S. A., and L. Deng. 2019a. “Axial load testing of helical pile groups in glaciolacustrine clay.” *Can. Geotech. J.* 56 (2): 187–197.
- Lanyi-Bennett, S. A., and L. Deng. 2019b. “Effects of inter-helix spacing and short-term soil setup on the behaviour of axially loaded helical piles in cohesive soil.” *Soils and Foundations* 59 (2): 337–350.
- Li, W. 2016. “Axial and lateral behavior of helical piles under static loads.” M.Sc. thesis, University of Alberta, Edmonton, AB, Canada.
- Li, W., D. Zhang, D. C. Segoo, and L. Deng. 2018. “Field testing of axial performance of large-diameter helical piles at two soil sites.” *ASCE J. Geotech. Geoenviron. Eng.* 144 (3): 06017021.

- Li, W., and Deng, L. 2019. "Axial load tests and numerical modeling of single-helix piles in cohesive and cohesionless soils." *Acta Geotechnica*, 14(2): 461-475.
- Liu, W. K., Belytschko, T., and Chang, H. 1986. "An arbitrary Lagrangian-Eulerian finite element method for path-dependant materials." *Comput. Methods Appl. Mech. Eng.*, 58, 227–245.
- Liu, W. K., Herman, C., Jiun-Shyan, C., and Ted, B. 1988. "Arbitrary Lagrangian-Eulerian Petrov-Galerkin finite elements for nonlinear continua." *Computer methods in applied mechanics and engineering*, 68(3): 259-310.
- Lutenegger, A. J. 2009. "Cylindrical shear or plate bearing?—Uplift behavior of multi-helix screw anchors in clay." *Geotechnical Special Publication No. 185*, IFCEE, Orlando, 456–463
- Lutenegger, A. J. 2009. "Cylindrical shear or plate bearing?—Uplift behavior of multi-helix screw anchors in clay." In *Contemporary Topics in Deep Foundations* (pp. 456-463).
- Ma, H., Zhou, M., Hossain, M. S., and Hu, Y. 2014. "Large deformation FE analysis of end-bearing piles installing in sand." In *The Twenty-fourth International Ocean and Polar Engineering Conference*. International Society of Offshore and Polar Engineers.
- Merifield, R. S., Sloan, S. W., and Yu, H. S. 2001. "Stability of plate anchors in undrained clay". *Géotechnique*, 51(2): 141-153.
- Merifield, R. S. 2011. "Ultimate uplift capacity of multiplate helical type anchors in clay." *Journal of Geotechnical and Geoenvironmental Engineering*, 137(7): 704-716.
- Merifield, R. S., and Smith, C. C. 2010. "The ultimate uplift capacity of multiplate strip anchors in undrained clay." *Comput. Geotech.*, 37(4): 504–514.
- Merifield, R. S., Lyamin, A. V., and Sloan, S. W. 2006. "Three-dimensional lower bound solutions for the stability of plate anchors in sand." *Géotechnique*, 56(2): 123–132.

- Merifield, R.S., Lyamin, A.V., Sloan, S.W., and Yu, H.S. 2003. "Three-dimensional lower bound solutions for stability of plate anchors in clay." *J. of Geotech. And Geoenviron. Eng.*, 129(3): 243–253.
- Meyerhof, G. G. 1973. "The uplift capacity of foundations under oblique loads." *Canadian Geotechnical Journal*, 10(1): 64-70.
- Meyerhof, G. G. 1976. "Bearing capacity and settlement of pile foundations." *Journal of the Geotechnical Engineering Division*, 102(3): 197-228.
- Meyerhof, G. G., and J. I. Adams. 1968. "The ultimate uplift capacity of foundations." *Can. Geotech. J.* 5(4): 225–244.
- Mitsch, M. P., and S. P. Clemence. 1985. "The uplift capacity of helix anchors in sand: Uplift behavior of anchor foundations in soil." In *Proc.*, ASCE, New York, N.Y., 26-47.
- Mooney, J. S., Adamczak, S. J., and Clemence, S. P. 1985. "Uplift capacity of helix anchors in clay and silt." *Proc., ASCE Convention, Uplift Behavior of Anchor Foundations in Soil*, ASCE, New York, 48–72.
- Nazem, M., Sheng, D., and Carter, J. P. 2006. "Stress integration and mesh refinement for large deformation in geomechanics." *International Journal for Numerical Methods in Engineering*, 65(7): 1002-1027.
- Perko, H. A. 2009. "Helical piles: a practical guide to design and installation." John Wiley & Sons.
- Poulos, H. G., and Davis, E. H. 1980. Pile foundation analysis and design (No. Monograph).
- Randolph, M. F., and Wroth, C. P. 1978. "Analysis of deformation of vertically loaded piles." *Journal of the geotechnical engineering division*, 104(12): 1465-1488.
- Randolph, M. F., and C. P. Wroth. 1979. "An analytical solution for the consolidation around a driven pile." *Int. J. for Numer. and Analy. Methods in Geomech.* 3(3): 217–229.

- Randolph, M. F., Wang, D., Zhou, H., Hossain, M. S., and Hu, Y. 2008. "Large deformation finite element analysis for offshore applications." *Proc. 12th Int. Conf. of the Int. Association for Computer Methods and Advances in Geomechanics*, IACMAG, Goa, India, 3307–3318.
- Rao, S. N., Y. V. S. N. Prasad, and C. Veeresh. 1993. "Behaviour of embedded model screw anchors in soft clays." *Geotechnique*, 43(4): 605–614.
- Rao, S. N., Y. V. S. N. Prasad, and M. D. Shetty. 1991. "The behaviour of model screw piles in cohesive soils." *Soils and Foundations*, 31(2): 35–50.
- Reese, L. C., and Seed, H. B. 1955. "Pressure distribution along friction piles." Institute of Transportation and Traffic Engineering, University of California.
- Sakr, M. 2009. "Performance of helical piles in oil sand." *Canadian Geotechnical Journal*, 46(9): 1046-1061.
- Sakr, M. 2013. "Relationship between installation torque and axial capacities of helical piles in cohesive soils." *DFI J.* 7(1): 44–58.
- Salgado, R. 2008. "*The engineering of foundations.*" McGraw Hill, New York, USA.
- Schiavon, J. A., Tsuha, C. D. H. C., and Thorel, L. 2016. "Scale effect in centrifuge tests of helical anchors in sand." *International Journal of Physical Modelling in Geotechnics*, 16(4): 185-196.
- Smith, E. A. L. 1962. "Pile-driving analysis by the wave equation." *Transactions of the American Society of Civil Engineers*, 127(1): 1145-1171.
- Soderberg, L. O. 1962. "Consolidation theory applied to foundation pile time effects." *Geotechnique*, 12(3): 217-225.
- Song, Z., Hu, Y., and Randolph, M. F. 2008. "Numerical simulation of vertical pullout of plate anchors in clay." *J. Geotech. Geoenviron. Eng.*, 1346: 866–875.

- Tang, C., and K. K. Phoon. 2018. "Statistics of model factors and consideration in reliability-based design of axially loaded helical piles." *J. of Geotech. and Geoenviron. Eng.* 144(8): 04018050.
- Tappenden, K. M., and Segoo, D. C. 2007. "Predicting the axial capacity of screw piles installed in Canadian soils." In *The Canadian Geotechnical Society (CGS), OttawaGeo2007 Conference* (pp. 1608-1615).
- Terzaghi, K. 1943. *Theoretical soil mechanics*, Wiley, New York.
- Tian, Y., Cassidy, M. J., Randolph, M. F., Wang, D., and Gaudin, C. 2014. "A simple implementation of RITSS and its application in large deformation analysis." *Computers and Geotechnics*, 56: 160-167.
- Tomlinson, M. J. 1957. "The adhesion of piles driven in clay soils." In *Proceedings of the 4th International Conference on Soil Mechanics and Foundation Engineering*, 2: 66–71.
- Tsuha, C. D. H. C., Aoki, N., Rault, G., Thorel, L., and Garnier, J. 2012. "Evaluation of the efficiencies of helical anchor plates in sand by centrifuge model tests." *Canadian Geotechnical Journal*, 49(9): 1102-1114.
- Tsuha, C. H. C., and N. Aoki. 2010. "Relationship between installation torque and uplift capacity of deep helical piles in sand." *Can. Geotech. J.* 47(6): 635-647.
- Tsuha, C. H. C., N. Aoki, G. Rault, L. Thorel, and J. Garnier. 2007. "Physical modelling of helical pile anchors." *International Journal of Physical Modelling in Geotechnics*, 7(4): 01-12.
- Ullah, S. N., Hou, L. F., Satchithanathan, U., Chen, Z., and Gu, H. 2018. "A 3D RITSS approach for total stress and coupled-flow large deformation problems using ABAQUS." *Computers and Geotechnics*, 99: 203-215.

- Vesić, A. S. 1971. “Break-out resistance of objects embedded in ocean bottom.” *Journal of the Soil Mechanics and Foundations Division*, 97(9): 1183-1205.
- Vesić, A. S. 1973. “Analysis of ultimate loads of shallow foundations.” *Journal of the Soil Mechanics and Foundations Division*, 99(1): 45-73.
- Vesić, A. S. 1975. Principles of pile foundation designs. Duke University, NC, USA.
- Wang, D., Bienen, B., Nazem, M., Tian, Y., Zheng, J., Pucker, T., and Randolph, M. F. 2015. “Large deformation finite element analyses in geotechnical engineering.” *Computers and Geotechnics*, 65: 104-114.
- Wang, D., Hu, Y., and Randolph, M. F. 2010. “Three-dimensional large deformation finite-element analysis of plate anchors in uniform clay.” *Journal of Geotechnical and Geoenvironmental Engineering*, 136(2): 355-365.
- Wang, D., Hu Y., and Randolph, M. F. 2009. “Three-dimensional large deformation finite element analysis of plate anchors in uniform clay.” *J. Geotech. Geoenviron. Eng.*, 136(2): 355–365.
- Wang, D., R. S. Merifield, and C. Gaudin. 2013. “Uplift behaviour of helical anchors in clay.” *Can. Geotech. J.* 50(6): 575–584.
- Weech, C. N., and J. A. Howie. 2012. “Helical piles in soft sensitive soils—A field study of disturbance effects on pile capacity.” In *Proc., Vancouver, BC: VGS Symp. on Soft Ground Engineering*. Richmond: CGS.
- Wroth, C. P., and G. T. Houlsby. 1985. “Soil mechanics—property characterization and analysis procedures.” In *Proc. of the Eleventh International Conference on Soil Mechanics and Foundation Engineering*. 1: 1–55. San Francisco: CRC Press.
- Yu, H. S. 2000. Cavity expansion methods in geomechanics. Springer Science & Business Media.

- Zambrano-Narvaez, G., and Chalaturnyk, R. J., 2014. "The New GeoREF Geotechnical Beam Centrifuge at the University of Alberta, Canada." In *Proceedings of the 8th International Conference on Physical Modelling in Geotechnics 2014 (ICPMG2014)*, Perth, Australia.
- Zhang, L. M., and Kong, L. G. 2006. "Centrifuge modeling of torsional response of piles in sand." *Canadian Geotechnical Journal*, 43(5): 500-515.
- Zhou, H., and Randolph, M. F. 2007. "Computational techniques and shear band development for cylindrical and spherical penetrometers in strain-softening clay." *Int. J. Geomech.*, 74: 287–295.

Appendix A: Drawings of Test Equipment

Additional critical drawings of the test equipment and devices are attached in case readers feel interested. All the drawings of the soil container were finalized by Jakob Brandl with a simple draft by the author. The rest of the drawings were prepared by the author alone.

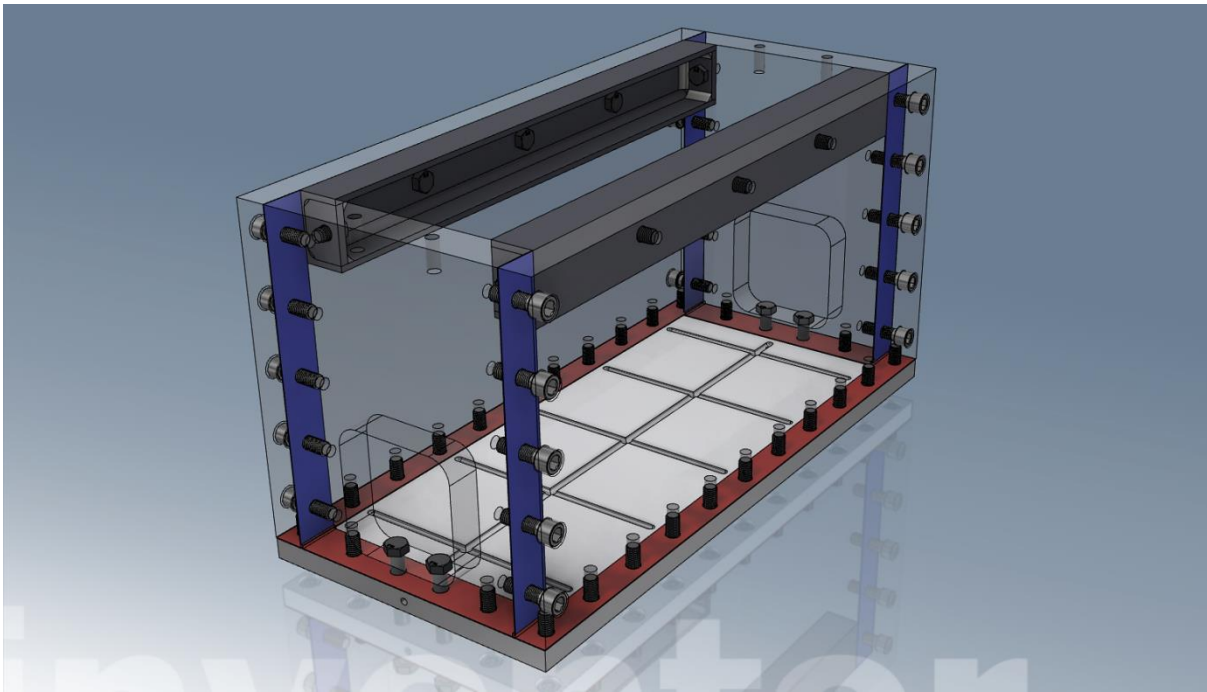


Figure A-1. Deployment of bolts in the soil container

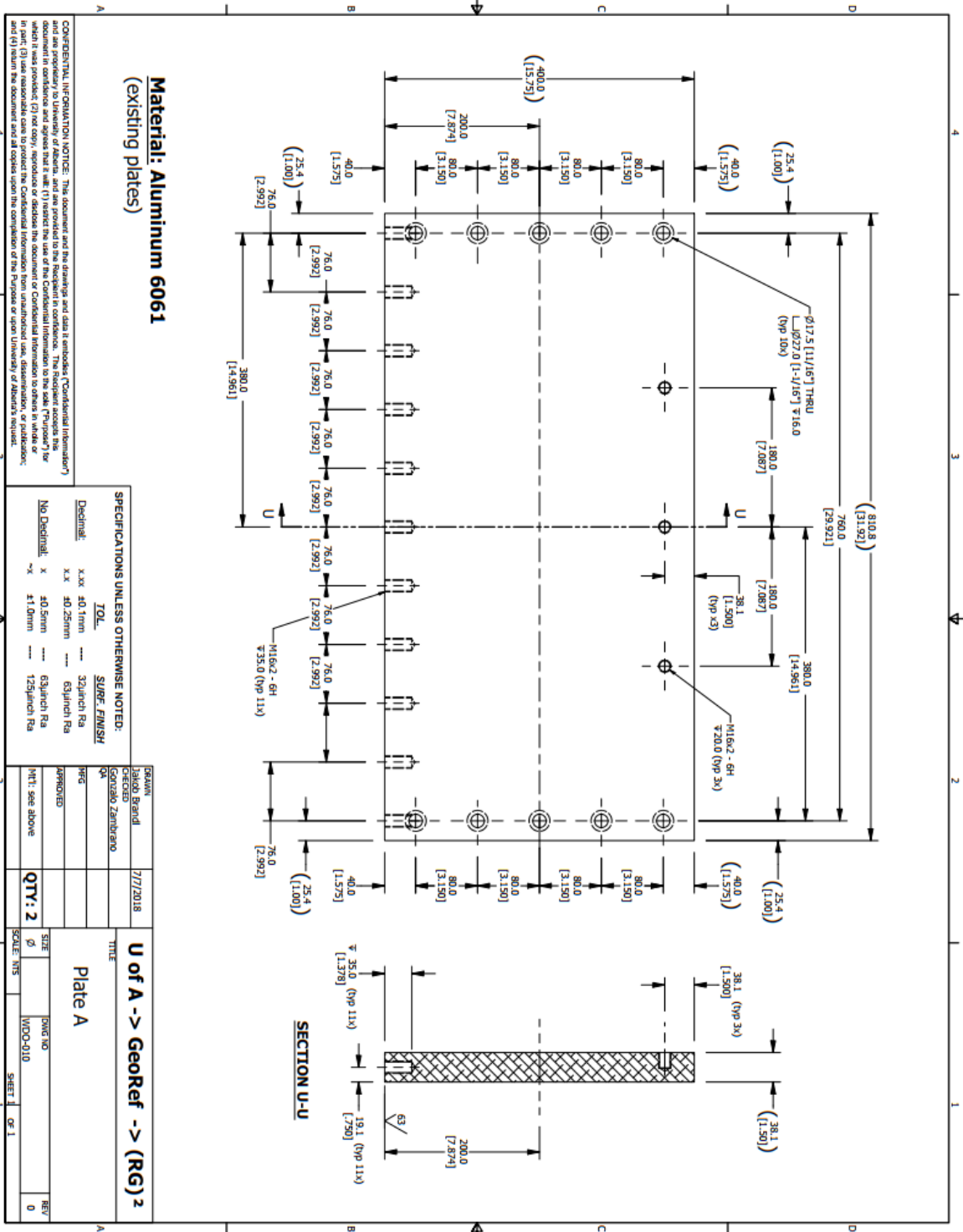


Figure A-2. Drawing of the soil container Plate A

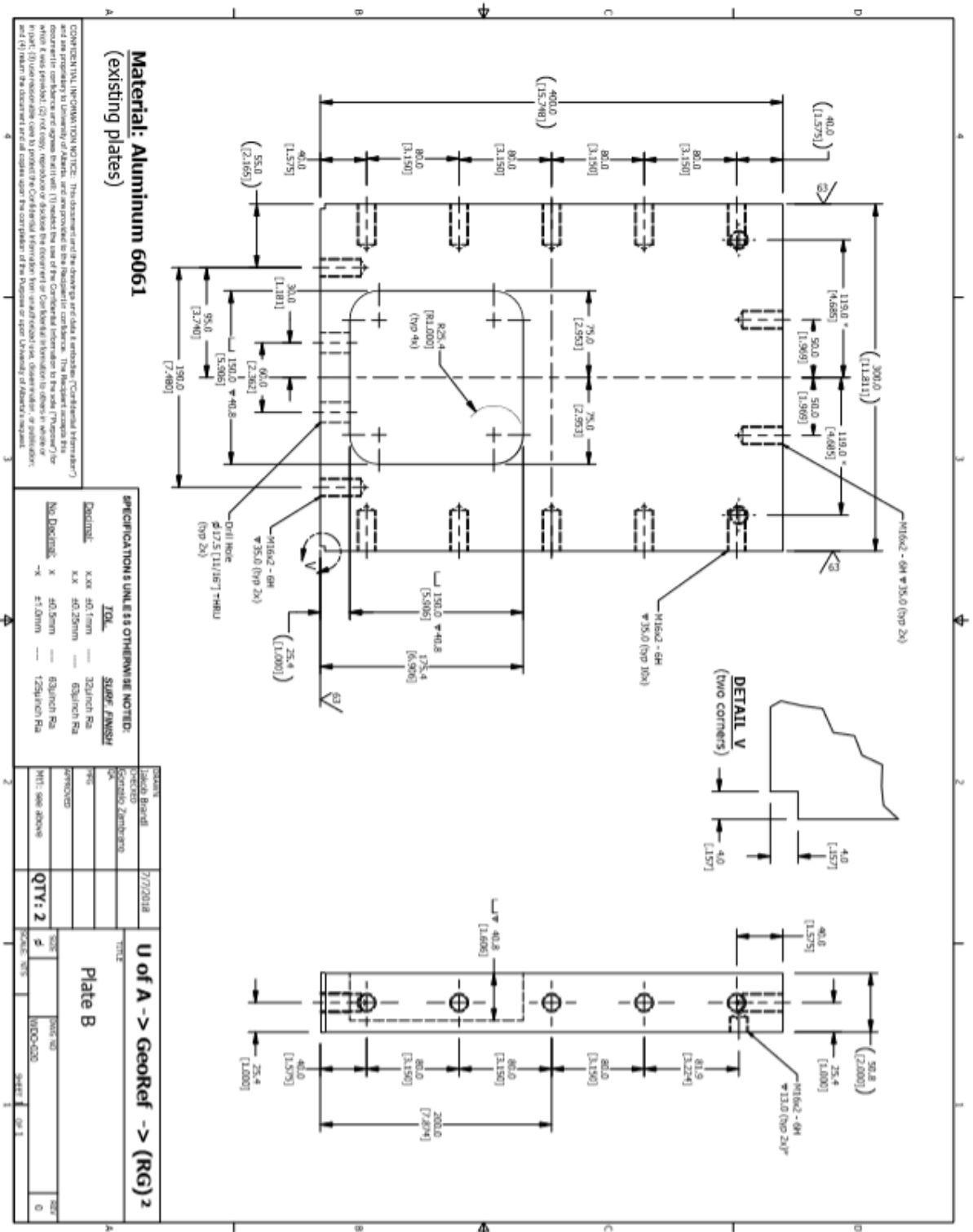


Figure A-3. Drawing of the soil container Plate B

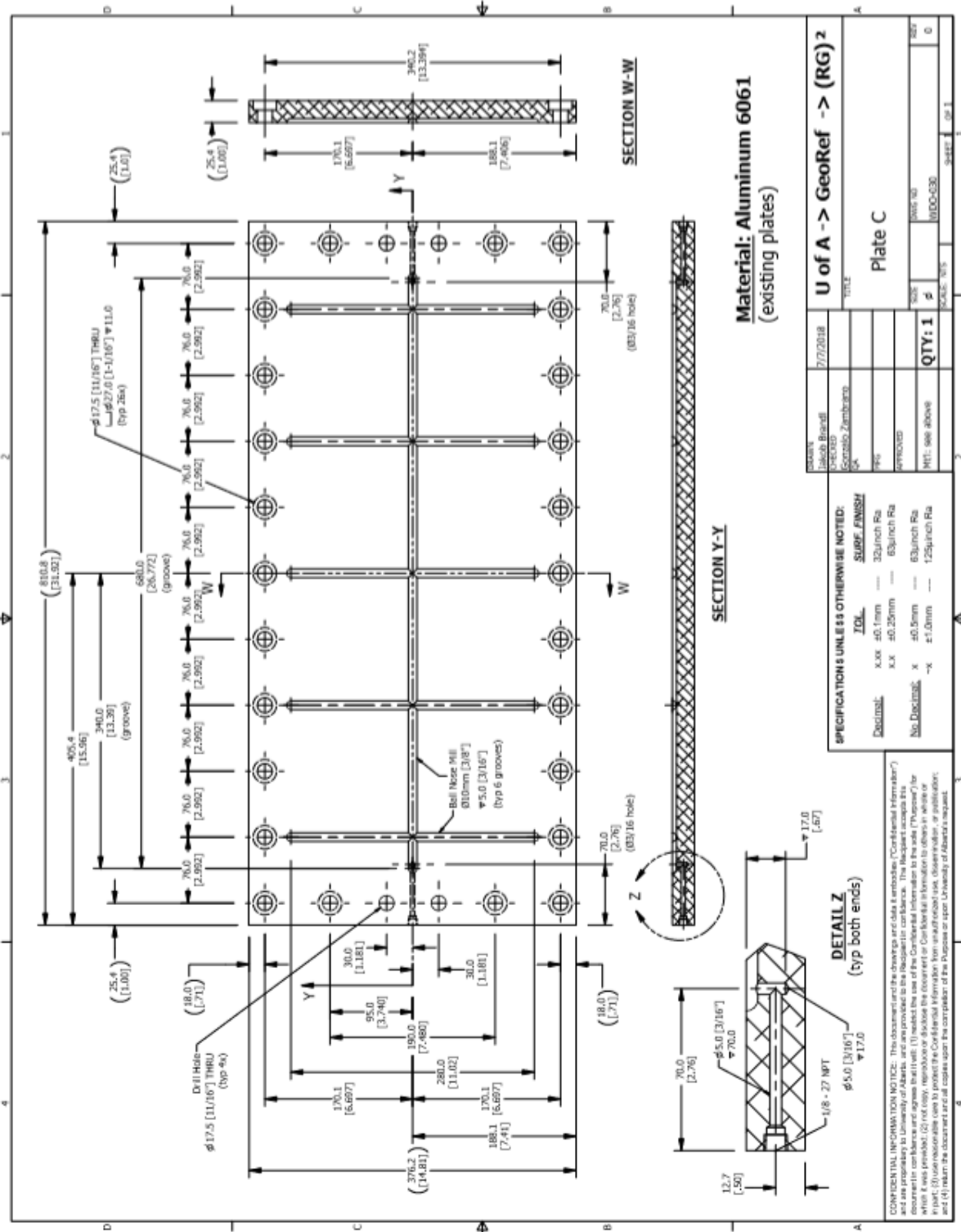


Figure A-4. Drawing of the soil container Plate C

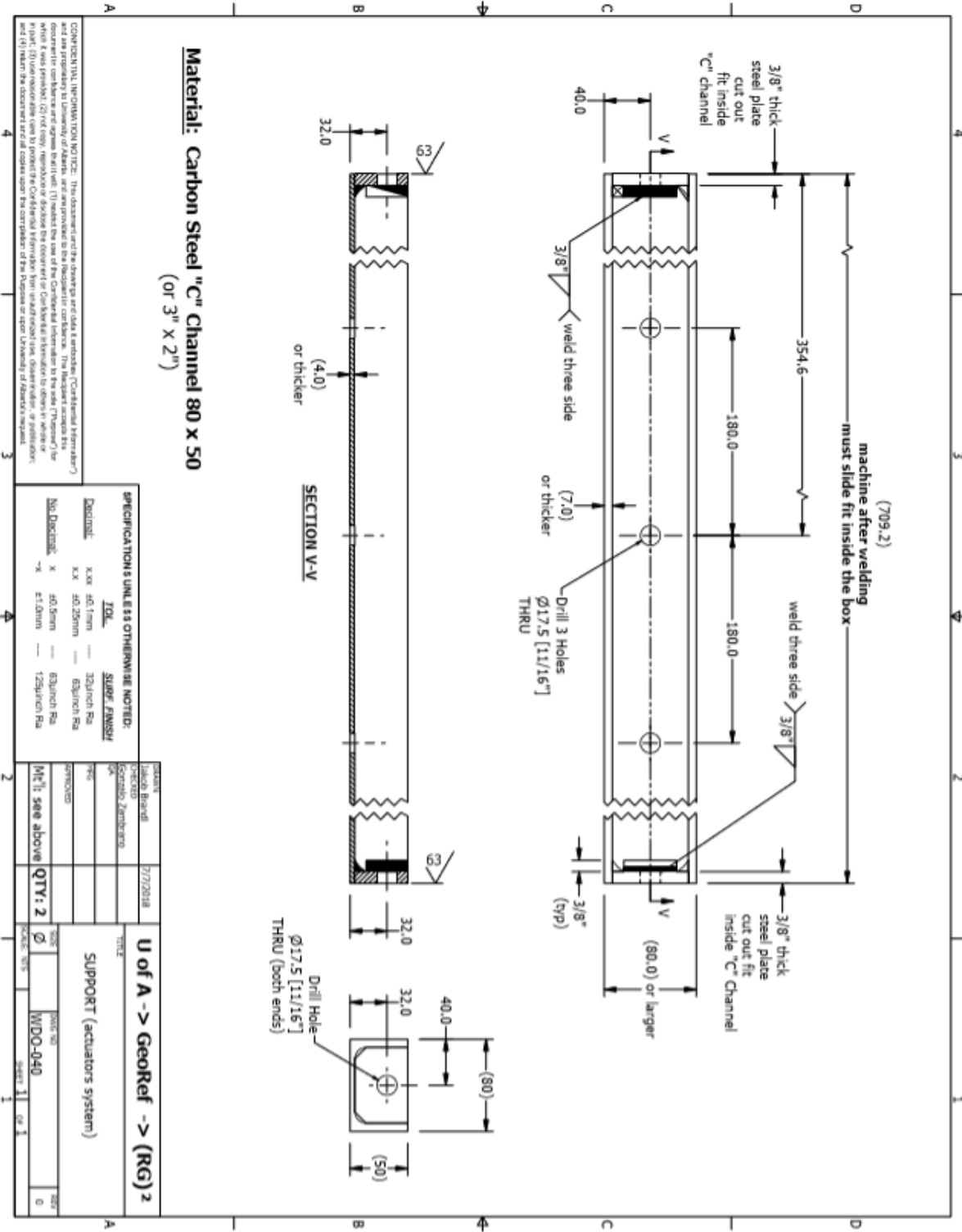
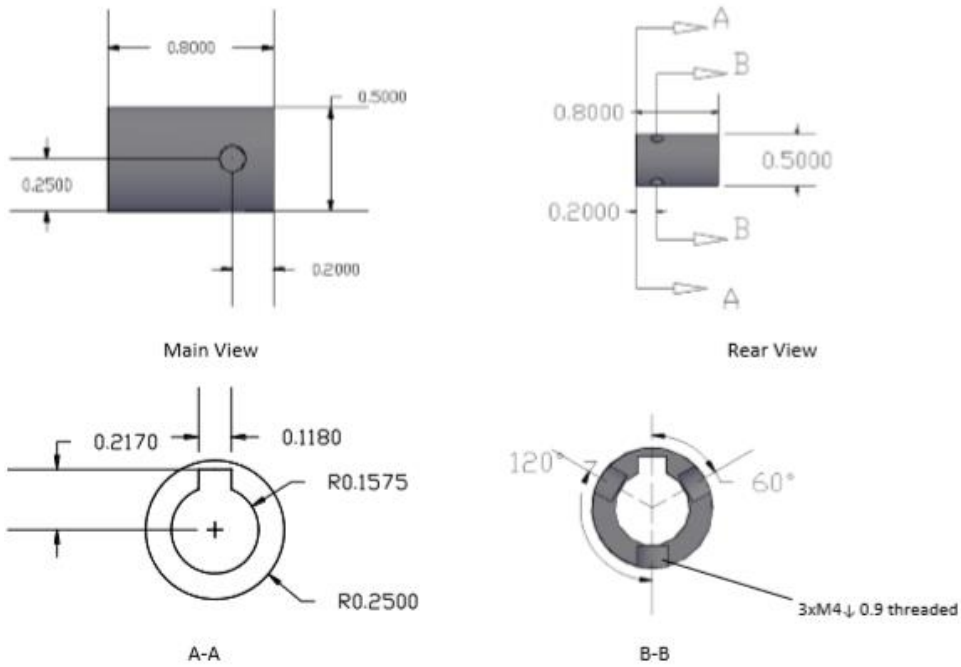


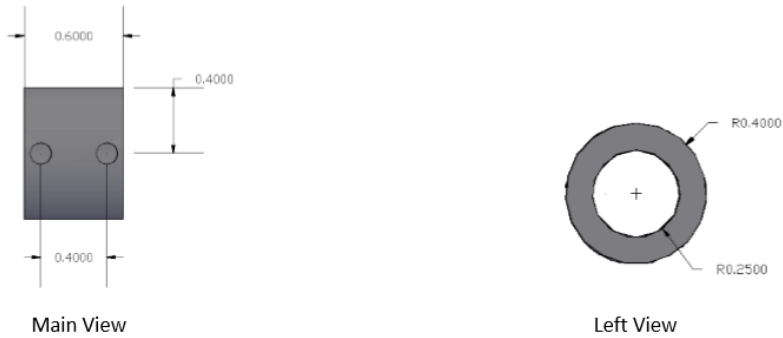
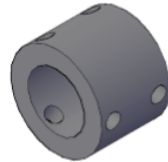
Figure A-5. Drawing of the soil container Plate D



Figure A-6. Drawings of the model pile shaft



Pin



6xM4 not threaded

Corresponding to the 6 threaded screw holes in part 1&2.

Figure A-7. Drawings of Adaptor 1

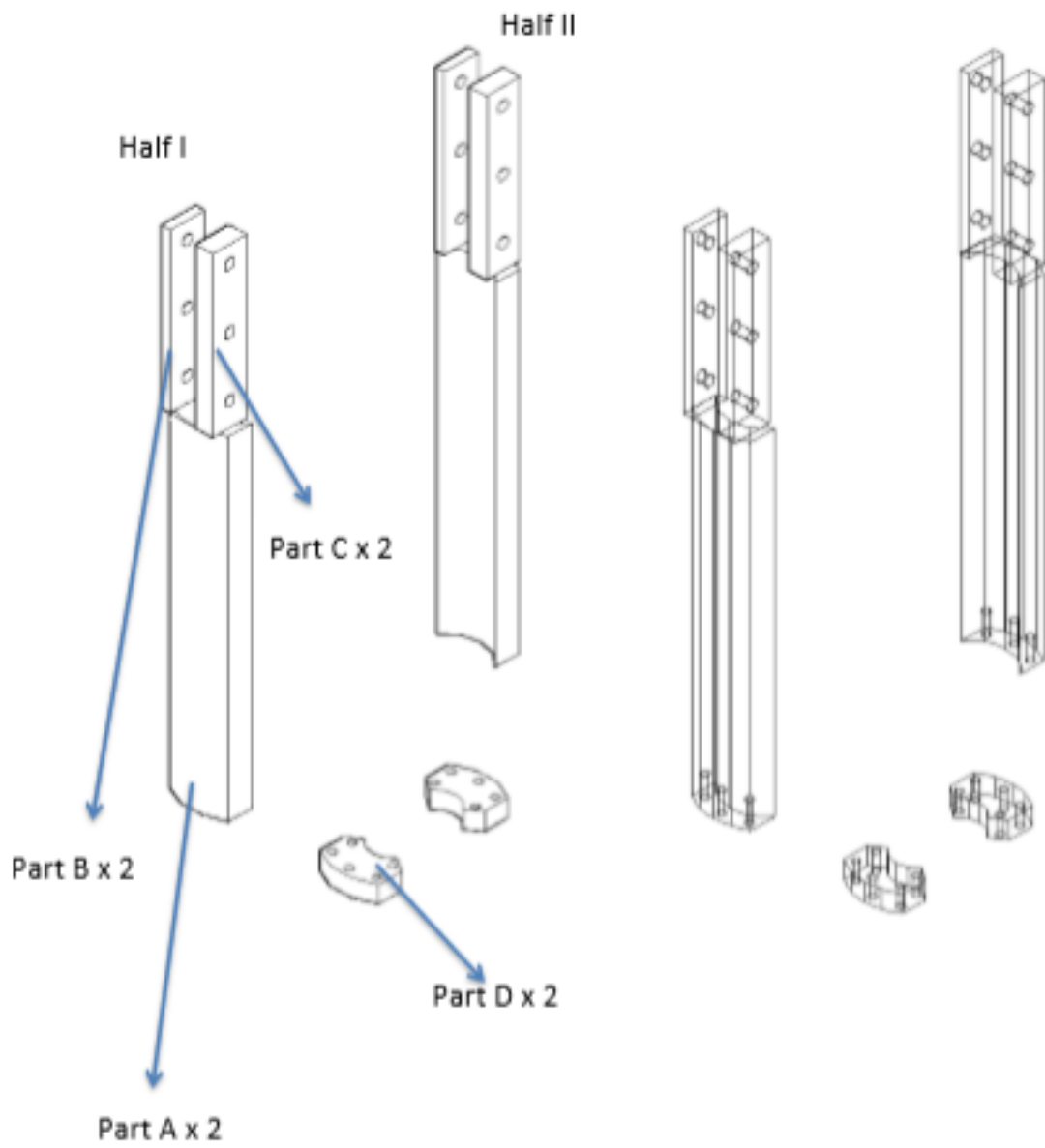


Figure A-8. Overview of Adaptor 2

Part A

Material: steel

Dimensions:

height: 197.0 mm

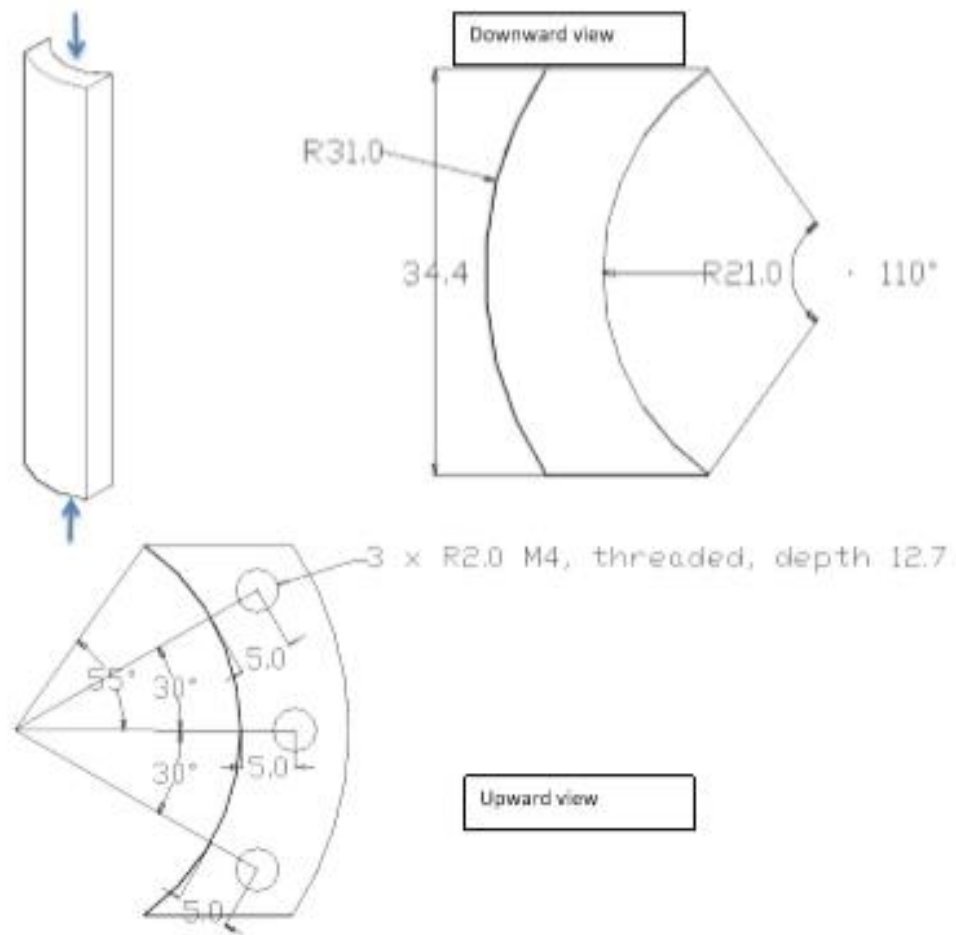


Figure A-9. Drawings of Part A, Adaptor 2

Part B

Material: steel

Dimensions:

height: 94.0 mm; width: 20.0 mm; thickness: 5.0 mm

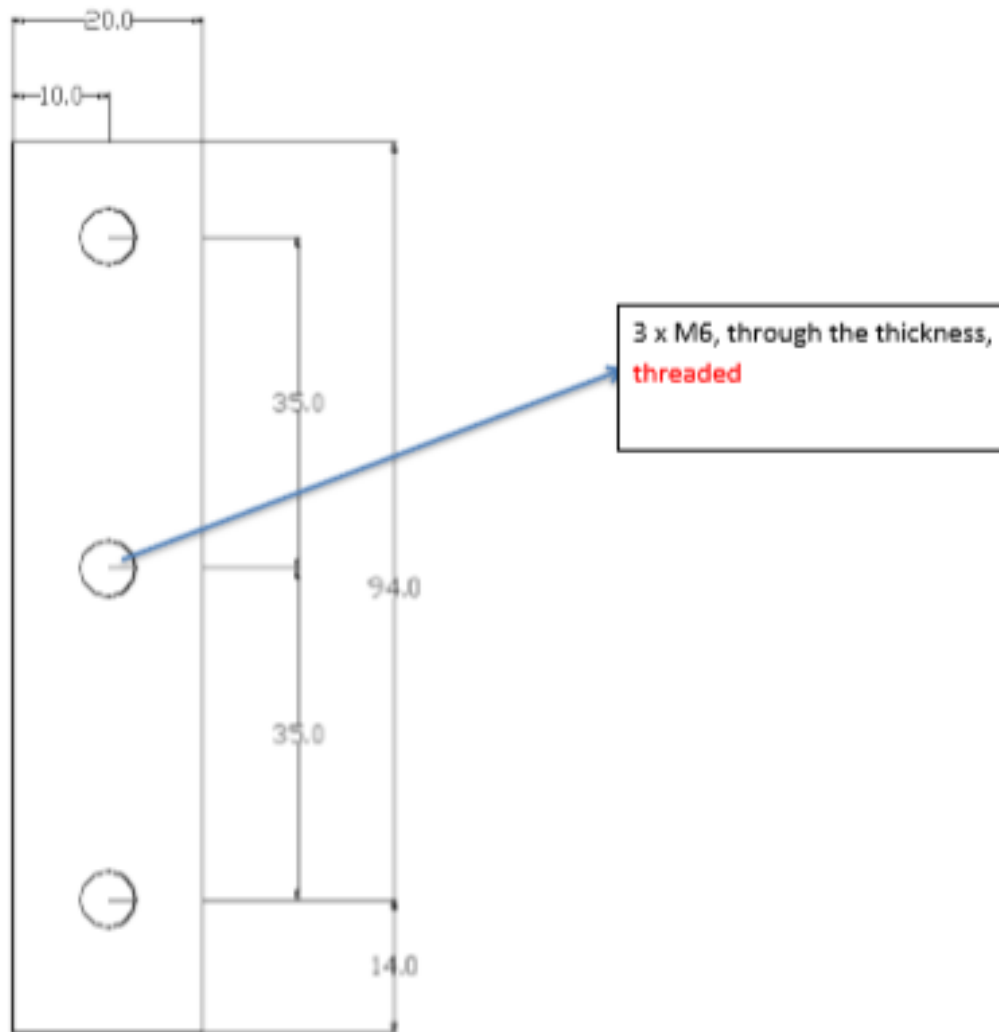


Figure A-10. Drawings of Part B and C, Adaptor 2

Part D

Material: Aluminum

Dimensions:

thickness: 10.0 mm

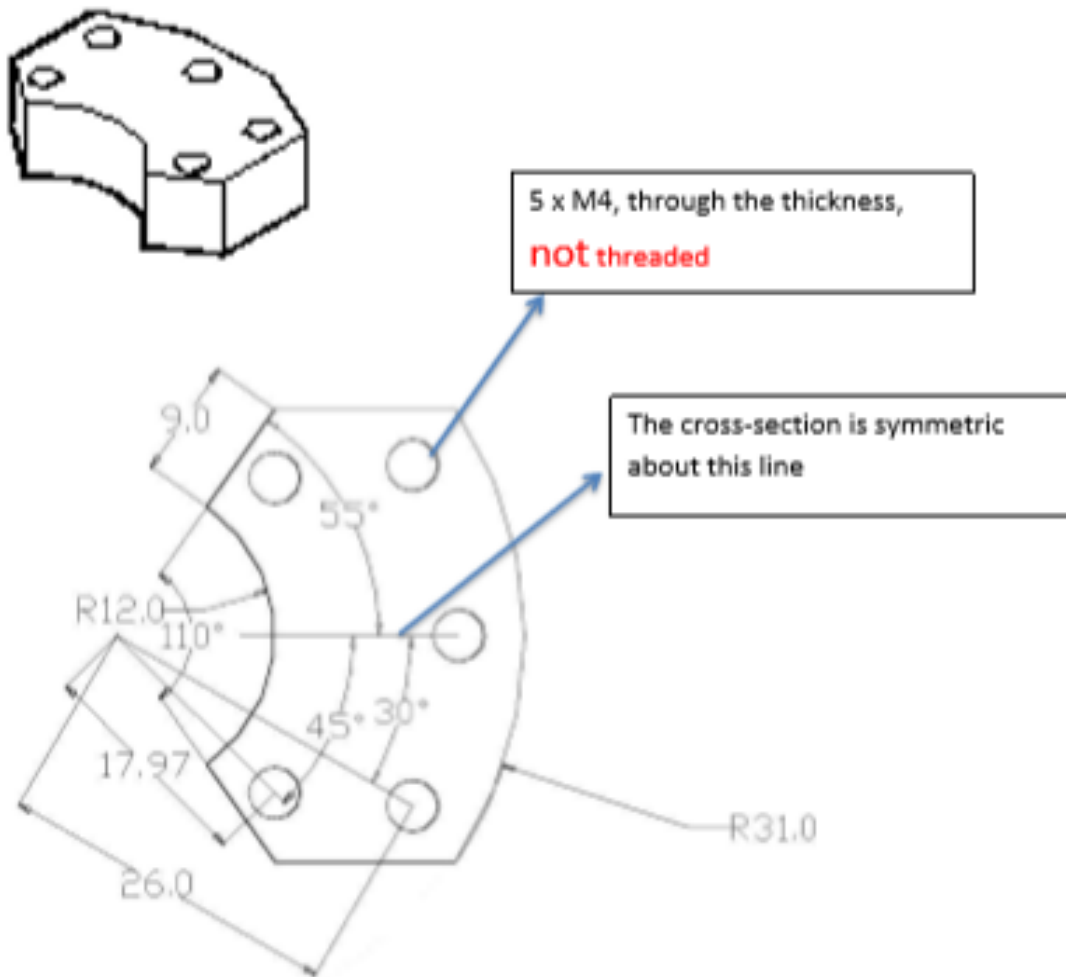


Figure A-11. Drawings of Part D, Adaptor 2

Welding Part B&C to Part A

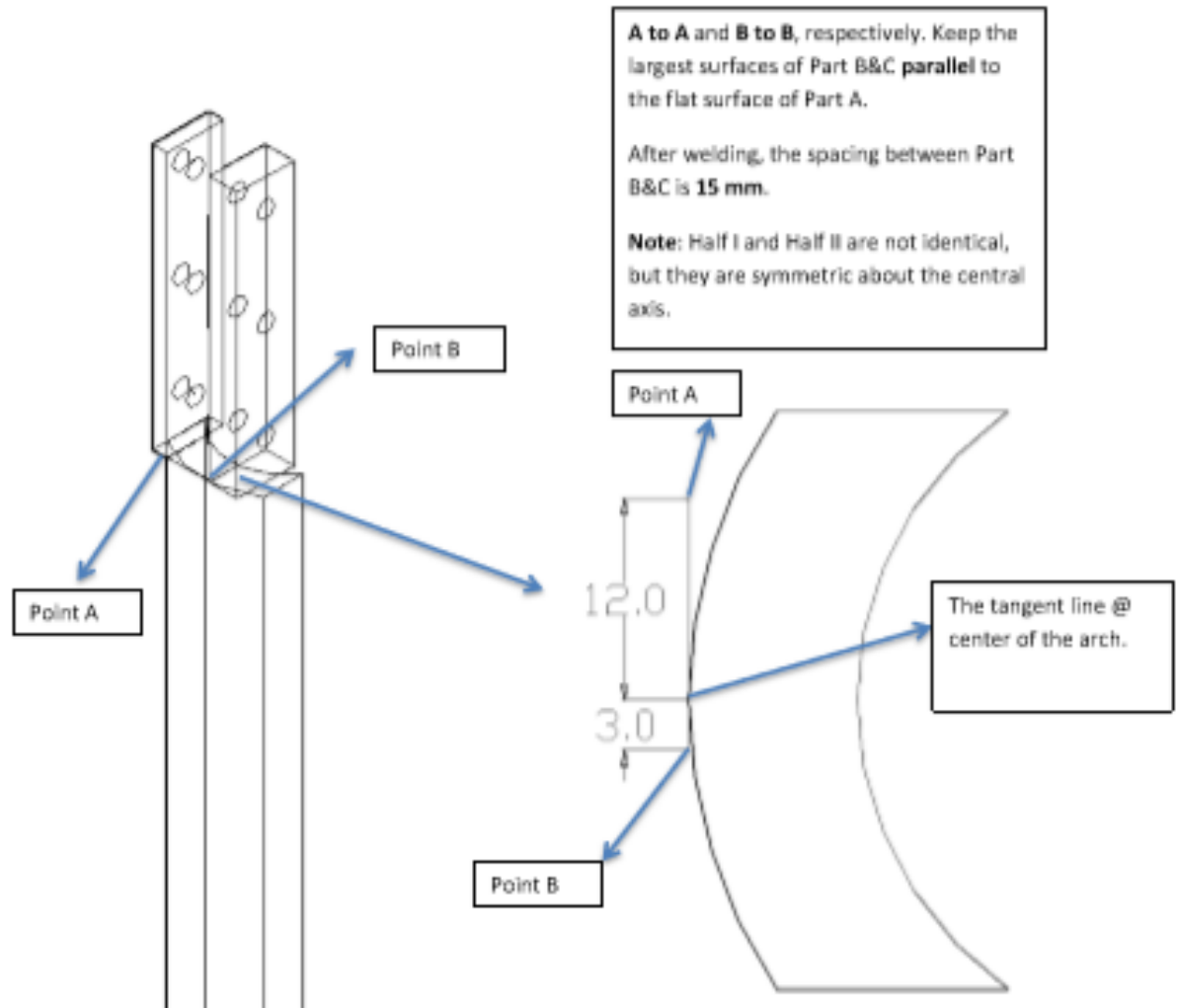


Figure A-12. Drawings Adaptor 2 assembly

Appendix B: Command Scripts of Electric Actuator

The scripts below describe every designated step to be executed by the actuator. This is a customized code by the manufacturer of the actuator. Both horizontal and vertical motions are implemented in these files.

[1] Command #0

```
1CLOSE          ; Close the previous program in "1" (Z) direction
1CLEARALL       ; Clear all previous settings in "1" (Z) direction
2CLOSE          ; Close the previous program in "2" (X) direction
2CLEARALL       ; Clear all previous settings in "2" (X) direction
1DECLAIR(StartTest) ; Print "StartTest"
1ON              ; Ready the movement in Z direction
1MI              ; Incremental preset moves
1V33.6          ; 1V8=1mm/s in Z direction
1H+              ; H+=downward
1D3200000       -; 1D64000=1 mm travel
1G              ; End of the movement
1ON              ;
1MI              ;
1V33.6          ;
1H-              ; H-=upward
1D3200000       -;
1G              ; End of the movement
```


2ON ; Ready the movement in X direction
 2MI ;
 2V33.6 ; 2V8=1mm/s in X direction
 2H+ ; H+=forward
 2D3200000 -;
 2G ; End of the movement
 2ON ;
 2MI ;
 2V33.6 ; 2V8=1mm/s
 2H- ; H-=backward
 2D3200000 -; 2D64000=1 mm travel
 2G ; End of the movement

[2]: Command #1

1CLOSE ; Close the previous program in “1” (Z) direction
 1CLEARALL ; Clear all previous settings in “1” (Z) direction
 1DECLAIR(StartTest) ; Print “StartTest”
 1ON ; Ready the movement in Z direction
 1MI ; Incremental preset moves
 1V33.6 ; 1V8=1mm/s in Z direction
 1H+ ; H+=downward
 1D11558400 -; 1D64000=1 mm travel
 1G ; End of the movement

[3]: Command #2

1CLOSE ; Close the previous program in “1” (Z) direction
1CLEARALL ; Clear all previous settings in “1” (Z) direction
1DECLAIR(StartTest) ; Print “StartTest”
1ON ; Ready the movement in Z direction
1MI ; Incremental preset moves
1V0.4 ; 1V8=1mm/s in Z direction
1H+ ; H+=downward
1D16000 -; 1D64000=1 mm travel
1G ; End of the movement

[2]: Command #1

1CLOSE ; Close the previous program in “1” (Z) direction
1CLEARALL ; Clear all previous settings in “1” (Z) direction
1DECLAIR(StartTest) ; Print “StartTest”
1ON ; Ready the movement in Z direction
1MI ; Incremental preset moves
1V33.6 ; 1V8=1mm/s in Z direction
1H+ ; H+=downward
1D11558400 -; 1D64000=1 mm travel
1G ; End of the movement

[4]: Command #3

1CLOSE ; Close the previous program in “1” (Z) direction
1CLEARALL ; Clear all previous settings in “1” (Z) direction
1DECLAIR(StartTest) ; Print “StartTest”
1ON ; Ready the movement in Z direction
1MI ; Incremental preset moves
1V0.4 ; 1V8=1mm/s in Z direction
1H+ ; H+=downward
1D16000 -; 1D64000=1 mm travel
1G ; End of the movement

Appendix C: More Results of Tests and Simulation

Table C-1. Su profile of WL01 before tests of Stage 1

Depth	model	(cm)	2	6	10	14	18
Depth	prototype	(m)	0.4	1.2	2	2.8	3.6
BH1A1	peak	(kPa)	22	33	42	49	55
BH1A1	residual	(kPa)	6.3	10	10.5	13.6	20
BH1A2	peak	(kPa)	19	32	40	51	52
BH1A2	residual	(kPa)	6.5	9	11	13.5	16
BH1A3	peak	(kPa)	20	32	42	49	52
BH1A3	residual	(kPa)	6.5	9	10.8	13	18
BH1B1	peak	(kPa)	20	29.5	39.9	45.6	51.3
BH1B1	residual	(kPa)	6.7	8.6	10	12	17.5
BH1B2	peak	(kPa)	19	31.4	39	47.5	50.4
BH1B2	residual	(kPa)	5.7	7.6	9.2	13.7	16
BH1B3	peak	(kPa)	19	30.4	40.9	45.6	50.4
BH1B3	residual	(kPa)	6.7	9.5	10	12	17

Table C-2. Su profile of WL01 after tests of Stage 2

Depth	model	(cm)	2	6	10	14	18
Depth	prototype	(m)	0.4	1.2	2	2.8	3.6
BH2A1	peak	(kPa)	26	32	35	40	43
BH2A1	residual	(kPa)	6	8	9	12	13.5
BH2A2	peak	(kPa)	27	38	38	40	43
BH2A2	residual	(kPa)	6	9	9	12	13
BH2A3	peak	(kPa)	26	36	37	40	42
BH2A3	residual	(kPa)	6.5	9	10	12	13
BH2B1	peak	(kPa)	22.8	32.3	34.2	39	40.9
BH2B1	residual	(kPa)	5.7	8.6	9.5	11.4	12.4
BH2B2	peak	(kPa)	23.8	34.2	34.2	37.1	40.9
BH2B2	residual	(kPa)	6.2	8.6	8.6	10.5	12.8
BH2B3	peak	(kPa)	21.9	32.3	35.2	39.9	39
BH2B3	residual	(kPa)	5.7	8.6	10	11.9	12.4

Table C-3. Su profile of WL02 before tests of Stage 1

Depth	model	(cm)	2	6	10	14	18
Depth	prototype	(m)	0.4	1.2	2	2.8	3.6
BH1A1	peak	(kPa)	54	83	106	130	140
BH1A1	residual	(kPa)	15	27	33	40	55
BH1A2	peak	(kPa)	50	80	102	135	135
BH1A2	residual	(kPa)	15	25	32	41	55
BH1A3	peak	(kPa)	51.2	82	104	132	137
BH1A3	residual	(kPa)	16	23	32	41	54
BH1B1	peak	(kPa)	50	79	106	127	130
BH1B1	residual	(kPa)	17	22	32	39	54
BH1B2	peak	(kPa)	49	83	100	122	129
BH1B2	residual	(kPa)	14	21	28	45	50
BH1B3	peak	(kPa)	47	80	101	123	127
BH1B3	residual	(kPa)	16	25	30	39	50

Table C-4. Su profile of WL02 after tests of Stage 2

Depth	model	(cm)	2	6	10	14	18
Depth	prototype	(m)	0.4	1.2	2	2.8	3.6
BH2A1	peak	(kPa)	52	79	93	105	112
BH2A1	residual	(kPa)	18	24	27	36	44
BH2A2	peak	(kPa)	55	80	98	108	115
BH2A2	residual	(kPa)	15	24	23	33	41
BH2A3	peak	(kPa)	52	75	97	103	114
BH2A3	residual	(kPa)	16	24	25	32	39
BH2B1	peak	(kPa)	49	78	98	102	113
BH2B1	residual	(kPa)	15	23	25	31	40
BH2B2	peak	(kPa)	51	83	97	101	112
BH2B2	residual	(kPa)	15	23	24	34	40
BH2B3	peak	(kPa)	48	79	92	109	109
BH2B3	residual	(kPa)	14	23	24	33	41

Table C-5. Basic properties of post loading soil, WL01

Depth (cm)	Shelby tube #1			Shelby tube #2		
	MC		Saturation	MC		Saturation
	(%)	(kg/m ³)	(%)	(%)	(kg/m ³)	(%)
5	46.8	1.64	90.7	47.8	1.61	92.5
10	46.6	1.70	95.7	45.6	1.73	93.8
15	47.4	1.70	96.9	46.0	1.75	93.9
20	49.8	1.64	93.3	49.5	1.66	96.1

Table C-6. Basic properties of post loading soil, WL02

Depth (cm)	Shelby tube #1			Shelby tube #2			Shelby tube #3		
	MC		Saturati	MC		Saturati	MC		Saturati
	(%)	(kg/m ³)	on (%)	(%)	(kg/m ³)	on (%)	(%)	(kg/m ³)	on (%)
5	37.						38.		
	6	1.77	94.0	38.4	1.74	91.9	2	1.75	92.6
10	38.						37.		
	1	1.80	97.7	38.8	1.77	95.4	8	1.78	95.3
15	37.						37.		
	0	1.82	98.6	37.2	1.80	96.7	2	1.81	97.7
20	37.						36.		
	4	1.83	100.0	37.1	1.83	99.8	9	1.81	97.4

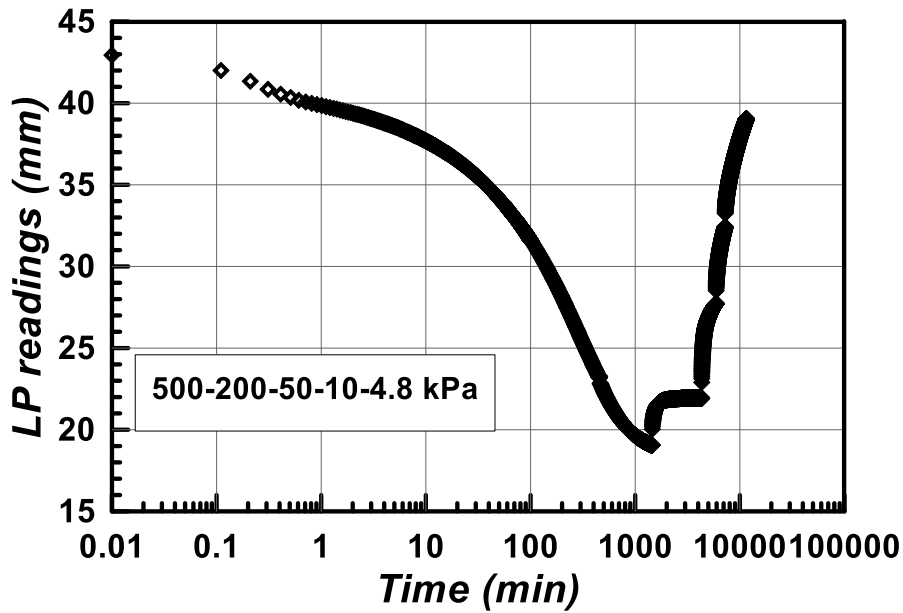


Figure C-1. The unloading process following the last load increment of consolidation for soil preparation, WL01.

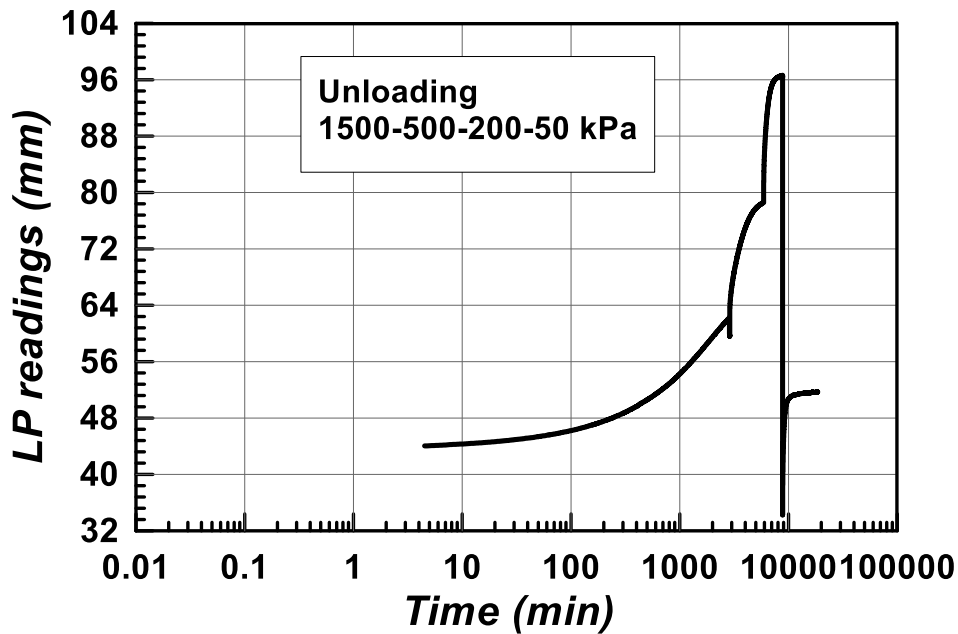


Figure C-2. The unloading process following the last load increment of consolidation for soil preparation, WL02

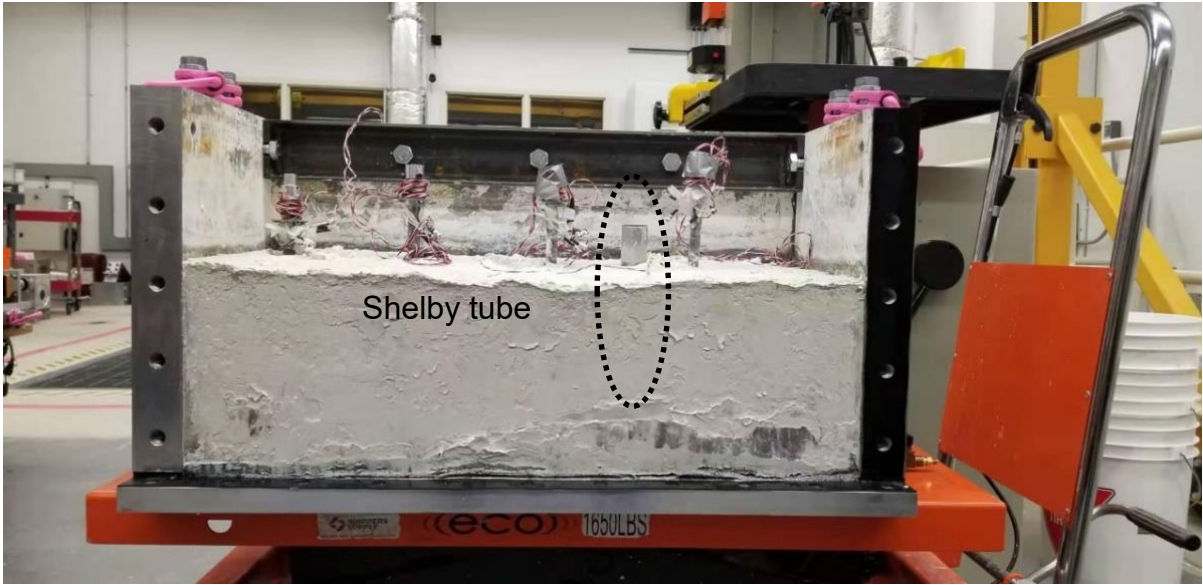


Figure C-3. Sampling of post testing soil using a Shelby tube



Figure C-4. Vertical cut of the cavity left behind the pulled-out piles

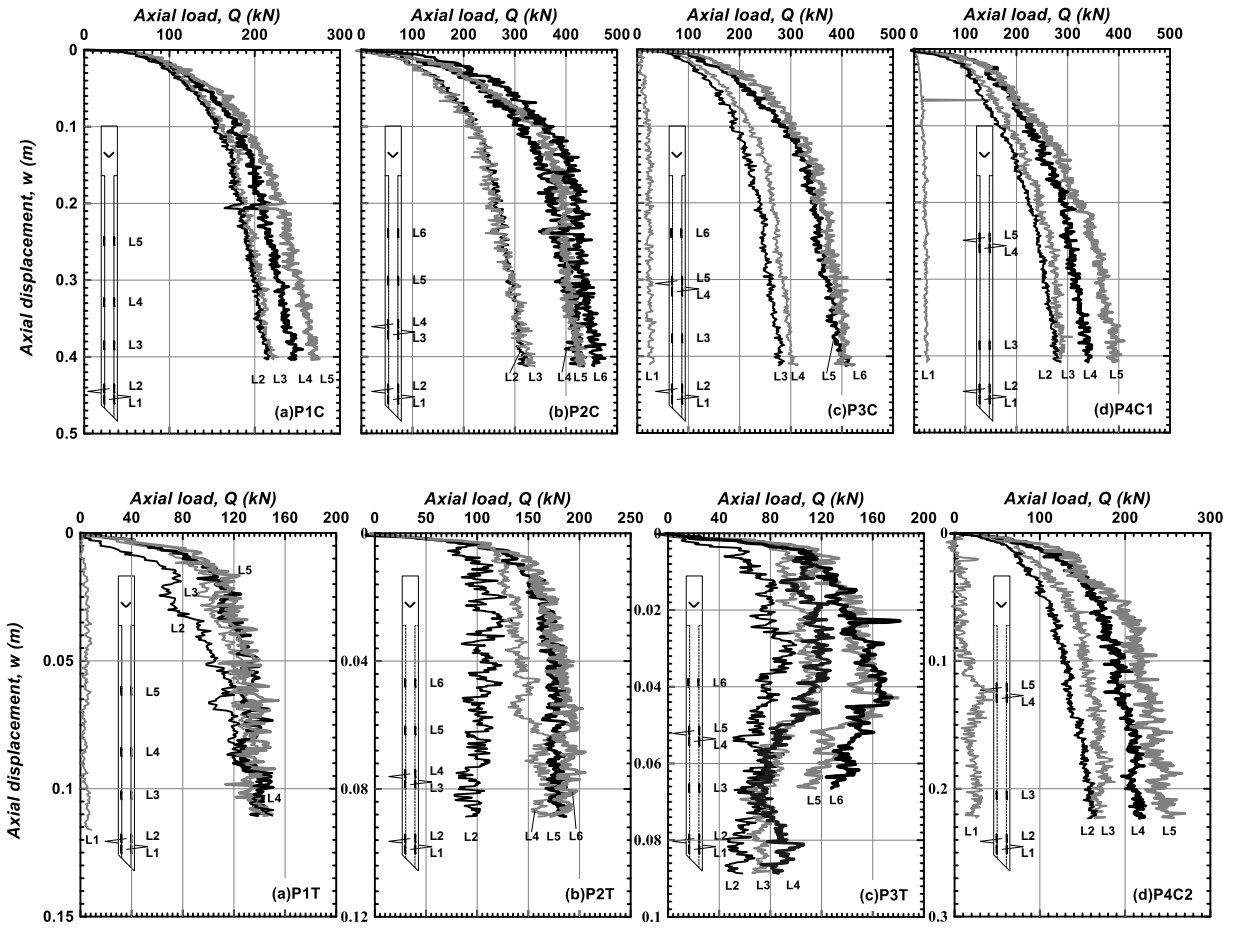


Figure C-5. Axial load displacement curves of WL01

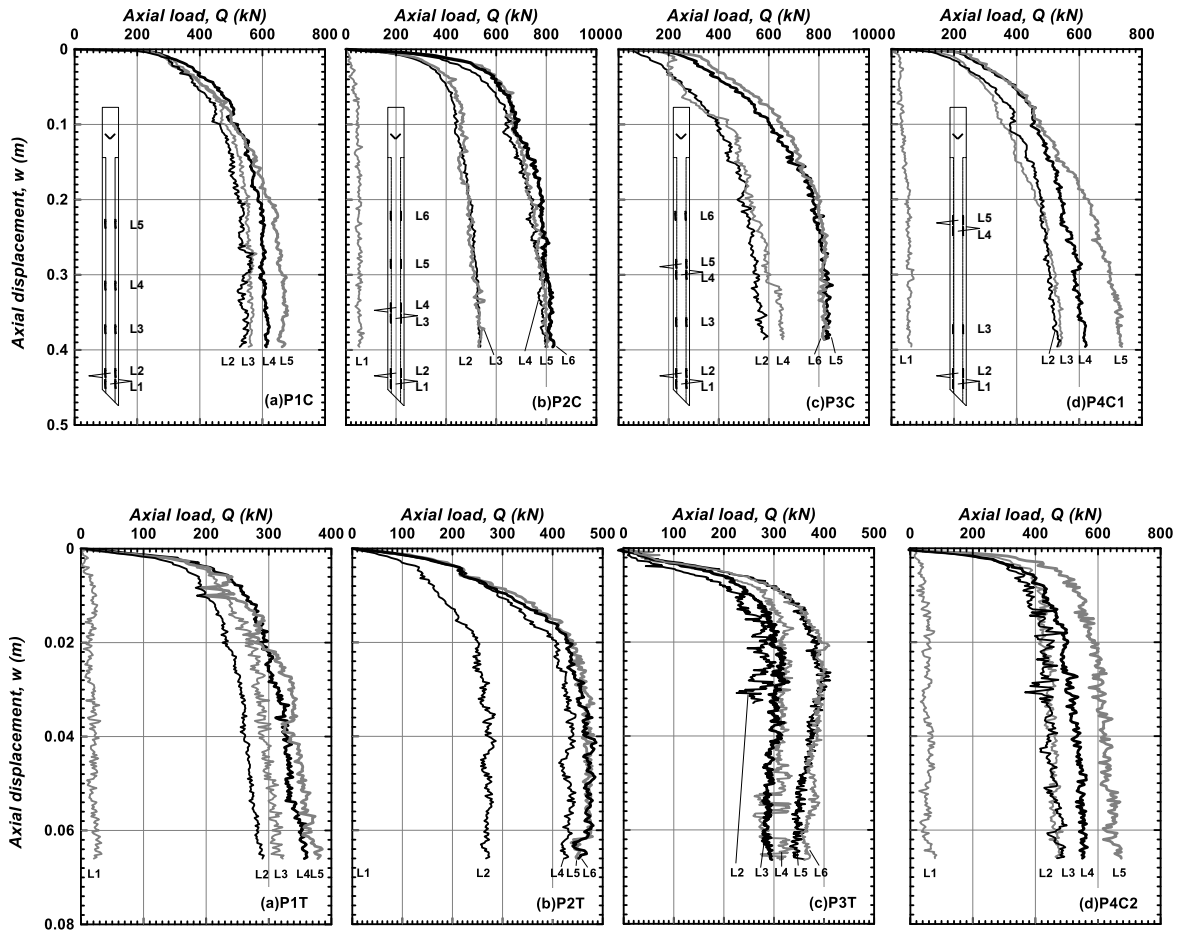


Figure C-6. Axial load displacement curves of WL02

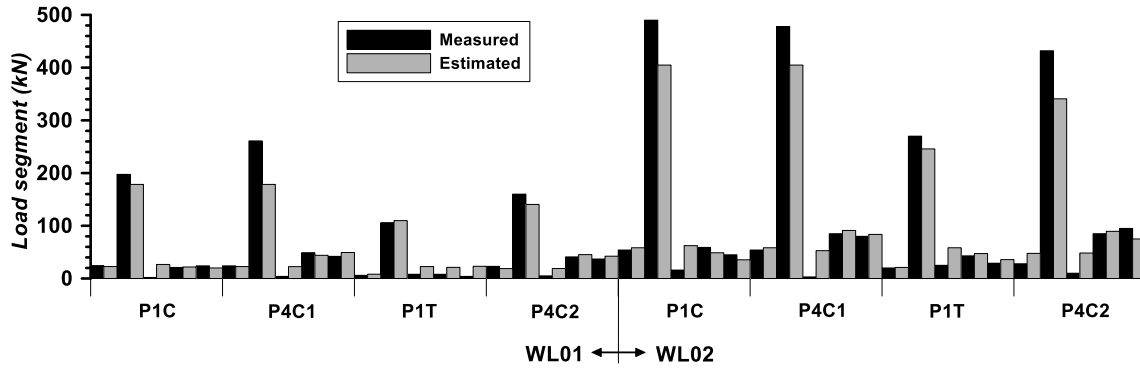


Figure C-7. Axial load distributions at limit state, for the rest of the piles (prototype scale): for each test, the five bar values from left to right = SG1, SG2-SG1, SG3-SG2, SG4-SG3, SG5-SG4, respectively.

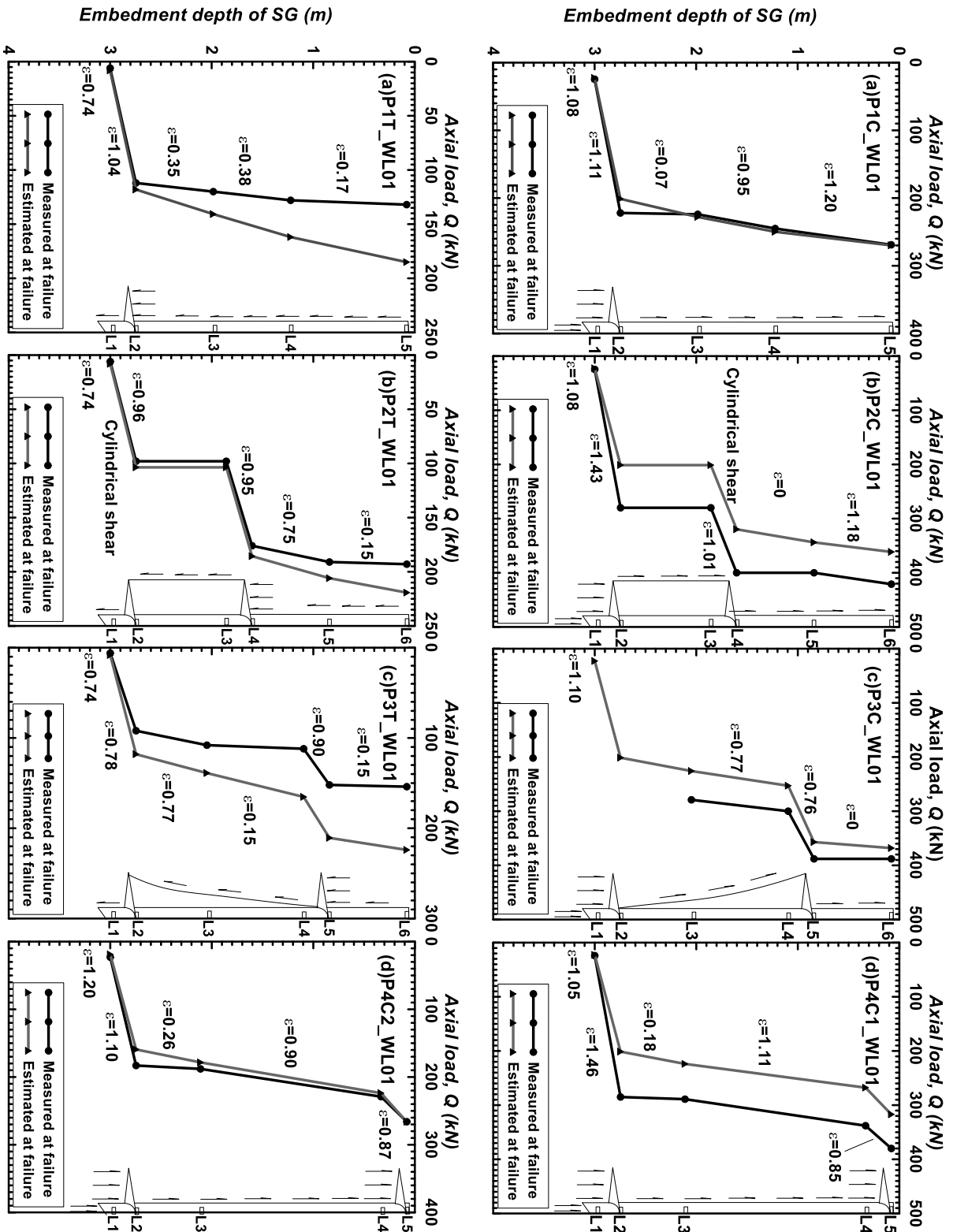


Figure C-8. Load distributions of all tests in WL01

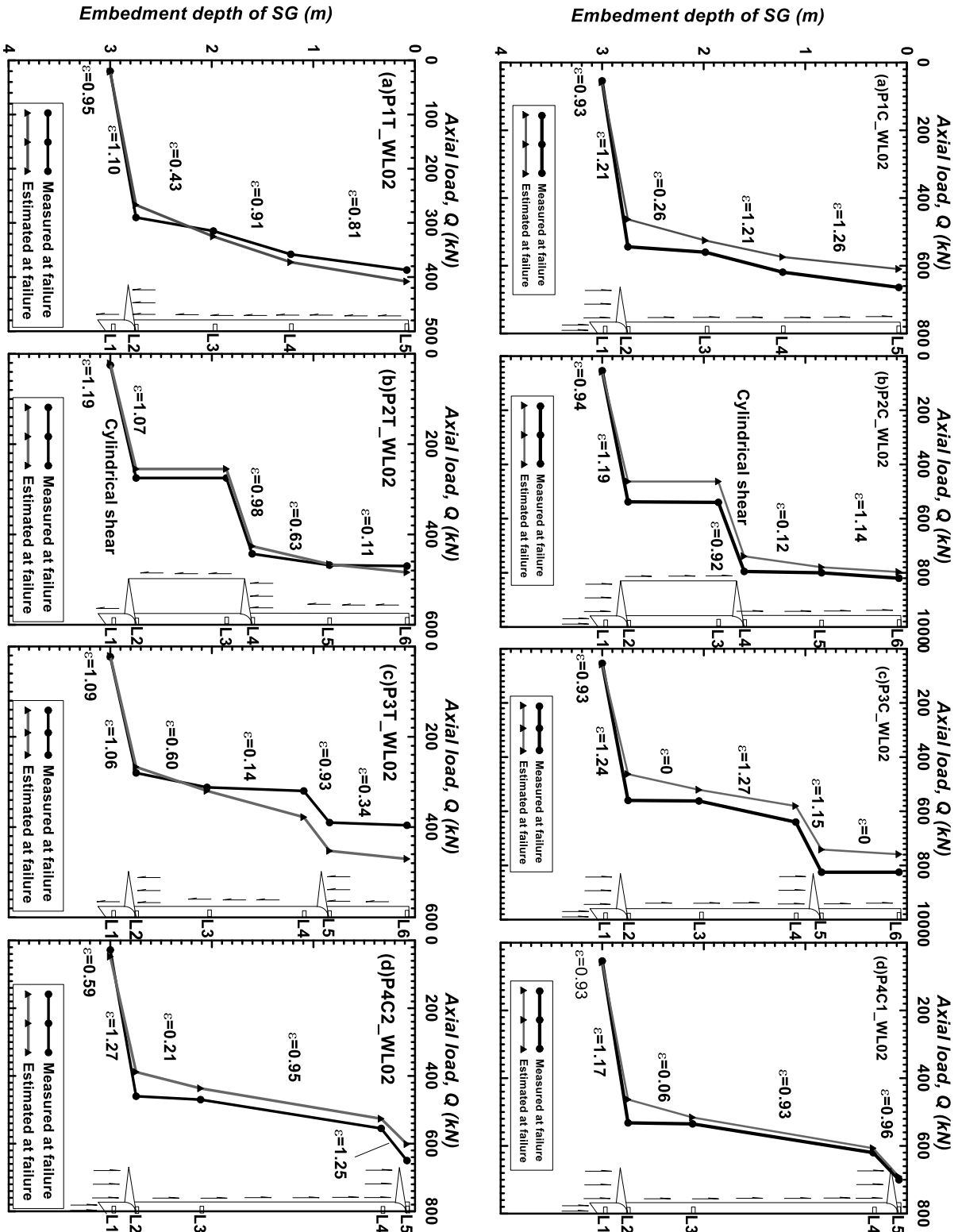


Figure C-9. Load distributions of all tests in WL02

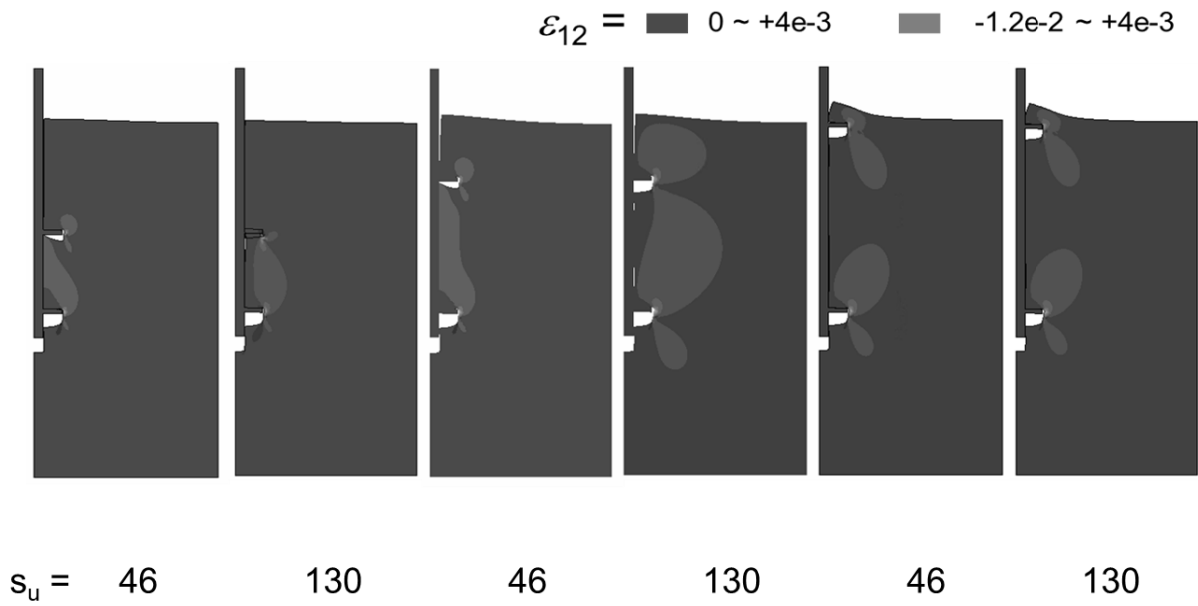


Figure C-10: Strain contours of selected simulations

Appendix D: Python Code Example for LDFE Analyses

This python code starts the simulation with building an undeformed model in ABAQUS including setting up the geometries, material properties, mesh, soil-pile interactions, and boundary conditions. The re-meshing and stress-strain field interpolation between every two small pile displacements were thereafter performed to convert the deformed model into a new un-deformed model. Iterations were continued until the expected large displacement was achieved. All operations were done by this python file without any user intervention.

A master code is a driver that executes the subcodes to carry out the original simulation, model remediation, remeshing, redefining sets and boundary conditions, solution mapping and remeshed simulation. All lines of the codes are attached as follows:

MASTER CODE

```
# Author: Weidong Li (weidong1@ualberta.ca)
# Edmonton, AB (Canada)
# Dec 2021
# *****
# This is the main script that drives the entire simulation.
# Create job and write input file for original job MESH-0*****
from abaqus import *
import part
import os, sys, re, osutils
import driverUtils, sys
```

```

from driverConstants import *
from abaqusConstants import *
from driverExceptions import *
from driverStandard import StandardAnalysis
from analysis import AnalysisApplication
sys.path.append(os.getcwd())

import uti

print "*****STARTING LDFE!*****"

platform = uti.getPlatform()

execfile('./Codes/original.py')

session.viewports['Viewport: 1'].setValues(displayedObject=udAssembly)
mdb.jobs[jobName+'1'].writeInput(consistencyChecking=OFF)

#*****Run original job *****
abq = driverUtils.getDriver()
cmd = []
cmd.append('-job')
cmd.append('%s' % jobName+'1' )
cmd.append('-input')
cmd.append('%s' % jobName+'1' )

```

```

cmd.append('-cpus')

cmd.append('%s' % '3' )

cmd.append('-interactive')

sys.stdout = sys.__stdout__

try:

    status = uti.spawnAndWait(abq, cmd)

except:

    print "Ooops..."

print 'First Incre'+ " Done!"

o1 = session.openOdb(

    name=jobName+'1+'.odb)

session.viewports['Viewport: 1'].setValues(displayedObject=o1)

session.viewports['Viewport: 1'].odbDisplay.display.setValues(plotState=(

    CONTOURS_ON_DEF, ))

#*****Run Remeshing Jobs*****

dispIncre = 0.01 # the

simulationNumber =2

while (simulationNumber <= 50):

    remeshJobName=jobName + "%i" % (simulationNumber)

    ancestorJobName=jobName + "%i" % (simulationNumber-1)

    execfile('./Codes/copyModelAndReplaceMesh.py')

    execfile('./Codes/redefineContacts.py')

```

```

execfile('./Codes/redefineBC.py')
execfile('./Codes/mapSolution.py')
execfile('./Codes/createRemeshedJobWriteInp.py')

cmd = []
cmd.append('-job')
cmd.append('%s' % remeshJobName )
cmd.append('-input')
cmd.append('%s' % remeshJobName )
cmd.append('-oldjob')
cmd.append('%s' % ancestorJobName )
cmd.append('-cpus')
cmd.append('%s' % '3' )
cmd.append('-interactive')
sys.stdout = sys.__stdout__

try:
    status = uti.spawnAndWait(abq, cmd)
except:
    print "Ooops..."

print "*****"

print "*****"+remeshJobName+" Done!*****"

print "*****"

simulationNumber=simulationNumber+1;

```

```
print "*****MESH-TO-MESH SOLUTION MAPPING HAS COMPLETED  
SUCCESSFULLY!*****"
```

```
print
```

```
*****"
```

```
mdb.save()
```



ORIGINAL MODEL

```
#  
# LDFE of Helical Piles in Clay, Weidong Li @ UAlberta  
#  
from abaqus import *  
from abaqusConstants import *  
from regionToolset import *  
from part import *  
from material import *  
from section import *  
from assembly import *  
from step import *  
from interaction import *  
from load import *  
from mesh import *  
from optimization import *  
from job import *  
from sketch import *  
from visualization import *  
from connectorBehavior import *  
session.viewports['Viewport: 1'].setValues(displayedObject=None)  
session.journalOptions.setValues(replayGeometry=COORDINATE,  
recoverGeometry=COORDINATE)
```

```

#-----
#Model input
#-----
# primary inputs
pileType = 3 # 2, 3, and 4 for Sr = 1.5, 2.5, and 3.5 respectively
suName = 130 # nominal su in kPa, for model naming purpose
EsuRatio = 235 # ratio of Young's modulus to su of the soil
CT = -1 # pile displacement direction -1 and +1 for Comp. and Tens. respectively

# secondary input
su = suName*1.0E+3 # undrained shear strength of the clay
EClay = su*EsuRatio # Young's modulus of soil
#-----

#-----
#Create model
#-----
Mdb()
udModel = mdb.models['Model-1'] # undeformed model
#-----
mdbName = 'P'+str(pileType)+'_'+str(suName)+'_'+str(CT)+'_'

```

```

odbName = 'P'+str(pileType)+'_'+str(suName)+'_'+str(CT)+'_'
jobName = 'P'+str(pileType)+'_'+str(suName)+'_'+str(CT)+'_'

mdb.saveAs(mdbName+'1')

#-----

#Create parts

#-----

# Sketches

sPile = udModel.ConstrainedSketch(name='sPile',
    sheetSize=10.0)    #create a sketch window for pile
sPile.sketchOptions.setValues(viewStyle=AXISYM)

sSoil = udModel.ConstrainedSketch(name='sSoil',
    sheetSize=10.0)    #create a sketch window for soil
sSoil.sketchOptions.setValues(viewStyle=AXISYM)

import numpy as np
import os

pCoords = np.loadtxt('./RITSS_Input/P'+str(pileType)+'ConfigL3D.txt') #import the node
coordinates of pile

sCoords = np.loadtxt('./RITSS_Input/P'+str(pileType)+'ClayConfigL3D.txt') #import the node
coordinates of soil

```



```

nNodePile=len(pCoords)-1 #number of geometry noded of pile
nNodeSoil=len(sCoords)-1 #number of geometry nodes of soil

sPile.ConstructionLine(point1=(pCoords[nNodePile-1,0], pCoords[nNodePile-1,1]),
    point2=(pCoords[nNodePile,0], pCoords[nNodePile,1])) # create construction line of pile
sketch
for i in range(nNodePile):
    sPile.Line(point1=(pCoords[i,0], pCoords[i,1]), point2=(pCoords[i+1,0], pCoords[i+1,1]))
#draw sketch of pile

sSoil.ConstructionLine(point1=(sCoords[nNodeSoil-1,0], sCoords[nNodeSoil-1,1]),
    point2=(sCoords[nNodeSoil,0], sCoords[nNodeSoil,1])) # construction line of soil sketch
for i in range(nNodeSoil):
    sSoil.Line(point1=(sCoords[i,0], sCoords[i,1]), point2=(sCoords[i+1,0], sCoords[i+1,1]))
#draw sketch of soil

#create parts based on the sketch
pPile = udModel.Part(name='pile', dimensionality=AXISYMMETRIC,
type=DEFORMABLE_BODY) #define pile part category
pPile.BaseShell(sketch=sPile) # create pile part
del udModel.sketches['sPile'] # delet the sketch

```

```

pSoil      =      udModel.Part(name='soil',      dimensionality=AXISYMMETRIC,
type=DEFORMABLE_BODY) #define soil part category
pSoil.BaseShell(sketch=sSoil) # create soil part
del udModel.sketches['sSoil'] # delet the sketch

#-----

#-----

#Create materials and sections, and assig materials to sections
#-----

# material of pile
Alum = udModel.Material(name='Alum') # create pile material, aluminum
udModel.materials['Alum'].Density(table=((2700.0, ), )) # assign density
udModel.materials['Alum'].Elastic(table=((69E+9, 0.3),)) # assign Young's modulus and Poisson
ratio
udModel.materials['Alum'].Plastic(table=((376E+6, 0.0),)) #assign yield strength and plastic
strain at yield point

# section of pile
udModel.HomogeneousSolidSection(material='Alum', name='Section-Alum', thickness=None) #
cretae pile section, zero thickniss
facesP = pPile.faces # mark the facse of pile
region1 = pPile.Set(faces=facesP, name='fPSet') # wrap up the pile face into a region

```

```

pPile.SectionAssignment(region=region1, sectionName='Section-Alum', offset=0.0,
    offsetType=MIDDLE_SURFACE, offsetField=") # assign the pile section to the pile part
geometry

# material of soil

Clay = udModel.Material(name='Clay') # create soil material
udModel.materials['Clay'].Density(table=((2000.0, ), )) # assign density
udModel.materials['Clay'].Elastic(table=((EClay, 0.49),)) # assign Young's modulus and Poisson
ratio
udModel.materials['Clay'].MohrCoulombPlasticity(table=((0.0,
    0.0), ), useTensionCutoff=False) #assign parameters to M-C plasticity: (friction angle, state
parameter)
udModel.materials['Clay'].mohrCoulombPlasticity.MohrCoulombHardening(
    table=((su, 0.0), )) #create hardening table, constant yield stress herein onwards zero plastic
strain

# section of soil

udModel.HomogeneousSolidSection(material='Clay', name='Section-Clay', thickness=None) #
create soil section, zero thickness

facesS = pSoil.faces # mark the faces of soil

region2 = pSoil.Set(faces=facesS, name='fSSet') # wrap up the pile face into a region

pSoil.SectionAssignment(region=region2, sectionName='Section-Clay', offset=0.0,

```

```

    offsetType=MIDDLE_SURFACE, offsetField=") # assign the pile section to the pile part
geometry
#-----

#-----

#Create instances
#-----

udAssembly = udModel.rootAssembly
udAssembly.DatumCsysByDefault(CARTESIAN) # default coordinate system is CARTESIAN
instancePile = udAssembly.Instance(name='insPile', part=pPile, dependent=ON) #pile instance
instanceSoil = udAssembly.Instance(name='insSoil', part=pSoil, dependent=ON) #soil instance
udAssembly.regenerate() # generate the assembly
#-----

#-----

# Meshing
#-----

# mesh pile part
pPile.setMeshControls(elemShape=QUAD, regions=facesP, allowMapped=True) # set controls
on edge meshing
pPile.seedEdgeBySize(edges=pPile.edges, size=0.03175, constraint=FREE) # seed the edge by
size

```

```

pPile.setElementType(elemTypes=(ElemType(
    elemCode=CAX4R, elemLibrary=STANDARD, secondOrderAccuracy=OFF,
    hourglassControl=DEFAULT, distortionControl=DEFAULT),ElemType(
    elemCode=CAX3, elemLibrary=STANDARD)), regions=(facesP,)) # define element type
pPile.generateMesh() # generate mesh on pile part

# mesh soil part
pSoil.setMeshControls(elemShape=QUAD, regions=facesS, allowMapped=True) # set controls
on edge meshing
pSoil.seedEdgeBySize(edges=pSoil.edges.getByBoundingBox(pCoords[0,0]-0.1, pCoords[0,1]-
0.1, 0.0,
    pCoords[nNodePile-1,0]+1.0, pCoords[nNodePile-1,1]+1.0,0.0), size=0.0211,
constraint=FREE) # seed the edge in contact with pile
pSoil.seedEdgeBySize(edges=pSoil.edges.getByBoundingBox(pCoords[0,0]+2.0, pCoords[0,1]-
3.0, 0.0,
    pCoords[nNodePile-1,0]+5.0, pCoords[nNodePile-1,1]+0.01,0.0), size=0.1, constraint=FREE)
# seed the edge in the far field
pSoil.seedEdgeBySize(edges=pSoil.edges.getByBoundingBox(pCoords[0,0]-0.1, pCoords[0,1]-
3.0, 0.0,
    pCoords[0,0]+0.01, pCoords[0,1]+0.01, 0.0), size=0.03175, constraint=FREE) # seed the
vertical edge under pile toe by size
pSoil.seedEdgeBySize(edges=pSoil.edges.getByBoundingBox(pCoords[0,0]-0.1, pCoords[0,1]-
3.0, 0.0,

```

```

    pCoords[0,0]+5.0, pCoords[0,1]-0.5, 0.0), size=0.05, constraint=FREE) # seed the bottom edge
by size
pSoil.seedEdgeBySize(edges=pSoil.edges.getByBoundingBox(pCoords[nNodePile-1,0]-0.1,
pCoords[nNodePile-1,1]-1.0, 0.0,
    pCoords[nNodePile-1,0]+5.0, pCoords[nNodePile-1,1], 0.0), size=0.05, constraint=FREE) #
seed the surface edge by size
pSoil.setElementType(elemTypes=(ElemType(
    elemCode=CAX4RH, elemLibrary=STANDARD, secondOrderAccuracy=OFF,
    hourglassControl=DEFAULT, distortionControl=DEFAULT), ElemType(
    elemCode=CAX3, elemLibrary=STANDARD)), regions=(facesS,)) # define element type
pSoil.generateMesh() # generate mesh on soil part
#-----

#Create time steps, geoStatic neglected
#-----

# load step
udModel.StaticStep(name='Step-1', adaptiveDampingRatio=None,
    continueDampingFactors=False, description='LoadIncre', initialInc=0.02,
    matrixSolver=DIRECT, matrixStorage=UNSYMMETRIC, maxInc=0.5, maxNumInc=100,
    nlgeom=ON, previous='Initial', solutionTechnique=FULL_NEWTON,
    stabilizationMethod=NONE)
udModel.steps['Step-1'].Restart(frequency=1, numberIntervals=0,

```

```

overlay=ON, timeMarks=OFF)

udModel.FieldOutputRequest(name='F-Output-1',

    createStepName='Step-1', variables=('S', 'U', 'E', 'COORD', 'PE', 'PEEQ'))

#-----

#-----

# create contacs

#-----

# contact surfaces on pile

for i in range(10):

    udAssembly.Surface(name='pContactSurface'+str(i+1), side1Edges=

instancePile.edges.findAt(((0.5*(pCoords[i,0]+pCoords[i+1,0]),0.5*(pCoords[i,1]+pCoords[i+1,

1]),0.0),)))

# contact surface on soil

for i in range(10):

    udAssembly.Surface(name='sContactSurface'+str(i+1), side1Edges=

instanceSoil.edges.findAt(((0.5*(sCoords[i,0]+sCoords[i+1,0]),0.5*(sCoords[i,1]+sCoords[i+1,1

]),0.0),)))

```

```

# merge surfaces on soil for contact

# Compression

udAssembly.SurfaceByBoolean(name='sConSurf-C1',
    surfaces=(udAssembly.surfaces['sContactSurface1'],
        udAssembly.surfaces['sContactSurface2'],
        udAssembly.surfaces['sContactSurface3']))

udAssembly.SurfaceByBoolean(name='sConSurf-C2',
    surfaces=(udAssembly.surfaces['sContactSurface6'],
        udAssembly.surfaces['sContactSurface7']))

# Tension

udAssembly.SurfaceByBoolean(name='sConSurf-T1',
    surfaces=(udAssembly.surfaces['sContactSurface5'],
        udAssembly.surfaces['sContactSurface6']))

udAssembly.SurfaceByBoolean(name='sConSurf-T2',
    surfaces=(udAssembly.surfaces['sContactSurface9'],
        udAssembly.surfaces['sContactSurface10']))

# Create contact properties and soil-pile interactions

udModel.ContactProperty('SoilPileContact') # create soil-pile contact

udModel.interactionProperties['SoilPileContact'].TangentialBehavior(
    formulation=ROUGH) # define soil-pile shear behavior

udModel.interactionProperties['SoilPileContact'].NormalBehavior(

```



```
allowSeparation=OFF, constraintEnforcementMethod=DEFAULT,  
pressureOverclosure=HARD) # define soil-pile normal interaction
```

```
# assembl contact pairs
```

```
if CT == 1:
```

```
udModel.SurfaceToSurfaceContactStd(adjustMethod=TOLERANCE,  
adjustTolerance=0.0005, clearanceRegion=None,  
datumAxis=None, initialClearance=OMIT,  
name='SoilPileS2S-T1A', createStepName = 'Initial',  
master=udAssembly-surfaces['pContactSurface5'],  
slave=udAssembly-surfaces['sConSurf-T1'],  
sliding=FINITE, interactionProperty = 'SoilPileContact')
```

```
udModel.SurfaceToSurfaceContactStd(adjustMethod=TOLERANCE,  
adjustTolerance=0.0005, clearanceRegion=None,  
datumAxis=None, initialClearance=OMIT,  
name='SoilPileS2S-T1B', createStepName = 'Initial',  
master=udAssembly-surfaces['pContactSurface6'],  
slave=udAssembly-surfaces['sConSurf-T1'],  
sliding=FINITE, interactionProperty = 'SoilPileContact')
```

```
udModel.SurfaceToSurfaceContactStd(adjustMethod=TOLERANCE,  
adjustTolerance=0.0005, clearanceRegion=None,  
datumAxis=None, initialClearance=OMIT,
```

```

name='SoilPileS2S-T2A', createStepName = 'Initial',
master=udAssembly-surfaces['pContactSurface9'],
slave=udAssembly-surfaces['sConSurf-T2'],
sliding=FINITE, interactionProperty = 'SoilPileContact')
udModel.SurfaceToSurfaceContactStd(adjustMethod=TOLERANCE,
adjustTolerance=0.0005, clearanceRegion=None,
datumAxis=None, initialClearance=OMIT,
name='SoilPileS2S-T2B', createStepName = 'Initial',
master=udAssembly-surfaces['pContactSurface10'],
slave=udAssembly-surfaces['sConSurf-T2'],
sliding=FINITE, interactionProperty = 'SoilPileContact')### Contact pairs of soil-to-pile in
Tens
elif CT == -1:
udModel.SurfaceToSurfaceContactStd(adjustMethod=TOLERANCE,
adjustTolerance=0.0005, clearanceRegion=None,
datumAxis=None, initialClearance=OMIT,
name='SoilPileS2S-C1A', createStepName = 'Initial',
master=udAssembly-surfaces['pContactSurface1'],
slave=udAssembly-surfaces['sConSurf-C1'],
sliding=FINITE, interactionProperty = 'SoilPileContact')
udModel.SurfaceToSurfaceContactStd(adjustMethod=TOLERANCE,
adjustTolerance=0.0005, clearanceRegion=None,
datumAxis=None, initialClearance=OMIT,

```

```

name='SoilPileS2S-C1B', createStepName = 'Initial',
master=udAssembly-surfaces['pContactSurface2'],
slave=udAssembly-surfaces['sConSurf-C1'],
sliding=FINITE, interactionProperty = 'SoilPileContact')
udModel.SurfaceToSurfaceContactStd(adjustMethod=TOLERANCE,
adjustTolerance=0.0005, clearanceRegion=None,
datumAxis=None, initialClearance=OMIT,
name='SoilPileS2S-C1C', createStepName = 'Initial',
master=udAssembly-surfaces['pContactSurface3'],
slave=udAssembly-surfaces['sConSurf-C1'],
sliding=FINITE, interactionProperty = 'SoilPileContact')
udModel.SurfaceToSurfaceContactStd(adjustMethod=TOLERANCE,
adjustTolerance=0.0005, clearanceRegion=None,
datumAxis=None, initialClearance=OMIT,
name='SoilPileS2S-C2A', createStepName = 'Initial',
master=udAssembly-surfaces['pContactSurface6'],
slave=udAssembly-surfaces['sConSurf-C2'],
sliding=FINITE, interactionProperty = 'SoilPileContact')
udModel.SurfaceToSurfaceContactStd(adjustMethod=TOLERANCE,
adjustTolerance=0.0005, clearanceRegion=None,
datumAxis=None, initialClearance=OMIT,
name='SoilPileS2S-C2B', createStepName = 'Initial',
master=udAssembly-surfaces['pContactSurface7'],

```

```

slave=udAssembly-surfaces['sConSurf-C2'],
sliding=FINITE, interactionProperty = 'SoilPileContact')
udModel.SurfaceToSurfaceContactStd(adjustMethod=TOLERANCE,
adjustTolerance=0.0005, clearanceRegion=None,
datumAxis=None, initialClearance=OMIT,
name='SoilPileS2S-C3', createStepName = 'Initial',
master=udAssembly-surfaces['pContactSurface10'],
slave=udAssembly-surfaces['sContactSurface10'],
sliding=FINITE, interactionProperty = 'SoilPileContact') ### Contact pairs of soil-to-pile in
Comp

```

```

#-----

```

```

#-----

```

```

#Create BC's

```

```

#-----

```

```

# Bottom of soil

```

```

soilBottomEdge = udAssembly.Set(edges=
udAssembly.instances['insSoil'].edges.findAt(((
0.5*sCoords[nNodeSoil-1,0]+0.5*sCoords[nNodeSoil-2,0],

```

```

0.5*sCoords[nNodeSoil-1,1]+0.5*sCoords[nNodeSoil-2,1], 0.0), )),
name='BC_bottomSoil')
# The bottom side of the soil is fixed in all dof's
udModel.DisplacementBC(amplitude=UNSET, createStepName='Initial',
distributionType=UNIFORM, fieldName="", localCsys=None, name='BC_bottomSoil',
region=soilBottomEdge, u1=SET, u2=SET, ur3=UNSET)
#
# Right side of soil
soilRightEdge = udAssembly.Set(edges=
udAssembly.instances['insSoil'].edges.findAt(((
0.5*sCoords[nNodeSoil-2,0]+0.5*sCoords[nNodeSoil-3,0],
0.5*sCoords[nNodeSoil-2,1]+0.5*sCoords[nNodeSoil-3,1], 0.0), )),
name='BC_rightSoil')
# The right side line of the soil is fixed in x
udModel.DisplacementBC(amplitude=UNSET, createStepName='Initial',
distributionType=UNIFORM, fieldName="", localCsys=None, name='BC_rightSoil',
region=soilRightEdge, u1=SET, u2=UNSET, ur3=UNSET)
#
#center line of soil
soilCenterEdge = udAssembly.Set(edges=
udAssembly.instances['insSoil'].edges.findAt(((

```

```

0.5*sCoords[nNodeSoil,0]+0.5*sCoords[nNodeSoil-1,0],
0.5*sCoords[nNodeSoil,1]+0.5*sCoords[nNodeSoil-1,1], 0.0), )),
name='BC_centerSoil')

# center line of the soil is fixed in x
udModel.DisplacementBC(amplitude=UNSET, createStepName='Initial',
distributionType=UNIFORM, fieldName="", localCsys=None, name='BC_centerSoil',
region=soilCenterEdge, u1=SET, u2=UNSET, ur3=UNSET)

#

#center line of pile
pileCenterEdge = udAssembly.Set(edges=
udAssembly.instances['insPile'].edges.findAt(((
0.5*pCoords[nNodePile,0]+0.5*pCoords[nNodePile-1,0],
0.5*pCoords[nNodePile,1]+0.5*pCoords[nNodePile-1,1], 0.0), )),
name='BC_centerPile')

# The center line of the pile is fixed in x
udModel.DisplacementBC(amplitude=UNSET, createStepName='Initial',
distributionType=UNIFORM, fieldName="", localCsys=None, name='BC_centerPile',
region=pileCenterEdge, u1=SET, u2=UNSET, ur3=UNSET)

#-----

#-----

#Create loads

```

```

#-----
# Disp. controlled load

dispIncr = 0.02 #each simulation increment is 10 mm

pileHeadEdge = udAssembly.Set(name='pileHeadLoadEdge',
    edges = instancePile.edges.findAt(((
    0.5*pCoords[nNodePile-1,0]+0.5*pCoords[nNodePile-2,0],
    0.5*pCoords[nNodePile-1,1]+0.5*pCoords[nNodePile-2,1], 0.0), )))

udModel.DisplacementBC(amplitude=UNSET, createStepName='Step-1',
    distributionType=UNIFORM, fieldName="", fixed=OFF, localCsys=None, name=
    'Penetration', region=pileHeadEdge, u1=
    UNSET, u2=CT*dispIncr, ur3=UNSET)

#-----

#-----

#Create Jobs

#-----

# This will creat the first odb file

mdb.Job(name=jobName+'1', model='Model-1', type=ANALYSIS,
    nodalOutputPrecision=SINGLE, description='Run the first incre simulation',
    multiprocessingMode=DEFAULT,
    numDomains=3, userSubroutine="", numCpus=3, memory=80,

```

```

memoryUnits=PERCENTAGE, scratch="", echoPrint=OFF, modelPrint=OFF,
contactPrint=OFF, historyPrint=OFF)

#-----

udModel.setValues(noPartsInputFile=OFF)

mdb.jobs[jobName+'1'].writeInput(consistencyChecking=OFF)

#Track all geometry vertices of the

for i in range(nNodePile):

    node=udAssembly.instances['insPile'].nodes.getClosest(((pCoords[i,0], pCoords[i,1], 0.0),),)

    nodeLabel=node[0].label

    udAssembly.SetFromNodeLabels('pileNodeSet'+str(i), (('insPile', (nodeLabel,)),))

#

for i in range(nNodeSoil):

    node=udAssembly.instances['insSoil'].nodes.getClosest(((sCoords[i,0], sCoords[i,1], 0.0),),)

    nodeLabel=node[0].label

    udAssembly.SetFromNodeLabels('soilNodeSet'+str(i), (('insSoil', (nodeLabel,)),))

#-----

mdb.jobs[jobName+'1'].writeInput(consistencyChecking=OFF)

mdb.save()

#-----

```


MODEL REMEDIATION AND REMESHING

Author: Weidong Li (weidong1@ualberta.ca)

Edmonton, AB (Canada)

Dec 2021

This is the script that redefines the sections and remeshes the model parts.

```
model = mdb.Model(name='Model-'+str(simulationNumber),
objectToCopy=mdb.models['Model-'+str(simulationNumber-1)])
```

NOTE: USER MUST DEFINE THESE VARIABLES.

anOdbName = ancestorJobName+'.odb' # Name of output database file.

angle = 15 # Feature angle.

importStep = 0 # Step number. 0 MEANS THE LAST STEP

Import orphan mesh part for pile

```
orphanPile=model.PartFromOdb(fileName=anOdbName,
name='orphanPile', instance='INSPILE', shape=DEFORMED, step=importStep)
```

Extract 2D profile and create a solid part for pile

```
pPile=model.Part2DGeomFrom2DMesh(name='pile',
part=orphanPile, featureAngle=angle)
```

Import orphan mesh part for soil

```
orphanSoil=model.PartFromOdb(fileName=anOdbName,
```

```

    name='orphanSoil', instance='INSSOIL', shape=DEFORMED, step=importStep)
# Extract 2D profile and create a solid part for soil
pSoil=model.Part2DGeomFrom2DMesh(name='soil',
    part=orphanSoil, featureAngle=angle)

del model.parts['orphanPile']
del model.parts['orphanSoil']

# Combine broken topo lines of pile and soil parts-----

# Call coordinates of the deformed geometry nodes
odb=session.openOdb(name='readOdb', path=anOdbName, readOnly=True)
frame=odb.steps['Step-1'].frames[-1]

coordPileNodes=[]
for i in range(nNodePile):
    pileNodeSet=odb.rootAssembly.nodeSets['PILENODESET'+str(i)]
    nodeCoordX=frame.fieldOutputs['COORD'].getSubset(region=pileNodeSet).values[0].data[0]
    nodeCoordY=frame.fieldOutputs['COORD'].getSubset(region=pileNodeSet).values[0].data[1]
    nodeCoordZ=0.0
    nodeCoords=(nodeCoordX, nodeCoordY, nodeCoordZ)
    coordPileNodes.append(nodeCoords)

```

```

coordSoilNodes=[]

for i in range(nNodeSoil):

    soilNodeSet=odb.rootAssembly.nodeSets['SOILNODESET'+str(i)]

    nodeCoordX=frame.fieldOutputs['COORD'].getSubset(region=soilNodeSet).values[0].data[0]

    nodeCoordY=frame.fieldOutputs['COORD'].getSubset(region=soilNodeSet).values[0].data[1]

    nodeCoordZ=0.0

    nodeCoords=(nodeCoordX, nodeCoordY, nodeCoordZ)

    coordSoilNodes.append(nodeCoords)

# ignore the unnecessary vertices

TOL = 0.0001

# pile part

pileVertices=pPile.vertices

pileVertexCoordList=[]

for i in range(len(pileVertices)):

    vertexCoords=pileVertices[i].pointOn[0]

    pileVertexCoordList.append(vertexCoords)

repeatedNodes=[]

for i in range(len(pileVertexCoordList)):

```

```

element1=pileVertexCoordList[i]
x1=element1[0]
y1=element1[1]
for j in range(len(coordPileNodes)):
    element2=coordPileNodes[j]
    x2=element2[0]
    y2=element2[1]
    if abs(x1-x2)<TOL and abs(y1-y2)<TOL:
        repeatedNodes.append(element1)
    else:
        pass

verPileToIgnoreList=list(set(pileVertexCoordList)^set(repeatedNodes))
for i in range(len(verPileToIgnoreList)):
    tupleX=verPileToIgnoreList[i][0]
    tupleY=verPileToIgnoreList[i][1]
    pPile.ignoreEntity(entities=(pPile.vertices.findAt(((tupleX, tupleY,
0.0), ), ), ))

print 'Pile edges are fixed!'

# Soil part
soilVertices=pSoil.vertices

```

```

soilVertexCoordList=[]
for i in range(len(soilVertices)):
    vertexCoords=soilVertices[i].pointOn[0]
    soilVertexCoordList.append(vertexCoords)

repeatedNodes=[]
for i in range(len(soilVertexCoordList)):
    element1=soilVertexCoordList[i]
    x1=element1[0]
    y1=element1[1]
    for j in range(len(coordSoilNodes)):
        element2=coordSoilNodes[j]
        x2=element2[0]
        y2=element2[1]
        if abs(x1-x2)<TOL and abs(y1-y2)<TOL:
            repeatedNodes.append(element1)
        else:
            pass

verSoilToIgnoreList=list(set(soilVertexCoordList)^set(repeatedNodes))
for i in range(len(verSoilToIgnoreList)):
    tupleX=verSoilToIgnoreList[i][0]
    tupleY=verSoilToIgnoreList[i][1]

```

```

pSoil.ignoreEntity(entities=(pSoil.vertices.findAt(((tupleX, tupleY,
0.0), )), ))

print 'Soil edges are fixed!'

#-----

#Create instances

#-----

assembly=model.rootAssembly #
instancePile = assembly.Instance(name='insPile', part=pPile, dependent=ON) #pile instance
instanceSoil = assembly.Instance(name='insSoil', part=pSoil, dependent=ON) #soil instance
assembly.regenerate() # generate the assembly

#Redefine geometry node sets-----

# update pCoords and sCoords in the initial order
for i in range(nNodePile):
    pCoords[i,0]=coordPileNodes[i][0]
    pCoords[i,1]=coordPileNodes[i][1]

for i in range(nNodeSoil):
    sCoords[i,0]=coordSoilNodes[i][0]
    sCoords[i,1]=coordSoilNodes[i][1]

```

```

#-----
print 'Deformed parts are now ready for remeshing.'

facesP = pPile.faces # mark the face of pile
region1 = pPile.Set(faces=facesP, name='fPSet') # wrap up the pile face into a region
pPile.SectionAssignment(region=region1, sectionName='Section-Alum', offset=0.0,
    offsetType=MIDDLE_SURFACE, offsetField='') # assign the pile section
facesS = pSoil.faces # mark the face of pile
region2 = pSoil.Set(faces=facesS, name='fSSet') # wrap up the pile face into a region
pSoil.SectionAssignment(region=region2, sectionName='Section-Clay', offset=0.0,
    offsetType=MIDDLE_SURFACE, offsetField='') # assign the soil section
assembly.regenerate()

# Mesh the pile part
facesP = pPile.faces # mark the face of pile
pPile.setMeshControls(elemShape=QUAD, regions=facesP, allowMapped=True) # set controls
on edge meshing
pPile.seedEdgeBySize(edges=pPile.edges, size=0.03175, constraint=FREE) # seed the edge by
size
pPile.setElementType(elemTypes=(ElemType(
    elemCode=CAX4R, elemLibrary=STANDARD, secondOrderAccuracy=OFF,
    hourglassControl=DEFAULT, distortionControl=DEFAULT),ElemType(
    elemCode=CAX3, elemLibrary=STANDARD)), regions=(facesP,)) # define element type

```

```

pPile.generateMesh() # generate mesh on pile part

# mesh soil part

pSoil.setMeshControls(elemShape=QUAD, regions=facesS, allowMapped=True) # set controls
on edge meshing

pSoil.seedEdgeBySize(edges=pSoil.edges.getByBoundingBox(sCoords[0,0]-0.1, sCoords[0,1]-
0.1, 0.0,
    sCoords[10,0]+0.5, sCoords[10,1]+0.1, 0.0), size=0.0211, constraint=FREE) # seed the edges
in contact with pile

pSoil.seedEdgeBySize(edges=pSoil.edges.getByBoundingBox(sCoords[12,0]-0.1,
sCoords[12,1]-0.1, 0.0,
    sCoords[11,0]+0.1, sCoords[11,1]+0.1, 0.0), size=0.1, constraint=FREE) # seed the edge in the
far field

pSoil.seedEdgeBySize(edges=pSoil.edges.getByBoundingBox(sCoords[13,0]-0.1,
sCoords[13,1]-0.1, 0.0,
    sCoords[14,0]+0.01, sCoords[14,1]+0.1, 0.0), size=0.03175, constraint=FREE) # seed the
vertical edge under pile toe by size

pSoil.seedEdgeBySize(edges=pSoil.edges.getByBoundingBox(sCoords[13,0]-0.1,
sCoords[13,1]-0.1, 0.0,
    sCoords[12,0]+0.1, sCoords[12,1]+0.1, 0.0), size=0.05, constraint=FREE) # seed the bottom
edge by size

pSoil.seedEdgeBySize(edges=pSoil.edges.getByBoundingBox(sCoords[10,0]-0.1,
sCoords[10,1]-0.1, 0.0,

```



```

    sCoords[11,0]+0.1, sCoords[11,1]+0.1, 0.0), size=0.05, constraint=FREE) # seed the surface
edge by size
pSoil.setElementType(elemTypes=(ElemType(
    elemCode=CAX4RH, elemLibrary=STANDARD, secondOrderAccuracy=OFF,
    hourglassControl=DEFAULT, distortionControl=DEFAULT), ElemType(
    elemCode=CAX3, elemLibrary=STANDARD)), regions=(facesS,)) # define element type
pSoil.generateMesh() # generate mesh on soil part
#-----
session.viewports['Viewport: 1'].setValues(displayedObject=assembly)
print 'Remshing completed. RITSS-'+str(simulationNumber)

```

REDEFINE SETS

```
# Author: Weidong Li (weidong1@ualberta.ca)

# Edmonton, AB (Canada)

# Dec 2021

# *****

# This is the msript that redefines the sets.

#Track all geometry vertices of the

for i in range(nNodePile):

    node=assembly.instances['insPile'].nodes.getClosest(((pCoords[i,0], pCoords[i,1], 0.0)),)

    nodeLabel=node[0].label

    assembly.SetFromNodeLabels('pileNodeSet'+str(i), (('insPile', (nodeLabel,)),))

#

for i in range(nNodeSoil):

    node=assembly.instances['insSoil'].nodes.getClosest(((sCoords[i,0], sCoords[i,1], 0.0)),)

    nodeLabel=node[0].label

    assembly.SetFromNodeLabels('soilNodeSet'+str(i), (('insSoil', (nodeLabel,)),))

#-----
```

REDEFINE CONTACTS

Author: Weidong Li (weidong1@ualberta.ca)

Edmonton, AB (Canada)

Dec 2021

This is the script that redefines the contact surfaces.

#-----

create contacs

#-----

contact surfaces on pile

for i in range(10):

vertex=instancePile.edges.getClosest(((0.5*(pCoords[i,0]+pCoords[i+1,0]),0.5*(pCoords[i,1]+pCoords[i+1,1]),0.0),))

edge=instancePile.edges.findAt((((vertex[0][1])),))

assembly.Surface(name='pContactSurface'+str(i+1), side1Edges=edge)

contact surface on soil

for i in range(10):

```
vertex=instanceSoil.edges.getClosest(((0.5*(sCoords[i,0]+sCoords[i+1,0]),0.5*(sCoords[i,1]+sC  
oords[i+1,1]),0.0),))
```

```
edge=instanceSoil.edges.findAt((((vertex[0][1])),))
```

```
assembly.Surface(name='sContactSurface'+str(i+1), side1Edges=edge)
```

```
# merge surfaces on soil for contact
```

```
# Compression
```

```
assembly.SurfaceByBoolean(name='sConSurf-C1',  
surfaces=(assembly-surfaces['sContactSurface1'],  
assembly-surfaces['sContactSurface2'],  
assembly-surfaces['sContactSurface3']))
```

```
assembly.SurfaceByBoolean(name='sConSurf-C2',  
surfaces=(assembly-surfaces['sContactSurface6'],  
assembly-surfaces['sContactSurface7']))
```

```
# Tension
```

```
assembly.SurfaceByBoolean(name='sConSurf-T1',  
surfaces=(assembly-surfaces['sContactSurface5'],  
assembly-surfaces['sContactSurface6']))
```

```
assembly.SurfaceByBoolean(name='sConSurf-T2',  
surfaces=(assembly-surfaces['sContactSurface9'],
```

```
assembly-surfaces['sContactSurface10']))
```

```
# assemble contact pairs
```

```
if CT == 1:
```

```
    model.SurfaceToSurfaceContactStd(adjustMethod=TOLERANCE,  
        adjustTolerance=0.0005, clearanceRegion=None,  
        datumAxis=None, initialClearance=OMIT,  
        name='SoilPileS2S-T1A', createStepName = 'Initial',  
        master=assembly-surfaces['pContactSurface5'],  
        slave=assembly-surfaces['sConSurf-T1'],  
        sliding=FINITE, interactionProperty = 'SoilPileContact')
```

```
    model.SurfaceToSurfaceContactStd(adjustMethod=TOLERANCE,  
        adjustTolerance=0.0005, clearanceRegion=None,  
        datumAxis=None, initialClearance=OMIT,  
        name='SoilPileS2S-T1B', createStepName = 'Initial',  
        master=assembly-surfaces['pContactSurface6'],  
        slave=assembly-surfaces['sConSurf-T1'],  
        sliding=FINITE, interactionProperty = 'SoilPileContact')
```

```
    model.SurfaceToSurfaceContactStd(adjustMethod=TOLERANCE,  
        adjustTolerance=0.0005, clearanceRegion=None,  
        datumAxis=None, initialClearance=OMIT,  
        name='SoilPileS2S-T2A', createStepName = 'Initial',
```

```

    master=assembly-surfaces['pContactSurface9'],
    slave=assembly-surfaces['sConSurf-T2'],
    sliding=FINITE, interactionProperty = 'SoilPileContact')
model.SurfaceToSurfaceContactStd(adjustMethod=TOLERANCE,
    adjustTolerance=0.0005, clearanceRegion=None,
    datumAxis=None, initialClearance=OMIT,
    name='SoilPileS2S-T2B', createStepName = 'Initial',
    master=assembly-surfaces['pContactSurface10'],
    slave=assembly-surfaces['sConSurf-T2'],
    sliding=FINITE, interactionProperty = 'SoilPileContact')### Contact pairs of soil-to-pile in

```

Tens

elif CT == -1:

```

    model.SurfaceToSurfaceContactStd(adjustMethod=TOLERANCE,
        adjustTolerance=0.0005, clearanceRegion=None,
        datumAxis=None, initialClearance=OMIT,
        name='SoilPileS2S-C1A', createStepName = 'Initial',
        master=assembly-surfaces['pContactSurface1'],
        slave=assembly-surfaces['sConSurf-C1'],
        sliding=FINITE, interactionProperty = 'SoilPileContact')
    model.SurfaceToSurfaceContactStd(adjustMethod=TOLERANCE,
        adjustTolerance=0.0005, clearanceRegion=None,
        datumAxis=None, initialClearance=OMIT,
        name='SoilPileS2S-C1B', createStepName = 'Initial',

```

```

master=assembly-surfaces['pContactSurface2'],
slave=assembly-surfaces['sConSurf-C1'],
sliding=FINITE, interactionProperty = 'SoilPileContact')
model.SurfaceToSurfaceContactStd(adjustMethod=TOLERANCE,
adjustTolerance=0.0005, clearanceRegion=None,
datumAxis=None, initialClearance=OMIT,
name='SoilPileS2S-C1C', createStepName = 'Initial',
master=assembly-surfaces['pContactSurface3'],
slave=assembly-surfaces['sConSurf-C1'],
sliding=FINITE, interactionProperty = 'SoilPileContact')
model.SurfaceToSurfaceContactStd(adjustMethod=TOLERANCE,
adjustTolerance=0.0005, clearanceRegion=None,
datumAxis=None, initialClearance=OMIT,
name='SoilPileS2S-C2A', createStepName = 'Initial',
master=assembly-surfaces['pContactSurface6'],
slave=assembly-surfaces['sConSurf-C2'],
sliding=FINITE, interactionProperty = 'SoilPileContact')
model.SurfaceToSurfaceContactStd(adjustMethod=TOLERANCE,
adjustTolerance=0.0005, clearanceRegion=None,
datumAxis=None, initialClearance=OMIT,
name='SoilPileS2S-C2B', createStepName = 'Initial',
master=assembly-surfaces['pContactSurface7'],
slave=assembly-surfaces['sConSurf-C2'],

```

```
sliding=FINITE, interactionProperty = 'SoilPileContact')
model.SurfaceToSurfaceContactStd(adjustMethod=TOLERANCE,
adjustTolerance=0.0005, clearanceRegion=None,
datumAxis=None, initialClearance=OMIT,
name='SoilPileS2S-C3', createStepName = 'Initial',
master=assembly-surfaces['pContactSurface10'],
slave=assembly-surfaces['sContactSurface10'],
sliding=FINITE, interactionProperty = 'SoilPileContact') ### Contact pairs of soil-to-pile in
Comp
```

```
#-----
print 'Contacts are redefined! RITSS-'+str(simulationNumber)
```


REDEFINE BOUNDARY CONDITIONS

```
# Author: Weidong Li (weidong1@ualberta.ca)
# Edmonton, AB (Canada)
# Dec 2021
# *****

# This is the script that redefines the boundary conditions.

# Contact surface on pile
# Bottom of soil
soilBottomEdge = assembly.Set(edges=
    assembly.instances['insSoil'].edges.getByBoundingBox(
        sCoords[nNodeSoil-1,0]-0.05, sCoords[nNodeSoil-1,1]-0.05, 0.0,
        sCoords[nNodeSoil-2,0]+0.05, sCoords[nNodeSoil-2,1]+0.05, 0.0),
    name='BC_bottomSoil')
# The bottom side of the soil is fixed in all dof's
model.DisplacementBC(amplitude=UNSET, createStepName='Initial',
    distributionType=UNIFORM, fieldName="", localCsys=None, name='BC_bottomSoil',
    region=soilBottomEdge, u1=SET, u2=SET, ur3=UNSET)
#

# Right side of soil
soilRightEdge = assembly.Set(edges=
```

```

assembly.instances['insSoil'].edges.getByBoundingBox(
sCoords[nNodeSoil-2,0]-0.05, sCoords[nNodeSoil-2,1]-0.05, 0.0,
sCoords[nNodeSoil-3,0]+0.05, sCoords[nNodeSoil-3,1]+0.05, 0.0),
name='BC_rightSoil')
# The right side line of the soil is fixed in x
model.DisplacementBC(amplitude=UNSET, createStepName='Initial',
distributionType=UNIFORM, fieldName="", localCsys=None, name='BC_rightSoil',
region=soilRightEdge, u1=SET, u2=UNSET, ur3=UNSET)
#
#center line of soil
soilCenterEdge = assembly.Set(edges=
assembly.instances['insSoil'].edges.getByBoundingBox(
sCoords[nNodeSoil-1,0]-0.05, sCoords[nNodeSoil-1,1]-0.05, 0.0,
sCoords[nNodeSoil,0]+0.05, sCoords[nNodeSoil,1]+0.05, 0.0),
name='BC_centerSoil')
# center line of the soil is fixed in x
model.DisplacementBC(amplitude=UNSET, createStepName='Initial',
distributionType=UNIFORM, fieldName="", localCsys=None, name='BC_centerSoil',
region=soilCenterEdge, u1=SET, u2=UNSET, ur3=UNSET)
#
#center line of pile

```

```

pileCenterEdge = assembly.Set(edges=
    assembly.instances['insPile'].edges.getByBoundingBox(
    pCoords[0,0]-0.01, pCoords[0,1]-0.01, 0.0,
    pCoords[nNodePile-1,0]+0.01, pCoords[nNodePile-1,1]+0.01, 0.0),
    name='BC_centerPile')
# The center line of the pile is fixed in x
model.DisplacementBC(amplitude=UNSET, createStepName='Initial',
    distributionType=UNIFORM, fieldName="", localCsys=None, name='BC_centerPile',
    region=pileCenterEdge, u1=SET, u2=UNSET, ur3=UNSET)
#-----

#-----

#Create loads
#-----

# Disp. controlled load
dispIncre = 0.01 #each simulation increment is 10 mm
pileHeadEdge = assembly.Set(name='pileHeadLoadEdge',
    edges = assembly.instances['insPile'].edges.getByBoundingBox(
    pCoords[nNodePile-1,0]-0.01, pCoords[nNodePile-1,1]-0.01, 0.0,
    pCoords[nNodePile-2,0]+0.01, pCoords[nNodePile-2,1]+0.01, 0.0))

model.DisplacementBC(amplitude=UNSET, createStepName='Step-1',

```

```
distributionType=UNIFORM, fieldName="", fixed=OFF, localCsys=None, name=
'Penetration', region=pileHeadEdge, u1=
UNSET, u2=CT*dispIncre, ur3=UNSET)
#-----
#-----
print 'Boundary conditions are redefined! RITSS-'+str(simulationNumber)
```

SOLUTION MAPPING

```
# Author: Weidong Li (weidong1@ualberta.ca)

# Edmonton, AB (Canada)

# Dec 2021

# *****

# This is the script that maps the solution from the ancestor job to the remeshed job.

mdb.models['Model-

'+str(simulationNumber)].keywordBlock.synchVersions(storeNodesAndElements=False)

def whereIsLastBlock(keyword):

    blocks = mdb.models['Model-'+str(simulationNumber)].keywordBlock.sieBlocks

    for k in range(len(blocks)):

        b=blocks[k]

        if b[:len(keyword)] == keyword:

            break

    return k

modelBlock = whereIsLastBlock("*Step") - 1

model.keywordBlock.insert(modelBlock, """"*MAP SOLUTION""")

print 'Solution is mapped! RITSS-'+str(simulationNumber)
```

CREATE REMESHED JOB AND WRITE INPUT FILE

```
# Author: Weidong Li (weidong1@ualberta.ca)

# Edmonton, AB (Canada)

# Dec 2021

# *****

# This script writes the input file for remeshed job.

mdb.Job(name=remeshJobName, model='Model-'+str(simulationNumber), type=ANALYSIS,
        nodalOutputPrecision=SINGLE, description='Run the Number: ' + str(simulationNumber)
+'simulation',
        multiprocessingMode=DEFAULT,
        numDomains=3, userSubroutine="", numCpus=3, memory=80,
        memoryUnits=PERCENTAGE, scratch="", echoPrint=OFF, modelPrint=OFF,
        contactPrint=OFF, historyPrint=OFF)

#-----

model.setValues(noPartsInputFile=OFF)

mdb.jobs[remeshJobName].writeInput(consistencyChecking=OFF)

#Track all geometry vertices of the

for i in range(nNodePile):
    node=assembly.instances['insPile'].nodes.getClosest(((pCoords[i,0], pCoords[i,1], 0.0)),)
    nodeLabel=node[0].label
    assembly.SetFromNodeLabels('pileNodeSet'+str(i), (('insPile', (nodeLabel,)),))
```

```
#
for i in range(nNodeSoil):
    node=assembly.instances['insSoil'].nodes.getClosest(((sCoords[i,0], sCoords[i,1], 0.0)),)
    nodeLabel=node[0].label
    assembly.SetFromNodeLabels('soilNodeSet'+str(i), (('insSoil', (nodeLabel,)),))

mdb.jobs[remeshJobName].writeInput(consistencyChecking=OFF)
#-----

mdb.save()

print 'The Number: ' +str(simulationNumber)+'remeshed job is ready to submit!'
```

AN EXAMPLE OF MODEL GEOMETRY COORDINATE FILE

P2Config (Pile geometry, P2)	P2ClayConfig (Soil geometry, P2)
0.0 0.0	0.0 0.0
0.127 0.0	0.127 0.0
0.127 0.34925	0.127 0.34925
0.381 0.34925	0.381 0.34925
0.381 0.41275	0.381 0.41275
0.127 0.41275	0.127 0.41275
0.127 1.49225	0.127 1.49225
0.381 1.49225	0.381 1.49225
0.381 1.55575	0.381 1.55575
0.127 1.55575	0.127 1.55575
0.127 3.90525	0.127 3.381
0.0 3.90525	3.5 3.381
0.0 0.0	3.5 -1.746
	0.0 -1.746
	0.0 0.0